

Revista Brasileira de Ciências Mecânicas

Journal of the Brazilian
Society of Mechanical Sciences

4

PUBLICAÇÃO DA ABCM - ASSOCIAÇÃO BRASILEIRA DE CIÊNCIAS MECÂNICAS

VOL. XX - No.4 - DECEMBER 1998

ISSN 0100-7386

JOURNAL OF THE BRAZILIAN SOCIETY OF MECHANICAL SCIENCES

REVISTA BRASILEIRA DE CIÊNCIAS MECÂNICAS

REVISTA BRASILEIRA DE CIÊNCIAS MECÂNICAS
JOURNAL OF THE BRAZILIAN SOCIETY OF
MECHANICAL SCIENCES

Vol. 1. Nº 1 (1979)-

Rio de Janeiro: Associação Brasileira de Ciências
Mecânicas
Trimestral

Inclui referências bibliográficas.

1. Mecânica

ISSN-0100-7386

EDITOR

Leonardo Goldstein Jr
UNICAMP - FEM - DEFF - C.P. 6122
13083-970 Campinas SP
Tel.: (019) 289-3005 Fax: (019) 289-3722
E-Mail: abcm@fem.unicamp.br

EDITORES ASSOCIADOS

Agenor de Talaco Fleury
IPT - Instituto de Pesquisas Tecnológicas
Divisão de Mecânica e Eletricidade - Agrupamento de Sistemas de Controle
Cidade Universitária - C.P. 7141
01064-970 São Paulo SP
Tel.: (011) 268-2211 Ramal 504 Fax: (011) 869-3353
E-Mail: agfleury@ipt.br

Alisson Rocha Machado
Universidade Federal de Uberlândia
Departamento de Engenharia Mecânica - Campus Santa Mônica
38400-206 Uberlândia MG
Tel.: (034) 239-4149 Fax: (034) 235-0382
E-Mail: alisson@ufu.br

Angela Curvo Nêckele
Pontifícia Universidade Católica do Rio de Janeiro
Departamento de Engenharia Mecânica
Rua Marquês de São Vicente, 225 Gávea
22453-900 Rio de Janeiro RJ
Tel.: (021) 238-0719 Fax: (021) 294-9148
E-Mail: nêckele@mec.puc-rio.br

Hans Ingo Weber
Pontifícia Universidade Católica do Rio de Janeiro
Departamento de Engenharia Mecânica
Rua Marquês de São Vicente, 225 Gávea
22453-900 Rio de Janeiro RJ
Tel.: (021) 529-5323 Fax: (021) 294-9148
E-Mail: hans@mec.puc-rio.br

Paulo Eigi Miyagi
Universidade de São Paulo - Escola Politécnica
Departamento de Engenharia Mecânica - Mecatrônica
Avenida Prof. Mello Moraes, 2231
05508-900 São Paulo SP
Tel.: (011) 818-5080 Fax: (011) 818-5471/813-1886
E-Mail: pemiya@usp.br

Seyyed Said Dana
Universidade Federal da Paraíba
Centro de Tecnologia-Campus I
Departamento de Tecnologia Mecânica
58069-900 João Pessoa PB
Tel.: (083) 216-7356 Fax: (083) 216-7179
E-Mail: dana@ctm.cit.ufpb.br

CONSELHO EDITORIAL

Alcir de Faro Orlando (PUC-RJ)
Antonio Francisco Fortes (UnB)
Armando A. Berrazi Jr. (UFSC)
Alan Rios Neto (UNIVAP)
Benedito Moraes Paquetere (EESC-USP)
Carlos Alberto de Almeida (PUC-RJ)
Carlos Alberto Martin (UFSC)
Clóvis Ramundo Maliska (UFSC)
Emanuel Rocha Worski (UNESP-FEIS)
Francisco Emílio Baccaro Nogueira (IPT-SP)
Francisco José Simões (UFPA)
Genésio José Manoel (EFEI)
Henrique Rozenfeld (EESC-USP)
Jair Carlos Dutra (UFSC)
João Alzire Herz de Jornada (UFRGS)
José João de Espindola (UFSC)
Jutandir Iltis Yanagibara (FAP-USP)
Lino Schaefer (UFERS)
Lourival Boehs (UFSC)
Luis Carlos Sandoval Goes (ITA)
Marcio Ziviani (UFMG)
Maru Ussyri (EMBRACQ)
Moyses Zindeluk (COPPE-UFRR)
Nisio de Carvalho Leão Brum (COPPE-UFRR)
Nivaldo Lemes Coppini (UNI-CAMP)
Paulo Afonso de Oliveira Sovero (ITA)
Rogério Martins Saldanha da Gama (LNCC)
Valder Stelma Jr. (UFU)

A REVISTA BRASILEIRA DE CIÊNCIAS MECÂNICAS
publica trabalhos que cobrem os vários aspectos da
ciência e da tecnologia em Engenharia Mecânica,
incluindo interfaces com as Engenharias Civil, Elétrica,
Química, Naval, Nuclear, Aeroespacial, Alimentos,
Agrícola, Petróleo, Materiais, etc., bem como aplicações
da Física e da Matemática à Mecânica.

INDEXED BY Applied Mechanics Reviews
and Engineering Information, Inc..

Publicação da / Published by
ASSOCIAÇÃO BRASILEIRA DE CIÊNCIAS MECÂNICAS
THE BRAZILIAN SOCIETY OF MECHANICAL SCIENCES

Secretária da ABCM - Ana Lúcia Fróes de Souza
Avenida Rio Branco, 124 18º Andar
20040-001 Rio de Janeiro RJ
Tel.: (021) 221-0438/Fax: (021) 509-7128

Presidente: Carlos Alberto de Almeida
Vice-Presidente: Hans Ingo Weber
Secretário: Paulo Batista Gonçalves
Diretor de Patrimônio: Felipe Bastos de F. Rachid
Secretário Geral: Nestor Alberto Z. Pereira

Secretária da RBCM: Maria de Fátima Alonso de Sousa
UNICAMP - FEM - C.P. 6122
13083-970 Campinas SP
Tel.: (019) 788-3205/Fax: (019) 289-3722
E-Mail: abcm@fem.unicamp.br

REVISTA FINANCIADA COM RECURSOS DO

Programa de Apoio a Publicações Científicas

MCT



In Memoriam

Prof. Cirus Macedo Hackenberg (1941 – 1998)

Prof. Cirus Macedo Hackenberg was born in the first day of August, 1941, in Curitiba, Brazil. He received his B.Sc. in Chemical Engineering from the Federal University of Paraná, Brazil, in 1963, the M.Sc. degree from COPPE/UFRJ-Federal University of Rio de Janeiro, Brazil, in 1965, and the Ph.D. from the University of Florida, USA, back in 1969, both degrees in Chemical Engineering. His thesis work was on the "Unsteady Resistance of Spherical Submerged Bodies". He was nominated for the Phi Kappa Phi National Honor Society, USA, for academic excellence during his Ph.D. studies. He spent the year of 1973/1973 as a post-doctoral fellow at the Mathematics Department of the Imperial College, London, UK. He joined the faculty of the Chemical Engineering Department of COPPE in 1965, where he developed a brilliant academic career until December 1996, when he retired. He achieved the Full Professor position in 1976 at COPPE, only 35 years old, and later at UFRJ, in 1988. At the time of his death he was an Invited Distinguished Professor at the Mechanical Engineering Department of EE/COPPE, and Academic Coordinator of the Thermal Engines and Combustion Laboratory, at UFRJ.

His major research interests were in Applied Mathematics (Moving Boundary Problems, Integral Transforms, Functional Analysis, Tensor Fields), Two-Phase Flow Systems (Direct Contact Evaporation, Thermal Storage), and Thermal Radiation (Selective Surfaces, Combustion Chambers, Solar Energy). More recently, his research efforts were directed to the application of Integral Transforms in Heat Transfer Problems, specially in conjugated radiative-conductive phenomena, in collaboration with the Laboratory of Transmission and Technology of Heat, at COPPE. Along his career, Prof. Hackenberg published more than 85 journal and conference papers, supervised more than 40 M.Sc. and D.Sc. thesis at COPPE, and occupied various administrative and collegiate positions within the University.

He served in the Scientific Council of the International Center of Heat and Mass Transfer, Ankara, Turkey, since 1986. He was in the Editorial Board of the Latin American Journal of Chemical Engineering and Applied Chemistry, since 1974, of the Latin American Journal of Heat and Mass Transfer, since 1975, and founding member of the Honorary Editorial Board of the Hybrid Methods in Engineering Journal. In addition, he served in the organizing committees of several national and international conferences and meetings, including the First World Congress on Chemical Engineering, Amsterdam, 1976. He was elected full member of the National Academy of Engineering in 1991, Brazil, in recognition to his pioneering advanced research work in heat transfer and fluid dynamics within the country.

Besides his qualifications as a researcher and educator, Prof. Hackenberg was also admired for his deep and broad culture level, as well as for his personal concern with his students and colleagues, always ready to assist and, at least, give a good piece of advice. He left wife and two daughters.

Cirus Macedo Hackenberg was an outstanding scientist and human being. We, his friends and colleagues of ABCM the Brazilian Society of Mechanical Sciences, will miss him very much, much more than we could put down in words within this editorial.

Analysis of Impedance Probes Behavior Applied to Liquid Film Thickness Measurements

Milton Biage

Universidade Federal de Uberlândia
Centro de Ciências Exatas e Tecnologia
Departamento de Engenharia Mecânica
38400-902 Uberlândia, MG Brazil

Abstract

A study of impedance probes behavior (conductive and capacitive), aimed at liquid film thickness measurement, is presented. Theory, principle of operation, calibration and error sources are discussed. This study was encouraged by the need to find low-cost solutions for problems involving local and instantaneous fluid measurements. The equipment in question can be used to study the liquid-gas interface behavior and related flow instability. Also, results can be used for the development of closure conditions in two-fluid flow modeling. Analysis of the probes dynamic behavior was carried out employing the experimental results obtained for the liquid film flow on a vertical rectangular channel, exposed to a counter-current gas flow. This study confirmed that the probes presented good response in frequency and spatial resolution. In fact, they characterize efficiently the transition process of a concurrent to counter-current flow.

Keywords: Two-phase Flow, Liquid film Thickness, Conductive Probe, Capacitive Probe.

Introduction

Film flow is found in several industrial processes, such as: evaporation, condensation, distillation, natural gas mining, oil pumping through piping, fuel injection in internal combustion engine, etc. Due to the complex film flow structure in most of the applications, it is necessary to perform experimental studies to know about the typical phenomena in these processes. Measurement of the local and instantaneous liquid film thicknesses is essential to understand the flow instability mechanisms in liquid-gas interfaces. In this case, statistical treatment of the instantaneous film thickness, such as auto-correlation, cross-correlation, spectral density and cross-spectral density functions are carried out to obtain information related to wave formation and propagation, characterizing the flow transition mechanisms as a result. Many studies related to film flow patterns can be found in the literature. The example of the liquid film flow on a channel wall with a gas flow in the opposite direction is included in this paper (Biage, 1989a and 1989b).

Studies on liquid film thickness measurement techniques were performed by Solesio (1978). Who presented a critical analysis, after studying the advantages and disadvantages of several measurement methods. Some of the conclusions described in his paper are included in this introduction.

The liquid film thickness can be measured by two absorption techniques sharing the same functioning of principle: the γ rays and the X rays. The first type of rays are produced by radioactive sources, and the second one by X tubes. A source with a constant intensity emits a constant and radiant energy beam through the liquid film, which is collected by a proper photomultiplier. Beam intensity is attenuated by the liquid film, keeping an exponential relationship with liquid thickness. The γ rays absorption technique presents the inconvenience of allowing only mean film thickness measurements. Nevertheless, it offers as advantages the low cost and small dimension of the devices what makes handling easier. On the other hand, the X ray attenuation method allows measurement of high frequency phenomena, having also good spatial resolution (beam diameter of the order of 0.1 mm). However, it presents as disadvantages high cost, size and weight, being unsuitable for simultaneous film thickness measurement at several points of the flow.

Others techniques can be considered to measure the liquid film thickness. The Laser diffusion is still being developed. The light absorption technique is not appropriate for wavy film flow study and the cost is high. Photography technique requires a specific geometry to illuminate the channel, preferentially by a laser source, and requires special camera positioning. It has the disadvantage of measuring the liquid film thickness at only one point at a time, and it is an expensive technique. The fluorescence method demands the same equipment and special assembly as the photographic technique, and it is also expensive. However, the impedance probe allows the liquid film thickness to be measured

at various points simultaneously with low cost. It detects high frequency phenomena, has good precision and it is not expensive. Although is that it presents a limited spatial resolution.

Conductive probes are applied to conductor liquid film thickness measurements when the liquid film is in touch with a non-conductor surface. It is related to the measurement of the conductance of portion of the a liquid film limited by two electrodes, sited on the wall and in contact with the liquid, distanced in the axial flow direction. Geometrically different shaped probes were used by several researchers. Hewitt *et al* (1962) and Mikieliewics and Hammit (1974) used two disc-shaped electrodes installed flush with the duct surface. Van Rossum (1959), Telles and Dukler (1974) and Webb (1970) used rectangular-shaped electrodes, also installed flush with the duct surface. Zabaras (1985) used a probe constituted by two parallel conductor wires stretched through the duct, separated in the axial flow direction by a distance. This sort of probe has the inconvenience of restraining liquid drops in between the two wires, what disguises measurements on flows with disperse drops in the gas-phase. Van Rossum (1959), Wicks (1967), Pashniak (1969), Brown (1978) and Qinggen (1984) used probes with two electrodes, one of them attached to the duct wall, and the other, able to move through a micrometer, opposedly sited. Coney (1973) presented a theoretical study on conductive probes made up by two rectangular-shaped and two protected guard electrodes on the borders, to make the electric field two-dimensional.

The conductance probe technique presents the inconvenience of being applicable only to electricity conductor liquids. The relationship between conductance and liquid film thickness depends on the liquid resistivity, however, this relationship is a function of the impurity level and temperature, which vary during the course of the experiment and are difficult to control. Another relevant inconvenience on conductive probes is that sensibility decreases as the liquid film thickness increases, nevertheless, the simplicity of this technique is its essential advantage.

The capacitive probe is based on the measurement of the capacitance between an electrically insulated conducting electrode and the conducting liquid polarized by an excitation electrode attached flush to the wet channel wall. The impedance of the liquid between the exciting electrode and the conducting electrode in contact with liquid is much lower than the impedance between that exciting electrode and the part of the conducting electrode in contact with the gas. The capacitance between the electrode and the liquid film is a linear function of the liquid film thickness. This technique, employed to determine liquid film thickness in the order of 0.5 mm, flowing on vertical plates and tubes, was first used by Dukler and Bergelin (1952), Taylby and Portalski (1960), Ozgu *et al.* (1973), Chu and Dukler (1974). The probes used in these studies were practically similar and were made up by two electrodes, one attached to the duct wall, and the other, capable of being moved through a micrometer, opposedly sited. Generally, this probe setup uses electrodes with a relatively large diameter, causing the spatial resolution to decrease and turning the transition analysis difficult.

This study presents the experimental setup, principles of work, calibration and error sources' analyses for the conductive and capacitive probes. The conductance measuring probe presents an original pattern being constituted by two cylindrical electrodes, flush with the channel surface, having two guard electrodes in the outside edge, to eliminate edge effects. In addition, a mini-probe, which permits either temperature effects or liquid chemical composition changes to be corrected, is used. Advantages of this probe are that it is almost insensitive to temperature, the cost is lower, allows instantaneous measurements in several positions, and has a response of high frequency. The capacitive wire probe, is constituted by of an electrically insulated conducting wire stretched through the liquid film (0.1 mm wire diameter) and an exciting electrode attached flush to the wet channel wall. This probe configuration is original and presents a response of high frequency, good spatial resolution and is almost low sensitivity to the liquid temperature. The use of this configuration improves the probe sensitivity, due to more meaningful capacitance changes, besides providing a better spatial resolution, due to the small wire diameter.

The analysis of the probes dynamic behavior was carried out with the experimental results from the liquid film flow through a vertical rectangular channel, exposed to a countercurrent gas flow. The study confirmed the probes good response in frequency and spatial resolution, characterizing efficiently the transition process from a concurrent to a counter-current flow.

Conductive Probes

The conductance technique is applied to an electrically conductive liquid flowing on a non-conductive wall. The conductance of a film portion between two electrodes is measured. The electrodes can be mounted in two ways: (i) as a flush with the channel surface, and (ii) as two parallel

wires, perpendicular to the fluid flow. The conductive probe setup in this work has cylindrical-shaped exciting, measuring and guard electrodes. In addition, it has a mini-probe, which permits either temperature effects or liquid chemical composition changes to be corrected, is used on it.

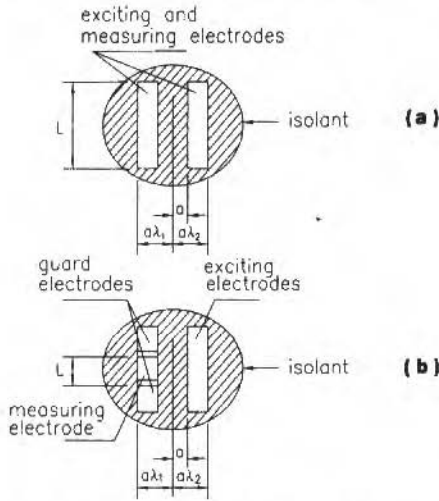


Fig. 1 Coney's probes: (a) with parallel rectangular electrodes, (b) with one electrode segmented (the measuring electrode is placed between two guard electrodes).

Coney (1973) presented a theoretical study for a two-dimensional geometry and for a uniform film thickness. In this study, the conductance, G , is defined as a function of the uniform film thickness, h , probe geometric parameters and the liquid conductivity, σ :

$$G = \sigma L f(h, a, \lambda_1 a, \lambda_2 a) \tag{1}$$

where a , L , λ_1 and λ_2 are as shown in Fig. 1, and f is a function to be determined. The non-dimensional form of Eq. 1 can be written as follows:

$$G^* = \frac{G}{l\sigma} = f^*(h^*, \lambda_1, \lambda_2) \tag{2}$$

where $h^* = h/a$. The determination of f^* theoretically or experimentally allows establishing a relationship between G^* and h^* .

Figure 2 shows the theoretical relation between G^* and h^* , obtained by Coney (1973), for various $\lambda = \lambda_1 = \lambda_2$. It can be seen that when the electrodes are close to each other (decreasing λ), the probe becomes saturated for a small h^* , which characterizes a decrease of the measurement interval of h . The relationship between G and h allows the calculation of the error $\Delta h/h$, as a function of the error $\Delta G/G$:

$$E_h = \frac{\Delta h}{h} = p \frac{\Delta G}{G} \tag{3}$$

where p is the error factor which can be determined from Eq. 2 and E_h is the relative error of h .

For non-saturation h , that depends of λ , as shown in Fig. 2, p is small and invariable. When saturation is reached for a relatively high h , the factor p increases considerably and, consequently, E_h as well.

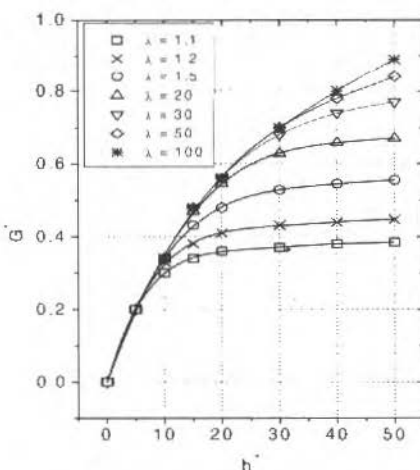


Fig. 2 Probe characteristics for various λ ($\lambda = \lambda_1 = \lambda_2$).

It should be mentioned that a two-dimensional model is valid only when distances between the external edges of the electrodes ($a\lambda_1$ and $a\lambda_2$) are small in comparison with the length L . However, if two guard electrodes are used, the real behavior approaches the two-dimensional theoretical behavior, even for a relatively high $a\lambda/L$.

The load transfer between the electrode solid surfaces and the liquid film are important parasitic phenomenon to be considered. This double layer phenomenon is characterized by a transfer of electrons between the two ion layers. The electron transfer happens in between the electrode surface and the liquid film surface which it is in contact with (Coney, 1973). When voltage is applied, the exciting electric current will be a function of the liquid film resistance and the capacitive effect produced by the double layer. The liquid resistance is a function of the film thickness. In practice, the equivalent electric circuit can be represented by a serial connection of a capacitor and resistor. In this case, the excitation frequency influences the liquid film thickness measurement. The excitation frequency has to be high enough, so that the capacitive impedance may be negligible compared to the resistance produced by the liquid film thickness. Moreover, electrochemical effects of the double layer must be considered. These effects are minimized when the exciting signal is alternated and the signal frequency is boosted.

With this type of probe, an increase of 1°C in the liquid temperature increases its conductivity by 2.5% (Coney, 1973). Thus, a small temperature change in the liquid leads to a significant measurement error since the conductance is proportional to the liquid conductivity. Coney (1973) suggests that temperature effects should be corrected by means of a complementary probe. The current I_c transmitted by the correcting probe and the current I_m transmitted by the measuring electrode are proportional to the liquid conductivity. Therefore, the ratio

$$D = \frac{I_m}{I_c} \quad (4)$$

is only a function of h . In the theoretical analysis of Coney (1973), no studies were made on either the temperature effect on the liquid conductivity or on the use of an adequate excitation frequency. Besides what, none of researchers used this kind of probe.

Capacitive Wire Probe Principle

This technique is based on the measurement of the capacitance existing between an electrically conducting wire insulated with a Teflon coating, stretched through the liquid film and the conducting liquid which is polarized by an exciting electrode attached flush to the wet channel wall. The liquid impedance between the excitation electrode and the part of the wire immersed in the liquid is much

lower than the impedance between that electrode and the part of the wire immersed in the gas. Thus, the film liquid measurements are not affected by the presence of gas flow. The capacitance between the wire and the liquid film is a linear function of the liquid film thickness. This probe offers three advantages:

- The relation between the capacitance and the liquid film thickness is linear, allowing thick liquid film measurements without saturation. (Conductive probes attached to the duct wall become unnoticeable when the film is very thick.);
- Spatial resolution is equivalent to the wire diameter, allowing high resolution measurements;
- Temperature effects are much milder than for conductive probes. The non-conductive Teflon permittivity coating is a function of the temperature, namely, $0.5\%/^{\circ}\text{C}$, while the water conductivity variation is $2.5\%/^{\circ}\text{C}$. The temperature effect for the capacitive wire probe is five times smaller than that of conductive probes. However, this effect for the capacitive wire probe is 1.5 times higher if compared to the flush conductive probes with temperature effect corrections. (Figs. 13 and Eq. 13).

A disadvantage of the capacitive wire probe is the flow disturbance, both in the liquid and the air. According to Gagliardini (1986), wakes with lengths of about 50 mm are produced by the wire in the flow.

Several kinds of electrodes have been used in probes for measuring liquid film thickness by the capacitive principle, as shown by Rogovaya et al. (1986), Ozgu et al. (1973), Solesio (1978) and Sun (1982). None of them, however, used a capacitive wire of a small diameter installed transversely in the duct to make the measurement as local as possible, as we have used. The electric diagram used in this study is presented in Fig. 3. The parameters indicated in this figure are as follows: R_L is the equivalent liquid film resistance between the excitation electrode and the wire; C_{wire} is the capacitance between the liquid film and the insulated wire; C_p is the capacitance of the wall, which in this case is Plexyglass; C_m is the counteraction capacitance of the amplifier; R_m is the counteraction resistance; R_g is the resistance of the generator; C_{L1} and C_{L2} are capacitances of the lines; and V_e and V are the excitation and output voltages. The actual electric circuit of the probe (Fig. 3b) simulates the behavior of the ideal circuit (Fig. 3a) only when its operational conditions are as follows:

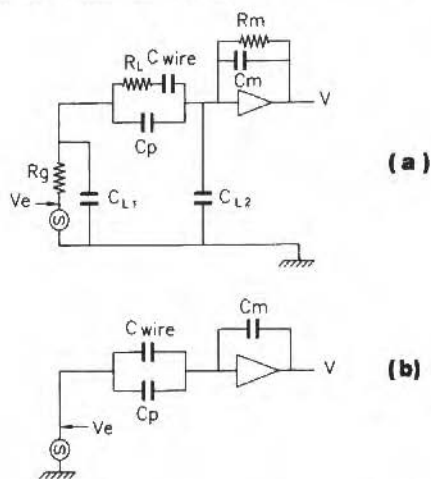


Fig. 3 (a) Capacitive wire probe electric circuit (ideal circuit) and (b) Actual electric circuit

- a. The excitation frequency F_e is comprised in the interval:

$$\frac{1}{2\pi R_m C_m} \leq F_e \leq \frac{2}{2\pi R_f C_{wire}} \quad (5)$$

Under this operational condition, resistances R_m and R_L are negligible and hence, the temperature effect is meaningless as well. The elimination of temperature effects on the wall is highly desirable;

- b. The restriction imposed by Eq. 5 must be followed. In addition, the parameters R_g , $C_{1,1}$ and $C_{1,2}$ also influence the circuit transfer function. Thus, an empirical way to select the adequate F_c range, is measuring the evolution of the output voltage V with frequency F_e (as shown in Fig. 12).

If the operational conditions described above are followed, the transfer function of the system, H , reads:

$$H = \frac{V}{V_e} = \frac{C_{wire} + C_p}{C_m} \quad (6)$$

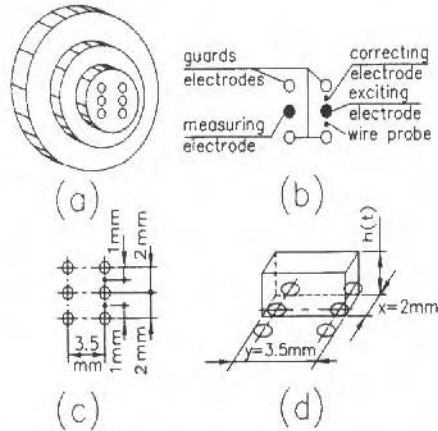


Fig. 4 (a) Probe layout, (b) Functional description of each electrode, (c) Electrode positions and (d) Measurement volume.

From Eq. 6 it follows that the transfer function depends only on C_{wire} , which is a function of the film thickness h , since the remaining parameters are independent of h . Calibration consists of measuring the normalized voltage (V/V_e) as a function of h , enabling the determination of the relation between C_{wire} and h .

Probe Behavior (Gauging and Analysis)

Figure 4 shows details of the probes used in our study. The measuring station consists of a double probe: a capacitive wire probe and a conductive probe flush to the duct wall. Figure 4b shows eight electrodes, seven of them embedded in the duct wall, making up the conductive probe. The exciting electrode of 1.5 mm diameter (Fig. 4b) is also connected to the capacitive wire probe. Furthermore, there is a measuring electrode of 1.5 mm diameter, two guard electrodes, also of 1.5 mm diameter and a temperature-correction electrode of 0.2 mm diameter (Fig. 4b). A 0.07 mm diameter wire coated with a Teflon insulating film (Fig. 4b) and installed transversely across the channel cross-section, together with the exciting electrode, make up the capacitive wire probe.

The conductance measuring technique is based on the conductance measurement between the exciting electrode and the measuring electrode (Fig. 4b), separated one from each other by 3.5 mm (Fig. 4c). The relation between the film conductance and the film thickness, h , is nonlinear, (Fig. 2). Two guard electrodes are placed on both sides of the measuring and exciting electrodes (Fig. 4b), to eliminate edge effects. It is possible to correct the temperature effect with a small electrode (Fig. 4b). The small size of this electrode (0.2 mm diameter), associated with the small distance (0.2 mm) separating it from the exciting electrode ensure current saturation for small liquid film thicknesses. Conductivity variations of the same magnitude produce interference that has the same proportional effect on the measuring and correcting signals. Thus, the temperature effects are compensated for by dividing the two signals. The spatial resolution of this type of probe is provided by the measurement volume (Figs. 4c and 4d).

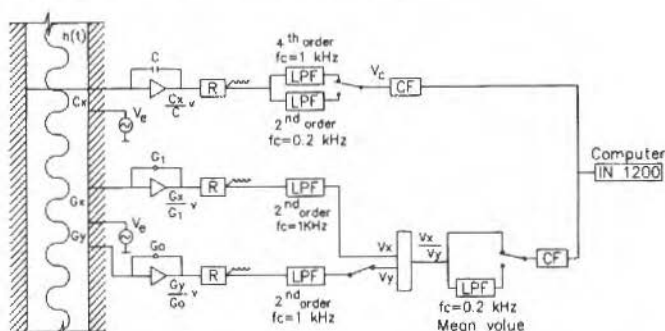


Fig. 5 Measurement process block diagrams.

Figure 5 shows the measurement process blocks diagram. The upper part shows the chain corresponding to the capacitive wire probe. The signal, generated by a voltage source V_e and a frequency F_e , is transmitted through the capacitance C_x , that is proportional to the film thickness. This signal is conditioned in the following stages:

- Pre-amplification of the signal, ensuring linearity between measuring voltage V_e and C_x ;

$$V_c = V_e \frac{C_x}{C} \quad (7)$$

where C is the counteraction capacitance of the amplifier;

- Rerouting of the alternate current signal, to eliminate the carrier frequency;
- A low-pass filter (LPF) with a high cutoff frequency (1 kHz) which provides the instantaneous signal, and a low-pass filter (LPF) with a low cutoff frequency (0.2 kHz) which provides the mean signal;
- Filtering through a fourth-order Chebychev filter (CF) with adjustable frequency and a nearly graded cutoff, which makes possible to lower the acquisition frequency.

The lower part of Fig. 5 shows the measuring chain for the conductive probe. The signal generated by the voltage V_e and frequency F_e source is transmitted two ways. On one side, through a conductance G_x that characterizes the measurement and, on the other side, through a conductance G_y , that characterizes the correction of the temperature effect on the water conductivity. These two signals are treated in the following stages:

- The signal is preamplified to ensure linearity between output voltages V_x and V_y and conductance G_x and G_y , respectively:

$$V_x = V \frac{G_x}{G_l} \quad (8)$$

$$V_y = V \frac{G_y}{G_0} \quad (9)$$

where G_0 , G_l are the counteraction conductances;

- Division of V_e by V_y in order to eliminate the temperature effect;
- The stages not mentioned are similar to the ones described in connection with the chain corresponding to the capacitive wire probe.

Calibration and Analysis of the Conductive Probe

The conductive probe was calibrated in an acrylic resin box. The box was kept filled with water and the film thickness was adjusted, in steps of 0.005 mm, displacing an insulating wall in front of the sensor. The insulating wall was driven by a 1 μm pitch screw micrometer. The water temperature inside

the box was kept constant. In order to homogenize the water temperature, the gauging box was placed on a magnetic agitator.

The probe was fed with a 60 kHz alternating current. This excitation frequency was fixed within the frequency range (10 kHz < Fe < 75 kHz) in which the impedance produced by the double layer was proportionally negligible concerning the resistance of the liquid film (Fig. 6). Also, the impedance produced by the capacitance of the material between the electrodes was sufficiently high compared to the liquid film resistance. Figure 7, curves (a) and (b), shows the gauging curves for both probes, measurement probe and temperature correcting probe, respectively.

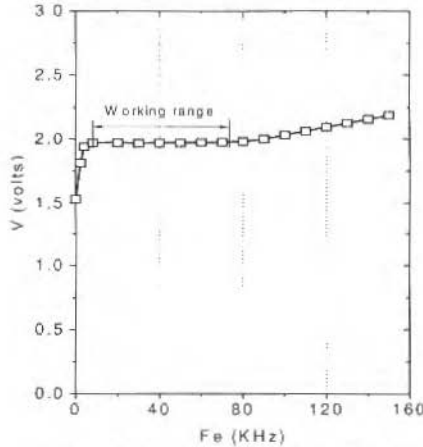


Fig. 6 Measuring voltage as a function of the excitation frequency.

The gauging curve was adjusted, with correction of the temperature effect by a second-degree polynomial. The dependent variable X is defined as:

$$X = -\ln\left(1 - \frac{V}{V_s}\right) \tag{10}$$

where V is the measuring voltage and V_s is the saturation voltage, that is, the voltage corresponding to a considerably large film thickness (in this case 19.6 mm). The ratio V/V_s was used to change the set of gauging curves into a standard one, not depending on the gain adjustment of the measuring chain. This was the procedure adopted by Biage (1989a) in his experimental analysis of the flooding phenomenon.

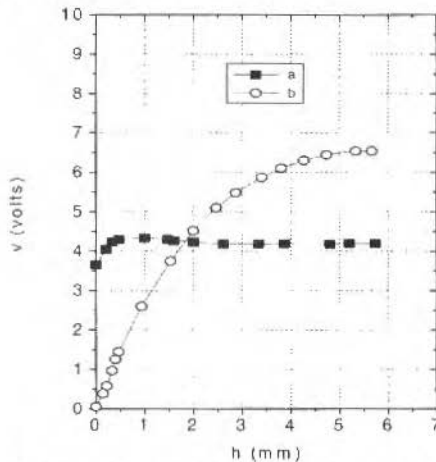


Fig. 7 Measuring voltage as a function of the liquid film thickness: (a) Measurement probe and (b) Temperature correcting probe.

Figure 8 shows the adjusted curve of one of the probes. It can be seen that the ratio between h and x is nearly linear and has the same value for all measuring stations. The correlation coefficient of the polynomial is 0.999 and the average interpolation error for all probes is less than 2%.

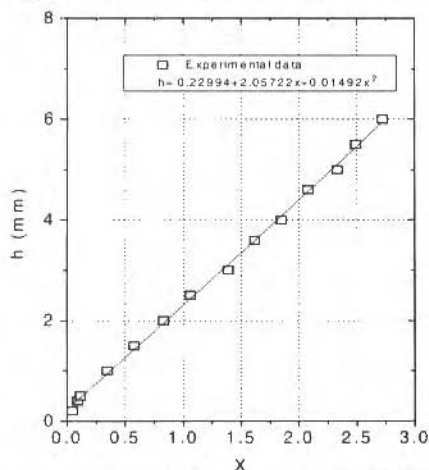


Fig. 8 Gauging curve fitting for the second-degree polynomial.

A pitch factor I_c can be defined as the ratio between the relative conductance increments, $(\Delta V/V = \Delta G/G)$ corresponding to a temperature increment ΔT :

$$I_c = \left(\frac{\Delta V}{V} \right) \frac{100}{\Delta T} \quad (11)$$

Figure 9 presents I_c as a function of h , for measurements with and without temperature correction. This figure shows that for $h=0.2$ mm, the temperature effect on the water conductivity can be satisfactorily corrected. In the linear portion of the curves $I_c = 2.44\%/^{\circ}\text{C}$ for measurements without temperature correction. This I_c is very close to the calculation made by Coney (1973), who found $I_c = 2.5\%/^{\circ}\text{C}$. For measurements with temperature corrections, $I_c = 0.3\%/^{\circ}\text{C}$. Therefore, the correction attenuates the temperature effect by a factor of about 8.

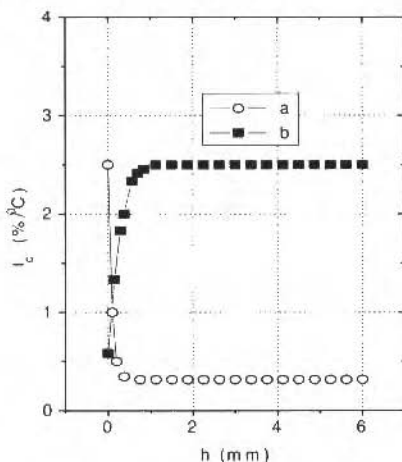


Fig. 9 Conductance pitch factor for the conductance as a function of the liquid film thickness: (a) With temperature correction and (b) without temperature correction.

Similarly to I_t , a pitch factor I_h can be defined by the ratio between the relative film thickness increment ($\Delta h/h$) and a corresponding temperature increment (ΔT):

$$I_h = \left(\frac{\Delta h}{h} \right) \frac{100}{\Delta T} \quad (12)$$

The relative increment of the film thickness ($\Delta h/h$) is related to the relative conductance increment ($\Delta V/V$) by Eq. 3. In this equation, p is estimated by the method of Coney (1973). Figure 10 shows I_h as a function of h , for measurements with and without temperature correction once more. This figure shows that the correction considerably reduces the temperature effect on the water conductivity: for measurements within the operational range ($0.2 \text{ mm} < h < 4 \text{ mm}$), I_h is approximately $0.5\%/^\circ\text{C}$ for measurements with temperature correction, compared to an average of about $4.10\%/^\circ\text{C}$ for measurements without it.

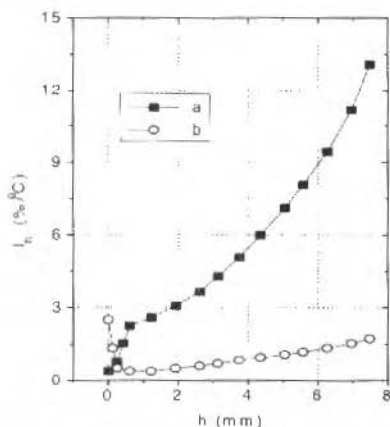


Fig. 10 Pitch factor for the liquid film thickness as a function of the film thickness: (a) With temperature correction and (b) without temperature correction.

To highlight the need of a temperature correction, Fig. 11 shows typical curves of liquid film and air flow temperature as a function of the gas superficial velocity, for a gas-liquid counter-current flow in a vertical rectangular channel (Biagi, 1989a and c). These temperatures were measured before the fluids were injected into the test channel, in a liquid closed circuit, with a cooled storage tank. The figure shows that the difference between water and air temperatures can grow up to 18°C . Therefore, there is an unknown temperature profile in the liquid film due to the heat exchange between the liquid and air flows. Researchers who have been using this type of probe have not considered this.

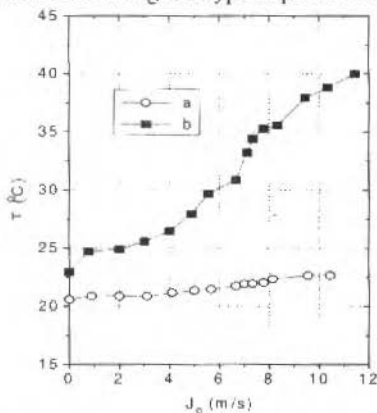


Fig. 11 Temperature at the 3.2 measuring position (Fig. 14), as a function of the superficial gas velocity, J_g : (a) liquid film and (b) air flow

Calibration and Analysis of the Capacitive Wire Probe

Figure 12 shows the output voltage V as a function of the excitation frequency F_e . The voltage remains nearly constant for:

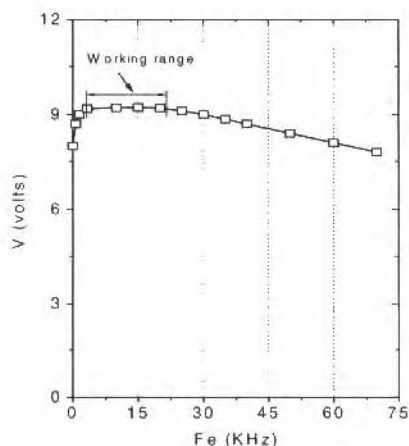


Fig. 12 Output voltage as a function of the excitation frequency

$$1\text{kHz} \leq F_e \leq 20\text{kHz}$$

(13)

As explained before, for $F_e > 20$ kHz, various parameters such as C_{wires} , C_{L1} , C_{L2} , C_p , and particularly R_f , have an influence on the transfer function, H . Therefore, the probe was gauged at a frequency within the working range, namely, 10 kHz, aiming to eliminate the effect of these parameters.

This probe was calibrated for the flooding experiments carried out by Biage (1989a). The capacitive wire probe output voltage was related to the average film thickness, measured with the conductive probe. The experiment is characterized by a liquid film flowing downward along the walls of a rectangular vertical channel and a gas flowing upward in counter-current.

Figure 13 shows the liquid film thickness as a function of (V/V_e) , where V_e is the excitation voltage. The output voltage (V) was normalized by V_e , to obtain curves independent of V_e . An excellent correlation coefficient (0.999) was obtained. The curve did not show any hysteresis.

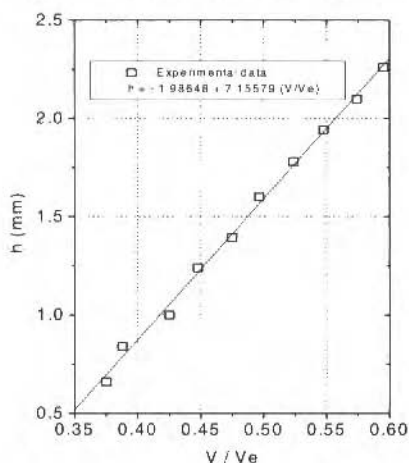


Fig. 13 Liquid film thickness as a function of (V/V_e) for the capacitive wire probe

Because the wire capacitance (C_{wire}) is linearly related to film thickness h , the relative increment on h , $\Delta h/h$, is equal to relative increment $\Delta C_{wire}/C_{wire} = V/V_e$. A pitch factor for h can be defined as follows:

$$I_h = \frac{\left(\frac{\Delta h}{h}\right) \times 100}{\Delta T} = \frac{\left(\frac{\Delta C_{wire}}{C_{wire}}\right) \times 100}{\Delta T} \quad (14)$$

The equality in Eq. 14 was observed by Gagliardini (1986), who found $I_h = 0.5\%/^{\circ}\text{C}$.

Dynamic Behavior of Probes

The data obtained from a study on a liquid film flow, downwards along the walls of a rectangular channel, counter-current to a gas flows are used to evince the probes dynamic behavior. Fig. 14 presents the probes setting scheme and the distance in between them, as well as the channel length. The probes were mounted along the axial direction and classified by numbers. Probe 5.2 was mounted near the point of liquid injection, and probe 1.2, near the point of liquid extraction.

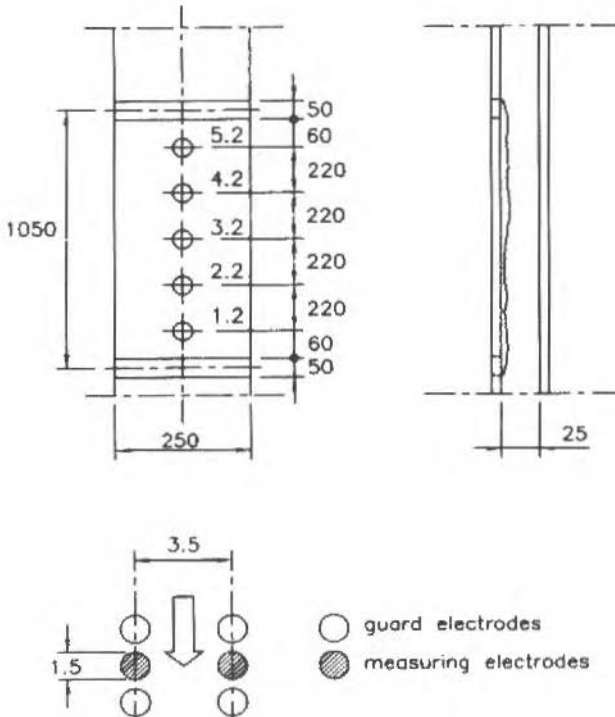


Fig. 14 Scheme of the test section (all dimension in mm).

The dynamic behavior of capacitive and conductive probes can be observed in Figs. 15 to 23. Figs. 15 and 16 show time histories of the liquid film thickness for a gas superficial velocity equal 9.32 m/s, close to the flooding velocity. The flooding velocity represents the gas superficial velocity that causes the concurrent flow transition to the countercurrent flow. The data shown in Figs. 15 and 16 were measured simultaneously.

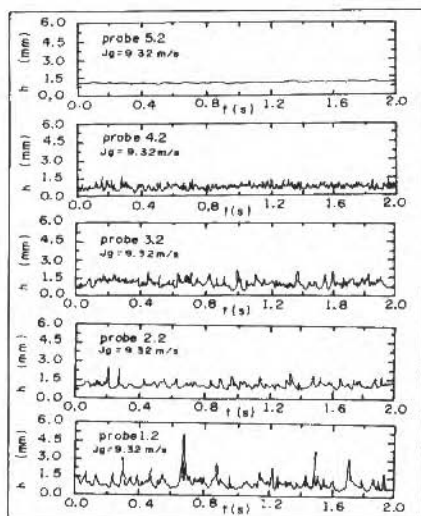


Fig. 15 Liquid film thickness time histories obtained with a capacitive probe in the 1.2 position, for $J_l=0.022$ m/s, $J_g=9.32$ m/s (close to the flooding velocity) and $L=1.05$ m.

The liquid and gas superficial velocities, J_k with $k=l$ or g , are defined by

$$J_k = \frac{Q_k}{A}, \quad \text{with } k=l \text{ or } g \quad (15)$$

where Q_k is either the liquid or gas volume flux per unit of channel width and A is the channel cross-section.

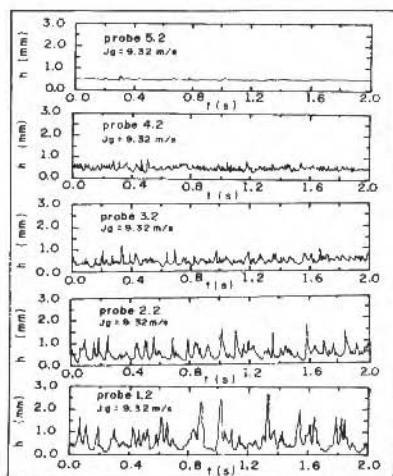


Fig. 16 Liquid film thickness time histories obtained with a conductive probe in the 1.2 position, for $J_l=0.022$ m/s, $J_g=9.32$ m/s (close to the flooding velocity) and $L=1.05$ m.

A comparison between Figs. 15 and 16 indicates very similar results for all positions, excepting the average values showed by the two kinds of probes, lightly different. The mean value measured at position 5.2 presents a particularly larger difference between the measurements performed by the probes. It occurs because of the highly complex flow pattern, caused by the drop deposition when the

gas superficial velocity approaches the flooding velocity, as the case showed on Figs. 15 and 16. The drops are drawn from the gas-liquid interface in the low region of the film and carried by the gas to the upper portions of the channel, the drops deposit on both the gas-liquid interface and on the opposite wall of the channel, being more intense in the region where probe 5.2 is located. Due to the presence of liquid on the channel opposite wall the measured film thickness increases, since the capacitive wire probe crosses the duct. Therefore, this regular difference in the average thickness is caused by an unique flow feature, and not by probe errors. It does not occur with the conductive probe because it is noticed only on the channel wall. This fact will be enhanced better below.

In general, dynamic responses for both probe types are similar. However, the amplitudes given by the capacitive probe 1.2 are much higher than the ones given by the conductive probe 1.2. This fact is a consequence of a conductive probe saturation effect for thicknesses above 3 mm, as explained before. Such effect considerably compromises the measurement accuracy of conductive probes.

Figure 17 shows the influence of the gas superficial velocity in the probability density function, $pdf(h)$, for both conductive and capacitive probes, at the position 5.2 and 1.2, respectively.

The $pdf(h)$ is defined by

$$pdf(h) = \lim_{w \rightarrow 0} \frac{P(h, w)}{w} \quad (16)$$

where $P(h, w)$ is the probability in which a numeric sequence, $h(t)$, presents values within the following interval:

$$\left(h - \frac{w}{2} \right) \leq h \leq \left(h + \frac{w}{2} \right) \quad (17)$$

w being a fixed window. $P(h, w)$ can be defined as

$$P(h, w) = \frac{N_h}{N} \quad (18)$$

N_h is the value numbers of $h(t)$ beyond the interval defined by Eq. 17 and N is the total value numbers of the sequence $h(t)$.

Figures 17a and 17b show the film structure obtained by a conductive and a capacitive probe, respectively, at the position 5.2, close to the injection liquid, for several gas superficial velocities. The film structure showed by these figures are completely similar, for gas superficial velocities lower than the flooding velocity. The $pdf(h)$ represented by these figures presents a narrow base that widens when the gas superficial velocity increases. In the film region, at the position 5.2, the structure of the gas-liquid interface is constituted by ripples (small capillary waves). This wave structure changes when the gas superficial velocity increases, since the interfacial shear stress also increases. As the flooding velocity is reached, the $pdf(h)$ characteristic obtained by the two kinds of probes is significantly different (curves d on the Figs. 17a and 17b). The $pdf(h)$ obtained with the conductive probe measurements (curve d on the Fig. 17a) shows the maximum probability value in a lower value of $h(t)$ (compared to the other curves for lower J_g). This behavior characterizes a decrease of liquid flowing down in the transition process (flooding) due to the partial dragging of the liquid film to the channel part above the liquid injection. On the other hand, the $pdf(h)$ obtained with the capacitive wire probe measurements (curve d on the Fig. 17b) does not show the maximum probability value for a lower value of $h(t)$, compared to the other curves for lower J_g , as it was expected. As explained above, the drop deposition on the opposite wall of channel which always take part in the measurements of liquid film with capacitive wire probe, causer the average liquid film thickness to increase. This does not occur with the conductive probe because the phenomena is noticed only at the channel wall.

Figures 17c and 17d show the film structure obtained by a conductive and a capacitive probe, respectively, at the position 1.2, 0.88 m below of the position 5.2. The remarks are the above, when comparing Figs. 17a and 17b. However, the film structure in the region surrounding position 1.2 is characterized by large amplitude waves, developed along the channel due to the gravitational effect. These waves flatten the $pdf(h)$, due to the intense fluctuation of the film liquid. Additionally, one can remark observe that the liquid film patterns two zones with clearly different structures the first is a

smoothed zone, near the liquid injection point, involving position 5.2, characterized by ripples (small capillary waves). The second zone takes place close to liquid withdraw, involving position 1.2, being characterized by large amplitude waves, that develop along the channel due to the gravitational effect (see Figs. 15 and 16). When J_g gets close to flooding, the wave amplitudes along the film increase (more significantly in the first zone). It brings about the homogenization of the interface structure along the whole channel, causing meaningful changes in its structures. This fact is responsible for the flatness of the pdf(h) base when J_g increases.

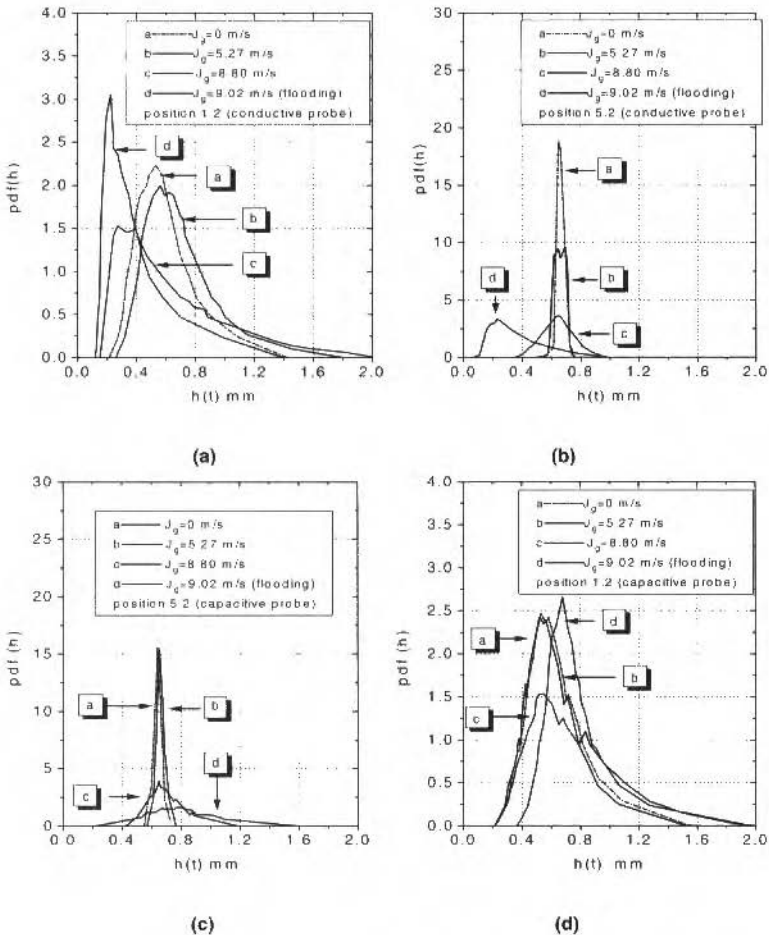


Fig. 17 Influence the gas superficial velocity in the probability density function of the liquid film thickness, for $J=0.035$ m/s. (a) position 5.2 (conductive probe), (b) position 5.2 (capacitive probe), (c) position 1.2 (conductive probe) and (c) position 1.2 (capacitive probe).

The behavior of the probes being studied is better characterized by time cross-correlation functions. Such sort of function is a similarity measurement of a variable - the liquid film thickness, in this application - taken in two different positions. Thus, the similarity of a variable is taken at a certain instant, t , obtained at a certain position, and its correspondent value at a later instant, $(t + \tau)$, obtained at a different position from the first. Periodic, or almost periodic signs keep their similarity through time and when are spatially dislocated. Therefore, the similarity rate is given by the predominance of a peak on the intercorrelation curve (Bendat and Piersol, 1986).

The cross-correlation function is calculated, in this study, for samples $x(t)$ and $y(t)$, obtained at two different positions and according to the following steps:

- Compute the 2N-point FFT for a complex number, giving $Z(k)$, for $k=0, 1, \dots, 2N-1$, where the first N points in $Z(k)$ are the real part and the last N points are the imaginary part. In this step obtain the $X(f_k)$ and $Y(f_k)$ values that correspond to the finite Fourier transform for $x(t)$ and $y(t)$;
- Compute the two-sided cross-spectral density function, $S_{xy}(f_k)$, estimated from

$$s_{xy}(f_k) = \frac{1}{N\Delta t} \sum_{n=0}^{N-1} \left\{ X^*(f_k) Y(f_k) \right\} \quad (19)$$

where $X^*(f_k)$ is the complex conjugate of $X(f_k)$ and Δt is the sampling time;

- Compute the inverse FFT of $S_{xy}(f_k)$ to obtain the cross-correlation, $R_{xy}(r\Delta t)$ for $r=0, 1, \dots, N-1$;
- Multiply $R_{xy}(r\Delta t)$, $r=0, 1, \dots, N-1$, by the scale factor $N/(r-N)$, to obtain the unbiased cross-correlation.
- The cross-correlation coefficient function, $C_{xy}(\tau)$, is the cross-correlation normalized as follow

$$C_{xy}(\tau) = \frac{R_{xy}(\tau)}{\left[R_{xx}(0) R_{yy}(0) \right]^{1/2}} \quad (20)$$

where τ is the delay time, $R_{xx}(0)$ and $R_{yy}(0)$ are the auto-correlation of the $x(t)$ and $y(t)$ samples, respectively, with zero delay time.

Figures 18 to 21 show the cross-correlation coefficient function between two successive positions for the conductive probe and the capacitive wire probe, respectively. The results presented in these figures refer to $J_g=0.053$ m/s and $L=1.05$ m, with $J_g=7.84$ m/s and $J_g=8.19$ m/s, respectively.

Figures 18 and 19 are for $J_g=7.84$ m/s corresponding to the previous flooding point and Figs. 20 and 21 are for $J_g=8.18$ m/s corresponding to the resulting flooding point. The flooding point represents the concurrent flow transition to countercurrent flow. The cross-correlation function presented a well-defined peak for all gas superficial velocities studied. Noticeable changes are observed between Figs. 18 and 20, referred to the capacitive wire probe; and between Figs. 19 and 21, referred to the conductive probe. This changing cross-correlation aspect defines the transition flow, similarly as was observed in the flow visualization by camera, as described in Biage (1989a). It is remarkable that the transition flow described with the two probes is completely similar.

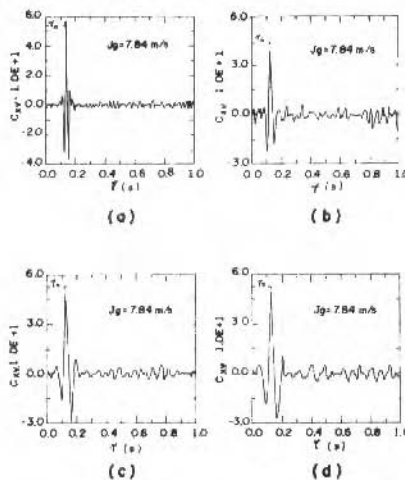


Fig. 18 Cross-correlation coefficient function between two successive positions by capacitive probes, for $J_g=0.053$ m/s, $J_g=7.84$ m/s and $L=1.05$ m: (a) between the probes 5.2 and 4.2, (b) between the probes 4.2 and 3.2, (c) between the probes 3.2 and 2.2 and (d) between the probes 2.2 and 1.2.

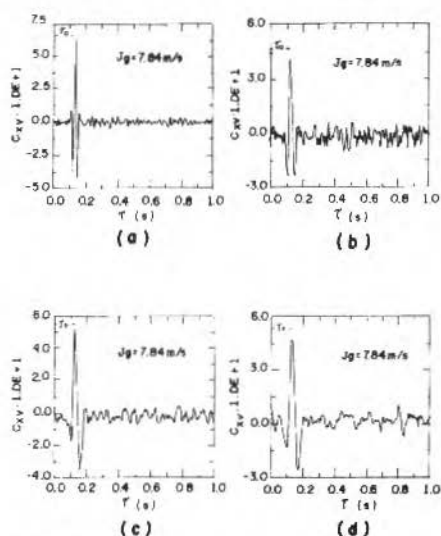


Fig. 19 Cross-correlation coefficient function between two successive positions by conductive probes, for $J_f=0.053$ m/s, $J_g=7.84$ m/s and $L=1.05$ m: (a) between probes 5.2 and 4.2, (b) between probes 4.2 and 3.2, (c) between probes 3.2 and 2.2 and (d) between probes 2.2 and 1.2.

We have evaluated the cross-correlation for a large range of gas superficial velocities, involving superficial velocities larger than those of transition flow. For all cases, the cross-correlation presented a peak, characterizing the signal correlation coefficient. The delay time, τ_0 , determined by this peak allows to evaluate the wave celerity:

$$C = \frac{d}{\tau_0} \quad (19)$$

where d is the distance between two consecutive probes.

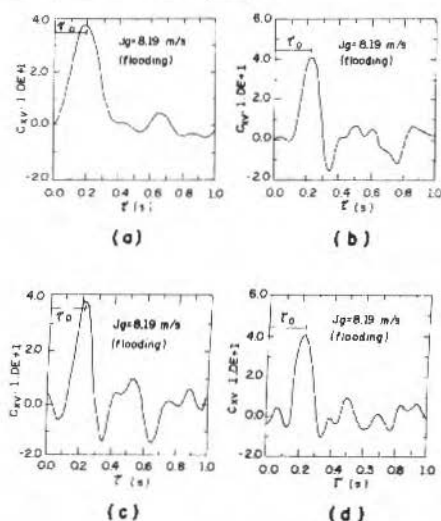


Fig. 20 Cross-correlation coefficient function between two successive positions by capacitive probes, for $J_f=0.053$ m/s, $J_g=8.19$ m/s and $L=1.05$ m: (a) between probes 5.2 and 4.2, (b) between probes 4.2 and 3.2, (c) between probes 3.2 and 2.2 and (d) between probes 2.2 and 1.2.

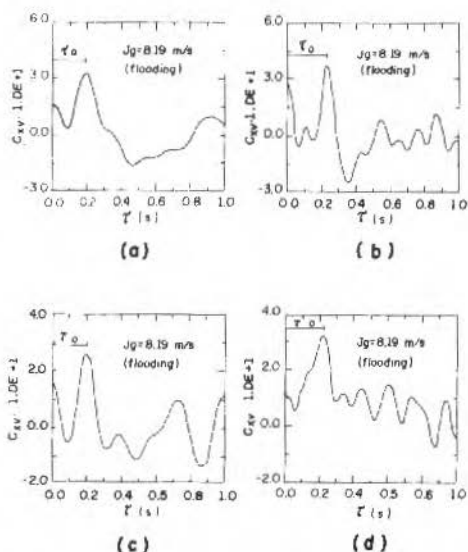


Fig. 21 Cross-correlation coefficient function between two successive positions by conductive probes, for $J_c=0.053$ m/s, $J_g=8.19$ m/s and $L=1.05$ m: (a) between probes 5.2 and 4.2, (b) between probes 4.2 and 3.2, (c) between probes 3.2 and 2.2 and (d) between probes 2.2 and 1.2.

Figures 22 and 23 show the wave celerity evaluated by the conductive probe and the capacitive wire probe. In these figures the maximum relative error was 3% for all range of gas superficial velocities studied. Additionally, both probes showed efficiently characterized the transition from concurrent to counter-current flow, a fact that is enhanced in Figs. 21 and 22 by the serious reduction of wave celerity during the flooding.

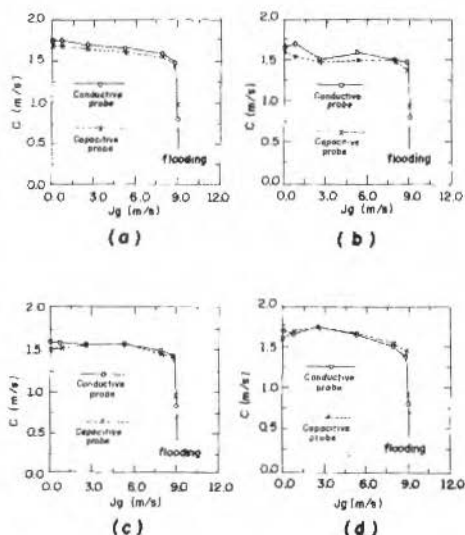


Fig. 22 Wave celerity evolution as a function of the gas superficial velocity, measured by conductive probes and capacitive probes, for $J_c=0.035$ m/s and $L=1.05$ m: (a) between probes 5.2 and 4.2, (b) between the probes 4.2 and 3.2, (c) between the probes 3.2 and 2.2 and (d) between the probes 2.2 and 1.2.

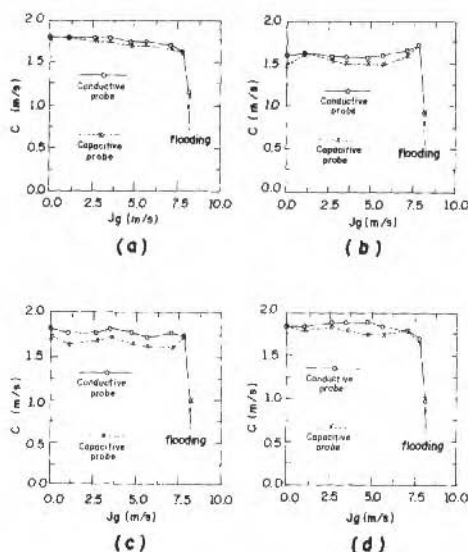


Fig. 23 Wave celerity evolution as a function of the gas superficial velocity, measured by conductive probes and capacitive probes, for $J_0=0.053$ m/s and $L=1.05$ m: (a) between the probes 5.2 and 4.2, (b) between the probes 4.2 and 3.2, (c) between the probes 3.2 and 2.2 and (d) between the probes 2.2 and 1.2.

Conclusion

Two kinds of probe were analyzed: a capacitive wire probe and a conductive one, whose main advantages are low cost, good response on frequency, and spatial resolution. The use of two guard electrodes on the edges and of one mini-probe in the conductive probe was rather efficient in minimizing errors. This kind of probe setup and the experimental study carried out are original and relevant for a large number of scientific and technological applications. Similarly, the capacitive probe setup used and the study carried out is original. The capacitive probe setup as we used, with a capacitive wire stretched along the channel and a exciting electrode kept flush with the duct wall, has a particular advantage that is not to cause drops rotation in flows with disperse drops in the gas-phase. In addition, it has the advantage of presenting a linear relationship between capacitance and film thickness, and a good spatial resolution, without shortcomings such as saturation and significant temperature effects.

As seen in the analysis, the conductive probe performed well when properly designed and suitably calibrated. The probe spatial resolution is directly related to the liquid film thickness range to be measured. When high spatial resolution is required, the film to be measured must be sufficiently thin, enabling the probe to work in a high sensitivity range (see Fig. 2). Moreover, correcting the temperature effect caused by saturation, reduces considerably the systematic error measurement. Therefore, the two types of probes presented in this study have satisfactory performance, while their shortcomings depend mainly on the flow conditions.

References

- Bendat, J. S. and Piersol, A. G. 1986 "Random data- analysis and measurement procedures". John Wiley and Sons, Inc., 2th edition.
- Biage, M. 1989a. "Structure de la surface libre d'un film liquide ruisselant sur une plaque plane verticale et soumis a un contre-courant de gaz: Transition vers l'ecoulement cocourant ascendant". Ph.D. Thesis, CENG/SETH/LEF, Grenoble-France.

- Biage, M., Delhacy, J. M. And Vernier, Ph., 1989b. "The flooding transition: a detailed experimental investigation of the liquid film flow before the flooding point.", ANS proceedings, 26th National Heat Transfer conference, ANS, 53-60, Philadelphia. August 6-8. 1989, USA.
- Biage, M., Delhaye, J. M. And Nakashi, R., 1989c. "The flooding transition: An experimental appraisal of the chaotic aspect of the liquid film flow before the flooding point". 26th National Heat Transfer Conference, AIChE Symposium Series 269, Vol. 85, Yilmaz, S. B., Ed. AIChE, 274-279, Philadelphia, August 6-8, 1989, USA.
- Brown, R.C., 1978. "The use of wire probes for the measurement of liquid film thickness in annular gas-liquid flows". The Can. J. Chem. Engng, Vol. 56, 754-757.
- Coney, M.W.E. 1973. "The theory and application of conductance probes for the measurement of liquid film thickness in two - phase flow". J. of Scientific Instruments, Vol. 6, 903-910.
- Gagliardini, H. 1986. "Contribution à l'étude expérimentale du phénomène de flooding". Rapport DEA Mécanique, Inst. Nat. Polyt. de Grenoble, CENG-SETh-LEF.
- Hewitt, G.S., King, R. D. and Lovegrove, P. C., 1962. "Techniques for liquid film and pressure drop studies in annular two-phase flow". Report AERE-R-3291.
- Mikielewicz, J. and Hammit, F.G. 1974. "Generalized characteristics of electrical conductance film thickness gauges". Report n^o UMICH 012 449-7-1, University of Michigan.
- Ozgu, M. R., Chen, J. C. And Eberhardt, N., 1973. "A capacitance method for measurement of film thickness in two-phase flow". Rev. Scientific Instrum., Vol. 44, n^o 12, A14-16.
- Pashniak, D.W. 1969. Thesis, Washington University.
- Qinggen, Y. 1984. "Technique conductimétrique, mesure de l'épaisseur de film et du frottement pariétal en écoulement diphasique à poche annulaire", LEMTA, 30-50.
- Rogovaya, A., Olevskii, V. M. and Runova, N. G., 1968. "Measurement of the thickness and profiles of liquid films". Priboryi Tekhnika Eksperimenta, n^o 1, 189-192.
- Solesio, J.N. 1978. "Mesure de l'épaisseur locale instantanée d'un film liquide reusselant sur une paroi - Examen des méthodes existantes mise en oeuvre d'une technique basée sur l'absorption de rayons X". Rapport CEA-R-4925, France.
- Sun, R.K., 1982. "Measurement of thickness of thin water film in two-phase flow by capacitance method". IEEE Transaction on Nuclear Science, Vol. NS-29, #1, 688-694.
- Telles, A.S. and Dukler, A.E. 1974. "Statistical characteristics of thin vertical wave liquid films". Ind. Engng. Chem. Fundam, 9, 416-421.
- Van Rossum, J.J. 1959. "Experimental investigation of horizontal liquid films". Chem. Eng. Sci., Vol. 11, 35-52.
- Webb, D. 1970. "Studies of the characteristics of downward annular two-phase flow". Report AERE-R-6426.
- Wicks, M. 1967. "Liquid film structure and drop size distribution in two-phase flow". Ph.D. Dissertation, University of Houston, Texas-USA.
- Zabaras, G.J. 1985. "Studies of vertical annular gas - liquid flows". Ph.D. Thesis, University of Houston.

A Parametric Study on the Influence of the Spark Plug Position on Combustion, Emissions and Performance of an Engine

J. R. Sodré, Ph.D.

Pontifícia Universidade Católica de Minas Gerais
Departamento de Engenharia Mecânica
30535-610 Belo Horizonte, MG Brazil
ricardo@pucminas.br

David A. Yates, Ph.D.

UMIST, Department of Mechanical Engineering
Thermodynamics and Fluid Mechanics Division
PO Box 88, George Begg Building
Manchester M60 1QD United Kingdom

Abstract

An analytical model has been developed to calculate the flame geometry parameters of a spark ignition engine. The model is based on a disc type combustion chamber. The flame geometry model is part of a computer program that simulates the cycle of spark ignition engines. The model requires the spark plug to be located in the cylinder head, and its position can be anywhere from the center to the corner with the cylinder liner. The effects of the spark plug position on combustion, emissions and performance have been investigated. A parametric analysis has shown that combustion takes shorter periods as the spark plug is closer to the center, for which higher cylinder pressures are attained. The performance parameters were insensitive to the plug position, but lower emission levels were verified when the plug was located in the corner. Experiments carried out on a research engine have provided the basic information to the program to perform the simulations.

Keywords: Internal Combustion Engines. Combustion. Models

Introduction

The need of the automotive industry to reduce and control emissions, to attend the regulation laws, contrasts with the always present objective to built more powerful engines. Car manufacturers have long been trying to overcome the problem by optimizing the combustion chamber design. In this work, the effects of the spark plug location on combustion, emissions and performance have been studied through simulations made with a flame geometry model. The flame geometry model is written on an analytical basis, based on a disc type combustion chamber, of flat surfaces. The spark plug can be located at any position in the cylinder head. A spherical flame front propagation is considered, with center in the spark plug. The flame geometry model is part of a spark ignition engine cycle simulation program, SPIE.

SPIE is a quasi-dimensional model, which does not account for flow fields and variations in the mixture temperature and properties through the combustion chamber. Combustion occurs according to a mean flame front model, and the flame structure model evaluates the turbulent flame speed from the laminar flame speed and a turbulent flame speed factor. The model calculates the engine performance parameters, such as power, specific fuel consumption and mean effective pressure, the exhaust concentration of the main pollutant gases (CO_2 , CO , NO , HC , etc.), and other information relevant to analyze the energy conversion in spark ignition engines. Better descriptions of the SPIE program are given by Benson et al. (1975), Benson and Baruah (1976) and Sodré (1995). Other quasi-dimensional models which include a flame geometry model are described by Keck et al. (1982 and 1987), Tabaczynski et al. (1977 and 1980), and Brehod et al. (1992).

Flame Geometry Calculation

The parameters calculated by the flame geometry model are the flame surface area and the flame contact areas with the cylinder head, cylinder liner and piston crown. These parameters are evaluated as a function of the flame radius. The calculation of the flame radius requires knowledge of the combustion products volume and the piston position. Cylinder bore, the vertical distance between cylinder head and piston at TDC (top dead center) position, and the minimum spark plug distance from

the cylinder liner are also required. Some integrals in the analytical process are solved numerically, as a result of their complexity.

There are eight possible flame positions for a flat combustion chamber, with the spark plug located in the cylinder head (Fig. 1). In the first case, the flame is described by a complete hemisphere, contacting the cylinder head only. In the second case, the flame is a hemisphere cut by the piston, contacting the cylinder head and the piston crown. The third case features the flame as a hemisphere cut on one side by the cylinder liner; the flame contacts the cylinder head and the cylinder liner. The fourth case is a sum of the second and the third cases. In the fifth case, the flame is a hemisphere cut all around by the cylinder liner, and do not contact the piston. In the sixth case, the flame is a hemisphere cut by the cylinder liner and the piston crown, and contacts the corner between those surfaces. Case seven is a sum of cases two and five. In the eighth case the flame has nearly covered the whole combustion chamber, the exception being the farthest corner from the plug, between the cylinder liner and the piston crown.

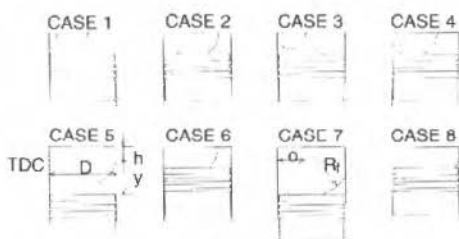


Fig. 1 Flame geometry for a flat combustion chamber.

Only in cases one and two is an exact solution presented for all the parameters. For the other cases, an exact solution is given just for the flame contact areas with the cylinder head (A_{ch}) and the piston crown (A_{pc}). The flame contact area with the cylinder liner (A_{cl}) and the flame surface area (S_f) are expressed in terms of integrals to be solved numerically. In most of the cases, the flame radius (R_f) appears as an implicit integral function of the products volume (V_b), and is determined through the application of a numerical iterative method.

Flame Position Case 1

Here, the flame is at its first stage, and contacts the cylinder head only, as it has not developed enough to reach the cylinder liner or the piston crown. This case is the first to be considered for any spark plug position in the cylinder head, except when it is located in the corner ($\alpha=0$). The expressions for V_b , A_{ch} , A_{cl} , A_{pc} , and S_f are as follows,

$$V_b = 2\pi R_f^3 / 3 \quad (1)$$

$$A_{ch} = \pi R_f^2 \quad (2)$$

$$A_{cl} = 0 \quad (3)$$

Nomenclature

A_{ch} = flame contact area with cylinder head (cm^2);	h = clearance distance (cm);	S_f = flame surface area (cm^2);
A_{cl} = flame contact area with cylinder liner (cm^2);	HC = hydrocarbons concentration (ppm);	TDC = top dead center position (non-dimensional);
A_{pc} = flame contact area with piston crown (cm^2);	IMEP = indicated mean effective pressure (bar);	V_b = products volume (cm^3);
CO = carbon monoxide concentration (ppm);	NO = nitric oxide concentration (ppm);	y = distance from piston to TDC position (cm);
CO ₂ = carbon dioxide concentration (%);	α = minimum distance from spark plug to cylinder liner (m);	$\alpha_1, \dots, \alpha_6$ = angles defined by Eqs. (11)-(16) (rad).
D = cylinder bore (cm);	R_f = flame radius (cm);	

$$A_{pc} = 0 \quad (4)$$

$$S_f = 2\pi R_f^2 \quad (5)$$

In this case, the flame radius is solved directly from Eq. (1),

$$R_f = (3V_b / 2\pi)^{1/3} \quad (6)$$

Flame Position Case 2

This is a continuation of case 1; the flame has now developed enough to contact the piston crown, although it does not touch the cylinder liner due to the close-to-center position of the spark plug. The geometric parameters are thus given,

$$V_b = \pi (y+h) [R_f^2 - (y+h)^2] / 3 \quad (7)$$

$$A_{ch} = \pi R_f^2 \quad (2)$$

$$A_{cl} = 0 \quad (3)$$

$$A_{pc} = \pi [R_f^2 - (y+h)^2] l \quad (8)$$

$$S_f = 2\pi R_f (y+h) \quad (9)$$

The flame radius can be written in an explicit form from Eq. (7),

$$R_f = [V_b / \pi (y+h) + (y+h)^2 / 3]^{1/2} \quad (10)$$

Flame Position Case 3

This case can be an extension of case 1, when the spark plug is located in a more off-center position than in case 2, or the flame beginning, for a plug located in the corner between the cylinder head and the cylinder liner. The flame touches the cylinder head and the cylinder liner, and has not developed enough to contact the piston crown.

It is now convenient to define the following parameters, as they are going to appear frequently in the forthcoming equations,

$$\alpha_1 = \arccos\{[o(D-o) - R_f^2] / 2R_f(D/2-o)\} \quad (11)$$

$$\alpha_2 = \arccos\{-[R_f^2 + o(D-o)] / R_f D\} \quad (12)$$

$$\alpha_3 = \arccos\left\{\frac{(D/2)^2 + (D/2-o)^2 - R_f^2}{D(D/2-o)}\right\} \quad (13)$$

$$\alpha_4 = \arccos \left\{ \frac{o(D-o) - [R_f^2 - (y+h)^2]}{2\sqrt{R_f^2 - (y+h)^2} (D/2-o)} \right\} \quad (14)$$

$$\alpha_5 = \arccos \left\{ \frac{R_f^2 - (y+h)^2 + o(D-o)}{D\sqrt{R_f^2 - (y+h)^2}} \right\} \quad (15)$$

$$\alpha_6 = \arccos \left\{ \frac{(D/2)^2 + (D/2-o)^2 - [R_f^2 - (y+h)^2]}{D(D/2-o)} \right\} \quad (16)$$

The flame geometric parameters are then written,

$$V_b = \frac{2}{3} \left\{ \pi R_f^3 - \int_0^{\alpha_1} \left[R_f^2 - \sqrt{(D/2-o)^2 \cos^2 \alpha + o(D-o)} \right]^{3/2} - (D/2-o) \cos \alpha \right\} dx \quad (17)$$

$$A_{ch} = [R_f^2 - (D/2)^2] (\pi - \alpha_1) + (D/2)^2 \alpha_2 - R_f (D/2-o) \left\{ 1 - \left[\frac{R_f^2 - o(D-o)}{2R_f(D/2-o)} \right]^2 \right\}^{1/2} \quad (18)$$

$$A_{cl} = D \int_0^{\alpha_3} \left\{ R_f^2 - (D/2)^2 - (D/2-o) [(D/2-o) - D \cos \alpha] \right\}^{1/2} d\alpha \quad (19)$$

$$A_{pc} = 0 \quad (4)$$

$$S_f = 2R_f \left\{ \pi R_f - \int_{\pi-\alpha_1}^{\alpha_2} \left[R_f^2 - \sqrt{(D/2-o)^2 \cos^2 \alpha + o(D-o)} \right]^{1/2} + (D/2-o) \cos \alpha \right\} dx \quad (20)$$

R_f must be solved by an iterative method from the expression for V_b . This process of solution is also adopted in the subsequent cases.

Flame Position Case 4

Case 4 is a continuity of either case 2 or case 3. The flame has reached a stage in which it contacts both the cylinder liner and the piston crown. The geometric parameters, then, become,

$$V_b = \pi (y+h) \left[R_f^2 - (y+h)^2 / 3 \right] - \frac{2}{3} \int_0^{\alpha_1} \left[R_f^2 - \sqrt{(D/2-o)^2 \cos^2 \alpha + o(D-o)} \right]^{3/2} - (D/2-o) \cos \alpha \right] dx \quad (21)$$

$$A_{ch} = \left[R_f^2 - (D/2)^2 \int (\pi - \alpha) + (D/2)^2 \alpha - R_f (D/2 - o) \right] \left\{ 1 - \left[\frac{R_f^2 - o(D-o)}{2R_f(D/2-o)} \right]^2 \right\}^{1/2} \tag{18}$$

$$A_{cl} = D \int_0^{\pi/3} \left\{ R_f^2 - (D/2)^2 - (D/2 - o) [(D/2 - o) - D \cos \alpha] \right\}^{1/2} d\alpha \tag{19}$$

$$A_{pc} = \pi \left[R_f^2 - (y+h)^2 \right] \tag{8}$$

$$S_f = 2R_f \left\{ \pi (y+h) - \int_{\pi-\alpha}^{\pi} \left[R_f^2 - \left((D/2-o)^2 \cos^2 \alpha + o(D-o) \right)^{1/2} + (D/2-o) \cos \alpha \right]^2 \right\}^{1/2} d\alpha \tag{22}$$

Flame Position Case 5

Case 5 is typical for a very early ignition, a very late ignition or a slow flame propagation. The flame has covered the whole cylinder head and contacts all around the cylinder liner, but has not reached the piston crown. This case evolves from either case 1 or case 3. The geometric parameters are,

$$V_b = \frac{2}{3} \left\{ \pi R_f^3 - \int_0^{\pi} \left[R_f^2 - \left((D/2-o)^2 \cos^2 \alpha + o(D-o) \right)^{1/2} - (D/2-o) \cos \alpha \right]^3 \right\}^{3/2} d\alpha \tag{23}$$

$$A_{ch} = \pi (D/2)^2 \tag{24}$$

$$A_{cl} = D \int_0^{\pi} \left\{ R_f^2 - (D/2)^2 - (D/2 - o) [(D/2 - o) - D \cos \alpha] \right\}^{1/2} d\alpha \tag{25}$$

$$A_{pc} = 0 \tag{4}$$

$$S_f = 2R_f \left\{ \pi R_f - \int_0^{\pi} \left[R_f^2 - \left((D/2-o)^2 \cos^2 \alpha + o(D-o) \right)^{1/2} + (D/2-o) \cos \alpha \right]^2 \right\}^{1/2} d\alpha \tag{26}$$

Flame Position Case 6

This case is an evolution of either case 3, if the spark plug is located in the corner (o=0), or case 4, for any other plug location in the cylinder head. Typical of an off-center plug position, the flame has completely covered one side of the combustion chamber. The flame then propagates parallel to the piston crown and cylinder head. The following equations describe the geometric parameters,

$$V_b = (y+h) \left\{ \left[R_f^2 - \frac{(y+h)^2}{3} \right] \pi - \left[R_f^2 - (D/2)^2 - \frac{(y+h)^2}{3} \right] \alpha_4 - (D/2)^2 \alpha_5 \right\} \\ - (y+h)(D/2-o) \left[R_f^2 - (y+h)^2 \right]^{1/2} \left\{ I - \left[\frac{o(D-o) - [R_f^2 - (y+h)^2]}{2[R_f^2 - (y+h)^2]^{1/2} (D/2-o)} \right]^2 \right\}^{1/2} \quad (27) \\ - \frac{2}{3} \int_{\alpha_4}^{\pi} \left[R_f^2 - \left((D/2-o)^2 \cos^2 \alpha + o(D-o) \right)^{1/2} - (D/2-o) \cos \alpha \right]^3 dx$$

$$A_{ch} = [R_f^2 - (D/2)^2] (\pi - \alpha_1) + (D/2)^2 \alpha_2 - R_f (D/2-o) \left\{ I - \left[\frac{R_f^2 - o(D-o)}{2R_f(D/2-o)} \right]^2 \right\}^{1/2} \quad (18)$$

$$A_{cl} = D \left\{ (y+h) \alpha_6 + \int_{\alpha_6}^{\pi} \left[R_f^2 - (D/2)^2 - (D/2-o) \right] (D/2-o) - D \cos \alpha \right\}^{1/2} dx \quad (28)$$

$$A_{pc} = [R_f^2 - (y+h)^2 - (D/2)^2] (\pi - \alpha_4) + (D/2)^2 (\pi - \alpha_5) \\ - (D/2-o) \left[R_f^2 - (y+h)^2 \right]^{1/2} \left\{ I - \left[\frac{R_f^2 - (y+h)^2 - o(D-o)}{2[R_f^2 - (y+h)^2]^{1/2} (D/2-o)} \right]^2 \right\}^{1/2} \quad (29)$$

$$S_f = 2R_f (y+h) (\pi - \alpha_4) - \\ 2R_f \int_{\pi - \alpha_1}^{\pi - \alpha_4} \left[R_f^2 - \left((D/2-o)^2 \cos^2 \alpha + o(D-o) \right)^{1/2} + (D/2-o) \cos \alpha \right]^2 dx \quad (30)$$

Flame Position Case 7

This is an extension of cases 2, 4 or 5, and is the ultimate stage of the flame for a central spark plug. The flame has covered all the cylinder head, touches all around the cylinder liner and contacts the piston crown. The geometric parameters are thus written,

$$V_b = \pi (y+h) \left[R_f^2 - \frac{(y+h)^2}{3} \right] \\ - \frac{2}{3} \int_0^{\pi} \left[R_f^2 - \left((D/2-o)^2 \cos^2 \alpha + o(D-o) \right)^{1/2} - (D/2-o) \cos \alpha \right]^3 dx \quad (31)$$

$$A_{ch} = \pi (D/2)^2 \quad (24)$$

$$A_{cl} = D \int_0^{\alpha} \left\{ R_f^2 - (D/2)^2 - (D/2 - o) \left[(D/2 - o) - D \cos \alpha \right] \right\}^{1/2} dx \quad (25)$$

$$A_{pc} = \pi \left[R_f^2 - (y+h)^2 \right] \quad (8)$$

$$S_f = 2R_f \left\{ \pi (y+h) - \int_0^{\alpha} \left[R_f^2 - \left((D/2 - o)^2 \cos^2 \alpha + o(D-o) \right)^{1/2} + (D/2 - o) \cos \alpha \right]^{1/2} dx \right\} \quad (32)$$

Flame Position Case 8

This is the last stage of the flame for an off-center plug. The flame has covered all the combustion chamber, except the corner region between the cylinder liner and the piston crown which is the farthest from the spark plug. The flame geometric parameters are so expressed,

$$\begin{aligned} V_b = (y+h) & \left\{ \left[R_f^2 - \frac{(y+h)^2}{3} \right] \pi - \left[R_f^2 - (D/2)^2 - \frac{(y+h)^2}{3} \right] \alpha_4 - (D/2)^2 \alpha_5 \right\} \\ & - (y+h)(D/2 - o) \left[R_f^2 - (y+h)^2 \right]^{1/2} \left\{ 1 - \left[\frac{o(D-o) - \left[R_f^2 - (y+h)^2 \right]}{2 \left[R_f^2 - (y+h)^2 \right]^{1/2} (D/2 - o)} \right]^2 \right\}^{1/2} \\ & - \frac{2}{3} \int_0^{\alpha} \left[R_f^2 - \left(\left[(D/2 - o)^2 \cos^2 \alpha + o(D-o) \right]^{1/2} - (D/2 - o) \cos \alpha \right)^2 \right]^{3/2} d\alpha \end{aligned} \quad (33)$$

$$A_{ch} = \pi (D/2)^2 \quad (24)$$

$$A_{cl} = D \left\{ (y+h) \alpha_6 + \int_{\alpha_6}^{\alpha} \left\{ R_f^2 - (D/2)^2 - (D/2 - o) \left[(D/2 - o) - D \cos \alpha \right] \right\}^{1/2} dx \right\} \quad (34)$$

$$\begin{aligned} A_{pc} = & \left[R_f^2 - (y+h)^2 - (D/2)^2 \right] (\pi - \alpha_4) + (D/2)^2 (\pi - \alpha_5) \\ & - (D/2 - o) \left[R_f^2 - (y+h)^2 \right]^{1/2} \left\{ 1 - \left[\frac{R_f^2 - (y+h)^2 - o(D-o)}{2 \left[R_f^2 - (y+h)^2 \right]^{1/2} (D/2 - o)} \right]^2 \right\}^{1/2} \end{aligned} \quad (29)$$

$$\begin{aligned} S_f = & 2R_f (y+h) (\pi - \alpha_4) \\ & - 2R_f \int_0^{\pi - \alpha_4} \left[R_f^2 - \left((D/2 - o)^2 \cos^2 \alpha + o(D-o) \right)^{1/2} + (D/2 - o) \cos \alpha \right]^{1/2} dx \end{aligned} \quad (35)$$

In the SPIE program, combustion is initiated with the products volume being considered as a very small part of the total volume in the cylinder, by a factor of $1/10^9$. The flame geometry subroutine always starts with case 1, and through a series of tests decides which way to follow. The flame propagation is determined by the flame structure model.

Experiments

The flame structure model employed by the simulation program calculates the turbulent flame speed from the laminar flame speed and the flame development angle. The flame development angle corresponds to the crank angle interval during which the laminar flame turns into turbulent. The flame development angle and the ratio between the turbulent and the laminar flame speeds are adjusted to make the calculated and experimental pressure diagrams coincide. The flame development angle and the flame speeds ratio were determined from experiments carried out in a single-cylinder research engine. The engine featured a disc type combustion chamber, with the spark plug located near the corner between the cylinder head and cylinder liner. The baseline engine conditions are shown in Table 1. The flame speeds ratio and the flame development angle were kept the same for all simulated plug positions.

Table 1 Baseline engine conditions.

Bore	76.22 mm
Stroke	111.23 mm
Engine speed	1500 rev/min
Fuel/air equivalence ratio	1.0
Compression ratio	8.0
Ignition timing	36° BTDC
Coolant and lubricant temperature	343 K
Minimum plug distance to cylinder liner	7.53 mm

Results

Results of simulation using the flame geometry model are shown next. The influence of the plug position on the flame related parameters can be observed in Figs. 2 to 6. A longer combustion time is noticed as the plug is farther from the center position, in Fig. 2, which is a consequence of a longer flame travel path. The flame surface area (Fig. 3) and the cylinder liner contact area (Fig. 5) are more sensitive to the plug position than the cylinder head and piston crown contact areas (Figs. 4 and 6). Central spark showed the biggest flame surface area (Fig. 3), while edge spark presented the biggest cylinder liner contact area (Fig. 5).

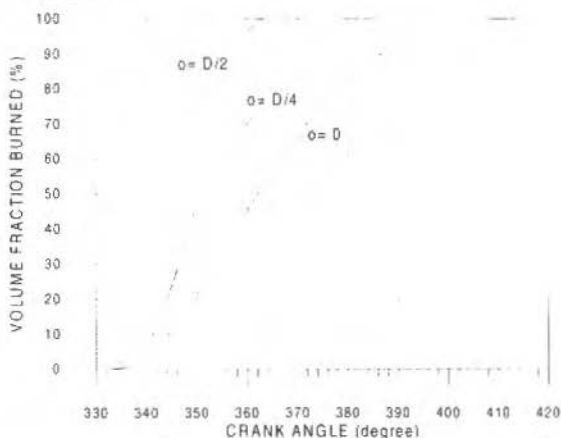


Fig. 2 Plug position effect on products volume.

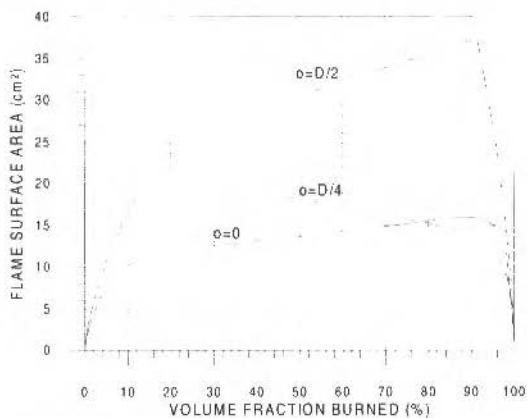


Fig. 3 Plug position effect on flame surface area.

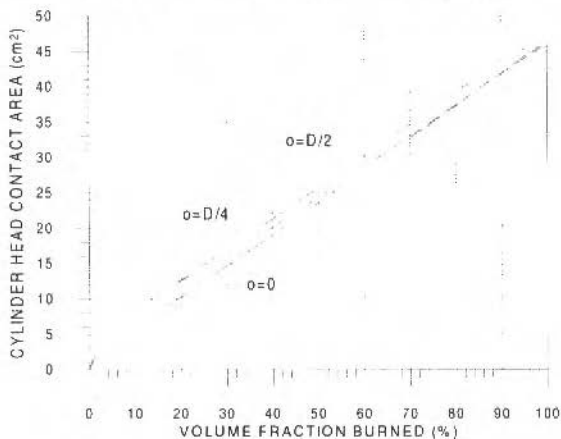


Fig. 4 Plug position effect on cylinder head contact area.

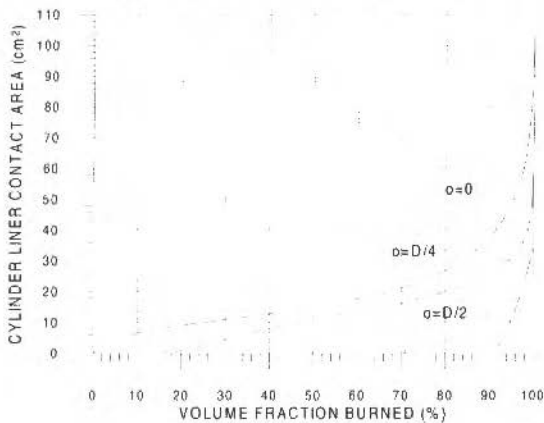


Fig. 5 Plug position effect on cylinder liner contact area.

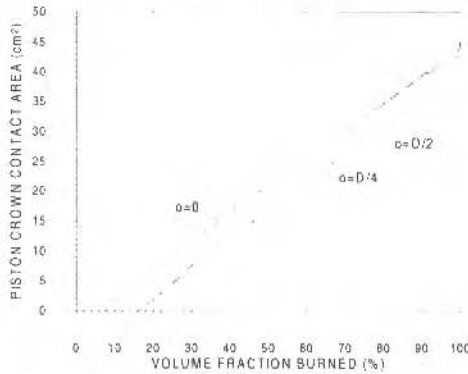


Fig. 6 Plug position effect on piston crown contact area.

Figure 7 shows the spark plug position effects on the indicated power and mean effective pressure. It is observed that there is no significant variation on the performance parameters when the spark plug position is altered. Figure 8 helps to explain why. Although a central plug position produces a higher peak pressure, it happens by the time the piston is in the TDC position. The volume of the cylinder contents varies little by this time, being the reason why there is no appreciable implementation on the work done. On the other hand, the peak pressure for an edge plug is smaller, but it happens when there is a bigger cylinder volume variation. In the end, the work done for all cases is approximately the same and, consequently, power and specific fuel consumption vary little.

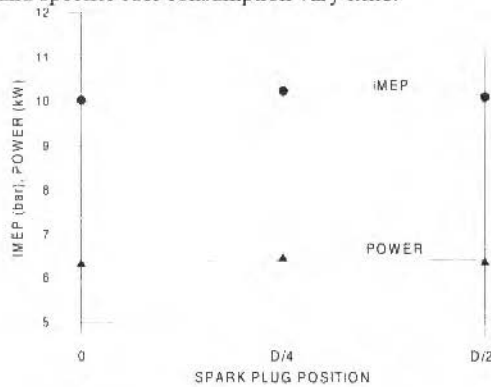


Fig. 7 Plug position effect on IMEP and power

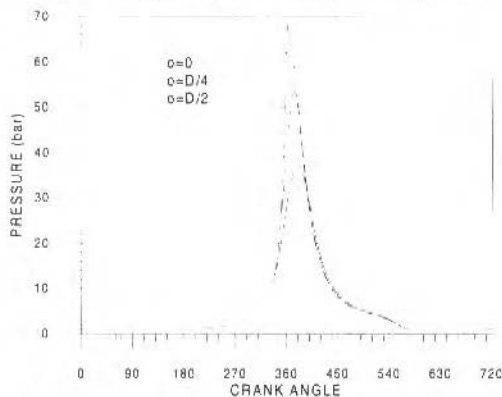


Fig. 8 Plug position effect on cylinder pressure.

It should be mentioned that this analysis was made based on a fixed spark timing for all plug positions. The engine conditions established in the simulation was set according to experiments for an edge plug, very near to the corner ($\alpha/D = 0.0099$). In real circumstances for a central plug, the spark timing could possibly have to be retarded, due to the very high peak pressure shown by the simulation. This measure might be necessary to avoid knock and structural problems on the engine.

Figure 9 shows the effects of varying the plug position on exhaust hydrocarbons (HC) and nitric oxide (NO). The HC concentration is seen to be higher for a central plug, and becomes lower as the

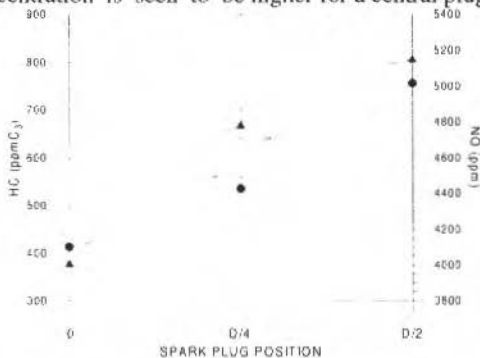


Fig. 9 Plug position effect on HC and NO emissions.

plug is closer to the corner. Combustion chamber sources, such as crevices and fuel absorption/desorption by the lubricating oil, produces more unburned HC for higher cylinder pressures (Sodré, 1995), which is the case for a central plug. Prior to combustion, when the cylinder pressure is rising, unburned mixture is forced into the combustion chamber crevices. The trapped mixture is released during the expansion and exhaust strokes, at decreasing cylinder pressures, to form unburned hydrocarbons in the exhaust. An amount of the fuel present in the unburned mixture is absorbed by the cylinder lubricating oil during the intake and compression strokes, being released during the expansion and exhaust strokes. This fuel will contribute to exhaust HC, and the amount taking part in the absorption/desorption process is directly proportional to the cylinder pressure. The NO formation is associated to high cylinder temperatures (Heywood, 1988). The calculated kinetic concentration of NO is higher for a central plug because at this condition higher cylinder pressure and temperature are reached in the chamber.

Finally, Fig. 10 shows the results for the equilibrium concentrations of carbon monoxide (CO) and carbon dioxide (CO₂). No representative variation is noticed for any of these elements, as they are more sensitive to the mixture strength rather than to pressure or temperature (Heywood, 1988). Carbon monoxide and carbon dioxide are products from combustion, and although the spark plug position may slow or speed up combustion (see Fig. 2), it does not interfere in the equilibrium between products and reactants.

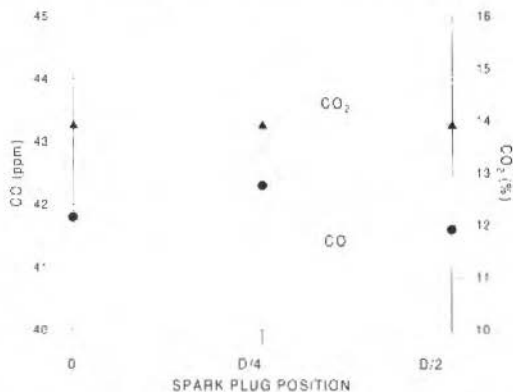


Fig. 10 Plug position effect on CO and CO₂ emissions.

Conclusion

From the results shown for the tested conditions, in which the spark timing and the other engine variables were kept the same, it is concluded that no implement in performance is achieved by varying the plug position. Combustion takes a shorter period for a central plug, in which case higher cylinder pressures are attained. Lower HC and NO emission levels are reached if the spark plug is located in the farthest position from the center, the corner between the cylinder head and the cylinder liner. The concentrations of CO and CO₂ have shown no variation with the spark location.

Acknowledgments

The authors wish to thank the Brazilian Government's Science and Technology Agency, CNPq, for the financial support to this project.

References

- Benson, R. S., Annand, W. J. D., and Baruah, P. C., 1975. "A Simulation Model Including Intake and Exhaust Systems for a Single Cylinder Four-Stroke Cycle Spark Ignition Engine". *International Journal of Mechanical Sciences*, Vol. 17, pp. 97-124.
- Benson, R. S., and Baruah, P. C., 1976. "A Generalized Calculation for an Ideal Otto Cycle with Hydrocarbon-Air Mixture Allowing for Dissociation and Variable Specific Heats", *IJMEE*, Vol. 4, n. 1, pp. 49-81.
- Brehod, D.D., and Newman, C.E., 1992, "Monte Carlo Simulation of Cycle by Cycle Variability", SAE 922165.
- Heywood, J. B., 1988, "Internal Combustion Engine Fundamentals", McGraw-Hill Book Company, Singapore.
- Keck, J.C., 1982, "Turbulent Flame Structure and Speed in Spark-Ignition Engines", *Proceedings of Nineteenth Symposium (Intl.) on Combustion*, pp. 1451-1466, The Combustion Institute.
- Keck, J.C., Heywood, J.B., and Noske, G., 1987, "Early Flame Development and Burning Rates in Spark Ignition Engines", SAE 870164, *SAE Transactions*, Vol. 96.
- Sodré, J. R., 1995, "Formulation and Experimental Validation of a Computer Model for Spark Ignition Engine Exhaust Hydrocarbons". Ph.D. Thesis, UMIST, UK.
- Tabaczynski, R.J., Ferguson, C.R., and Radhakrishnan, K., 1977, "A Turbulent Entrainment Model for Spark-Ignition Engine Combustion", SAE 770647, *SAE Transactions*, Vol. 83.
- Tabaczynski, R.J., Trinker, F.H., and Shannon, B.A.S., 1980. "Further Refinement and Validation of a Turbulent Flame Propagation Model for Spark-Ignition Engines", *Comb. & Flame*, Vol. 39, pp. 111-121.

Thermodynamic Analysis and Modeling of an Adsorption-Cycle System for Refrigeration from Low-Grade Energy Sources

Antonio Pralon Ferreira Leite

Universidade Federal da Paraíba
Departamento de Engenharia Mecânica
58109-970 Campina Grande, PB Brazil
pralon@lctf.ufpb.br

Abstract

A theoretical analysis of an adsorption-cycle, employing low-grade thermal sources, for application to a cooling system is presented. The basic fundamentals of adsorption processes and some considerations about the most commonly used adsorbent-adsorbate pair in refrigeration, the activated carbon-methanol pair, are described. It is established from the analysis of the main isotherms of adsorption that the Dubinin-Astakhov equation as the most suitable equation of state to represent the adsorption of methanol in activated carbon. An expression to calculate the liberated heat from the adsorption process, or the isosteric heat of adsorption, is deduced and aspects related to the kinetics of adsorption are also considered. A thermodynamic analysis of the adsorption cycle has been carried out in order to obtain a simple ratio between condensation temperature and regeneration temperature and to evaluate the coefficient of thermal performance (COP) of an ideal quadrithermal machine. Finally, the energy equation for an adsorptive bed interacting with other components of a simple effect cooling machine that operates at moderate temperatures is given, and some of their terms are detailed. This theoretical analysis can be applied to an adequate modeling and design of a refrigeration system, based on an adsorption cycle operating from a low-grade energy source.

Keywords: Microporous Media, Adsorption Potential, Isosteric Heat, Adsorption Cooling Cycle.

Introduction

The basic principle of the refrigeration cycle is to transfer an amount of heat from a low temperature medium to another at a higher temperature utilizing a thermodynamic cycle. This heat transfer is possible since there is an available energy source which can be either mechanical energy (compression cycles) or internal energy (sorption cycles). The input energy can come from the thermodynamic conversion of several thermal sources and, particularly for sorption cycles, from low-grade heat from different origins such as residual heat or solar energy.

On the other hand, several environmental studies on the global greenhouse effect being carried recently, including those on fluorocarbon emissions from refrigerating units, indicate adsorption cycles as one of the possible remedies to that ecological problem. In the last two decades, predictions have been conformed that chlorine compounds of chlorofluorocarbons (CFCs) leads to a decrease in the thickness of the ozone layer (Mégie, 1992).

Solid sorption processes have been considered for use in refrigeration cycles as a serious alternative to the usual vapor compression systems, especially adsorption techniques which allow the cycling of large amounts of refrigerant fluid and, thus, high efficiencies compared with other sorption systems, like those based on liquid absorption or solid absorption (chemical adsorption) processes. In the present study a refrigeration system based on a solid-adsorption cycle from low-grade energy sources, is analyzed and thermodynamic considerations are presented.

Adsorption and Adsorbents

Generically, the *adsorption* can be defined as the capacity that certain bodies have to selectively fix the molecules of a fluid. *Physical adsorption*, or *adsorption* as commonly is called, is a solid sorption process where the binding forces between fluid molecules and the solid medium are from electrostatic origin or dispersion-repulsion forces (Van der Waals forces). The gas adsorption on a solid adsorbent is an exothermic process due to the gas-liquid phase change. The quantity of the energy liberated in the adsorption process is called *isosteric heat*; its intensity depends on the nature of the adsorbent-adsorbate pair. In general, an adsorbent material can be characterized as a porous medium.

A porous medium is a body composed of a solid structure which contains cavities, called pores, that are usually interconnected and is susceptible to containing one or more fluid phases (Marle, 1985). The

porous media can be classified as macropores (diameter greater than 500\AA), mesopores (diameter between 500\AA and 20\AA) and micropores (diameter less than 20\AA). The main adsorptive property of a body is its microporous structure. Among the most well known adsorbents which have a high porosity, are the following: silica gel, activated carbon, activated alumine and zeolite. The physical parameters that characterize the porosity of a material are: the volume of pores, the specific surface area and the distribution of the pore diameters. The specific surface area of the activated carbon and of the zeolite structure, the most used adsorbents in refrigeration systems, varies from 300 to $2.500\text{ m}^2/\text{g}$ and from 500 to $800\text{ m}^2/\text{g}$, respectively (Yang, 1987).

The zeolite distinguishes itself from the above mentioned adsorbents because it presents a porous structure characterized by a molecular sieve. The others adsorbents have a pore size distribution, with an average diameter, which are controlled by the fabrication process. This difference in the microporous structure determines the selective grade and the capacity of the adsorbent. In the case of activated carbon, its pore size distribution allows a penetration of a large quantity of the fluid molecules into its porous structure. This signifies little selectivity, but a great capacity of adsorption. Concerning the zeolite, due to its molecular sieve structure, there is a large selectivity of the adsorbed molecules as a function of their dimensions.

The majority of the adsorbents are produced in agglomerated pellet form with a biporous structure, or double porosity, which is characterized by the so called *diffusion pores* placed between particles (the macro and mesopores) and the intraparticle micropores. The adsorption occurs mainly at the microporous surface, under conditions of capillary condensation, initially at the macroporous surface, then reaching the micropores after.

Thermodynamics of Adsorption

The thermodynamic equilibrium of an adsorbent-adsorbate pair can be described by an equation of state, called the *isotherm of adsorption*, correlating temperature T , pressure P and concentration of the adsorbed phase a (adsorbed mass/adsorbent mass) in the form $f(T, P, a) = 0$. Several models are found in the literature, the main ones being:

- Theory of Gibbs: the adsorbate is treated in microscopic and two-dimensional form. The fundamental thermodynamic equations are established in terms of a "surface energy" π (Ruthven, 1984):

Nomenclature

a	= concentration of adsorbed mass	k	= thermal conductivity	t	= time
A	= area of heat transfer	k	= equilibrium constant of adsorption	T	= temperature
b	= equilibrium constant	L	= latent heat	U	= internal energy
c	= concentration of gaseous phase	L_1	= length of tube	V	= volume of adsorbate
C	= specific heat coefficient at constant pressure	m_1	= mass of adsorbent	V_0	= total volume of micropores
COP	= coefficient of performance	n	= number of moles	W_0	= parameter of state equation (Eq. 14)
d	= characteristic parameter of adsorption	n	= parameter of state equation (Eq. 14)	z	= spatial coordinate in z direction
D	= parameter of state equation (Eq. 14)	P	= pressure	α	= coefficient of thermal expansion
D_e	= effective diffusion coefficient	P_s	= saturation pressure	A	= two-dimensional surface
D_i	= diffusion coefficient	Q	= heat flux	β	= gas parameter
D_k	= Knudsen's diffusion coefficient	q_{st}	= isosteric heat	B	= fractional amount of pores
D_m	= molecular diffusion coefficient	r	= spatial coordinate in radial direction	ϵ	= potential of adsorption
D_p	= Poiseuille's diffusion coefficient	r_g	= radius of the grain	μ	= chemical potential
G	= Gibbs free energy	r_1	= radius of the tube	ρ_1	= specific mass of adsorbate
h	= thermal conductance	R	= gas constant	ν	= tortuosity of the medium
H	= enthalpy	S	= entropy	π	= surface energy

$$dG = -S dT + V dP - \pi dA + \mu dn \quad (1)$$

and

$$G = -\pi A + \mu n \quad (2)$$

where: G is the Gibbs free energy, S is entropy, P is pressure, V is volume, μ is chemical potential, n is the number of moles, A is the "two-dimensional surface" (corresponding to n) of the adsorbent.

From equations (1) and (2), it can be obtained:

$$-S dT + V dP + A d\pi - n d\mu = 0 \quad (3)$$

If the volume of the adsorbed phase, V , is negligible and the temperature is considered constant during the adsorption process, then:

$$A d\pi - n d\mu = 0 \quad (4)$$

Assuming an equilibrium between the adsorbed phase and the gaseous phase:

$$d\mu = \frac{RT dP}{P} \quad (5)$$

and

$$\frac{A}{n RT} d\pi = \frac{dP}{P} \quad (6)$$

where R is the universal gas constant.

These equations, called *isotherm of Gibbs* represent a general relation that can be simplified for particular cases such as the Henry's Law or the Langmuir's approach.

The Gibbs' model is based on an implicit hypothesis about the adsorption equilibrium: a dynamic adsorbed phase whose thermodynamic property can be represented by an equation of state. An alternative approach is based on a thermodynamic statistical analysis that considers the probability of the molecular occupation of the porous surface. It is possible to demonstrate that the isotherm of Gibbs is the limiting case of the statistical approach when the molecular interchange between the pores is fast (Hill, 1960; Ruthven, 1984).

- Henry's Law. This establishes, for weak concentrations, a linear relation between the concentration of the gaseous phase and the adsorbed phase, which is considered as a perfect gas:

$$a = \frac{n}{A} = \frac{\pi}{RT} = k c \quad (7)$$

where c is the concentration of the gaseous phase and k the equilibrium constant of adsorption.

- Langmuir's Approach. This assumes that the adsorption process occurs in monomolecular layers and that there is a dynamic equilibrium: the adsorbed mass flow (condensation on the adsorbent surface) is equal to the desorbed mass flow (evaporation from the adsorbent). This model takes into account the following hypothesis: 1) the molecules are adsorbed in a definite number of pores; 2) each pore can contain only one molecule; 3) the adsorption energy is constant for all pores; 4) there is no interaction between adjoining adsorbed molecules.

The isotherm of Langmuir can be deduced, similarly to the Van der Waals' equation, from the Gibbs' equation:

$$\pi (A - \beta) = n RT \quad (8)$$

thus,

$$\frac{dP}{P} = - \frac{A dA}{(A - \beta)^2} \quad (9)$$

When the adsorbed concentration is not so high, it can be assumed that $\beta \ll 2A$, and the term β^2 can be neglected

$$bP = \frac{2\beta/A}{1 - 2\beta/A} = \frac{B}{1 - B} \quad (10)$$

where b is the equilibrium constant, β is a gas parameter and B is the fractional amount of the pores occupied by the molecules, or the ratio between the concentration of the adsorbed phase and the total number of pores per unit of adsorbent volume.

For weak pressures ($P \rightarrow 0$), or $B \ll 1$, this formulation becomes a linear function as described by Henry's law. The Langmuir's approach is usually applied to gas separation processes.

- Theory of the Adsorption Potential. It was recently developed by Dubinin and his collaborators (Dubinin and Astakhov, 1971; Bering et al, 1972; Dubinin and Stoeckly, 1980) from the theory originally proposed by Polany towards the end of the 1920's (Polany, 1932). This theory is a purely thermodynamic approach, which can be very well suitable to characterize adsorption in microporous materials. It is based on the surface forces, distribution at the microporous surface of the adsorbent.

The potential of adsorption ϵ is defined by Polany as the necessary work to transport a molecule of the gaseous phase as far as a determined point in the adsorbed phase subjected to the adsorption force field. It can be calculated directly from the ratio between equilibrium pressure of the adsorbed phase P and the saturation pressure of the gaseous phase P_s :

$$\epsilon = -RT \ln \left(\frac{P}{P_s} \right) \quad (11)$$

The relation between the volume V of adsorbate on top of the adsorbent surface and the potential ϵ is called the *characteristic curve*, which is considered independent of the temperature. For adsorbents with a Gaussian distribution of pore diameter; Dubinin and Radushkevich (Dubinin and Stoeckly, 1980), proposed the following characteristic curve:

$$V = V_0 e^{-\epsilon/d^2} \quad (12)$$

where V_0 is the total volume of micropores and d is a characteristic parameter of the adsorption. If $D = d/R^2$, then:

$$V = V_0 \exp \left\{ -D \left[-T \ln(P/P_s) \right]^2 \right\} \quad (13)$$

This characteristic curve represents a concise correlation which has practical applications to engineering problems. However, the hypothesis of temperature independence is not applicable to all adsorption systems, particularly under weak concentrations, since this equation of state can not be reduced to Henry's law.

Dubinin-Astakhov Equation

For adsorption processes in microporous materials whose distribution of pore dimensions is a polymodal type, such as activated carbon, Dubinin and Astakhov (1971) proposed the following characteristic function:

$$a = W_0 \rho_l(T) \exp\left\{-D[T \ln(P_s/P)]^n\right\} \quad (14)$$

where W_0 is the maximum capacity of adsorption (volume of adsorbate/mass of adsorbent), ρ_l the specific mass of the adsorbate in liquid state, D the "coefficient of affinity" and n is a characteristic parameter of the adsorbent-adsorbate pair.

This equation is a generalization of the characteristic curve of Dubinin-Rudshkevich, where $n = 2$, but it has an application field wider than the previous equation because it depends on 3 parameters (W_0 , D , n). Nevertheless, this correlation has an empirical character, since it admits a variable distribution of the adsorption potential. It is particularly suitable for the activated carbon-methanol pair under conditions of low-grade thermal energy which allows its use in several engineering applications in the field of refrigeration such as those concerning solar energy. Experimental results obtained by Passos (1986) have demonstrated the validity of the Dubinin-Astakhov isotherm to model the adsorption of methanol in activated carbon for a large range of adsorbed mass concentrations and for a wide variety of moderate temperatures.

Isosteric Heat of Adsorption

The partial derivation of the Gibbs isotherm in the integral form, related to the temperature, leads to a function denoted as *isoster* (a constant adsorbed mass function) given as:

$$\left(\frac{\partial \ln P}{\partial T}\right)_a = -\frac{q_{st}}{R T^2} \quad (15)$$

where q_{st} is the "isosteric heat" of the adsorption process. This relation is known as the *Clausius-Clapeyron formula*.

Applying this equation to the saturation condition ($P = P_s$), the latent heat of phase change L is obtained:

$$L = -R T^2 \left(\frac{\partial \ln P_s}{\partial T}\right)_a \quad (16)$$

The derivation of the Dubinin-Astakhov equation gives:

$$\frac{\partial \ln P}{\partial T} = \frac{\partial \ln P_s}{\partial T} + \ln(P_s/P) \left\{ T^{-1} + \frac{\alpha}{nD} [T \ln(P_s/P)]^n \right\} \quad (17)$$

with

$$\alpha = W_0 \frac{\partial \ln(\rho_l/a)}{\partial T} \quad (18)$$

where α represents the coefficient of thermal expansion of the liquid adsorbate.

Multiplying each term of the differential equation by $(RT)^2$, a final expression for the isosteric heat as function of pressure and temperature is obtained:

$$q_{st} = L + R T \ln(P_s/P) + \left[\frac{\alpha R T}{nD} \right] [T \ln(P_s/P)]^{(1-n)} \quad (19)$$

Kinetics of Adsorption

Sometimes the adsorption process is not rapid, and the adsorbed phase must be considered with the thermodynamic variables as function of time.

Generally, the adsorption in microporous materials is mainly controlled by the diffusion inside the porous structure, since at the surface of the grains the diffusion is fast enough. In the case of materials with a disperse structure, like activated carbon, two diffusion mechanisms are found: a diffusion of the gaseous phase through the transport pores (mesoporous and macroporous diffusion) and a diffusion of the adsorbed phase in the micropores (microporous diffusion). The relative importance of these mechanisms on the global effect of the diffusion is essentially dependent on pressure. According to Dubinin and Erashko (1975), for pressures lower than 10 mbar, the mesoporous and macroporous diffusion prevail, while, for pressures greater than 10 mbar, microporous diffusion tends to control the mass transfer process.

Thomas and Gluckauf, cited by Sakoda and Suzuki (1984), proposed an approach for the interparticle diffusion based on two main hypotheses: the temperature of the grain is uniform; and the concentration at the solid interface is equal to an equilibrium concentration. They established, for modeling the mass transfer resistance, a linear equation as following:

$$\frac{\partial a}{\partial t} = \frac{15 D_i}{r_g^2} (a_{eq} - a) \quad (20)$$

where D_i is the diffusion coefficient, a_{eq} the concentration at the interface (adsorbed mass/adsorbent mass, given by an isotherm) and r_g the average radius of the grain.

In the mesopores and macropores, different mechanisms contribute simultaneously to the diffusion process whose relative influence depends on the pore dimensions. Four of these mechanisms were identified: superficial diffusion D_s , molecular diffusion D_m , Knudsen's diffusion D_k and diffusion due to Poiseuille's flow D_p . For the global diffusion analysis, usually an *effective diffusion coefficient* D_e is considered, given by:

$$D_e = \frac{l}{v} (D^* - D_p) \quad (21)$$

with

$$D^* = \left(\frac{l}{D_m} + \frac{l}{D_k} \right) \quad (22)$$

where v is the tortuosity of the medium.

Despite the fact that kinetics theory is generically important for modeling many adsorptive processes, experience has demonstrated that the mass transport resistance can be neglected, even if the system is submitted to moderate thermal powers. Kariogas and Meunier (1986) have proved, for the adsorption of methanol in activated carbon, that the mass resistance is negligible when the incident thermal energy is lower than 50 W/kg.

In summary, for modeling of adsorption processes related to low-grade energy sources, it is not necessary to consider the diffusion through the porous media. Moreover, it can be considered for many of these applications, that instantaneous equilibrium between the adsorbed and gaseous phases exists which can be represented by a characteristic function, such as the Dubinin-Astakhov equation.

Thermodynamic Analysis of the Adsorption-Cycle

The main difference between the vapor compression cycle and the adsorption cycle is related to the energy source which is utilized to transfer heat from a low temperature reservoir to a high temperature reservoir. While the first cycle uses mechanical energy, the second utilizes the internal energy of a fluid interacting with a solid medium. Two main advantages of the adsorption cycle can be mentioned:

- the system can operate without mobile parts;
- elevated performance related to the Carnot-cycle, for low temperatures of the thermal source.

This analysis will be restricted to an adsorption cycle without heat recovery, or the so called intermittent cycle. This principle leads to the conception of a simple machine in which the necessary

energy for the regeneration of the adsorbent (*desorption* process) is coming from an external thermal source of low-grade energy, such as residual heat or solar energy.

The Carnot cycle relating to an adsorption cooling cycle can be represented by an ideal three-temperature machine, namely a *trithermal machine*, as shown in Fig. 1. This idealized device can be decomposed in two coupled machines, where one supplies the mechanical energy W that the other utilizes to produce refrigeration.

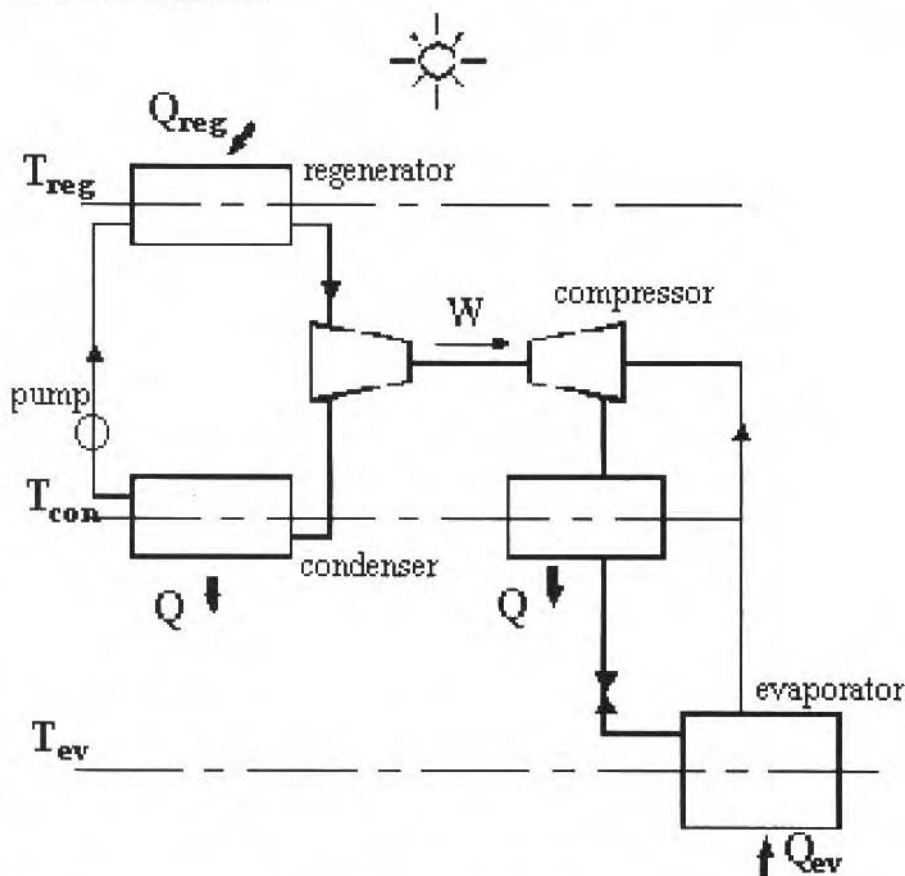


Fig. 1 Schematic of an ideal three-temperature machine

Based on the ideal performance of each machine, given by the Carnot principle, the global thermal performance coefficient (COP) can be obtained:

$$COP = \frac{Q_{ev}(Q_{reg} - Q_{con})}{Q_{reg}(Q_{con} - Q_{ev})} = \frac{T_{ev}(T_{reg} - T_{con})}{T_{reg}(T_{con} - T_{ev})} \quad (23)$$

where Q_{ev} and Q_{con} are the heat extracted from the evaporator and the condenser at T_{ev} and T_{con} temperatures, respectively; Q_{reg} is the provided heat to the fluid from the regenerator, at the regenerating temperature T_{reg} ; and T_{con} is the condenser temperature.

According to this relation, COP increases with the temperature difference between the regenerator and the condenser, and it decreases with the temperature difference between the evaporator and the condenser. For example, if the condensation temperature is 30°C , the performance of the machine for an application of air conditioning ($T_{ev} = 7^{\circ}\text{C}$) shall be 60% higher than that which is obtained for ice production ($T_{ev} = -5^{\circ}\text{C}$), for a regeneration temperature of 100°C . On the other hand, for fixed

evaporation and condensation temperatures, COP becomes an increasing function of the regenerating temperature, tending asymptotically to $T_{ev}/(T_{con} - T_{ev})$, as shown in Fig. 2.

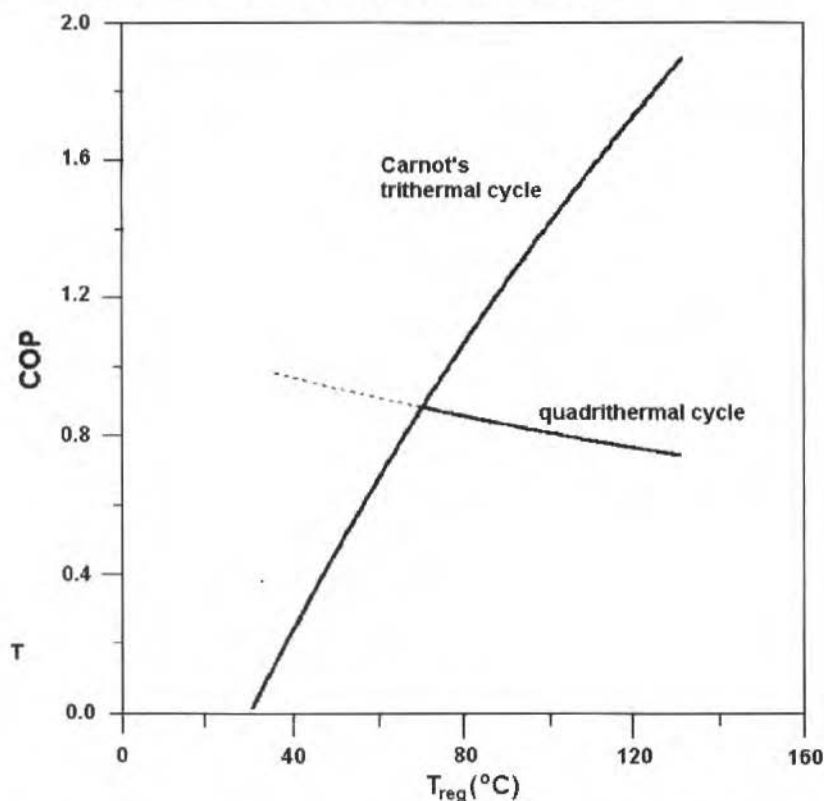


Fig. 2 Variations of COP as function of the regenerating temperature ($T_{ev} = -5^{\circ}\text{C}$, $T_{con} = T_0 = 30^{\circ}\text{C}$)

Ideal Four-Temperature Machine

The real adsorption cooling cycle deviates from the ideal trithermal machine cycle because it needs 4 temperature levels. Therefore, the ideal cycle for adsorption shall be that of an hypothetical *quadrithermal machine* (Fig. 3), corresponding to the coupling of two machines at two temperatures operating with the same condensable fluid and without mechanical energy conversion (Guilleminot et al, 1980).

The Carnot COP of a quadrithermal machine can be expressed as:

$$COP = \frac{1 - \frac{T_{con}}{T_{reg}}}{\frac{T_0}{T_{ev}} - 1} \quad (24)$$

where T_0 is a reference temperature, equivalent to the maximum temperature above the ambient temperature at which adsorption can occur.

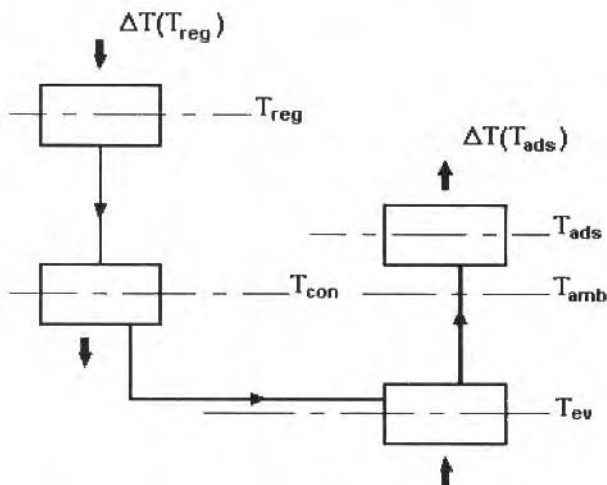


Fig. 3 Schematic of an ideal four-temperature machine

During regeneration of the adsorbent, mass transfer occurs from the adsorbed phase at the temperature, T_{reg} , to the liquid phase at the condensation temperature, T_{con} . This transfer leads to a production of internal energy, resulting from the difference of binding energy between the adsorbed phase and the liquid phase. In the course of the cooling production, the mass transport from the liquid state takes place at a low temperature, T_{ev} , to the adsorbed state at a reference temperature, T_0 .

The concept of reference temperature results from the difference of magnitudes between the energy generated in one stage and that utilized in the other. When the internal energy produced in the regeneration process is equal to the energy necessary for the adsorption, the case of the trithermal machine is realized. Another reference temperature T_0 , representing the minimum regenerating temperature necessary for the realization of the cycle, can also be defined.

Applying the fundamental laws of thermodynamics to the regenerating process, it can be written:

$$\Delta H - L = \Delta Q + U \tag{25}$$

$$\frac{\Delta H}{T_{reg}} - \frac{(L + \Delta Q)}{T_{con}} \leq 0 \tag{26}$$

where the inequality represents the irreversible process; where ΔH is the enthalpy of adsorption, L the latent heat of condensation, ΔQ the thermal energy from an external source and U the internal energy generated.

Combining Eqs. (25) and (26), the internal energy becomes:

$$U \leq \Delta H \left(1 - \frac{T_{con}}{T_{reg}} \right) \tag{27}$$

Analogously, for the process of refrigeration production, considering now the temperatures T_{ev} and T_{ads} , the internal energy utilized can be evaluated as:

$$U \geq \Delta H \left(1 - \frac{T_{ev}}{T_{ads}} \right) \tag{28}$$

where T_{ads} is the temperature of adsorption.

Comparing Eq. (27) and Eq. (28), and taking into account that ΔH is not only dependent on the temperature but also on the adsorbed phase concentration, the difference between the trithermal machine and the quadrithermal machine becomes evident. Actually, if the internal energy, U , produced in the regeneration is higher than that necessary to the adsorption, this last process can occur at a temperature higher than the condensation (or ambient) temperature, as shown in Fig. 3.

The reference temperature T_0 can be determined through the Clausius-Clapeyron formula (Eq. 15), with aid of the isosters of the adsorbent-adsorbate pair indicated in Fig. 4.

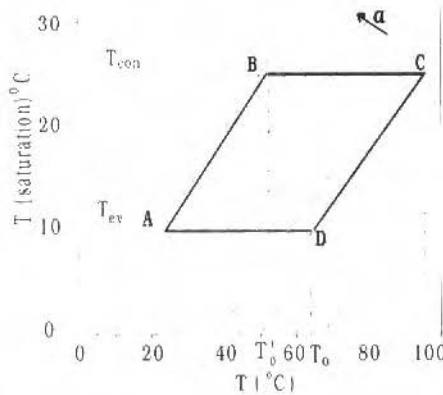


Fig. 4 Adsorption cycle and isosters on an equilibrium diagram

Integrating Eq. (15) along the desorption process (isoster AB), the following is valid for the adsorbed phase:

$$\ln \frac{P_{con}}{P_{ev}} = \int_{T_{ads}}^{T_0} \frac{\Delta H(a, T)}{RT^2} dT \quad (29)$$

where P_{con} and P_{ev} are the saturation pressures at temperatures T_{con} and T_{ev} , respectively, and a is the concentration (adsorbed mass/adsorbent mass).

And for the liquid phase:

$$\ln \frac{P_{con}}{P_{ev}} = \int_{T_{ev}}^{T_{con}} \frac{L(T)}{RT^2} dT \quad (30)$$

According to Eqs. (29) and (30):

$$\int_{T_{ev}}^{T_{con}} L d\left(\frac{1}{T}\right) = \int_{T_{ads}}^{T_0} \Delta H d\left(\frac{1}{T}\right) \quad (31)$$

Assuming that L and ΔH are constant during the isosteric process, then:

$$L \left(\frac{1}{T_{ev}} - \frac{1}{T_{con}} \right) = \Delta H \left(\frac{1}{T_{ads}} - \frac{1}{T_0} \right) \quad (32)$$

Utilizing a similar procedure for the adsorption process (isoster CD):

$$L \left(\frac{1}{T_{ev}} - \frac{1}{T_{con}} \right) = \Delta H \left(\frac{1}{T_o} - \frac{1}{T_{reg}} \right) \quad (33)$$

Combining Eqs. (32) and (33) a correlation between T_o and T_o' can then be written as:

$$\frac{1}{T_{ads}} - \frac{1}{T_o'} = \frac{1}{T_o} - \frac{1}{T_{reg}} \quad (34)$$

Coefficient of Thermal Performance

The COP of a quadrithermal machine represents the ideal thermodynamic efficiency, corresponding to those four temperatures (T_{ev} , T_{ads} , T_{con} and T_{reg}) of the cycle. It indicates the maximum performance of a machine operating in a continuous cycle with an ideal sensible heat recovery. Then, it can be expressed as:

$$COP = \frac{L(T_{ev})}{\Delta H(T_{reg})} \quad (35)$$

According to Eq. (33) the COP relation reduces to:

$$COP = \frac{\frac{1}{T_o} - \frac{1}{T_{reg}}}{\frac{1}{T_{ev}} - \frac{1}{T_{con}}} \quad (36)$$

This equation is equivalent to Eq. (24), which was established for the Carnot COP.

Considering the state of equilibrium between the adsorbed and gaseous phases, the entropy variation of the system ΔS_e can be described from Clausius-Clapeyron as:

$$\Delta S_e = \frac{\Delta H}{T_{reg}} - \frac{L}{T_{con}} \quad (37)$$

In view of Eq. (35) and introducing a $L/\Delta H$ term from Eq. (37), the COP can be alternatively expressed as:

$$COP = \frac{T_{con}}{T_{reg}} \frac{1}{\left(1 + \frac{T_{con} \Delta S_e}{L} \right)} \quad (38)$$

Assuming that $T_{con} \Delta S_e \approx 0$, the thermal performance coefficient of a quadrithermal machine can be described as a function of a simple ratio between the condensation and regeneration temperatures, as following:

$$COP \cong \frac{T_{con}}{T_{reg}} \quad (39)$$

The variation of this coefficient with the regeneration temperature is shown in Fig. 2. For $T_{reg} = 100^\circ\text{C}$, its value is 0.81, while the COP of a trithermal machine is 1.44. These values are coincident when $T_{reg} \approx 72^\circ\text{C}$.

Experience has demonstrated that the performance of intermittent adsorption cooling systems are much lower than maximum values related to the quadrithermal machine, due to the degradation of the available energy in the form of sensible heat (Meunier and Douss, 1990). The best COP values obtained at present are between 0.4 and 0.5. In fact, real adsorptive machines have low performances because heat transfer occurs at several temperature levels.

Coefficient of Real Thermal Performance

The real COP of an intermittent adsorptive cooling machine is evaluated considering the sensible heat variation of the system, which is composed of a reactor (adsorbent bed), a quantity of adsorbate and a heat exchanger coupled to the reactor. For a given regenerating temperature T_{reg} , the COP can be expressed as:

$$COP = \frac{m_1 \Delta a L(T_{ev}) - Q_3}{m_1 \Delta a \Delta H(T_{reg}) + Q_1 + Q_2} \quad (40)$$

where:

m_1 - mass of adsorbent

Δa - variation of adsorbate concentration

Q_1 - quantity of sensible heat transferred to cool the adsorbate from the condensation temperature to the evaporation temperature

Q_2 - quantity of sensible heat necessary to increase the temperature of the reactor and the exchanger from the adsorption temperature to the condensation temperature

Q_3 - variation of the internal energy of the adsorbed mass corresponding to the temperature variation of the reactor from the adsorption temperature to the condensation temperature.

Energy Equation

The reactor is composed of a porous bed occupying the annular space of a metallic cylinder coupled externally to a heat exchanger. It is connected to an evaporator and a condenser.

The basic assumptions concerning the adsorption process were described in the prior thermodynamic of adsorption analysis. However, the following hypotheses for the heat transfer in the adsorbent medium can be added: a) the pressure is uniform and constant; b) heat conduction occurs only in the radial direction; c) the adsorbent-adsorbate pair is treated as a continuous medium for the thermal conduction effect; and d) convective effects and pressure drops inside the reactor are negligible.

Then, the space-time relationship for the heat transfer in an adsorbent bed, including mass transfer, can be expressed by the following equation:

$$[\rho_l (C_1 + a C_2)] \frac{\partial T}{\partial t} = k \left(\frac{\partial^2 T}{\partial r^2} + \frac{1}{r} \frac{\partial T}{\partial r} \right) + q_{st} \rho_l \frac{\partial a}{\partial t} \quad (41)$$

where C is the heat capacity (subscripts 1 and 2 relate to the adsorbent and to the adsorbate, respectively), ρ is the specific mass, k is the conductivity of the adsorbent and r is the distance along radial direction.

After some algebraic operations, the following expression for the kinetics of adsorption $\partial a / \partial t$ is obtained:

$$\frac{\partial a}{\partial t} = b \left[\frac{d \ln P}{dt} - \frac{q_{st}}{RT^2} \frac{dT}{dt} \right] \quad (42)$$

with

$$b = an DT^n \left(\ln \frac{P_s}{P} \right)^{n-1} \quad (43)$$

where n and D are parameters of the Dubinin-Astakhov equation.

Then, a final equation can be obtained as follows:

$$\left[\rho_l (C_1 + a C_2) + \frac{b \rho_l q_{st}^2}{RT^2} \right] \frac{\partial T}{\partial t} = \left(\frac{\partial^2 T}{\partial r^2} + \frac{1}{r} \frac{\partial T}{\partial r} \right) + b \rho_l q_{st} \frac{d \ln P}{d t} \quad (44)$$

The $d \ln P / dt$ term is determined as a function of the process that occurs in the reactor. For an isosteric process, when the reactor is isolated, it can be written:

$$\frac{d \ln P}{d t} = \frac{\iint b(a, T, P) \frac{q_{st}}{RT^2} r dr dz}{\iint b(a, T, P) r dr dz} \quad (45)$$

When the condensation or evaporation takes place, the pressure of the system, P , becomes equal to the saturation pressure, $P_s(t)$.

Boundary and Initial Conditions

It is assumed that there is a thermal resistance at the interface metallic/porous bed ($r = r_l$); thus, if T_p is the metal temperature and T_n the adsorbent temperature near the wall, the boundary condition is given by:

$$-k \left(\frac{\partial T}{\partial r} \right)_{r=r_l} = h(T_p - T_n) \quad (46)$$

where h is the thermal conductance at the exchanger/adsorbent surface.

At the interface porous bed/adsorbate tube ($r = r_o$), the boundary is assumed to be adiabatic:

$$\left(\frac{\partial T}{\partial r} \right)_{r=r_o} = 0 \quad (47)$$

For modeling of a refrigeration cycle system, the initial conditions are fixed based on the ambient temperature and on the properties of the considered adsorbent/adsorbate pair: $P|_{t=0} = P_0$, $T(r)|_{t=0} = T_{con}|_{t=0} = T_{amb}|_{t=0} = T_0$.

Conclusion

The principle of the adsorption process and considerations about adsorbents, especially concerning activated carbon, have been described. The main isotherms of adsorption were presented and compared. It has been concluded that the most suitable equation representing the adsorption of methanol in activated carbon is the Dubinin-Astakhov equation. From the thermodynamic analysis of the adsorption-cycle has been carried out, a simple ratio between condensation temperature and regeneration temperature was deduced, in order to evaluate the COP of a ideal quadrithermal machine. Finally, the energy equation for an adsorptive bed of an intermittent cooling machine, operating from moderate temperatures was established and detailed.

This theoretical analysis can be useful for an adequate design of a refrigeration system based on an adsorption cycle operating from a low-grade energy source.

References

- Bering, B.P., Dubinin, M.M. and Serpinsky, V.V., 1972, "On Thermodynamics of Adsorption in Micropores", *Journal of Colloid Interface Sciences*, Vol. 38, pp. 185-194.
- Dubinin, M.M. and Astakhov, V.A., 1971, "Development of the Concept of Volume Filling of Micropores in the Adsorption of Gases and Vapors by Microporous Adsorbents", American Chemical Society, Washington, DC, USA.
- Dubinin, M.M. and Erashko, I.T., 1975, "Kinetics of Physical Adsorption by Carbonaceous Adsorbents of Adsorbents of Biporous Structure", *Carbon*, Vol. 13, pp. 193-200.
- Dubinin, M.M. and Stoeckli, H.F., 1980, "Homogeneous and Heterogeneous Micropore Structures in Carbonaceous Adsorbents", *Journal of Colloid Interface Sciences*, Vol. 75, pp. 34-42.
- Guilleminot, J.J., Meunier, M. and Mischler, B., 1980, "Etude de Cycles Intermittents à Adsorption Solide pour la Réfrigération Solaire", *Revue de Physique Appliquée*, Paris, France, Vol. 15, pp. 441-452.
- Hill, T.L., 1960, "Introduction to Statistical Thermodynamics", Addison-Wesley Reading, Mass., USA.
- Kariogas, M. and Meunier, F., 1986, "Etude de la Relaxation d'un Réacteur à Zéolite pendant la Désorption Eclair Provoquée par un Echelon de Pression", *Chem. Eng. J.*, Vol. 32, pp. 171-192.
- Marle, C., 1985, "Principes Fondamentaux des Transferts en Milieu Poreux", Les Bruyères, Gironde, France Mérie, G., 1992, "Evolution of the Ozone Layer: Myth or Reality", *Refrigeration Science and Technology*, Proc. Symposium on Solid Sorption Refrigeration, Paris, France, Vol. 1, pp. 19-25.
- Meunier, F. and Douss, N., 1990, "Performance of Adsorption Heat Pumps: Active Carbon-Methanol and Zeolite-Water Pairs", *Transactions of ASHRAE Meeting*, Saint Louis, EUA, pp. 491-498.
- Passos, E.F., 1986, "Etude des Couples Charbon Actif-Methanol et de leur Application a la Réfrigération Solaire", Ph.D. Thesis, Ecole Polytechnique Fédérale de Lausanne, Switzerland.
- Polany, M., 1932, *Trans. of Faraday Society*, Vol. 28, pp. 316-338.
- Ruthven, D.M., 1984, "Principles of Adsorption & Adsorption Processes", Wiley-Interscience Publication, New York.
- Sakoda, A. and Suzuki, M., 1984, "Fundamental Study on Solar Powered Adsorption Cooling System", *Journal of Chemical Engineering, Japan*, Vol. 17, pp. 52-57.
- Yang, R.T., 1987, "Gas Separation by Adsorption Processes" Butterworths, London, England.

Rapid Thermal Processing Furnace With Three Heating Zones

A. J. Silva Neto¹
M. J. Fordham
W. J. Kiether
F. Y. Sorrell

North Carolina State University
Department of Mechanical and Aerospace Engineering
Raleigh, NC 27695-7910 USA

Abstract

A new rapid thermal processing (RTP) furnace configuration is described, and the mathematical model, model predictions and experimental results are presented. The ultimate design objective is to achieve uniform wafer temperature distribution throughout the complete heating cycle. It is accomplished as demonstrated by the uniformity of the measured film thickness after polycrystalline silicon deposition. The three-zone RTP system was also designed for operation with thin quartz windows, for minimum window heating.

Keywords: Rapid Thermal Processing, Modeling, Thermal Radiation, Temperature Uniformity.

Introduction

In search of higher packing density, the development of integrated circuits technology has been accompanied by a reduction of device sizes. The standard technique of silicon wafer processing in diffusion furnaces (Schravendijk et al., 1987) is not capable of meeting the new manufacturing requirements, mainly because of the undesirable high product *temperature x time*, and difficulty in achieving uniformity and repeatability. Rapid Thermal Processing (RTP) using infrared radiation is the most promising alternative (Singh, 1988), being already used in several semiconductor processing steps (Moleshi et al., 1992), and most recently, the Rapid Thermal Oxidation (RTO) and the Rapid Thermal Chemical Vapor Deposition (RTCVD) processes have been the subject of intensive research (Öztürk et al., 1991, Sadana et al., 1990, 1991, Sorrell et al., 1994, 1995).

Since the early stages of use and development in the rapid thermal annealing process (Seidel et al., 1985, Hasenack et al., 1985, Sheets, 1985, Stein et al., 1986), it has been observed that the fast heating ramp-up and cooling ramp-down rates as well as the short periods of time at high temperatures, i.e. *low thermal budget*, associated with RTP, minimizes dopant diffusion and enhances elimination of the semiconductor crystalline lattice damage (Lunnon et al., 1985, Peter et al., 1988).

RTP is a single wafer process, with the potential for better wafer-to-wafer uniformity, i.e. repeatability (Gyuresik et al., 1991). Another asset of the RTP single wafer process is the reduced equipment footprint on clean room floor.

The key to the successful application of rapid thermal furnaces in wide scale manufacturing use lies on obtaining a uniform temperature distribution over the entire surface of the wafer (Schaper et al., 1994). This has proven to be a major task. Defects caused by thermal stresses have been described and analysed (Bentini et al., 1984, Lord, 1988, Jongste et al., 1994). Öztürk et al. (1992) discussed a self-induced degrading mechanism triggered by a nonuniform temperature distribution that causes nonuniform radiation absorption across the wafer, yielding nonuniform film thickness in Chemical Vapor Deposition (CVD) processes. Kakoschke et al. (1991) described the formation of slip lines originated by temperature transient gradients.

Many configurations of rapid thermal furnaces have been designed, built and tested. The flat plate reactors require quite thick quartz windows to separate the heating lamps from the low pressure operating chamber. As cooling of the inner wall of the quartz window becomes difficult, film deposition at that surface may occur during Chemical Vapor Deposition (CVD), interfering with the process. Another drawback is the wafer temperature nonuniformity due to the radiant heat loss at the wafer edge (Zöllner et al., 1993). Lamp contouring (Gyuresik et al., 1991, Sorrell et al., 1992, Henda et

¹ Visiting Assistant Professor. Permanent Address: Instituto Politécnico/UERJ. Rua Alberto Rangel S/No., Nova Friburgo, Rio de Janeiro, 28630-050, Brazil. e-mail: ajsneto@iprj.uerj.br

al., 1994), thermal guard rings (Lord, 1988, Knutson et al., 1994) and dedicated reflectors or furnace walls with varying properties (Kersch et al., 1991) have been tested in order to achieve better wafer surface temperature uniformity. It seems however that the best approach would be the multizone heating with multisensor active control (Campbell et al., 1991), with one heat source located at the wafer edge (Campbell and Knutson, 1992, Kakoschke and Bußmann, 1989, Kakoschke et al., 1990).

Chapman et al. (1991) designed and built a cylindrical reactor to avoid problems associated with the rather thick quartz windows required by the flat plate reactors. Due to the cylindrical geometry the quartz wall can be reduced by a factor of two to five.

To capture the benefits of both the multizone heating and the cylindrical furnace, Kiether et al., 1994 developed the three-zone rapid thermal furnace, that will be described and modeled in this work.

Another possible source of temperature nonuniformity is the convection cooling at the wafer surface in processes that are carried out at or near atmospheric pressure. The usual approach in order to take this mechanism into account is to measure a heat transfer coefficient (Lord, 1988) or to calculate it using commercially available software like FLUENT (FLUENT, 1993) or SIMPLER (Patankar, 1980). The heat transfer coefficient is then used in the heat flux boundary condition at the wafer surface. This aspect will not be covered in this paper because it has been discussed elsewhere (Sorrell et al., 1994, Campbell et al., 1991).

Three-Zone RTP Furnace

The three-zone RTP prototype has been designed to process wafers up to 6 inches in diameter, and has been constructed as the initial module on the *North Carolina State University* cluster tool, as part of an ongoing effort towards single wafer, low thermal budget, in situ processing. The cluster tool presently consists of the three-zone RTP module, a central wafer handler, a commercial RTP module, an etch module, and a multiple wafer load lock (Kiether et al., 1994).

A diagram of the three-zone RTP module is shown in Fig. 1. The top heating lamp bank, zone A, is used to provide nearly uniform bulk heating of the wafer. As presently designed, zone A provides a radiant heat flux approximately 10% higher at the wafer center than at the edge. The heating lamp bank of zone B heats primarily the wafer edge, and the radiant heat from zone C is nearly uniform across the wafer planar surface.

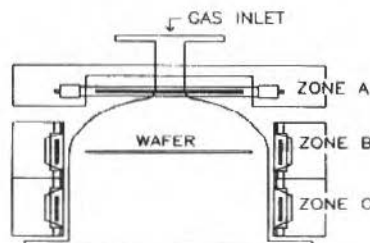


Fig. 1 Diagram of the three-zone RTP system.

In practice, the power to each of the three zones can be varied to produce a very uniform temperature distribution over the wafer surface.

Zone A is composed of ten 2.0 kW tungsten-halogen lamps with a filament length of 16.51 cm (6.5 in). They are arranged in a flat linear array. The use of wafer rotation and close packing of the lamps within the array, compensates for the lack of axial symmetry. Each of zones B and C consists of thirty two 1.0 kW tungsten-halogen lamps with a filament length of 1.91 cm (0.75 in).

The primary wafer process position as shown in Fig. 1, is right at the center of the lamp filaments of zone B. The top lamp bank, zone A, is located 13.34 cm (5.25 in) above that position, and the center of the lamp filaments of zone C is 10.16 cm (4 in) below the primary wafer process position.

The quartz process tube consists of a modified bell jar, with an internal diameter of 17.78 cm (7 in), an overall height of 31.75 cm (12.5 in) and wall thickness of 0.5 cm (0.2 in). Air is blown vertically upward along the cylinder from the quartz base for cooling.

Cho et al. (1994) have also proposed an RTP furnace configuration with a vertical quartz tube, but the lamps are distributed on a hexagonal arrangement.

Thermal Model

There has been considerable effort in modeling RTP furnaces. The main motivation for taking this approach has been the evaluation of RTP geometry, improvement of existing equipment at low cost, and design of new configurations (Kersch et al., 1991, Sorrell et al., 1992, 1994). Also model-based control has the greatest potential for controlling temperature in RTP (Cho and Kailath, 1993), with low-order models being developed for real-time applications (Schaper et al., 1992).

The simulation methodology for RTP furnaces consists basically of two modules. These are: (1) computation of the heat flux at the surface and edge of the wafer due to radiant heat sources and (2) computation of the wafer temperature distribution, given the irradiation calculated in module (1). Other modules should be added if chemical vapor deposition or thermal oxidation processes are being analysed. These additional modules would be related to fluid flow and chemical process analysis. Here we will concentrate on modules (1) and (2).

The easiest and less accurate approach for module (1) is to assume uniform irradiation at the wafer surface (Shieh and Carter, 1989). Due to its simplicity, it has been used to investigate the interaction of the furnace, temperature sensing technique and the control system (Sorrell et al., 1990).

Sorrell et al. (1992) and Gyuresik et al. (1991) used a raytrace technique in which the lamp/reflector geometry was used to determine the solid angle subtended by a specific area on the wafer. Fordham (1991) and Sorrell et al. (1994, 1995) developed a slightly different approach in which a large number of rays with constant solid angle are tracked throughout the furnace. This approach will be described briefly later.

The diffuse view-factor approach has been used (Lord, 1988, Knutson et al., 1994) although the reflections occurring inside the chamber are mostly specular. Kersch et al. (1991) used an iterative procedure to account for multiple reflections. View factors are often not known accurately or require ray tracing or Monte Carlo methods to be determined (Cole et al., 1994, Li et al., 1997). Therefore it seems that although being time consuming, the straightforward ray tracing technique seems to be the most convenient approach for solving module (1). As reflections at the furnace walls are primarily specular, this method is also more accurate.

Sato (1967) showed that doped silicon specimens are essentially opaque. Therefore, absorption or reflection of radiation occurs at the wafer surface, and heat is transferred within the wafer solely by conduction. Consequently, module (2), i.e. the computation of the transient temperature distribution across the wafer, requires only the solution of the parabolic heat diffusion equation (including proper boundary and initial conditions). Here we used finite difference approximations (Özisik, 1994) to take into account variable wafer properties. A summary of the approach here described has been presented by Silva Neto and Sorrell (1995).

Module (1) - Ray-Trace Algorithm

The lamp filament is divided in a number of segments, each with a length dz as shown in Fig. 2.

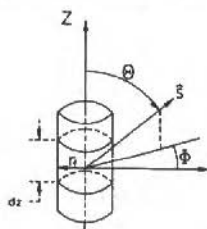


Fig. 2 Lamp segment and the coordinate system.

Any differential area dA at the surface of the filament, given by

$$dA = dz r_f d\phi \quad (1)$$

is assumed to be a black body at temperature T_f . Therefore, the power emitted by the differential area dA into the solid angle $d\Omega$ around the direction represented by the unit vector \hat{s} is given by (Modest, 1993)

$$P_{d\Omega} = \frac{\sigma T_f^4}{\pi} dA (\hat{n} \cdot \hat{s}) d\Omega \quad (2)$$

where

$$d\Omega = \sin\theta \, d\theta \, d\phi \quad (3)$$

\hat{n} is the unit outward normal to differential area dA , and σ is the Stefan-Boltzmann constant.

Assuming azimuthal symmetry around the filament axis, and integrating over all differential areas that contribute to the power emitted into $d\Omega$ around \hat{s} , the total power, i.e. energy per unit time, due to a particular segment of the filament is given by

$$P = \left(\frac{2\sigma}{\pi} T_f^4 r_f \right) \sin\theta \, dz \, d\Omega \quad (4)$$

The ray-trace algorithm consists on tracking a large number of rays emitted from the lamps. First, the solid angle $d\Omega$ is chosen as a small number to ensure that when the ray hits the wafer it delivers its energy to only one cell of the mesh that is used to represent the wafer surface. The polar angle domain $0 < \theta < \pi$ is divided in a large number of angles, n_θ , say $n_\theta = 2000$ or 3000 . Then from Eq.(3) the increment on the azimuthal angle, $d\phi$, is calculated such that $d\Omega$ is kept almost constant. As $0 < \phi < 2\pi$, the number of divisions of the azimuthal angle domain, n_ϕ , can now be calculated using $d\phi$.

The term in parenthesis in Eq.(4) can be related to the total power output of the lamp, avoiding the troublesome requirement of knowing the temperature of the filament.

For each pair (θ_i, ϕ_j) , $i = 1, 2, \dots, n_\theta$ and $j = 1, 2, \dots, n_\phi$, it is considered that a ray with the power calculated using Eq.(4) is emitted. This ray may hit the wafer directly or after reflections on the inner surfaces of the furnace, or may escape the furnace.

If the ray hits the side wall, ceiling or bottom of the furnace, it is specularly reflected and the power of the ray is attenuated by a fraction given by the absorptivity of the surface. To avoid an excessive computation time, the number of bounces allowed is limited, i.e. the ray is followed throughout the chamber, and if it does not hit the wafer at a specified number of bounces, it is discarded.

Fordham (1991) and Sorrell et al. (1994, 1995) have analysed the convergence of the ray-trace algorithm for the cylindrical RTP system, and concluded that using 2000 to 3000 divisions on the polar angle domain, i.e. $n_\theta = 2000$ or 3000 , and a limit of 5 bounces, converged results were obtained at acceptable computational times. The same is true for the three-zone RTP system.

During our experimental work with the tungsten-halogen lamps of zones B and C, we observed that the dependence of the power emitted, P , with the polar angle, θ , does not follow a sinusoidal distribution as prescribed by Eq.(4). In Fig.3 we show the actual distribution obtained from experiments. This dependence has been incorporated in the ray-trace algorithm.

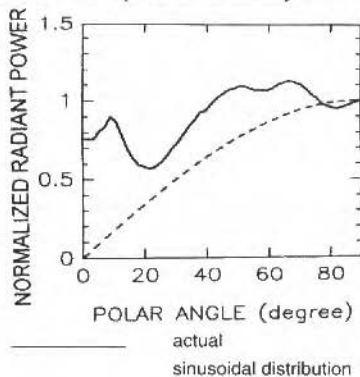


Fig. 3 Angular dependence of lamp emitted thermal radiation.

Module (2) - Wafer Temperature Distribution

The transient temperature distribution across the wafer is obtained from the solution of the equation of heat diffusion with proper initial and boundary conditions. To derive the equation of heat conduction through the wafer, consider a differential element $dV = r dr d\phi l$, as shown in Fig. 4, where l is the wafer thickness, q''_x is the radiative heat flux due to the lamps heating, q''_c is the convective heat flux, and q''_e represents the radiant heat flux emitted by the wafer.

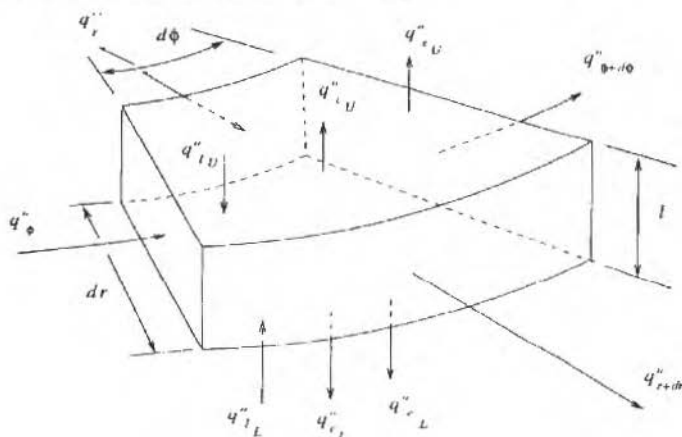


Fig. 4 Differential wafer element.

Applying the energy balance equation to the differential element dV and considering

$$q''_r = -k \frac{\partial T}{\partial r} \quad (5)$$

$$q''_\phi = -\frac{k}{r} \frac{\partial T}{\partial \phi} \quad (6)$$

$$q''_l = q''_{lU} + q''_{lL} = \varepsilon l(r, \phi, t) \quad (7)$$

$$q''_e = q''_{eU} + q''_{eL} = \varepsilon \sigma T^4(r, \phi, t) \quad (8)$$

one gets

$$\frac{1}{r} \frac{\partial}{\partial r} \left(k r \frac{\partial T}{\partial r} \right) + \frac{1}{r^2} \frac{\partial}{\partial \phi} \left(k \frac{\partial T}{\partial \phi} \right) + g(r, \phi, t) = \rho c_p \frac{\partial T}{\partial t} \quad (9)$$

where

$$g(r, \phi, t) = \frac{1}{l} [\varepsilon (l - \sigma T^4) - q_c] \quad (10)$$

$T(r, \phi, t)$ is the wafer temperature, $\rho(T)$ is the silicon density, $k(T)$ is the silicon thermal conductivity, $c_p(T)$ is the silicon specific heat, $l(r, \phi, t)$ is the total radiation heat flux that arrives on the wafer from all the other surfaces (directly from the lamps filaments or after specular reflections at the furnace walls), $q''_c(r, \phi, t)$ is the heat flux lost by convection, ε is the wafer emissivity (or absorptivity, considering that Kirchhoff law holds), and σ is the Stefan-Boltzmann constant.

The total irradiation $I(r, \phi, t)$ is calculated with the ray-trace algorithm taking into account multiple specular reflections inside the furnace as described in module (1).

As the amount of energy emitted by the wafer and reflected back by the furnace walls is negligible in comparison to the total irradiation due to the lamps, it is not taken into account in the energy balance described above. Numerical experiments validated this procedure.

Note that the boundary conditions of radiation and convection are included on the equivalent heat source term $g(r, \phi, t)$. A similar source term is derived for the differential elements at the wafer edge. Note also that on the derivation of Eq. (9) it was assumed a uniform temperature across the wafer thickness. This is justified by the fact that the wafer radius is much larger than its thickness.

The initial temperature of the silicon wafer is considered known

$$T(r, \phi, t) = T_i \text{ for all } r, \phi \text{ and } t = 0 \quad (11)$$

Sato (1967) collected experimental data on the spectral emissivity of undoped and doped silicon wafers. The tungsten-halogen lamps used in the three-zone RTP module described previously behaves approximately as a black body emitter at temperatures up to 3100 K with a dropoff at 3.5 microns due to the quartz housing.

RTP processes typically involve the use of doped wafers. Within the range of wavelengths where most of the energy is emitted by the lamps it can be seen from the data obtained by Sato that the emissivity of the doped silicon presents a weak dependence with the wavelength as well as with the temperature, being 0.7 a good approximation for this property. This assumption of gray body behaviour greatly simplifies the wafer thermal model.

To approximate the solution of Eqs.(9)-(11), an explicit finite difference discretization is used. The thermal properties do not present steep gradients with temperature, and the total time for rapid thermal processing is short, i.e. less than a minute. Therefore, the requirements on the time step to be used to ensure stability are not too strict, not posing any problem with regard to computational time, justifying the use of the straightforward explicit time discretization of the equations.

For the mesh interior nodes is written

$$\begin{aligned} T_{i,j}^{n+1} = & T_{i,j}^n + \left(\frac{\Delta t}{\rho_{i,j}^n c_{p,i,j}^n} \right) \left(\frac{I}{r_i \Delta r^2} \right) [k_{i+\frac{1}{2},j}^n r_{i+\frac{1}{2}} (T_{i+\frac{1}{2},j}^n - T_{i,j}^n) - k_{i-\frac{1}{2},j}^n r_{i-\frac{1}{2}} (T_{i,j}^n - T_{i-\frac{1}{2},j}^n)] \\ & + \left(\frac{\Delta t}{\rho_{i,j}^n c_{p,i,j}^n} \right) \left(\frac{I}{r_i^2 \Delta \phi^2} \right) [k_{i,j+\frac{1}{2}}^n (T_{i,j+\frac{1}{2}}^n - T_{i,j}^n) - k_{i,j-\frac{1}{2}}^n (T_{i,j}^n - T_{i,j-\frac{1}{2}}^n)] \\ & + \left(\frac{\Delta t}{\rho_{i,j}^n c_{p,i,j}^n} \right) g_{i,j}^n \quad 2 \leq i \leq M-1, \quad 2 \leq j \leq N-1 \end{aligned} \quad (12)$$

where

$$r_i = (i-1)\Delta r, \quad i = 1, 2, \dots, M \quad (13)$$

$$\phi_j = (j-1)\Delta \phi, \quad j = 1, 2, \dots, N \quad (14)$$

$$t_n = n\Delta t, \quad n = 1, 2, \dots, L \quad (15)$$

$$\Delta r = \frac{R}{M-1} \quad (16)$$

$$\Delta \phi = \frac{2\pi}{N} \quad (17)$$

$$k_{i+\frac{1}{2},j}^n = \frac{1}{2} (k_{i,j}^n + k_{i+1,j}^n) \quad (18)$$

R is the wafer radius and the other three values for the thermal conductivity used in Eq.(12), $k_{i-1/2,j}^n$, $k_{i,j+1/2}^n$ and $k_{i,j-1/2}^n$, are obtained similarly to $k_{i+1/2,j}^n$ shown in Eq.(18).

For the center node Eq.(12) does not hold because r goes to zero. It is considered then an average on the neighbouring nodes, yielding

$$T_c^{n+1} = T_c^n + \left(\frac{\Delta t}{2 \rho_c^n c_{p,c}^n \Delta r^2} \right) [4 \bar{T}_j^n k_c^n - T_c^n (4 k_c^n + 4 \bar{k}_j^n) + 4 \overline{k_j^n T_j^n}] + \left(\frac{\Delta t}{\rho_c^n c_{p,c}^n} \right) g_c^n \quad (19)$$

where \bar{T}_j^n , \bar{k}_j^n and $\overline{k_j^n T_j^n}$ are mean temperature, mean thermal conductivity, and mean product of thermal conductivity and temperature, respectively, for nodes surrounding the wafer center.

Fictitious nodes at radius $r = M \Delta r$, i.e. beyond wafer edge, are included in the finite difference mesh. Their temperatures are obtained with the edge radiation boundary condition. Once these temperatures, T_{M+1}^n , are known, Eq.(12) is written for node $i = M$. Now there is a complete set of equations to determine the temperatures $T_{i,j}^{n+1}$ with $i = 1, 2, \dots, M$ and $j = 1, 2, \dots, N$, for $n = 1, 2, \dots, L$. For $i = 1$, $T_{i,j}^{n+1} = T_c^{n+1}$ with $j = 1, 2, \dots, N$.

Results and Discussion

Model results for the three-zone RTP system are given in Figs. 5 and 6. Figure 5 shows the calculated radial distribution of radiant heat flux, or total irradiation, incident on the wafer surface. No angular dependence on the azimuthal angle ϕ is considered because of the rotation of the wafer. Due to the small thickness of the wafer, i.e. 0.5 mm (0.02 in), the temperature gradient across the wafer thickness is negligible, i.e. 1-2 °C (Sorrell et al., 1995). The total irradiation profiles given by each of the heating zones as well as for two combinations of them are presented.

From these results we conclude that by adequately configuring the power delivered to heating zones A and C, a nearly uniform irradiation distribution over the planar surface of the wafer may be obtained. Additionally, the power delivered by heating zone B can be adjusted to compensate for the wafer edge heat loss. The inherent flexibility of the three heating zones in controlling the irradiation distribution is illustrated.

The irradiation profiles shown for zone C were in fact obtained with only 40 % of the lamp power available.

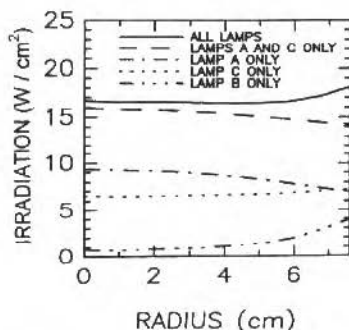


Fig. 5 Computed radiant heat flux distribution.

The irradiation profiles shown in Fig. 5 were obtained using the ray-trace algorithm described previously, and they were used to calculate the wafer temperature distribution shown in Fig. 6.

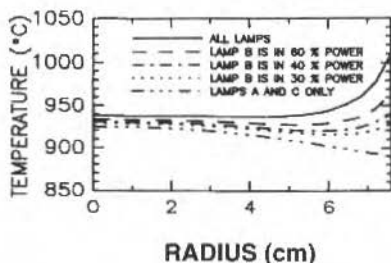


Fig. 6 Predicted wafer temperature distribution.

Experimental trials have been performed to test and verify the capabilities of the three-zone RTP system in regard to both the model predictions and overall performance. These trials were performed on six inch silicon wafers with thermocouples attached to them to allow temperature measurements. As shown in Fig. 7 the use of top lamp bank, zone A, alone, overheats the center, with significant edge cooling. The bottom ring, zone C, results are nearly uniform across the entire wafer, while the edge ring, zone B, shows the ability to directly heat the wafer edge.

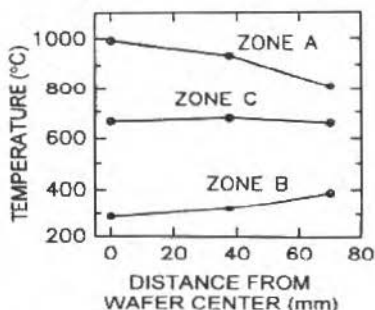


Fig. 7 Measured wafer temperature distribution.

The uniformity during a typical polycrystalline silicon (poly) rapid thermal chemical vapor deposition (RTCVD) was also investigated. Figure 8 shows the measured thickness profile for a 6 inch wafer. The electric power delivered to all three lamp banks was adjusted in order to produce a very uniform thickness distribution. As the thickness of the film is directly related to the temperature, the results in Fig. 8 demonstrate the ability of the three-zone RTP system to produce a nearly uniform temperature distribution.

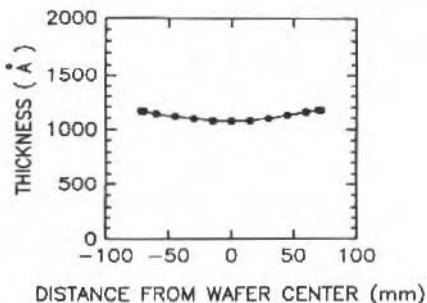


Fig. 8 Polysilicon deposition thickness profile.

Conclusions and Future Trends

The three-zone RTP system here described was designed to produce temperatures high enough for all desired processes, and to provide a nearly uniform temperature distribution across the wafer surface during ramp-up, steady state processing and ramp-down.

The modeling approach was used in the stages of development of the system, and has been validated with experimental data. The present system handles wafers up to 6 inches in diameter, but the simulations show that the present design can be easily extended to 12 inch wafers. Some work has already been done by Knutson et al. (1994) on 8 inch wafers.

Acknowledgements

This work has been supported by the NSF Engineering Research Centers Program through the Center for Advanced Electronic Materials Processing (Grant CDR 8721505), The Semiconductor Research Corporation (SRC Contract # 93-MP-132) and the SRC SCOE program at NCSU (SRC Contract # 93-MC-509).

References

- Bentini, G., Corraera, L. and Donolato, C., 1984, "Defects Introduced in Silicon Wafers During Rapid Isothermal Annealing: Thermoelastic and Thermoplastic Effects", *J. Appl. Phys.*, Vol. 56, No. 10, pp. 2922-2929.
- Campbell, S. A., Ahn, K. H., Knutson, K. L., Liu, B. Y. H. and Leighton, J. D., 1991, "Steady-State Thermal Uniformity and Gas Flow Patterns in a Rapid Thermal Processing Chamber", *IEEE Transactions on Semiconductor Manufacturing*, Vol. 4, No. 1, pp. 14-20.
- Campbell, S. A. and Knutson, K. L., 1992, "Transient Effects in Rapid Thermal Processing", *IEEE Transactions on Semiconductor Manufacturing*, Vol. 5, No. 4, pp. 302-307.
- Chapman, D. T., Melzak, J. M., Fordham, M. J., Wortman, J. J., Öztürk, M. C. and Sorrell, F. Y., 1991, "A Cylindrical Tube Based Rapid Thermal Processor", *179th Electrochemical Soc. Mtg.*, Vol. 358, pp. 541.
- Cho, B.-J., Vandenabeele, P. and Maex, K., 1994, "Development of a Hexagonal-Shaped Rapid Thermal Processor Using a Vertical Tube", *IEEE Transactions on Semiconductor Manufacturing*, Vol. 7, No. 3, pp. 345-353.
- Cho, Y. M. and Kailath, T., 1993, "Model Identification in Rapid Thermal Processing Systems", *IEEE Transactions on Semiconductor Manufacturing*, Vol. 6, No. 3, pp. 233-245.
- Cole, J. V., Knutson, K. L. and Jensen, K. F., 1994, "Monte Carlo Simulation of Radiative Heat Transfer in Rapid Thermal Processing (RTP) Systems", *Proc. Materials Research Society, Symp. G, MRS Vol. 342*, pp. 425-430.
- Fluent, 1993, Version 4.2. Fluent Inc., Lebanon, N. H.
- Fordham, M. J., 1991, A Temperature Uniformity Model for Semiconductor Wafer Rapid Isothermal Processing, M. S. Thesis, N. C. State University, Raleigh, N.C.
- Gyuresik, R. S., Riley, T. J. and Sorrell, F. Y., 1991, "A Model for Rapid Thermal Processing: Achieving Uniformity Through Lamp Control", *IEEE Transactions on Semiconductor Manufacturing*, Vol. 4, No. 1, pp. 9-13.
- Hasenack, C. M., Souza, J. P. and Baumvol, I. J. R., 1985, "The Suppression of Residual Defects in Silicon Implanted with Arsenic by Rapid Isothermal Annealing", *Nuclear Instruments and Methods in Physics Research B*, Vol. 9, pp. 341-343.
- Henda, R., Scheid, E. and Bielle-Daspert, D., 1994, "A 3-Dimensional Temperature Uniformity Model for a Rapid Thermal Processing Furnace", *Proc. Materials Research Society, Symp. G, MRS Vol. 342*, pp. 419-424.
- Jongste, J. F., Oosterlaken, T. G. M., Bart, G. C. J., Janssen, G. C. A. M. and Radelaar, S., 1994, "Deformation of Si (100) Wafers During Rapid Thermal Annealing", *J. Appl. Phys.*, Vol. 75, No. 6, pp. 2830-2836.
- Kakoschke, R. and Bußmann, E., 1989, "Simulation of Temperature Effects During Rapid Thermal Processing", *Proc. Materials Research Society, Symp. B*.
- Kakoschke, R., Bußmann, E. and Föll, H., 1990, "Modelling of Wafer Heating During Rapid Thermal Processing", *Appl. Phys. A*, Vol. 50, pp. 141-150.
- Kakoschke, R., Bußmann, E. and Föll, H., 1991, "The Appearance of Spatially Nonuniform Temperature Distributions During Rapid Thermal Processing", *Appl. Phys. A*, Vol. 52, pp. 52-59.
- Kersch, A., Schäfer, H. and Werner, C., 1991, "Improvement of Thermal Uniformity of RTP-CVD Equipment by Application of Simulation", *International Electron Devices Meeting, Washington D.C.*, pp. 34.3.1-34.3.4.
- Kiether, W. J., Fordham, M. J., Yu, S., Silva Neto, A. J., Conrad, K. A., Hauser, J. R., Sorrell, F. Y. and Wortman, J. J., 1994, "Three-Zone Rapid Thermal Processor System", *Proc. 2nd International Rapid Thermal Processing Conference*, pp. 96-101.

- Knutson, K. L., Campbell, S. A. and Dunn, F., 1994, "Modeling of Three-Dimensional Effects on Temperature Uniformity in Rapid Thermal Processing of Eight Inch Wafers", IEEE Transactions on Semiconductor Manufacturing, Vol. 7, No. 1, pp. 68-72.
- Li, B.-W., Tao, W.-Q., and Liu, R.-X., 1997, "Ray Effect in Ray Tracing Method for Radiative Heat Transfer", Int. J. Heat Mass Transfer, Vol. 40, No. 14, pp. 3419-3426.
- Lord, H. A., 1988, "Thermal and Stress Analysis of Semiconductor Wafers in a Rapid Thermal Processing Oven", IEEE Transactions on Semiconductor Manufacturing, Vol. 1, No. 3, pp. 105-114.
- Lunnon, M. E., Chen, J. T. and Baker, J. E., 1985, "Diode Structures Formed by Rapid Thermal Annealing of Boron Implanted Silicon", Appl. Phys. Lett., Vol. 46, No. 1, pp. 35-37.
- Modest, M. F., 1993, Radiative Heat Transfer, McGraw-Hill, New York.
- Moleshi, M. M., Davis, C. and Bowling, A., 1992, "Microelectronics Manufacturing Science and Technology: Single-Wafer Thermal Processing and Wafer Cleaning", TI Technical Journal, Vol. 9, No. 5, pp. 44-64.
- Özsisik, M. N., 1994, Finite Difference Methods in Heat Transfer, CRC Press, Boca Raton.
- Öztürk, M. C., Sorrell, F. Y., Wortman, J. J., Johnson, F. S. and Grider, D. T., 1991, "Manufacturability Issues in Rapid Thermal Chemical Vapor Deposition", IEEE Transactions on Semiconductor Manufacturing, Vol. 4, No. 2, pp. 155-165.
- Öztürk, M. C., Sanganeria, M. K. and Sorrell, F. Y., 1992, "A Uniformity Degradation Mechanism in Rapid Thermal Chemical Vapor Deposition", Appl. Phys. Lett., Vol. 61, No. 22, pp. 2697-2699.
- Patankar, S. V., 1980, Numerical Heat Transfer and Fluid Flow, McGraw-Hill, New York.
- Peter, C. R., Souza, J. P. and Hasenack, C. M., 1988, "Prolonged and Rapid Thermal Annealing of Boron Implanted Silicon", J. Appl. Phys., Vol. 64, No. 5, p.2696-2699.
- Sadana, D. K., Souza, J. P. and Cardone, F., 1990, "N Doping of Gallium Arsenide by Rapid Thermal Oxidation of a Silicon Cap", Appl. Phys. Lett., Vol. 57, No. 16, pp. 1681-1683.
- Sadana, D. K., Souza, J. P. and Cardone, F., 1991, "Formation of Highly n-Doped Gallium Arsenide Layers by Rapid Thermal Oxidation Followed by Rapid Thermal Annealing of Silicon-Capped Gallium Arsenide", Appl. Phys. Lett., Vol. 58, No. 11, pp. 1190-1192.
- Sato, T., 1967, "Spectral Emissivity of Silicon", Japanese Journal of Applied Physics, Vol. 6, No. 3, pp. 339-347.
- Schaper, C. D., Cho, Y. M. and Kailath, T., 1992, "Low-Order Modeling and Dynamic Characterization of Rapid Thermal Processing", Appl. Phys. A, Vol. 54, pp. 317-326.
- Schaper, C., Moleshi, M., Saraswat, K. and Kailath, T., 1994, "Control of MMST RTP: Repeatability, Uniformity and Integration for Flexible Manufacturing", IEEE Transactions on Semiconductor Manufacturing, Vol. 7, No. 2, pp. 202-219.
- Schravendijk, B. J., De Koning, W. L. and Nuijen, W. C., 1987, "Modeling and Control of the Wafer Temperature in a Diffusion Furnace", J. Appl. Phys., Vol. 61, No. 4, pp. 1620-1627.
- Seidel, T. E., Lischner, D. J., Pai, C. S. and Landau, S. S., 1985, "Temperature Transients in Heavily Doped and Undoped Silicon Using Rapid Thermal Annealing", J. Appl. Phys., Vol. 57, No. 4, pp. 1317-1321.
- Sheets, R. E., 1985, "Automatic Cassette to Cassette Radiant Impulse Processor", Nuclear Instruments and Methods in Physics Research B, Vol. 6, pp. 219-223.
- Shieh, T.-J. and Carter, R. L., 1989, "RAPS - A Rapid Thermal Processor Simulation Program", IEEE Transactions on Electron Devices, Vol. 36, No. 1, pp. 19-24.
- Silva Neto, A. J. and Sorrell, F. Y., 1995, "Thermal Radiation Analysis in a Rapid Thermal Processing Furnace", Proc. 13th Brazilian Congress of Mechanical Engineering.
- Singh, R., 1988, "Rapid Isothermal Processing", J. Appl. Phys., Vol. 63, No. 8, pp. R59-R114.
- Sorrell, F. Y., Harris, J. A. and Gyurcsik, R. S., 1990, "A Global Model for Rapid Thermal Processors", IEEE Transactions on Semiconductor Manufacturing, Vol. 3, No. 4, pp. 183-188.
- Sorrell, F. Y., Fordham, M. J., Öztürk, M. C. and Wortman, J. J., 1992, "Temperature Uniformity in RTP Furnaces", IEEE Transactions on Electron Devices, Vol. 39, No. 1, pp. 75-80.
- Sorrell, F. Y., Fordham, M. J., Yu, S. and Silva Neto, A. J., 1994, "RTP Modeling for CVD and Thermal Oxidation", Mat. Res. Soc. Symp. Proc., Vol. 342, pp. 407-417.
- Sorrell, F. Y., Yu, S. and Fordham, M. J., 1995, "A Methodology for Analysis of RTP CVD Systems", IEEE Transactions on Semiconductor Manufacturing, Vol. 8, No. 3, pp. 280-285.
- Stein, H. J., Hahn, S. K. and Shatas, S. C., 1986, "Rapid Thermal Annealing and Regrowth of Thermal Donors in Silicon", J. Appl. Phys., Vol. 59, No. 10, pp. 3495-3502.
- Zöllner, J. P., Patzschke, I., Pietzuch, V., Pezoldt, J. and Eichhorn, G., 1993, "To the Influence of the Wafer Edge in RTP", Mat. Res. Soc. Symp. Proc., Vol. 303, pp. 177-182.

Tensões Viscosas e Microturbilhões: As Causas da Hemólise Mecânica no Interior de Uma Bomba Centrífuga

Shear Stresses and Turbulent Eddies: The Causes of Mechanical Hemolysis in a Centrifugal Blood Pump

Marcos Pinotti

Universidade Federal de Minas Gerais
Escola de Engenharia
Departamento de Engenharia Hidráulica e Recursos Hídricos
30100-060 Belo Horizonte, MG Brazil
pinotti@cce.ufmg.br

Domingo M. Braile

FAMERP - Faculdade de Medicina de São José do Rio Preto
15091-450 São José do Rio Preto, SP Brazil
domingo@braile.com.br

Abstract

The lack of basic information about the performance of mechanical hemolysis severely affects centrifugal blood pump handling. The present work faced this problem by studying the flow structures and the way hemolytic potential is influenced by them. Two distinct approaches were applied: numerical simulation of a single channel of the pump, in order to understand the interaction of inertial, viscous and pressure forces in different operational situations, and non-invasive measurements of the velocity field to provide a general picture of the flow field as well as the interaction between the flow generated by each channel. Solving the momentum equations, that were written in generalized orthogonal coordinates, using the stress-flux formulation, was the challenge of the numerical method. The computational program was devised by employing the finite volume method and it was implemented in FORTRAN language. The velocity measurements were performed by a Laser Doppler anemometer system capable of acquiring and processing two simultaneous orthogonal velocity components. The main contribution of the present study concerns the development of a specific methodology which provides the link between the flow structures and the potential damage to the red blood cells.

Keywords: *Laser Doppler Anemometer, Turbulent Flow, Hemolysis, Centrifugal Blood Pump, Bioengineering.*

Resumo

A falta de informação básica sobre os mecanismos responsáveis pela hemólise mecânica impede, na maioria dos casos, o uso adequado da bomba centrífuga. Visando a preencher esta lacuna, este trabalho foi conduzido de modo a se estudar as estruturas básicas do escoamento no interior de uma bomba centrífuga e relacioná-las a um potencial de hemólise. Foram empregadas duas abordagens distintas: simulação numérica de um canal isolado da bomba, com o objetivo de compreender a interação entre as forças inerciais, viscosas e de pressão em diversas situações operacionais, e medição experimental do campo de velocidade nos canais internos da bomba, com a finalidade de se obter uma visão global do escoamento e da interação entre os diferentes canais. O desafio do método numérico foi resolver as equações do movimento escritas em coordenadas ortogonais generalizadas a partir da formulação de fluxo de tensão. O programa computacional foi implementado em FORTRAN, empregando um algoritmo baseado no método dos volumes finitos. As medidas de velocidade foram realizadas por um anemômetro laser Doppler, capaz de medir duas componentes simultâneas de velocidade. A contribuição deste trabalho foi o desenvolvimento de uma metodologia de análise que relaciona as estruturas básicas do escoamento ao potencial de danos às células vermelhas do sangue.

Palavras-chave: *Anemômetro Laser Doppler, Escoamento Turbulento, Hemólise, Bomba Centrífuga de Sangue, Bioengenharia.*

Introdução

Dispositivos para bombeamento de sangue são frequentemente empregados em duas situações clínicas distintas: assistência ventricular, quando ocorre falência cardíaca, e substituição da função do coração, em operações de *bypass* cardiopulmonar. *Bypass* cardiopulmonar é o nome da técnica, utilizada principalmente em operações cardíacas, pela qual as funções do coração e do pulmão são substituídas temporariamente por um circuito extracorpóreo que oxigena o sangue e o conduz de volta

ao paciente. O sangue é desviado do sistema venoso até um reservatório, bombeado através de um circuito que realiza a oxigenação extracorpórea (utilizando oxigenador tipo membrana ou de bolhas) e injetado no sistema arterial. Uma bomba (de roletes ou centrífuga) é instalada neste circuito para realizar a movimentação do sangue do reservatório até a cânula conectada à aorta.

Do ponto de vista de engenharia, a assistência ventricular e o *bypass* cardiopulmonar diferenciam-se pelo nível de pressão em que os dispositivos operam. No caso da assistência ventricular, a bomba movimenta o sangue contra a resistência vascular sistêmica do paciente (de 92×10^6 à 130×10^6 Nsm⁻³) em assistência ao ventrículo esquerdo. O nível de resistência hidráulica aumenta quando outros dispositivos são adicionados entre a saída da bomba e o paciente, como é o caso de um procedimento típico de *bypass* cardiopulmonar. Desta forma, a diferença de pressão requerida para a operação da bomba será maior. Oxigenador, trocador de calor, filtro de linha e conectores são adicionados ao circuito para cumprir seu papel durante a operação, fazendo a resistência hidráulica global do circuito (dispositivos mais paciente) chegar a valores de quatro a seis vezes maiores que a resistência vascular sistêmica do paciente.

Por este motivo, bombas centrífugas devem ser usadas com critério em procedimentos de *bypass* cardiopulmonar devido às suas características de operação. O efeito de um aumento na resistência hidráulica na descarga se reflete na queda da vazão, como consequência da recirculação do fluido na bomba. Além disso, quando não está sendo acionada ou operando em baixa rotação, não oferece resistência ao fluxo retrógrado, o que é indesejável em um circuito de circulação extracorpórea, pela possibilidade da entrada de ar no fluxo de sangue que vai ao paciente com grande potencial de embolia gasosa (geralmente fatal). Para evitar estes riscos, dispositivos adicionais são introduzidos no circuito, tais como sensores de fluxo retrógrado e válvulas unidirecionais. Não são recomendados procedimentos de pinçamento parcial das linhas de sucção e descarga da bomba para controle de fluxo. A oclusão destas linhas favorece a criação de zonas de baixa pressão (no caso da oclusão da linha de sucção), o que provoca cavitação no sangue, como também aumenta as zonas de recirculação dentro da bomba (no caso da oclusão da linha de descarga), responsáveis por um maior risco de hemólise (rompimento das células vermelhas do sangue) e formação de trombos.

A falta de informação básica sobre os mecanismos responsáveis pela hemólise mecânica impede, na maioria dos casos, o uso adequado da bomba centrífuga. Existe atualmente no Brasil um número crescente de equipes de cirurgia cardíaca que empregam bombas centrífugas durante o procedimento de *bypass* cardiopulmonar. O argumento utilizado para justificar a substituição das "ultrapassadas" bombas de roletes pelas bombas centrífugas é que estas últimas são menos hemolíticas que as primeiras. Este argumento, no entanto, perde sua força quando as equipes presenciaram níveis de hemólise iguais ou maiores do que aqueles que consideravam normais durante a circulação extracorpórea (CEC) utilizando bombas de roletes.

Dentre os dispositivos centrífugos utilizados em CEC, a Bio-pump (*Medtronic*, Estados Unidos) tem uso mais difundido. O projeto original, da década de 70 (Kletschka *et al.*, 1975), é de um dispositivo de assistência ventricular que encontrou rapidamente aplicação em operações de *bypass* cardiopulmonar (Lynch *et al.*, 1978). Considerando o fato que, durante a década de 70 e grande parte da década de 80, o oxigenador de bolha era o dispositivo mais empregado em operações cardíacas (dispositivo que introduzia baixa resistência hidráulica), utilizar um dispositivo projetado para operar contra a resistência vascular periférica do paciente em um circuito de CEC não acarretava grandes problemas. No entanto, com a introdução do oxigenador de membrana, permitindo melhorar a eficiência da troca gasosa do circuito de CEC, e do uso mais difundido de filtros de linha arterial, tornando o procedimento mais seguro, aumentou-se a resistência hidráulica que a bomba deve superar para a movimentação do sangue no circuito.

A questão a ser tratada neste trabalho é como se comporta o escoamento no interior de uma bomba centrífuga sem pás (Fig. 1), disponível comercialmente, ao operar em condições semelhantes àquelas que ocorrem em um circuito de CEC, durante uma operação cardíaca com *bypass* cardiopulmonar, e como isto afeta o seu potencial de danos às células do sangue.

Este estudo foi conduzido seguindo duas abordagens distintas: a simulação numérica de um escoamento laminar passando por um canal formado por duas superfícies de revolução concêntricas e de geometria idêntica a um dos canais internos da bomba (canal formado pelos cones 1 e 2) e medidas experimentais do campo de velocidade estabelecido no interior deste dispositivo, utilizando um anemômetro laser Doppler (ALD) de última geração, capaz de medir duas componentes simultâneas de velocidade.

O procedimento numérico foi implementado com o objetivo de estudar as estruturas do escoamento que surgem quando um canal isolado da bomba é submetido a diferentes condições de vazão e de rotação. Além disso, foi possível a obtenção dos campos de velocidade e de pressão que forneceram

informações sobre possíveis regiões de recirculação, grandes gradientes de velocidade, distribuição da pressão ao longo do canal e de grande potencial hemolítico, e também sobre como estas regiões foram afetadas ao se variar a vazão através do canal ou a sua velocidade de rotação.

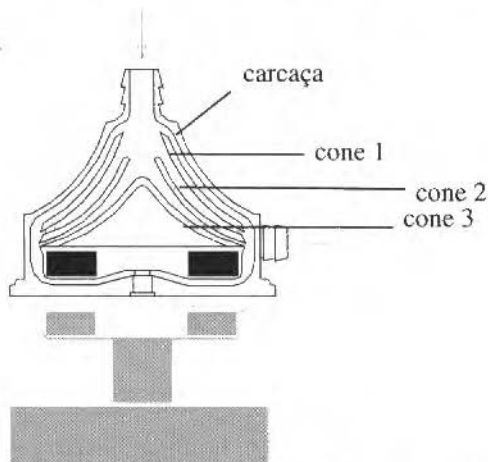


Fig. 1 Desenho esquemático da bomba centrífuga sem pás. O rotor da bomba e o eixo do motor estão acoplados magneticamente.

O objetivo das medidas experimentais do campo de velocidade foi obter as características gerais do escoamento, destacando a interação entre os canais internos da bomba. As medidas de velocidade foram realizadas seguindo um protocolo experimental que foi capaz de superar os principais obstáculos associados ao acesso óptico às regiões de interesse e à similaridade entre as condições de testes e as fisiológicas. Realizaram-se as medidas onde se esperava encontrar condições críticas do escoamento, ou seja, regiões com grandes acelerações, pontos de estagnação e regiões de recirculação. A questão da hemólise foi abordada de uma maneira alternativa, onde as grandezas turbulentas obtidas diretamente das medidas experimentais de velocidade puderam ser relacionadas a um maior ou menor potencial de danos às células vermelhas do sangue.

Hemólise Mecânica em Escoamento Laminar e Turbulento

O modelo de solicitação e destruição das células vermelhas em um escoamento cisalhante, ilustrado na Fig. 2 (Pinotti, 1996), supõe que a atuação das forças viscosas sobre a membrana celular é o fator responsável pela hemólise mecânica.

Baseado neste modelo, é possível estimar o potencial hemolítico de um determinado escoamento utilizando a tensão de cisalhamento e o tempo de exposição. Um estudo realizado por Wurzinger *et al.* (1986) revelou que as tensões de cisalhamento e o tempo de exposição podem ser relacionados à porcentagem de liberação de hemoglobina pela seguinte fórmula empírica, Eq. 1:

$$\% \text{Hb} = 3,62 \cdot 10^{-5} \cdot t^{0,79} \cdot \tau^{2,4} \quad (1)$$

onde t é o tempo de exposição [s] e τ é a tensão de cisalhamento [N m^{-2}].



Fig. 2 Simulação gráfica da deformação e fragmentação de uma célula vermelha em um escoamento cisalhante (Pinotti, 1996). Os quadros representam diferentes fases da solicitação da membrana até o seu rompimento. O quadro 1 mostra uma célula vermelha em seu estado não solicitado. Os quadros 2 e 3 mostram a ação do campo de tensão de cisalhamento. O quadro 4 mostra a célula danificada por causa da solicitação excessiva de sua membrana.

A grande contribuição de Wurzinger foi a obtenção de dados experimentais em situações de tensão de cisalhamento uniforme, com tempo de exposição compatível com valores encontrados em órgãos artificiais (ordem de grandeza de milissegundos), tais como válvulas e bombas cardíacas. A Figura 3 (Pinotti, 1996) mostra a representação tridimensional de como se comporta, segundo a Eq.1, a porcentagem de liberação de hemoglobina em função da tensão de cisalhamento e do tempo de exposição.

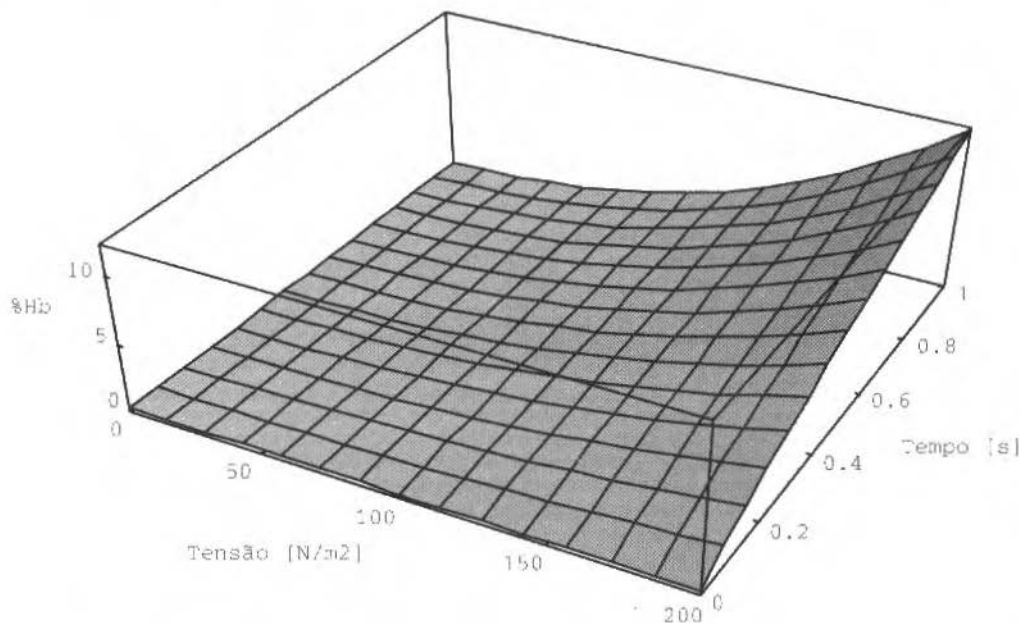


Fig. 3 Gráfico tridimensional que ilustra a influência do tempo de exposição e da tensão de cisalhamento sobre a porcentagem de hemoglobina liberada, gerado a partir da fórmula empírica de Wurzinger.

A aplicação deste modelo para escoamento laminar é imediata, uma vez que as tensões de cisalhamento são proporcionais ao gradiente de velocidade. No caso de um escoamento turbulento, outros fatores influenciam a solicitação das células vermelhas. Além de o escoamento turbulento estar associado a grandes velocidades, induzindo maiores gradientes de velocidade em regiões próximas às paredes, é caracterizado pela presença de estruturas tridimensionais chamadas turbilhões. Estes turbilhões possuem tamanhos variados, da ordem de grandeza da espessura da região turbulenta a alguns centésimos de milímetro (microescalas de Kolmogorov). A energia é introduzida no escoamento através dos grandes turbilhões e dissipada, a nível microscópico, pelos pequenos turbilhões. O processo pelo qual a energia é transferida da escala macroscópica à microscópica é conhecida como Cascata de Energia. A idéia básica deste conceito é que os turbilhões maiores transferem continuamente sua energia a turbilhões menores através de interação inercial. À medida que o tamanho dos turbilhões diminui, os efeitos viscosos tornam-se cada vez mais importantes até a completa dissipação desta energia no escoamento. Quando os menores turbilhões, no fim da Cascata de Energia, forem do tamanho do eritrócito, sua energia será dissipada na membrana celular. Esta dissipação causará rompimento da membrana com a conseqüente liberação da hemoglobina. Por outro lado, se a dimensão destes turbilhões forem maiores do que o eritrócito, a célula será transportada pelo turbilhão e sua membrana será solicitada somente pela tensão de cisalhamento gerada pelo gradiente de velocidade ao longo de sua trajetória.

Kramer (1970) foi o primeiro a reconhecer que a caracterização do trauma às células vermelhas devido ao regime turbulento depende da dimensão dos turbilhões presentes no escoamento.

É importante lembrar que as tensões de Reynolds são termos convectivos e o nome "tensão de cisalhamento de Reynolds" está associado ao seu efeito sobre os perfis da velocidade média e não sobre as forças locais (White, 1991), o que faz com que a tensão de cisalhamento de Reynolds não tenha nenhuma relação aparente com a taxa de hemólise. Além disso, as tensões de Reynolds possuem relação direta com as escalas macroscópicas do escoamento em contraste com a atuação das forças viscosas, que se dá a nível microscópico. Apesar de as medidas de velocidade, no nível da escala onde ocorre a dissipação viscosa, potencialmente perigosa para as hemácias, exigir uma resolução espacial além da capacidade da instrumentação disponível hoje em dia, procedimentos para obtenção das tensões de Reynolds vêm sendo descritos na literatura nas últimas décadas para anemômetro de fio quente, anemômetro laser Doppler e ultra-som Doppler pulsado.

A dimensão dos menores turbilhões (L_s) que ocorrem em um escoamento turbulento pode ser relacionada às dimensões macroscópicas do escoamento turbulento pela seguinte expressão (Panton, 1984):

$$L_s = \left(\frac{v^3 L_e}{u_0^3} \right)^{0,25} \quad (2)$$

onde v é a viscosidade cinemática [$m^2 s$], L_e é a dimensão característica dos grandes turbilhões [m] que possuem a mesma ordem de grandeza das dimensões características do sistema e u_0 é a velocidade RMS (valor médio quadrático) característica do escoamento local [$m s^{-1}$].

Não se sabe, ainda, quais são exatamente as grandezas turbulentas que possuem relação direta com a hemólise, porém a Eq.2 fornece uma ligação entre a dissipação viscosa dos turbilhões de menor dimensão que atuam a nível celular e as grandezas turbulentas mensuráveis a nível macroscópico. Portanto, quando L_s , conhecida também como escala de Kolmogorov, for da mesma ordem de grandeza de uma hemácia, o escoamento tem grande potencial hemolítico pois a energia turbulenta estará sendo dissipada a nível celular.

Resultados

Simulação Numérica

O potencial hemolítico (ou potencial de hemólise) de um escoamento laminar pode ser definido como o aumento percentual da hemoglobina livre que seria gerada em um escoamento de sangue com 100 % das hemácias intactas. Desta forma, uma determinada região do canal com, por exemplo, 1 % de potencial hemolítico significa que 1 % da hemoglobina presente nas hemácias que estão passando através desta região está sendo liberada no escoamento devido à hemólise mecânica. A porcentagem de hemoglobina liberada pode ser prevista utilizando a fórmula empírica de Wurzingler *et al.* (1986) em função da tensão de cisalhamento e do tempo de exposição locais, como mostra a Eq.1. As variáveis primitivas do escoamento (u , v , w e P), assim como as tensões normais e de cisalhamento foram obtidas a partir de um programa FORTRAN que utilizou o método dos volumes finitos (não foi empregado nenhum modelo de turbulência) para resolver as equações completas de Navier-Stokes (Pinotti, 1996).

Adotou-se o modelo de solitação uniaxial para a determinação da tensão de cisalhamento que atua sobre as hemácias (Pinotti e Rosa, 1995). Dally e Riley (1978) ensinam que a tensão de cisalhamento máxima (τ_{max}) que atua em um volume infinitesimal é a resultante da ação de 3 tensões normais, σ_{11} , σ_{22} e σ_{33} , e de 6 tensões de cisalhamento, σ_{12} , σ_{13} , σ_{21} , σ_{23} , σ_{31} , σ_{32} , que atuam nas faces deste volume, e pode ser determinada a partir das tensões principais.

$$\tau_{max} = \frac{1}{2} (\sigma_{max} - \sigma_{min}) \quad (3)$$

onde σ_{max} e σ_{min} [$N m^{-2}$] são o maior e o menor valor das tensões principais obtidas da Eq.4 (Dally e Riley, 1978), a seguir.

$$\sigma_n^3 - I_1 \sigma_n^2 + I_2 \sigma_n - I_3 = 0 \quad (4)$$

A Figura 5 mostra a evolução de %Hb na região adjacente a uma cone 2 da *Biopump*, ao longo do canal, para três situações de interesse. Nota-se que a velocidade de rotação atuou de maneira decisiva sobre a %Hb. Comparando-se os casos que possuem a mesma vazão (8 l/min) mas diferentes velocidades de rotação, 1200 e 1800 RPM (rotações por minuto), observou-se que o nível de %Hb na saída do canal para 1800 RPM foi cerca de duas vezes e meia maior do que aquele para 1200 RPM. Por outro lado, mantendo-se a rotação constante e aumentando-se a vazão (11 l/min), observou-se um pequeno aumento, de aproximadamente 5 pontos percentuais, no nível de %Hb, em comparação com aquela observada quando variou-se a rotação.

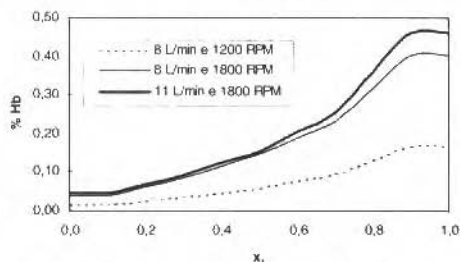
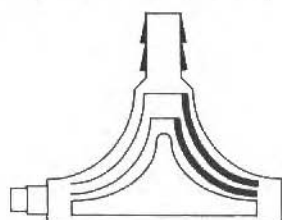


Fig. 5 Potencial hemolítico na face superior do cone 2 em função da coordenada x_1 para os três casos descritos. A %Hb é fortemente influenciada pela velocidade de rotação do canal. A posição $x_1 = 0$ representa a entrada e $x_1 = 1$ representa a saída do canal destacado na figura à esquerda.

A Figura 6 mostra os perfis de velocidade na direção x_1 (ao longo do canal) em três posições distintas: entrada do cone $x_1 = 0$; posição intermediária $x_1 = 0,4$ e saída do canal $x_1 = 1$. A direção do eixo x_2 é perpendicular às paredes do canal. Desta forma, $x_2 = 0$ e $x_2 = 1$ representam as superfícies rotativas do cone 2 e do cone 1, respectivamente.

Observa-se que para a condição de operação de 8 l/min e 1800 RPM ocorre escoamento retrógrado na saída do canal, o qual é evidenciado pelo perfil da velocidade na direção x_1 naquela posição. O efeito deste escoamento retrógrado sobre o potencial hemolítico do escoamento pode ser observado na Fig. 7. Nota-se que existem dois picos na curva de potencial hemolítico e que coincidem com a região de cisalhamento provocada pelo escoamento retrógrado. Nesta região, o tempo de exposição e a tensão de cisalhamento crescem simultaneamente gerando, desta forma, os picos do potencial hemolítico (ver Eq.1) da Fig. 7.

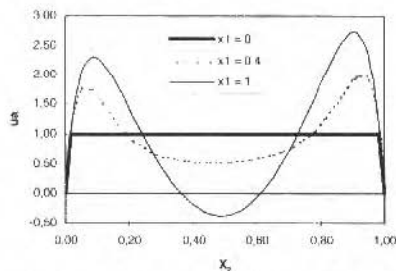
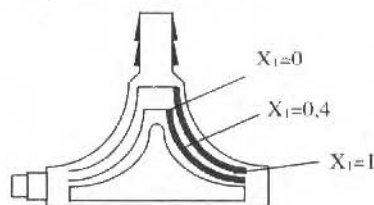


Fig. 6 Evolução dos perfis da velocidade adimensional ao longo da direção x_1 (ua) para a condição de operação de 8 l/min e 1800 RPM. Note que ocorre fluxo retrógrado na saída do canal ($x_1 = 1$).

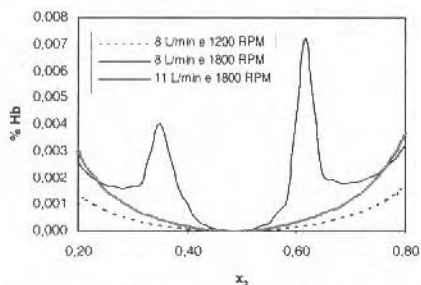
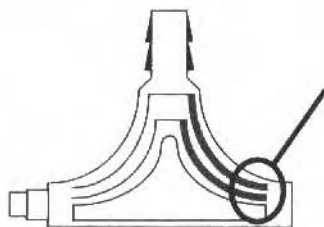


Fig. 7 Potencial hemolítico na saída do canal formado pelos cones 2 e 3. Nota-se os picos de hemólise na região central do canal devido ao escoamento retrógrado.

onde I_1 , I_2 e I_3 são as tensões invariantes, definidas nas Eqs. 5 a 7.

$$I_1 = \sigma_{22} + \sigma_{11} + \sigma_{33} \quad (5)$$

$$I_2 = \sigma_{22}\sigma_{11} + \sigma_{11}\sigma_{33} + \sigma_{33}\sigma_{22} - \sigma_{13}^2 - \sigma_{32}^2 - \sigma_{21}^2 \quad (6)$$

$$I_3 = \sigma_{22}\sigma_{11}\sigma_{33} - \sigma_{11}\sigma_{32}^2 - \sigma_{33}\sigma_{21}^2 - \sigma_{22}\sigma_{13}^2 + 2\sigma_{13}\sigma_{32}\sigma_{21} \quad (7)$$

O tempo de exposição, utilizado na equação de Wurzinger, foi obtido para cada ponto nodal, utilizando o conceito do tempo de trânsito de uma partícula no volume de controle (V.C.) que envolvia o ponto de interesse, definido na Eq.8, a seguir:

$$t_{ij} = \frac{h_{ij} \Delta x_{ij}}{ABS(\bar{u}_{ij})} \quad (8)$$

onde o subscrito ij representa a grandeza tomada no ponto na linha i e na coluna j da malha computacional, t_{ij} é o tempo de trânsito de uma partícula pelo V.C. [s], o produto $h_{ij} \Delta x_{ij}$ é a distância percorrida pela partícula ao longo da direção x_1 [m] e u_{ij} é a velocidade média da partícula que passa através do V.C. [$m s^{-1}$]. ABS () significa que foi tomado o valor absoluto da grandeza que estava dentro dos parênteses.

Para cada caso simulado numericamente, utilizou-se diretamente os valores dos campos de tensões normais e de cisalhamento e do campo de velocidades armazenados na memória para gerar o campo do potencial de hemólise. Isto destaca mais uma vantagem da formulação do fluxo de tensão empregada no programa computacional (Pinotti, 1996): todas as tensões, obtidas ao longo do processo iterativo, já estavam convenientemente armazenadas para serem utilizadas no pós-processamento.

A Figura 4 mostra uma malha 5×9 , sendo 5 pontos nodais ao longo de x_2 e 9 pontos ao longo de x_1 , obtida a partir da subrotina geradora da malha (Pinotti, 1996).

Como a espessura do canal diminui de forma significativa ao longo de x_1 , foi necessário desenhá-lo com escala diferente de 1:1 para facilitar a visualização das linhas coordenadas na saída. Este é o motivo pelo qual, apesar de a malha gerada ser ortogonal, suas linhas não se interceptam a 90 graus em sua representação na Fig. 4. Nos casos simulados e apresentados neste trabalho, a malha empregada foi de 61×11 .

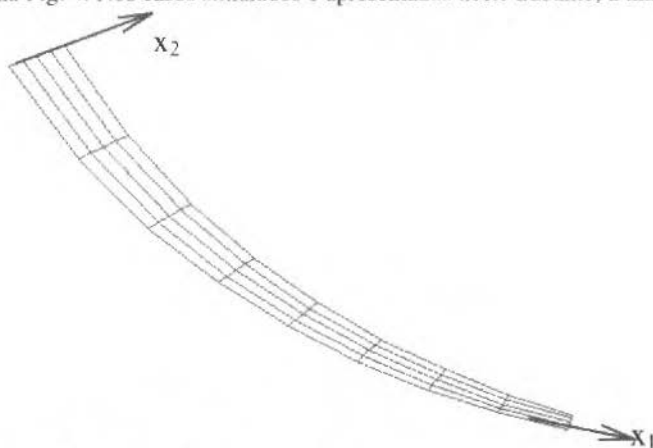


Fig. 4 Malha computacional de 5×9 pontos nodais. O espaçamento entre os pontos nodais é menor ao longo da direção x_2 (normal à superfície do canal) para tornar a malha mais sensível aos gradientes de velocidade presentes no escoamento nesta direção.

Medidas Experimentais

Foram obtidos os perfis de velocidade média e RMS em diferentes planos no interior da bomba utilizando um anemômetro laser Doppler (Pinotti e Paone, 1996). A configuração disponível para as medidas (especificações na Tab.1) consistia em um laser de íons de Argônio configurado de forma a medir duas componentes de velocidade simultaneamente. A fonte de laser (*Innova 70 Coherent*, potência nominal de 4 W) produzia um feixe de laser com três comprimentos de onda típicos (verde, azul e violeta), sendo que o verde ($\lambda = 514,5$ nm) e o azul ($\lambda = 488$ nm) eram separados por filtros ópticos e utilizados no sistema de medida. Os feixes monocromáticos eram divididos em pares e um feixe de cada par passava por uma célula de Bragg para o deslocamento na frequência de 40 MHz (*Transmitter 60-40, DANTEC*). Uma vez preparados para a medição, os feixes eram conduzidos até a sonda por um cabo de fibra-óptica multimodo. A sonda foi instalada em um sistema mecânico de posicionamento, controlado parcialmente por computador. Movimentos ao longo dos eixos X e Y eram realizados por motores de passo, controlados por computador, com resolução de 0,01 mm e os deslocamentos da sonda ao longo do eixo Z eram realizados manualmente por sistema de parafuso cremalheira de precisão, com passos de 0,05 mm. A Figura 8 mostra, esquematicamente, a configuração utilizada nas medidas: (a) Laser de Íons de Argônio; (b) divisor de feixe; (c) célula de Bragg; (d) fotomultiplicador; (e) Cabo de fibra-óptica multimodo; (f) lente de focalização; (g) lente de recepção. As lentes de focalização e recepção eram montadas em uma sonda e os feixes emitidos e a luz refletida pelas partículas viajavam até o fotomultiplicador por um cabo de fibra ótica, que, na configuração empregada, possuía cerca de 20 metros. Este tipo de configuração é chamada de *backscattering*.

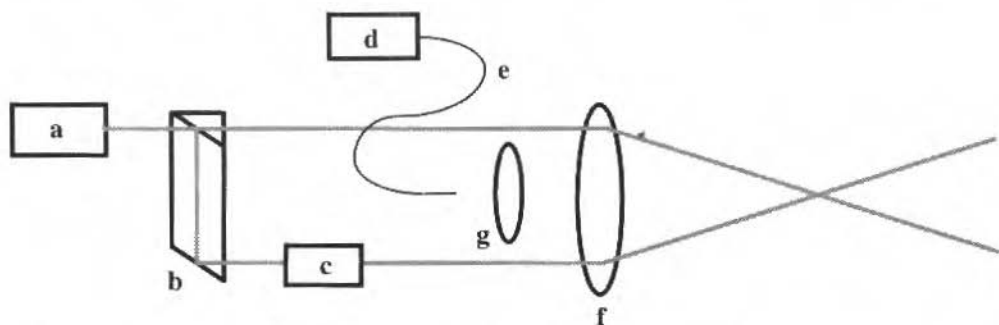


Fig. 8 Configuração utilizada nas medidas. A lente mais externa (f) focalizava os feixes no local da medida e direcionava a luz dispersa pelas partículas para a lente mais interna (g) que, por sua vez, focalizava o feixe de retorno na entrada da fibra óptica (e), que transmitia as informações ao fotomultiplicador (d).

A Tabela 1 mostra os parâmetros ópticos do ALD, configurado para operar em *backscattering*.

Tabela 1 Parâmetros ópticos dos feixes utilizados no anemômetro laser Doppler. Estes parâmetros são referentes ao uso de uma lente convergente com distância focal de 160 mm.

	Verde (514,5 nm)	Azul (488 nm)
Ângulo de separação φ [°]	13,5	13,5
Distância entre franjas* [μm]	2,189	2,076
C [$\text{m s}^{-1} \text{MHz}^{-1}$]	2,189	2,076
Diâmetro do volume de medida no ar [mm]	0,078	0,074
Comprimento do volume de medida no ar [mm]	0,658	0,626

* Esta configuração proporcionava a formação de 35 franjas no volume de medida.

Detalhes das medidas com o ALD e do protocolo experimental podem ser encontrados em trabalhos anteriores (Pinotti, 1996; Pinotti e Paone, 1996).

Utilizando os campos de velocidade média e RMS obtidos experimentalmente, foi possível, empregando a Eq.2, gerar os perfis das escalas de Kolmogorov em algumas regiões de interesse no interior da bomba. Estes perfis são mostrados nas Figs. 9 a 10 para diferentes condições de operação. É importante notar que o eixo das ordenadas, que representa os valores de L_s , inicia-se em 10 μm , que é a dimensão aproximada de uma hemácia. Desta forma, quanto mais o perfil de L_s se aproximar da origem

do eixo ordenado, maior será o potencial de danos às células vermelhas do sangue devido à ação dos microturbilhões.

A Figura 9 mostra as escalas de Kolmogorov, L_s , nas proximidades da superfície de ataque do cone 2, para três condições de operação:

- Condição de controle: 2,5 l/min; 293 mmHg; 2850 RPM; $(925 \pm 6) \times 10^6 \text{ N.s.m}^{-5}$;
- Condição com resistência hidráulica alterada: 2,1 l/min; 305 mmHg; 2850 RPM; $(1150 \pm 11) \times 10^6 \text{ N.s.m}^{-5}$;
- Condição com resistência hidráulica e rotação alteradas: 3,4 l/min; 473 mmHg; 4000 RPM; $(1098 \pm 10) \times 10^6 \text{ N.s.m}^{-5}$.

É importante notar que a principal diferença entre as condições 1 e 2 é o aumento de 25% da resistência hidráulica do circuito. Já em relação às condições 1 e 3, além das diferenças de resistência hidráulica existe a diferença entre as rotações da bomba. Desta forma, foi possível avaliar a influência do aumento da resistência hidráulica de forma isolada e, também, de forma acoplada com o aumento da rotação da bomba sobre o tamanho dos menores turbilhões.

Observa-se na Fig. 9 que aumentando-se a resistência hidráulica do circuito, o perfil de L_s sofre uma pequena variação. Por outro lado, aumentando-se simultaneamente a rotação da bomba e a resistência hidráulica do circuito observa-se uma sensível variação do perfil de L_s , mostrando que, para estas condições o tamanho dos menores turbilhões diminui.

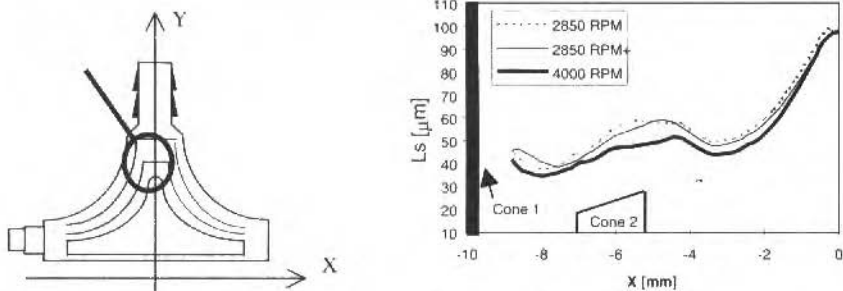


Fig. 9 Dimensão dos menores turbilhões presentes nas proximidades da borda de ataque do cone 2. Os maiores potenciais hemolíticos localizam-se na região de sucção do canal formado pelos cones 1 e 2 ($x = -8 \text{ mm}$) e a montante da entrada do canal formado pelos cones 2 e 3 ($x = -3 \text{ mm}$).

A Figura 10 mostra a dimensão dos menores turbilhões presentes no escoamento através do canal externo e naquele formado pelos cones 1 e 2, na posição mostrada na figura. Da mesma forma que a figura anterior, foram obtidos os perfis de L_s para três condições distintas:

- Condição de controle: 2,3 l/min; 266 mmHg; 2400 RPM; $913 \times 10^6 \text{ N.s.m}^{-5}$;
- Condição 1: 2,1 l/min; 311 mmHg; 2400 RPM; $1169 \times 10^6 \text{ N.s.m}^{-5}$;
- Condição 2: 3,4 l/min; 504 mmHg; 4200 RPM; $1170 \times 10^6 \text{ N.s.m}^{-5}$;

Observa-se que os menores valores das escalas de Kolmogorov ocorrem em regiões distantes das superfícies rotativas. Isto acontece porque a condição de não-deslizamento presente nas superfícies dos cones aumentam a taxa de dissipação da energia dos turbilhões e, desta forma, impõe limites para a cascata da energia do escoamento turbulento. Portanto, nas proximidades das paredes a cascata de energia é abreviada fazendo com que a dimensão dos menores turbilhões seja maior que aquela observada em regiões distantes das paredes. Já nas regiões distantes das paredes, a única força adversa à propagação da cascata da energia é a dissipação viscosa. Por este motivo, no seio do escoamento a dimensão dos menores turbilhões será menor do que aquela observada nas proximidades das paredes.

Observa-se, também, na Fig. 10 que, para ambos os canais da figura, mantendo-se a resistência hidráulica inalterada e aumentando-se a rotação da bomba, a dimensão dos menores turbilhões (L_s) diminui. Portanto, quanto maior a rotação da bomba aumenta-se o potencial de danos às células do sangue.

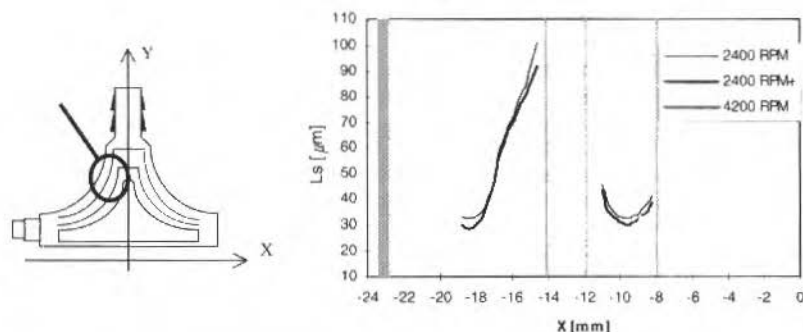


Fig. 10 Dimensão dos menores turbilhões presentes no canal. O menor valor para a escala de Kolmogorov ocorreu no interior do canal formado pelo cone 1 e a carcaça.

Comentários Sobre a Previsão da Hemólise e Sua Implicação na Operação de uma Bomba de CEC.

É importante destacar que a tensão de cisalhamento viscosa é a causa do rompimento da membrana da hemácia tanto em escoamento laminar como turbulento, podendo ser aplicada a equação empírica de Wurzinger para prever a taxa de liberação de hemoglobina. No entanto, para o escoamento em regime turbulento, existem fatores adicionais que contribuem para o aumento da taxa de hemólise. A mais importante está relacionada às dimensões dos menores turbilhões, ao final da Cascata de Energia, que dissipam a energia produzida pelos grandes turbilhões. Quando a dimensão destes turbilhões é da mesma ordem de grandeza das hemácias, a interação destas estruturas com a parede celular faz com que ocorra destruição da membrana e cause a liberação de hemoglobina. Este fenômeno, quando ocorre, faz com que a taxa de hemólise cresça em relação àquela prevista somente considerando a tensão de cisalhamento viscosa.

A correlação entre dimensão dos menores turbilhões (escala de Kolmogorov) e hemólise pode ser checada se forem analisados os valores de L_s publicados na literatura sobre o estudo das propriedades da membrana das hemácias e sobre as tensões turbulentas obtidas no interior de órgãos artificiais (Pinotti, 1997).

As duas abordagens empregadas neste trabalho para a previsão do potencial hemolítico em uma bomba de CEC destacaram os mecanismos pelos quais as células vermelhas do sangue são danificadas pela ação do escoamento. A simulação numérica e as medidas de turbulência não foram realizadas com a intenção de comparação entre os dados numéricos e experimentais. No entanto, estas abordagens são úteis para a análise do potencial hemolítico em função da mudança das condições de operação da bomba. Portanto, os resultados das simulações e dos experimentos apresentados neste trabalho servem para descrever, de maneira genérica, a influência das condições de operação da bomba sobre os mecanismos básicos de hemólise.

O primeiro mecanismo, associado às forças viscosas, é caracterizado pela ação de um gradiente de velocidade ao longo da extensão da hemácia. Desta forma, este mecanismo de destruição das células vermelhas do sangue estará presente em regiões de intenso gradiente de velocidade que se manifestam próximo às superfícies sólidas e em regiões com grande aceleração. No canal estudado numericamente, as regiões críticas, apontadas pelo modelo de Wurzinger *et al.* (1986), localizavam-se nas adjacências dos cones rotativos e, sob influência do fluxo retrógrado, ao longo da seção transversal na saída do canal.

O segundo mecanismo, ligado à estrutura do escoamento turbulento, é caracterizado pela ação dos pequenos turbilhões sobre a membrana celular. Esta interação, onde a energia produzida à escala macroscópica é dissipada a nível celular, ocorre da seguinte forma: turbilhões da ordem de grandeza da hemácia são letais, do contrário irão promover o transporte das células de um lugar para outro no escoamento. De acordo com este critério, as regiões nas proximidades das paredes são inócuas, pois a presença de superfícies sólidas aumenta a taxa de dissipação da energia turbulenta e faz com que a Cascata de Energia seja abreviada. Por outro lado, em regiões afastadas das paredes, onde a única

limitação para o tamanho dos turbilhões é a dissipação viscosa, um maior nível de energia cinética turbulenta produz uma maior chance de hemólise.

Os resultados apresentados neste capítulo tornam evidentes algumas características do escoamento que têm aplicação prática na operação de uma bomba centrífuga sem pás em um circuito de CEC. O potencial hemolítico da bomba é maior quando aumenta-se a velocidade de rotação dos cones (crescimento dos níveis de tensão de cisalhamento viscosa) e/ou quando a resistência hidráulica do circuito cresce (diminuição do tamanho dos turbilhões). A Tabela 2 apresenta, de forma sucinta, as relações de causa e efeito que propiciam condições para a hemólise mecânica. Por simplicidade, o mecanismo hemolítico associado às forças viscosas foi chamado de "hemólise tipo Wurzinger" e aquele associado à interação entre os menores turbilhões e as hemácias foi chamado de "hemólise tipo Kramer".

Tabela 2 Relações de causa e efeito associadas aos mecanismos de hemólise que ocorrem na Bio-pump utilizada em CEC.

Causa	Efeito	Mecanismo de hemólise
Aumento da velocidade de rotação da bomba	Aumento da tensão de cisalhamento nas paredes dos cones	Hemólise tipo Wurzinger
	Aumento do tempo de exposição devido ao possível refluxo na saída do canal	Hemólise tipo Wurzinger
Aumento da resistência hidráulica do circuito	Aumento da energia cinética turbulenta	Hemólise tipo Kramer
	Aumento da energia cinética turbulenta	Hemólise tipo Kramer
	Aumento do tempo de exposição devido ao possível refluxo na saída do canal	Hemólise tipo Wurzinger

Agradecimentos

Os autores gostariam de agradecer aos Professores Enrico Primo Tomasini e Nicola Paone da Università di Ancona, Itália, pelo apoio e encorajamento durante as medidas com o anemômetro laser Doppler e ao Prof. Eugênio S. Rosa do Departamento de Energia da UNICAMP. Este trabalho foi financiado pelo CNPq (Proc. n. 201586/92-4 SWE).

Referências

- Dally J. M. e Riley W. F., 1978, "Experimental stress analysis", New York, McGraw Hill.
- Kletschka, H.D., Rafferty, E.H., Olsen, D.A., Clausen, E.W., Hubbard, L.C., Robinson, A.R., e Larson, W.H., 1975, "Artificial heart III. Development of efficient atraumatic blood pump. A review of the literature concerning in vitro testing of blood pumps for hemolysis", Minnesota Medicine (October), pp.757-781.
- Kramer, C., 1970, "Studies on Flow Induced Mechanical Haemolysis". Advisory Group for Aerospace Research and Development Conference Proceedings on Fluid Dynamics of Blood Circulation and Respiratory Flow - North Atlantic Treaty Organisation, Vol.65, Naples.
- Lynch, M.F., Peterson e D., Baker, V., 1978, "Centrifugal blood pumping for open heart surgery", Minn. Medicine, (september), pp.536-537.
- Panton, R.L., 1984, "Incompressible Flow", New York, John Wiley and Sons.
- Pinotti, M., 1996, "Escoamento no Interior de um Dispositivo Centrífugo Utilizado em Circulação Extracorpórea", Tese de Doutorado, Universidade Estadual de Campinas, Campinas-SP.
- Pinotti, M., 1997, "Turbulent microscale: The key parameter to evaluate mechanical blood trauma in tiny rotary blood pumps". Revista Brasileira de Engenharia - Caderno de Engenharia Biomédica, Vol.13, n.2, pp.7-17.
- Pinotti M. e Paone, N., 1996, "Estimating mechanical blood trauma in centrifugal blood pump: LDA measurements of the mean velocity field". Artif. Organs, Vol.20, n.6, pp.546-552.
- Pinotti M. e Rosa E. S., 1995, "Computational prediction of hemolysis in a centrifugal ventricular assist device", Artificial Organs, Vol.19, n.3, pp.267-273.
- White, F.M., 1991, "Viscous fluid flow", New York: McGraw-Hill.
- Wurzinger, L.J., Optiz, R. e Eckstein, H., 1986, "Mechanical blood trauma: An overview", Angiologie, Vol.38, n.3, pp.81-97.

An Absorption Algorithm and Its Implementation for Irregular Ocean Waves in a Test Tank

Ben T. Nohara

Mitsubishi Heavy Industries
Technical Headquarters
9-1 Iwatsuka Nakamura Japan
drben@utd.nmw.mhi.jp

Abstract

This paper describes a newly developed absorbing algorithm and its implementation for irregular ocean waves in a test tank. In a tank test, while using a wave maker for determining ocean wave tolerance of floating body structures, as well as ships, there is a problem: reflective waves from the test body or a tank termination disturb the target waves. These reflective waves make test performance undependable, because the test body is exposed to reflective waves along with target waves. An accurate test must keep the test body out of reflective waves. Past studies have made the conditions for complete absorption of regular waves clear. However the conditions for absorption of irregular waves is only partially obtained using hydrodynamic force acting on a wave board. The authors propose a complete absorption algorithm, which utilizes sensing of water surface elevation instead of hydrodynamic force, and its implementation for irregular waves. The authors have obtained good experimental results from this algorithm. Also in this paper, the authors introduce time-frequency analysis, using a short-time Fourier transform technique, for visualizing the state of absorption.

Keywords: Wave Maker, Absorption, Irregular Wave, Short-Time Fourier Transform

Introduction and Motivation

The close relationship between human kind and ocean has continued since the Age of Great Voyages. However we still lack complete knowledge of the whole ocean. Nevertheless the development of the off shore has progressed. For example, Japan has plans for the construction of the *mega-float* (Official Gazette, 1995), which means a large off shore floating structure, for multipurpose use. From the view point of protection of the earth's environment, ocean development is a significant problem.

The motivation of this research is based on improvement of ocean space management. An offshore floating structure must have sufficient tolerance for ocean waves. Scale model testing in a test basin is usually performed to verify wave tolerance. This paper describes a newly developed absorbing algorithm and its implementation for irregular ocean waves in a test tank.

In a tank test, while using a wave maker for determining ocean wave tolerance of floating body structures, as well as ships, there is a problem: reflective waves from the test body or a tank termination disturb the target waves. Reflective waves make test performance undependable, because the test body is exposed to reflective waves along with target waves. An accurate test must keep the test body out of reflective waves.

Nomenclature

a = Amplitude of the water surface elevation	C = Coefficient calculated by Eq.(8)	j = denotes the number defined by Eq.(9)
a = Amplitude of the motion of a wave board	H = Wave height	D = denotes the symbol of the surface elevation of the target waves in front of a wave board
f = Signal	K = Wave number	I = denotes the target waves
g = Acceleration due to gravity	L^2 = Square-integrable function space	R = denotes reflective waves or real number space
h = Uniform water depth in the test tank	T = Wave period	0 = denotes the water surface elevation in front of a wave board
n = the number of frequency component waves of the irregular wave	X = Displacement of a wave board	\wedge = denotes spectrum
t = Time	ϵ = the random phase lag	\cdot = denotes the conjugate
(x, z) = Coordinate system in the test tank	ϕ = Velocity potential	
A = Coefficient calculated by Eq.(7)	η = Water surface elevation	
	ω = Angular frequency	
	\hat{u} = Short-time Fourier transform or Gabor transform	
	Suffix	
	i = denotes i -th frequency	

Past studies have made the conditions for complete absorption of regular waves clear (Salter, 1981; Kawaguchi, 1986). However the conditions for absorption of irregular waves are only partially obtained using hydrodynamic force acting on a wave board (Naito, Huang and Nakamura, 1987).

The authors propose a complete absorption algorithm, which utilizes sensing of water surface elevation instead of hydrodynamic force, and its implementation for irregular waves. Also in this paper, the authors introduce time-frequency analysis, using a short-time Fourier transform technique, for visualizing the state of absorption.

The following section explains the general details of the work of a wave maker in a test tank. The third section presents the control law for absorption and generation of irregular waves. The fourth section deals with control installations of the developed algorithm. The fifth section is concerned with the experiments in the test tank and presents time-frequency analysis of experimental data using a short-time Fourier transform technique. The final section contains the concluding remarks.

Wave Maker

A modernized wave maker has some segmented wave boards and can generate the multi-directional irregular waves, so called short crested waves in the real ocean, by controlling each wave board independently (Nohara, Yamamoto and Matsuura, 1995).

A wave maker with a wave board installed in a scale-modeled test tank is dealt with here, as shown in Photograph 1. Figure 1 shows the coordinate system and tank installations of a test tank. A brushless AC servo motor is used for driving the system. The AC servo motor rotates a ball screw connected with a linear guide to a rod and then to a wave board, mechanically. The mechanism of a linear guide and a linear way converts the rotational motion of a ball screw into the straight-line motion of a wave board. (This is the so called piston type.) Thus the motion of a wave board generates the waves. The method of generating wave characteristics, for example, wave height, wave period and wave spectrum, etc., is based on the operation of the wave board. Therefore the state-of-the-art wave maker requires a high performance computer system (Nohara, Yamamoto and Matsuura, 1996). The electronic servo driving system has been used recently due to some advantages such as higher dynamic performance, no leakage of oil to the basin, and maintenance free motor system, etc., compared with the hydraulic systems.

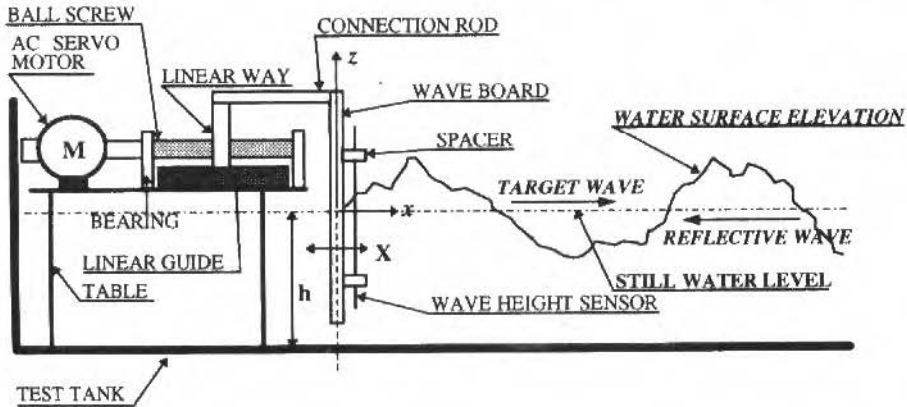


Fig. 1 Coordinate system and tank installations of a test tank

Control Law for the Absorption and Generation of Irregular Waves

Let the surface elevation of the target wave and the reflective wave be η^t and η^r respectively. Then η^t and η^r are described by the following equations.

$$\eta^t = \sum_{i=1}^n a_i^t \cos(\omega_i t - K_i x + \varepsilon_i^t) \quad (1)$$

$$\eta^R = \sum_{i=1}^n a_i^R \cos(\omega_i t + K_i x + \varepsilon_i^R) \quad (2)$$

Here a , t , x , K , ε , ω indicate the amplitude of the wave, time, the coordinate of the position of the target wave or the reflective wave, the wave number, random phase lag and angular frequency, respectively. Moreover suffix i denotes the frequency component of the irregular waves, which are considered as the superposition of n different frequency component waves, and the suffix I and R denote the target wave and the reflective wave, respectively. K_i is obtained from the dispersion relation:

$$\omega_i^2 = gK_i \tanh K_i h \quad (3)$$

where g and h indicate the acceleration due to gravity and the water bed, respectively.

The following equation is obtained by decomposing the displacement X of a wave board to the one X^I for generation of the target wave η^I and the one X^R for absorption of the reflective wave η^R .

$$\begin{aligned} X &= X^I + X^R \\ &= \sum_{i=1}^n \{ e_i^I \sin(\omega_i t + \varepsilon_i^I) - e_i^R \sin(\omega_i t + \varepsilon_i^R) \} \\ &= \sum_{i=1}^n X_i \end{aligned} \quad (4)$$

Here e denotes the amplitude of the motion of a wave board. The velocity \dot{X} of a wave board is obtained by the derivative of Eq.(4) with respect to t as follows:

$$\begin{aligned} \dot{X} &= \sum_{i=1}^n \{ e_i^I \omega_i \cos(\omega_i t + \varepsilon_i^I) - e_i^R \omega_i \cos(\omega_i t + \varepsilon_i^R) \} \\ &= \sum_{i=1}^n \dot{X}_i \end{aligned} \quad (5)$$

From small amplitude wave theory (for example, Crapper, 1984), the velocity potential $\phi(x, z, t)$ is presented as follows under the two conditions: generation of the target wave toward the positive direction x by the displacement X^I and absorption of the reflective wave toward the negative direction x by the displacement X^R .

$$\begin{aligned} \phi(x, z, t) &= \sum_{i=1}^n \left\{ A_i e_i^I \frac{g}{\omega_i} \frac{\cosh K_i(z+h)}{\cosh K_i h} \sin(\omega_i t - K_i x + \varepsilon_i^I) \right. \\ &\quad + A_i e_i^R \frac{g}{\omega_i} \frac{\cosh K_i(z+h)}{\cosh K_i h} \sin(\omega_i t + K_i x + \varepsilon_i^R) \\ &\quad - \cos(\omega_i t + \varepsilon_i^I) \sum_{j=1}^{\infty} C_{ij} e_i^I \frac{g}{\omega_i} \frac{\cos K_{ij}(z+h)}{\cos K_{ij} h} \exp(-K_{ij} x) \\ &\quad \left. + \cos(\omega_i t + \varepsilon_i^R) \sum_{j=1}^{\infty} C_{ij} e_i^R \frac{g}{\omega_i} \frac{\cos K_{ij}(z+h)}{\cos K_{ij} h} \exp(-K_{ij} x) \right\} \end{aligned} \quad (6)$$

In Equation (6), the first and second terms of the right hand side represent the velocity potential of the target generation wave and the one of the reflective wave, respectively, and the rest represents one of the local waves. A_i and C_{ij} are written by

$$A_i = \frac{2 \cdot \sinh^2 K_i h}{K_i h + \sinh K_i h \cdot \cosh K_i h} \quad (7)$$

$$C_{ij} = \frac{2 \cdot \sin^2 K_{ij} h}{K_{ij} h + \sin K_{ij} h \cdot \cos K_{ij} h} \quad (8)$$

and K_{ij} is obtained by the following dispersion relation.

$$\omega_i^2 = -g K_{ij} \tan K_{ij} h \quad (9)$$

To let the first term and second term of Eq.(6) give the agreement with η^I and η^R , respectively, the next equations must stand up.

$$A_i e_i^I = a_i^I \quad \therefore e_i^I = \frac{a_i^I}{A_i} \quad (10)$$

$$A_i e_i^R = a_i^R \quad \therefore e_i^R = \frac{a_i^R}{A_i} \quad (11)$$

The surface elevation η_0 in front of the wave board (at $x=0$) is obtained by

$$\eta_0 = \frac{1}{g} \frac{\partial \phi(x, z, t)}{\partial t} \Big|_{z=0}^{x=0} \quad (12)$$

and using Eq.(4), Eq.(10) and Eq.(11), the next equation is obtained.

$$\eta_0 = \sum_{i=1}^n \{ a_i^I \cos(\omega_i t + \varepsilon_i^I) + a_i^R \cos(\omega_i t + \varepsilon_i^R) + \sum_{j=1}^{\infty} C_{ij} X_j \} \quad (13)$$

Moreover the following relation is obtained from Eqs. (5), (10) and (11):

$$\sum_{i=1}^n \frac{A_i}{\omega_i} \dot{X}_i = \sum_{i=1}^n a_i^I \cos(\omega_i t + \varepsilon_i^I) - \sum_{i=1}^n a_i^R \cos(\omega_i t + \varepsilon_i^R) \quad (14)$$

Elimination of a_i^R using Eq.(13) and Eq.(14) gives the equation:

$$\sum_{i=1}^n \frac{A_i}{\omega_i} \dot{X}_i = 2 \sum_{i=1}^n a_i^I \cos(\omega_i t + \varepsilon_i^I) - \eta_0 + \sum_{i=1}^n \sum_{j=1}^{\infty} C_{ij} X_j \quad (15)$$

In Equation (15), the first term in the right hand side represents the surface elevation of the target wave at $x=0$. Let this term be η_D , then Eq.(15) is written as

$$\sum_{i=1}^n \frac{A_i}{\omega_i} \dot{X}_i = 2\eta_D - (\eta_0 - \sum_{i=1}^n \sum_{j=1}^{\infty} C_{ij} X_i). \quad (16)$$

In Equation (16), A_i , C_{ij} , can be computed in Eq. (7) and Eq. (8); ω_i is a priori value: the i -th angular frequency of the target wave and η_D is the surface elevation of the target wave; η_0 is the surface elevation in front of a wave board, therefore it can be measurable by a wave height sensor. Moreover the displacement X of a wave board is also measurable by an appropriate sensor, for example, an encoder attached in a motor, a potentiometer installed in a driving system, etc. Accordingly, the i -th velocity \dot{X}_i of a wave board can be calculated under the estimation of the i -th displacement of a wave board. As a result, the velocity \dot{X} of a wave board is controlled by

$$\dot{X} = \sum_{i=1}^n \dot{X}_i, \quad (17)$$

and both absorption of the reflective wave and generation of the target wave can be accomplished. In the case of the regular wave ($n=1$ in Eq. (6)), the following results are induced:

$$\begin{aligned} \phi = & A e^I \frac{g}{\omega} \frac{\cosh K(z+h)}{\cosh Kh} \sin(\omega t - Kx + \varepsilon^I) \\ & + A e^R \frac{g}{\omega} \frac{\cosh K(z+h)}{\cosh Kh} \sin(\omega t + Kx + \varepsilon^R) \\ & - \cos(\omega t + \varepsilon^I) \sum_{j=1}^{\infty} C_j e^I \frac{g}{\omega} \frac{\cos K_j(z+h)}{\cos K_j h} e^{-K_j x} \\ & + \cos(\omega t + \varepsilon^R) \sum_{j=1}^{\infty} C_j e^R \frac{g}{\omega} \frac{\cos K_j(z+h)}{\cos K_j h} e^{-K_j x} \end{aligned} \quad (18)$$

$$A = \frac{2 \sinh^2 Kh}{Kh + \sinh Kh \cosh Kh} \quad (19)$$

$$C_j = \frac{2 \sin^2 K_j h}{K_j h + \sin K_j h \cos K_j h} \quad (j=1, 2, 3, \dots) \quad (20)$$

$$\omega^2 = gK \tanh Kh \quad (21)$$

$$\omega^2 = -gK_j \tan K_j h \quad (j=1, 2, 3, \dots) \quad (22)$$

$$\dot{X} = \frac{\omega}{A} \{ 2\eta_D - (\eta_0 - \sum_{j=1}^{\infty} C_j X) \} \quad (23)$$

These are consistent with the previous result (Kawaguchi, 1986).

Control Installations

Figure 2 shows the control installations for the proposed algorithm using filter banks which are realized by software on a digital computer. A filter bank consists of n filters, shown in Fig. 3, whose detection frequencies are set by component frequencies of the irregular waves. The gain k works the balance of the input and output.

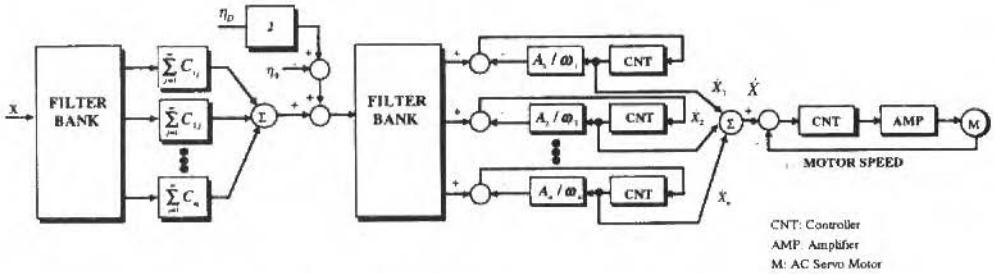


Fig. 2 Control algorithm implementation for absorption of irregular waves

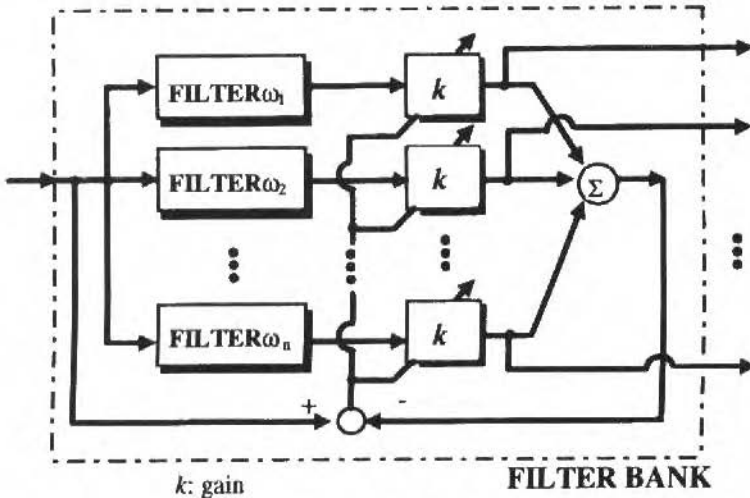


Fig. 3 Filter bank

The first filter bank decomposes the displacement X of a wave board into its constituent elements X_i . The second filter bank also decomposes the right hand side of Eq.(16) into each frequency component. The command signal \dot{x} for the motor speed is then obtained by the summation of \dot{X}_i .

Experiments in the Test Tank and Time-Frequency Analysis

Experiments in the test tank

The test tank is 3m long, 0.1m wide and 0.3m deep. The wave maker has a single wave board of 0.1m width with a small clearance to both side walls. Two wave makers are installed at both ends of the test tank shown in Fig. 4. In the experiments, one wave maker is used for generation and the other for absorption.

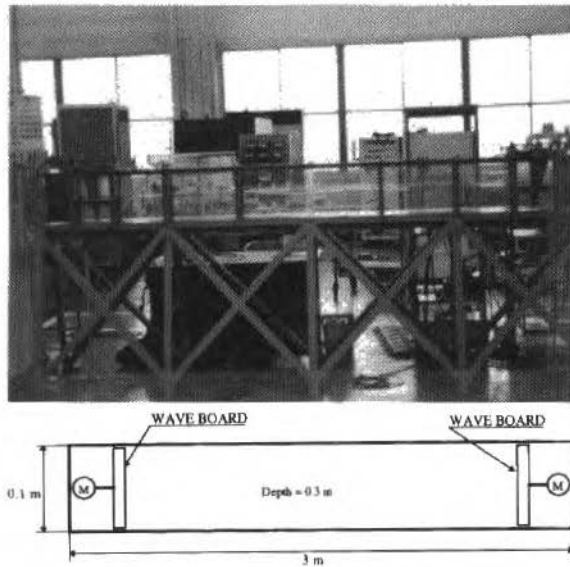
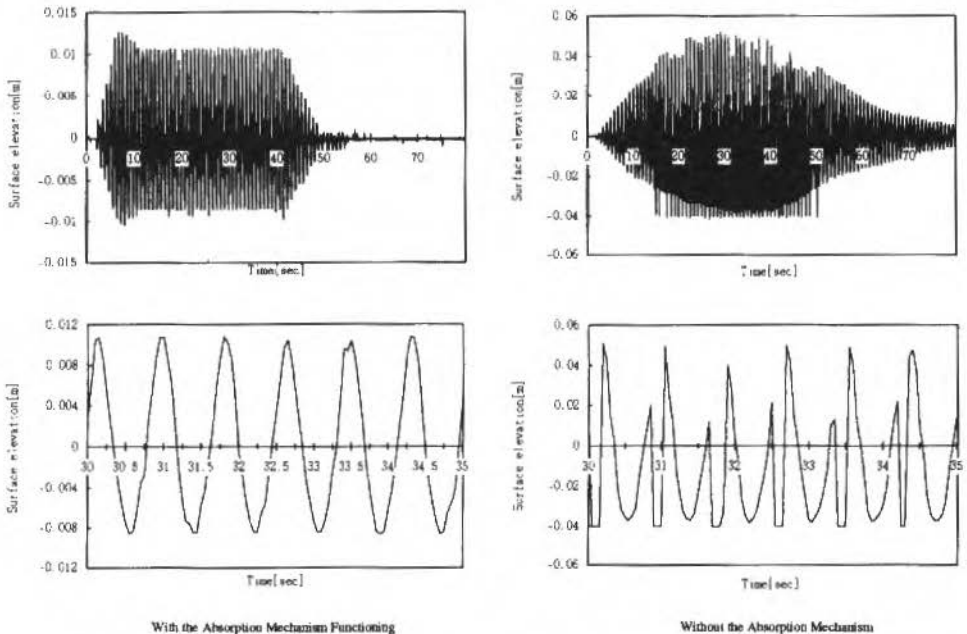


Fig. 4 Test tank

Figure 5 shows the time histories of the surface elevation at the longitudinal middle point in the test tank generated by the regular wave whose parameters are as follows: $H=1.5\text{cm}$, $T=0.83\text{s}$. The left charts show the state of generation with working of absorption. The fade-in and fade-out functions are working at the start sequence and the stop sequence, respectively. The non-linearity of the test tank affects the target wave height, that is, the measured wave height is a little lower than the given wave height. The absorption mechanism is working well, therefore the progressive regular wave is obtained. Moreover the absorption mechanism makes the water surface still as soon as waves generation stops.

Fig. 5 Time histories of the surface elevation by the regular wave ($H=1.5\text{cm}$, $T=0.83\text{sec}$)

Whereas the right charts show the state of the case without absorption mechanism. The standing waves form because of the superposition of the generated waves and the reflective waves from the tank termination.

The lower charts represent the time expansion charts of the uppers.

Figure 6 corresponds to the irregular waves, which consist of two component frequency waves: $H_1=1.2\text{cm}$, $T_1=0.83\text{s}$ and $H_2=1.2\text{cm}$, $T_2=0.67\text{s}$. Similarly, the left charts show the state of generation with working of absorption and the right the state of the case without absorption mechanism. The absorption mechanism is working very well also in the case of the irregular waves.

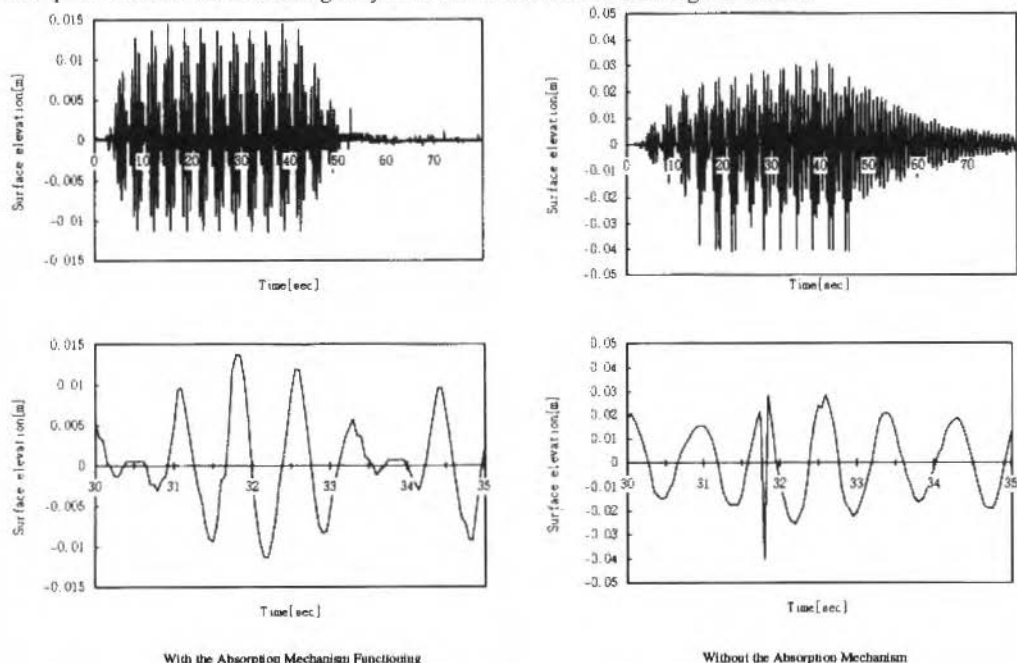


Fig. 6 Time histories of the surface elevation by the irregular wave $H_1 = 1.2\text{cm}$, $T_1 = 0.83\text{sec}$, $H_2 = 1.2\text{cm}$, $T_2 = 0.67\text{sec}$

Time-frequency analysis

Using the short-time Fourier transform technique, validation of the experimental data is verified.

Time histories have little information concerning frequency. Frequency information can be obtained by the frequency analysis based on the Fourier transform. However Fourier analysis has a disadvantage: frequency information can only be extracted for the complete duration of an original time-history signal $f(t)$. Since the integral in the Fourier transform:

$$\hat{f}(\omega) = \int_{-\infty}^{\infty} \exp(-i\omega t) f(t) dt \quad (24)$$

extends over all time, from $-\infty$ to ∞ , the information it provides arises from an average over the whole length of the signal. Moreover, a local oscillation representing a particular feature at some point in the lifetime of $f(t)$ will contribute to the spectrum in all frequency range, but its location on the time axis will be lost.

In contrast to Fourier analysis, the short-time Fourier transform can overcome this disadvantage. The short-time Fourier transform is defined as follows (for example, Kaiser, 1994):

Let the function: $w(t)$ ($w(t) \in L^2(R)$) and $\hat{w}(\omega)$ satisfy

$$tw(t) \in L^2(R) \quad (25)$$

and

$$\omega \hat{w}(\omega) \in L^2(R), \quad (26)$$

then the window-Fourier transform using $w(t)$ as the window function:

$$(G_b f)(\omega) = \int_{-\infty}^{\infty} (\exp(-i\omega t) f(t)) w^*(t-b) dt \quad (27)$$

is the short-time Fourier transform. Here suffix * denotes the conjugate.

The short-time Fourier transform can provide an alternative way of breaking a signal down into its constituent parts and a way of knowing a specific point in which the particular oscillation occurs.

Figures 7 and 8, compared to Fig. 5 and Fig. 6, respectively, show the time-frequency charts computed using Gabor transform (see Appendix), one of the short-time Fourier transforms. The upper charts in these figures show the state of generation with the absorption mechanism functioning. Only the generated frequency components are evident from the start of generating waves in the developed algorithm. However the lower charts show the state without the absorption mechanism. In these charts, undesired frequency components occur due to the reflective waves.

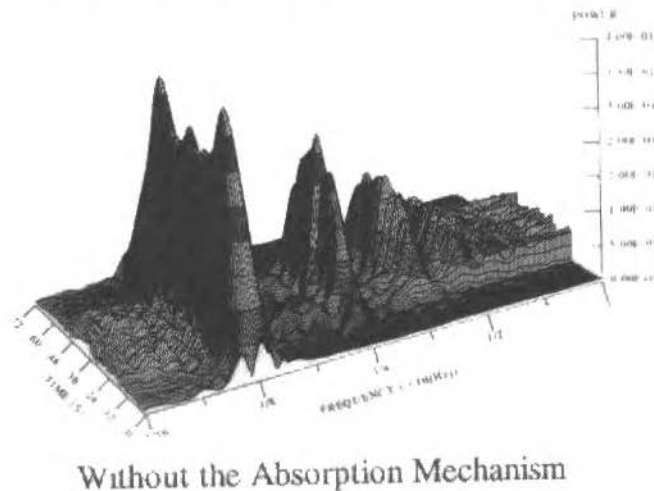
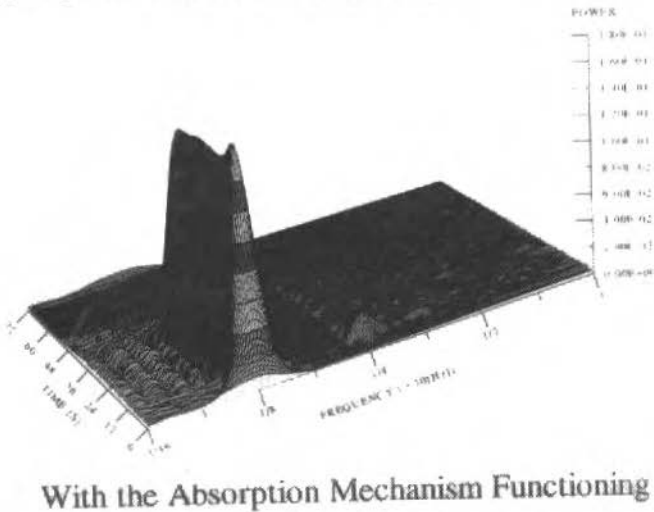
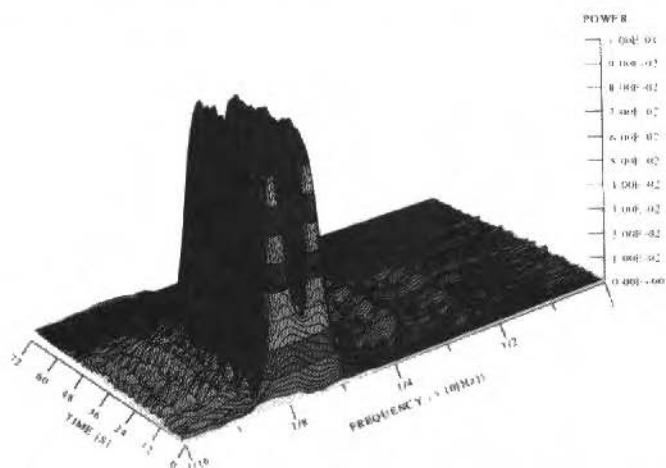
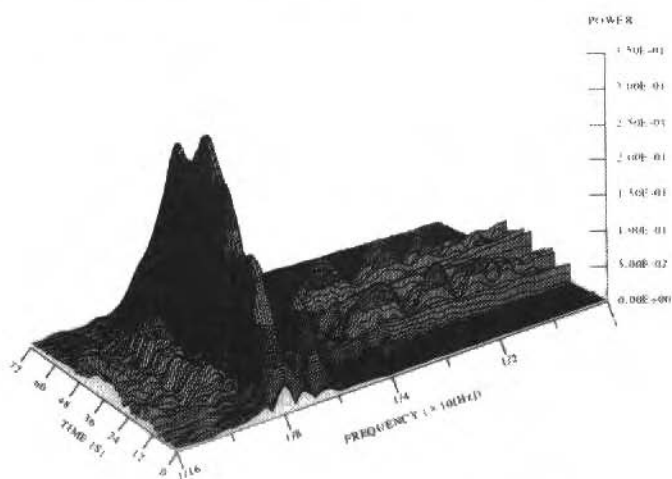


Fig. 7 Time-frequency charts (in case of regular wave, compared to Fig. 5)



With the Absorption Mechanism Functioning



Without the Absorption Mechanism

Fig. 8 Time-frequency charts (In case of irregular wave, compared to Fig. 6)

Concluding Remarks

An absorption algorithm for irregular waves was extended from that of regular waves and its validity was verified by experiments using a scale-modeled test tank. Moreover, using a short-time Fourier transform technique, the effectiveness of the proposed algorithm was shown. The time-frequency representation of the experimental data maps its waveform into a three-dimensional function of time, frequency and its power over the time-frequency plane. This displays the localization in time of the signal's frequency components.

The experiments dealt with irregular waves which have two frequency components due to the limitations of the scale-modeled test tank, which include such parameters as: limited tank length and the lack of stroke length of the wave board, etc. The authors plan work include experiments for spectrum

shaped irregular waves such as ISSC (Huang, Tung and Long, 1990), JONSWAP (Hasselmann, et al., 1973) and Bretschneider-Mitsuyasu (Mitsuyasu, 1970), etc. at the large scale test basin (Matsuura, et al., 1997).

The ocean occupies 71% of the surface of the earth and plays an important role in the resources and environment of the earth. The next century will see the need a total development system, in which the ocean must be considered in the company of the land, and international corporation. The authors hope that this paper will contribute to ocean development.

Acknowledgment

The authors would like to mention Mr. T. Baba and Mr. K. Yamashita who have been in charge of the coordination of this research project. Our thanks are particularly due to Mr. M. Umeda and Mr. K. Tajima for their assistance of the experiments in the test tank.

References

- Chui, C.K., 1992. "An Introduction of Wavelets". Academic Press.
- Crapper, G.D., 1984, "Introduction to Water Waves", Ellis Horwood Ltd.
- Hasselmann, K., et al., 1973, "Measurement of wind-wave growth and swell decay during the Joint North Sea Wave Project (JONSWAP)", Deutsche Hydrograph, Z., A8(No.12).
- Huang, N. E., Tung, C. and Long, S. R., 1990, "Wave Spectra", Ocean Engineering Science, The Sea, Volume 9, Part A, pp.197-237.
- Kaiser, G., 1994. "A Friendly Guide to Wavelets", Birkhäuser.
- Kawaguchi, T., 1986, "Absorbing Wave Making System with Wave Sensor and Velocity Control", Technical Report of Mitsui Shipbuilding, No.128, pp.20-24.
- Matsuura, M., Yamaguchi, Y., Nohara, B.T. and Yamamoto, I., 1997, "An Improved Method to Calculate Generation Signal of Multi-Directional Irregular Waves", The 27th I.A.H.R. Congress, to appear.
- Mitsuyasu, W., 1970, "Development of Spectra of Wind and Waves(2)", the 17th Coastal Engineering Conference, pp.1-7.
- Naito, S., Huang, J. and Nakamura, S., 1987, "Research on the Absorb-Making of Irregular Waves with the Terminal Device", Journal of Kansai Shipbuilding Society, pp.25-32.
- Nohara, B.T., Yamamoto, I. and Matsuura, M., 1995, "Multi-Directional Wave Maker and Its Real Time Wave Control System Applied to a Seakeeping Model Basin", International Towing Tank Conference, Wave Generation'95, pp.175-194.
- Nohara, B.T., Yamamoto, I. and Matsuura, M., 1996, "The Organized Motion Control of Multi-Directional Wave Maker", 4th International Workshop on Advanced Motion Control, AMC-MIF'96, pp.470-475.
- Official Gazette, 1995, August, "About How to Maintain Harbor Facilities", The Ministry of Transport(in Japanese).
- Salter, S.H., 1981, "Absorbing wave-makers and wide tanks", Proc. of the Conf. on Directional Wave Spectra Applications, pp.185.

Appendix (for example, Chui, 1992)

For $f \in L^2(R)$, the Gabor transform is defined as

$$(G_b^\alpha f)(\omega) = \int_{-\infty}^{\infty} (\exp(-i\alpha t) f(t)) g_\alpha(t-b) dt, \quad (A1)$$

where g is the Gaussian function:

$$g_\alpha(t) = (1/(2\sqrt{\pi\alpha})) \exp(-t^2/(4\alpha)). \quad (\alpha > 0) \quad (A2)$$

This $(G_b^\alpha f)(\omega)$ gives a local time-frequency analysis of the signal $f(t)$ in the sense that it provides accurate information about $f(t)$ simultaneously in the time domain and in the frequency domain. Moreover Gabor transform provides the optimal localization in time in the meaning of the uncertainty principle, which states that sharp localization in time and in frequency is mutually exclusive.

Boundaries of Safe Motion Through a Coarse Grid-of-Starts

Jessé Rebello de Souza Jr.

Universidade de São Paulo
Escola Politécnica
Departamento de Engenharia Naval e Oceânica
05508-900 São Paulo, SP - Brazil
jsouza@usp.br

Steven R. Bishop

University College London
Centre for Nonlinear Dynamics and Its Applications
WC1E 6BT London UK

Abstract

This paper describes computational methods for the evaluation of safe limits of operation of driven mechanical systems. We define the problem of evaluating the safety of transient and steady-state motions in terms of the escape from a potential well. We then describe a simple, robust method of determining boundaries of safe operation in control space, and we conclude by applying the method to a number of examples.

Keywords: *Nonlinear Dynamics, Escape Phenomena, Potential Wells, Nonlinear Oscillators*

Introduction

Many physical systems have their behaviour largely determined by the interplay between "internal", potential forces and "external" excitation. Potential wells are associated with local minima of the potential energy of the system, and systems are often designed to make desirable operational conditions coincide with the minima of some generalised potential energy, so that in the absence of disturbances the system remains in a desired state. Common examples of potential wells include those generated by elastic forces, and by gravitational and electromagnetic fields. Perhaps an important question is, does the system remain *close* to the desirable condition in the presence of *external perturbations*. Obviously, any system will only endure a certain amount of disturbance, beyond which no stable or safe operation will be possible. One way of characterising the failure of the system is therefore by identifying failure with the *escape of the system from a safe potential well*.

Clearly, it is of great interest to be able to predict which conditions may lead to failure. A comprehensive answer to this question is generally very difficult to obtain. Exact calculations are impossible in all but the simplest cases. In fact, it has been observed that even one- and two-degree-of-freedom, periodically driven nonlinear oscillators can display an enormous variety and complexity of escape mechanisms, comprising many local and global bifurcations, non-periodic and even chaotic responses, see for example Thompson (1989a) and Thompson and de Souza (1996). Some useful information can, however, be obtained without excessive use of computational resources. In particular, we focus here on the approximate determination of *boundaries of safe motion in the space of control parameters*. We propose that a coarse grid-of-starts suitably placed in phase space can be an efficient instrument for the estimation of those boundaries. We demonstrate the use of this method for one- and two-degree-of-freedom nonlinear mechanical systems.

Loss of Engineering Integrity

For a given configuration of control parameters, the set of initial conditions in phase space that lead to safe motions is called the *safe basin* of the system. The size, shape and location of safe basins is an important measure of the engineering integrity of the system. Clearly, those properties will evolve as control parameters are changed, and a key information about the system is the location of regions of control parameter space that lead to a loss of engineering integrity (unacceptable safe basins).

A variety of phenomena can be involved in the process of loss of dynamic integrity of a system. de Souza (1995) has presented a preliminary classification of such processes based on observations of the macroscopic evolution of safe basins as control parameters of the system are changed. It has been proposed that processes of loss of dynamic stability of motions inside a potential well can be broadly classified as:

Gradual

Resulting from a macroscopically continuous and relatively slow reduction of safe basins. Safe basins can gradually shift in phase space and/or have their boundaries (but not their bulk) eroded by thin fractal striations. Fig.1 shows an example of such behaviour observed in the system described by Eq. 4. See the Appendix for numerical details.

Sudden

Usually associated with the fractal erosion of the bulk of the safe basin. The fact that fractal incursions sweep rapidly across the safe basin means that the whole process occurs within a narrow range of parameter values. Fig.2 shows an example of such behaviour observed in the system described by Eq. 4. See the Appendix for numerical details.

Catastrophic

These are commonly given by discontinuous changes in shape, size, or position of the safe basin that result from a dynamic bifurcation, such as a jump to resonance. In these cases the remote attractor to which solutions eventually converge may lie outside the region of acceptable motion, and the safe basin can vanish abruptly.

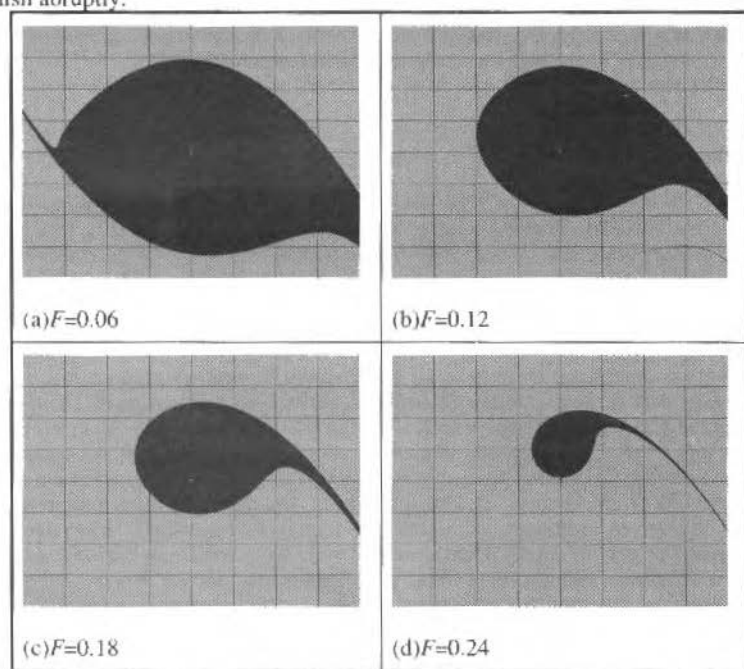


Fig. 1 Evolution of safe basins for Eq. 4 with $\omega = 0.55$

Nomenclature

c = Coefficients of restoring function in Eq. 6	p = Number of integration points per cycle of the forcing	ϕ = General function in Eq. 2
d = Escape distance	t = Time	ω = Frequency of excitation
f = Restoring function	T = Period of the forcing	
F = Amplitude of excitation	V = Potential energy function	
g = Damping function	x = Phase variable	
m = Number of cycles of the forcing	α = Coefficients of restoring function in Eq. 5	
M = Grid starting coordinates	β = Damping coefficient	
N = Number of starting conditions		

Subscripts and symbols

$(\dot{})$ = Differentiation of () wrt time
 esc = Escape

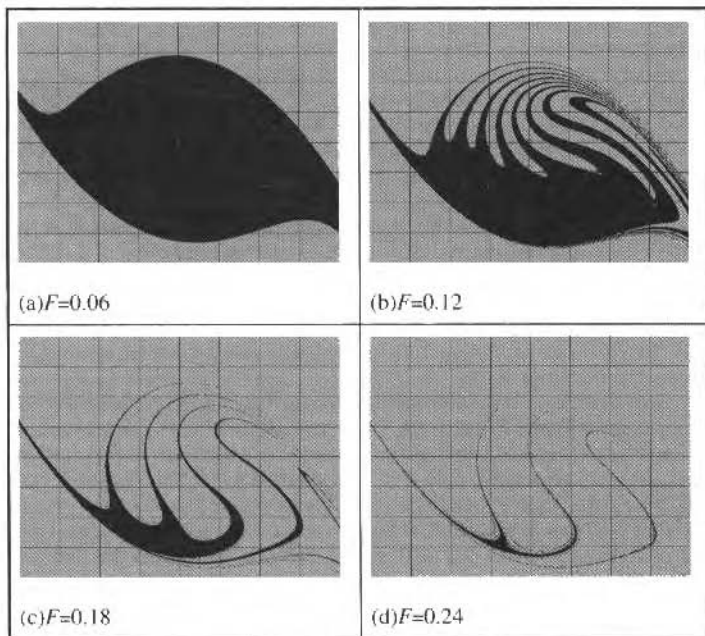


Fig. 2 Evolution of safe basins for Eq. 4 with $\omega = 0.85$

The heuristics of the method proposed here is that a coarse grid of starting conditions suitably placed in the phase space of the system can locate regions of parameter space corresponding to a loss of engineering integrity resulting from any of the processes described above.

Methodology

We consider coupled mechanical oscillators described by systems of the form:

$$\begin{aligned} \ddot{x}_1 + g_1(\dot{x}) + f_1(x) &= F_1 \sin(\omega t) \\ \ddot{x}_2 + g_2(\dot{x}) + f_2(x) &= F_2 \sin(\omega t) \end{aligned} \tag{1}$$

Here $x = (x_1, x_2)$ is a vector of space coordinates describing the motion of the system, and a dot denotes differentiation with respect to time t . The system is driven by periodic forcing of amplitude F and period ω , and incorporates positive damping $g(x) = (g_1(\dot{x}), g_2(\dot{x}))$.

Interesting systems will typically display at least one local minimum of the potential energy function $V(x) = \int f_1(x) dx_1 + \int f_2(x) dx_2$, corresponding to a stable fixed point of the unforced, undamped system. We assume that the origin of our coordinate system is some (non-degenerate) minimum of $V(x)$ which we deem a desirable condition for the system.

For systems described by Eq. (1), a *general grid of starting conditions* is the product set of discrete vectors of starting coordinates $M = s_1 \otimes s_2 \otimes s_3 \otimes s_4$, where $s_i = \{s_{i1}, s_{i2}, \dots, s_{iN_i}\}, i = 1, 2, 3, 4$, and N_i is the number of starting coordinates in the grid for phase variable x_i . Having defined a suitable grid, the method consists of solving numerically a series of initial-value problems:

$$\begin{aligned} \dot{x}(t) &= \phi(x, F, \omega, t), \quad t \in [0, t_f] \\ x(0) &= x_0, \quad x_0 \in M \end{aligned} \tag{2}$$

to generate $N=N_1 \times N_2 \times N_3 \times N_4$ series of discrete points $\{x(k), k = 1, 2, \dots, m \cdot p\}$. The $\{x(k)\}$ are numerical approximations to transient trajectories, where m is the number of cycles of the forcing (of period $T = 2\pi/\omega$), and p is the number of integration points per cycle of the forcing. The parameter m defines the maximum duration of transients, $t_t = mT$. Each point of $\{x(k)\}$ is then tested against the escape criterion, and classified as safe or escaping. If any point of $\{x(k)\}$ is classified as escaping the trajectory it approximates is considered to be an escaping trajectory. For each frequency of the forcing term the method consists of determining the minimum value of the amplitude of the forcing such that escape occurs for any point of the grid.

With respect to escape criteria we adopt a simple approach throughout this study. We take the distance between the origin and the nearest maximum of potential energy as a reference. For systems with a one-dimensional potential well we assume that escape has occurred when the displacement phase variable has gone a certain fraction (we have used 20% throughout this study) of that distance beyond the maximum. Higher dimensional systems require that the distance in the phase space of displacement coordinates is used. We also restrict simulations to transient motions of no more than 10 cycles of the forcing. If escape has not occurred within 10 cycles we consider the point as safe and move on to the next point of the grid or to a larger amplitude of the forcing. Throughout this study we have employed a 4th-order Runge-Kutta numerical integrator with fixed step size of 1/80 of the period of the forcing.

The dimension of a general grid is the dimension of the phase space of the system under study. We however limit our numerical experiments to reduced grids in which only phase variables associated with the potential energy are varied along the grid, effectively reducing the dimension of the grids. Phase variables not associated with the potential energy (in mechanical oscillators these are the velocities) are kept constant along the grid at their equilibrium value (usually zero). In previous works we have analysed the effect of the two main parameters defining the grid: grid length (distance in phase space between extremes of the grid), and grid size (number of points that constitute the grid), Bishop and de Souza (1993). In that study we concentrated on the escape equation Eq. (3), and we concluded that the length of the grid is the most important factor. Grids of three points yield essentially the same results as grids of more than a hundred points, provided that they have the same length. The length of the grid however was shown to have a large effect on the final result. Several lengths were used, and longer grids were shown to indicate lower escape values, particularly in conditions far from the main resonance. We therefore concentrate here on grids of three points in each direction considered: the origin (i.e. the minimum of the potential well) and two other points symmetrically placed around it. We also include for comparison results from one-point grids (always the stable, desired condition).

Since our previous studies focused on one-degree-of-freedom systems and their associated one-dimensional potential wells, we investigate here the effect of the extra dimension found in Eq. (7).

Results: sensitivity study

With the purpose of demonstrating the applicability of the method we propose here, we have selected from the recent international literature four different one-degree-of-freedom systems, and a two-degree-of-freedom system. They are all periodically-driven nonlinear oscillators in which failure can be viewed as the escape from a potential well. The basic criterion used in the selection of these specific systems was the availability of diagrams in the control plane depicting safe (non-escaping) and unsafe regions of operation.

The dynamical systems considered here are:

System 1 (the escape equation) - Asymmetric potential well with quadratic nonlinearity, Virgin et al. (1992), Thompson (1989b).

$$\ddot{x} + \beta \dot{x} + x - x^2 = F \sin(\omega t) \quad (3)$$

System 2 (a Duffing equation) - Symmetric potential well with cubic nonlinearity, Virgin et al. (1992), Kan (1992).

$$\ddot{x} + \beta \dot{x} + x - x^3 = F \sin(\omega t) \quad (4)$$

System 3 (a modified Duffing equation used in one-mode analysis of shallow arch) - Asymmetric potential well with quadratic and cubic nonlinearities, Virgin et al. (1992).

$$\ddot{x} + \beta \dot{x} + \omega_0^2 x + \alpha_2 x^2 + \alpha_3 x^3 = F \sin(\omega t) \tag{5}$$

System 4 (roll motion of a ship) - Asymmetric potential well with cubic and fifth order nonlinearities, Soliman and Thompson (1991).

$$\ddot{x} + \beta_1 \dot{x} + \beta_2 |x| \dot{x} + c_1 x + c_3 x^3 + c_5 x^5 = F \sin(\omega t) \tag{6}$$

System 5 (two-degree-of-freedom system) - Symmetric two-dimensional potential well, Virgin et al. (1992).

$$\begin{aligned} \ddot{x}_1 + \beta \dot{x}_1 + x_1 - 4x_1 x_2^2 &= F \sin(\omega t) \\ \ddot{x}_2 + \beta \dot{x}_2 + 2.25x_2 - 4x_1^2 x_2 &= F \sin(\omega t) \end{aligned} \tag{7}$$

We start our investigation with a sensitivity study involving the main parameters defining a grid-of-starts: grid length, and grid size. For each one of the systems represented above by Eqs. (3)-(7) we perform the numerical determination of boundaries of safe motion under transient conditions, using three different grids. For Eqs. 3 to 6 the influence of grid size is assessed by including a one-point grid as well as two three-point grids; the influence of grid length is evaluated by taking different lengths for the two three-point grids. For Eq. 7 we have also performed a comparison between one- and two-dimensional grids with three points in each direction.

In the legends to Figs. 3 to 8 the length of the grid is always expressed in terms of fractions of the distance between the origin of the potential well and the nearest maximum of the potential function: 0.00 (corresponding to a one-point grid), 0.30 and 0.65. The number of points comprising the grid is denoted by $N_1 \times N_2$ (for two-dimensional phase space) or $N_1 \times N_2 \times N_3 \times N_4$ (for four-dimensional phase space) where N_i is the number of points in the grid in the direction of x_i .

Results for this sensitivity study are shown in Figs. 3 to 8 where the minimum values of F for escape (F_{esc}) are plotted for a range of frequencies of the forcing. The results of this sensitivity study confirm that grid length is an important parameter both for one- and two-dimensional wells, especially in far-from-resonance conditions. In some cases, as with Eqs. (3) and (5), escape values predicted by longer grids can be less than half of those predicted by a one-point grid. This signals for the necessity of longer grids if an accurate global picture of safe boundaries is to be achieved through the method proposed here. The difference in results between one- and two-dimensional grids for Eq. 7 are less pronounced but nevertheless significant in off-resonance conditions, see Figs. 7 and 8. In view of the results described above, we have selected the longer grids for comparison with the international literature, and the two-dimensional grid for Eq. 7.

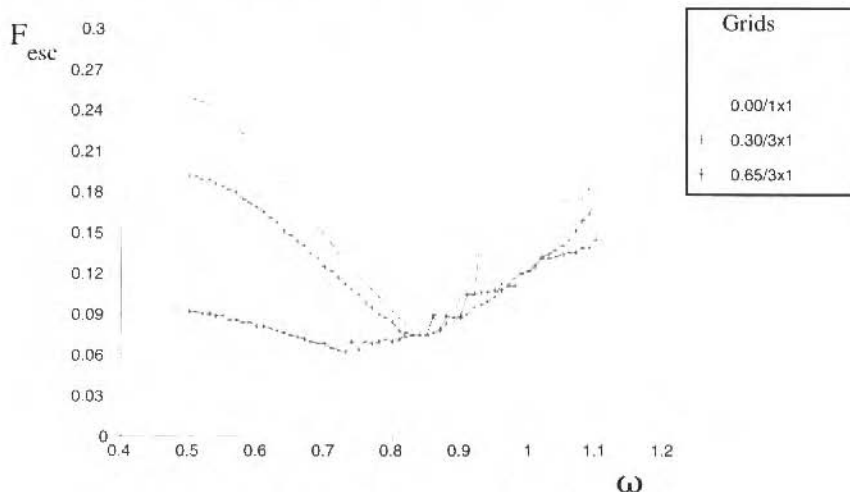


Fig. 3 Sensitivity study for Eq. 3

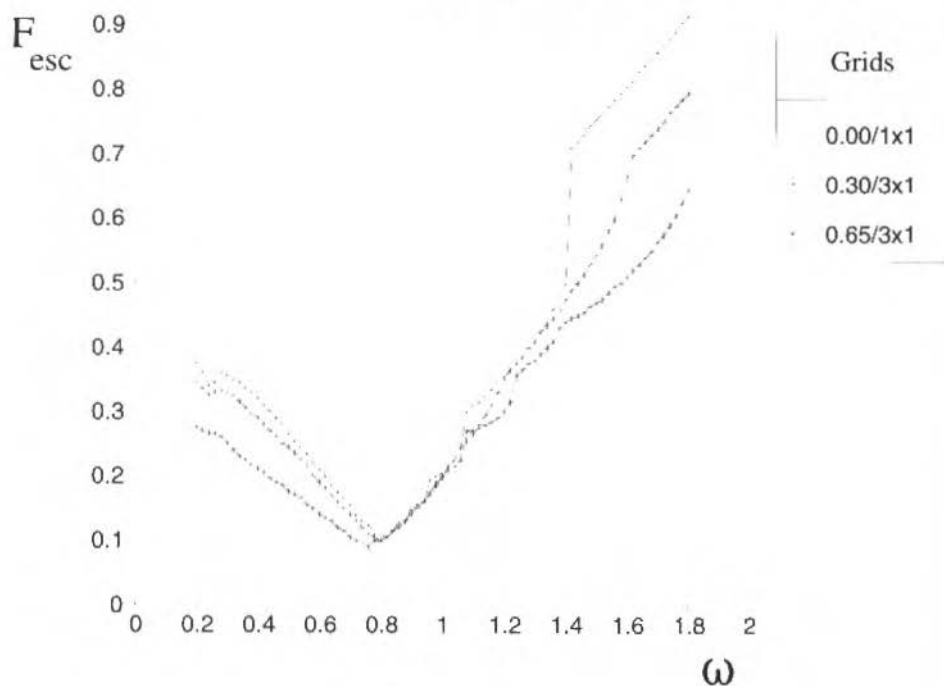


Fig. 4 Sensitivity study for Eq. 4

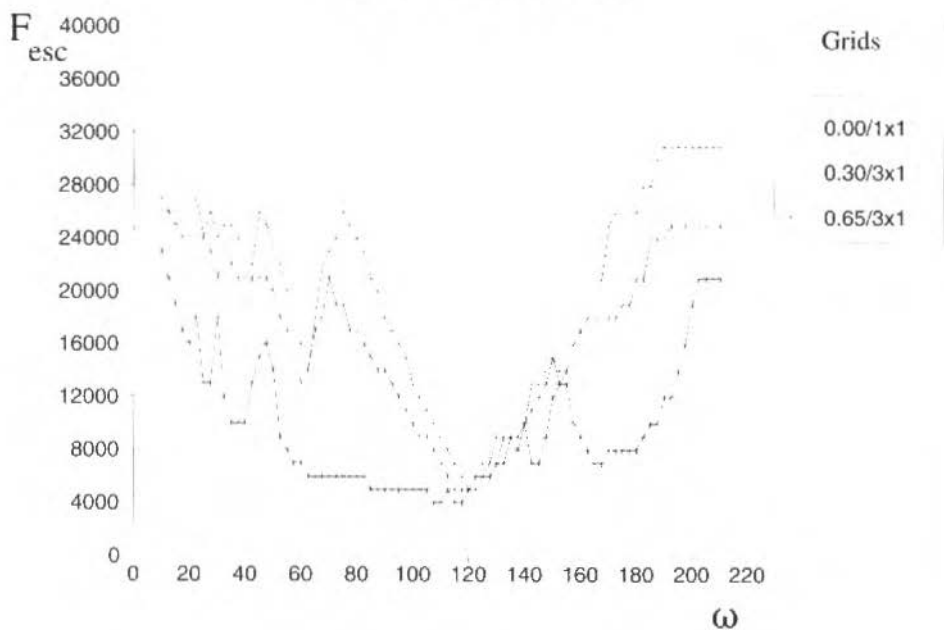


Fig. 5 Sensitivity study for Eq. 5

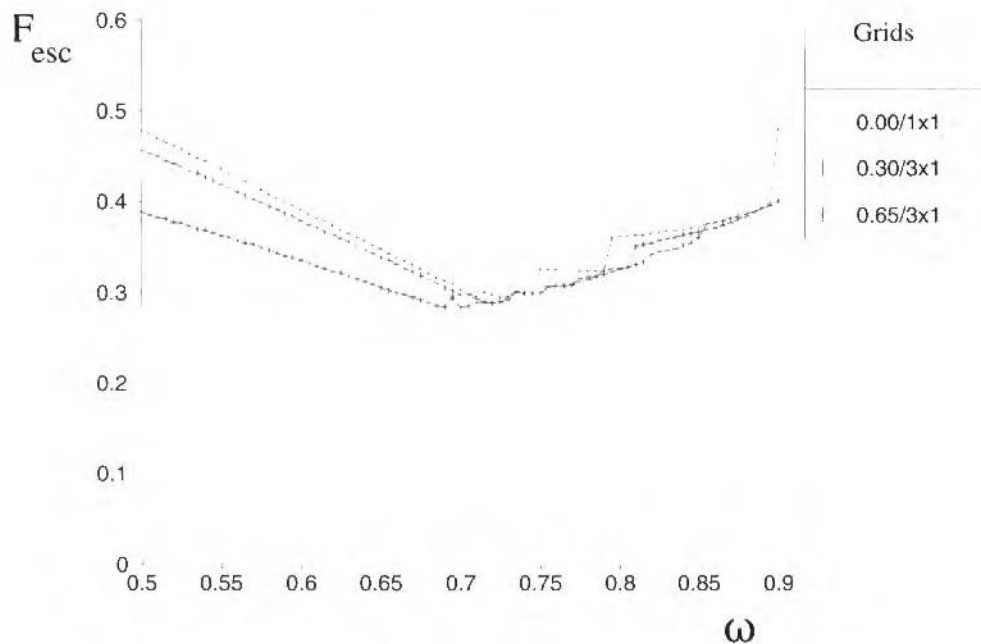


Fig. 6 Sensitivity study for Eq. 6

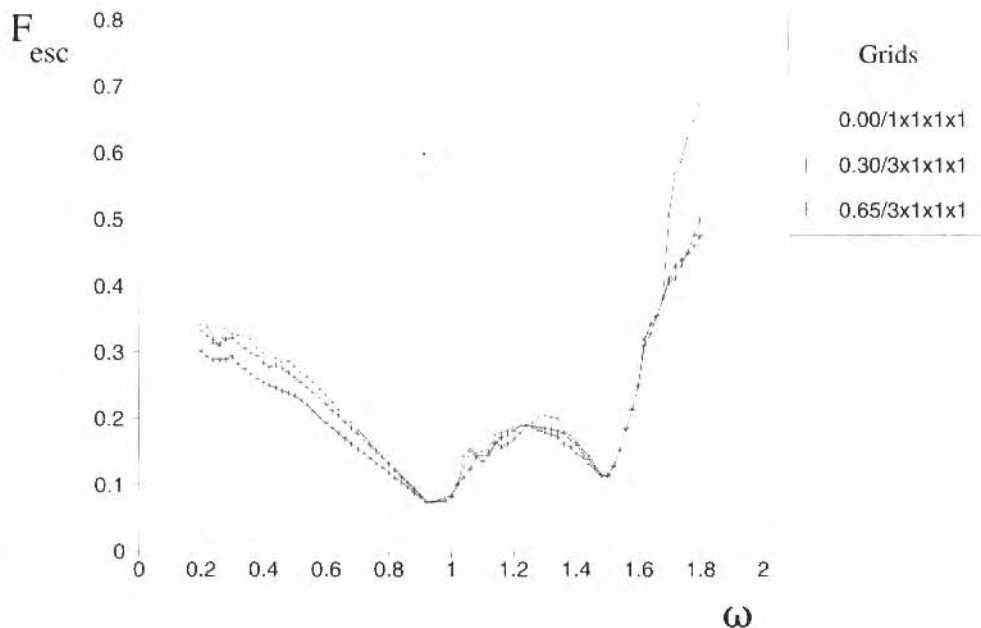


Fig. 7 Sensitivity study for Eq. 7 - one-dimensional grids

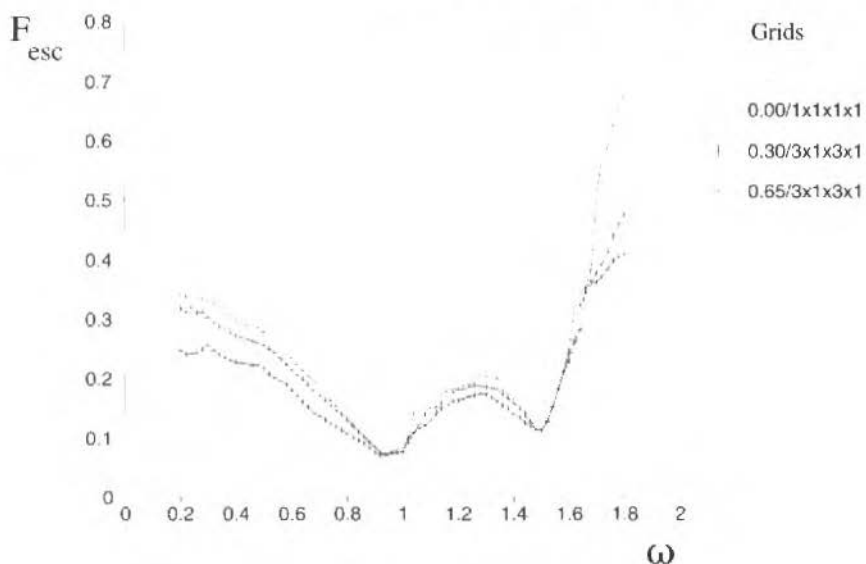


Fig. 8 Sensitivity study for Eq. 7 - two-dimensional grids

Results: comparison with the literature

Table 3 in the Appendix summarises the main numerical features of the data we are using here for comparison. In our own simulations we have employed the same parameter values, but we have used different starting points, maximum transient duration, and escape criteria. Our escape criterion is based on the distance to the nearest local maximum of potential energy: the system is deemed to have escaped if the magnitude of the displacement variable x exceeds 1.2 of that distance. For asymmetric potential wells, namely Eqs. (3) and (5), only displacements in the direction of escape are considered. In the case of Eq. (7) with its two-dimensional potential well, we have used a similar criterion: escape is assumed to have occurred if the distance in the phase space of displacement variables between a point in the trajectory and the origin $d(x) = \sqrt{x_1^2 + x_2^2}$ exceeds 1.2 of the distance between the origin and the nearest unstable fixed point of the unforced system.

With respect to starting points we have used grids symmetrically placed around the origin. The length of the grids is always 0.65 of the distance between the origin and the nearest unstable fixed point of the unforced system. For one-dimensional wells, that point is just the lowest local maximum of potential energy adjacent to the origin. For Eq. (7) the length of the grid in each direction is taken as 0.65 of the distance *along that direction* between the origin and the nearest saddle-like fixed point of the unforced system.

It should be noted that actual starting points are placed at the centre of each rectangle defined by the grid, which means for example that extreme starting points are placed at less than half the total length of the grid in each direction. For a three-point grid extreme points are actually placed at 1/3 of that distance.

Figures 9 to 13 show boundaries of safe motion obtained from the recent international literature, together with results from our own simulations for the same systems. The first point to be noted is the general agreement between those results. Boundaries follow approximately similar patterns. *Global* minima of amplitude of excitation for escape are remarkably similar, especially considering the differences in starting points, maximum transient duration, and escape criteria between our studies and the ones selected for comparison. Once again, this can be interpreted as evidence for the rapid erosion of safe basins of attraction that seems to dominate the loss of integrity under increasing amplitude of forcing in near-resonance conditions, Thompson (1989b).

But as far as a complete picture of safe motion is concerned, i.e. the whole boundary of safe motion covering the entire range of frequencies, we see once more that major differences can be obtained with

the use of longer, larger grids. The results from one-point grids extracted from the literature tend to overestimate minimum amplitudes of excitation necessary for escape. This fact is reflected on higher boundaries of safe motion, and is particularly noticeable at the extremes of frequencies covered by the numerical experiments. In most cases amplitudes of excitation leading to escape from one-point grids can be as much as twice the value predicted by our three-point grids, see for example Fig. 9, Fig. 10, Fig. 11. It is interesting to note that our maximum duration of transients is shorter than in any of the other experiments, a fact that could in principle lead to higher amplitudes for escape. Our escape criterion is also more stringent than those used in the other experiments, with the exception of the results from Kan (1992) for Eq. (4) and Thompson (1989b) for Eq. (3).

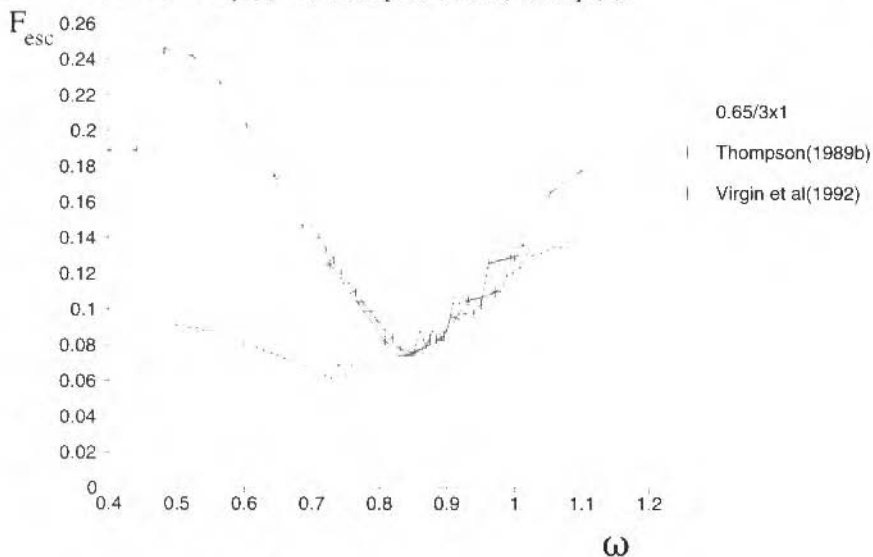


Fig. 9 Boundaries of safe motion for Eq. 3

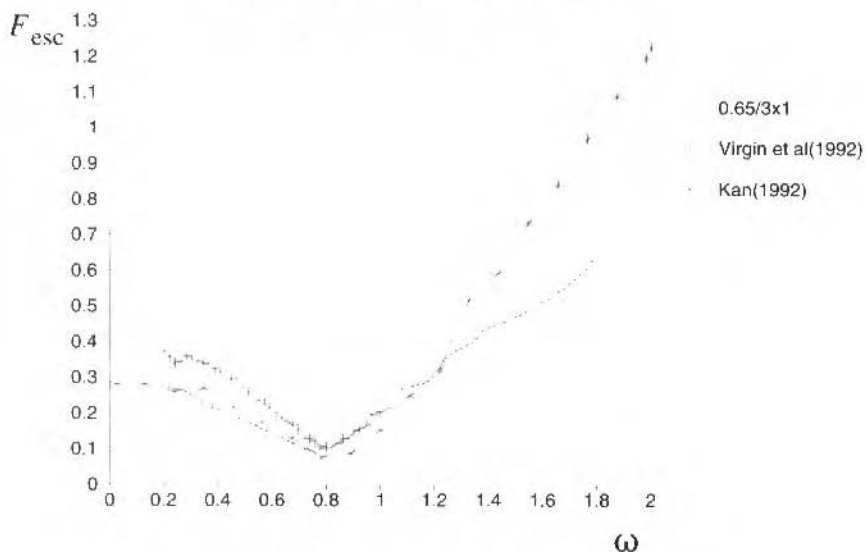


Fig. 10 Boundaries of safe motion for Eq. 4

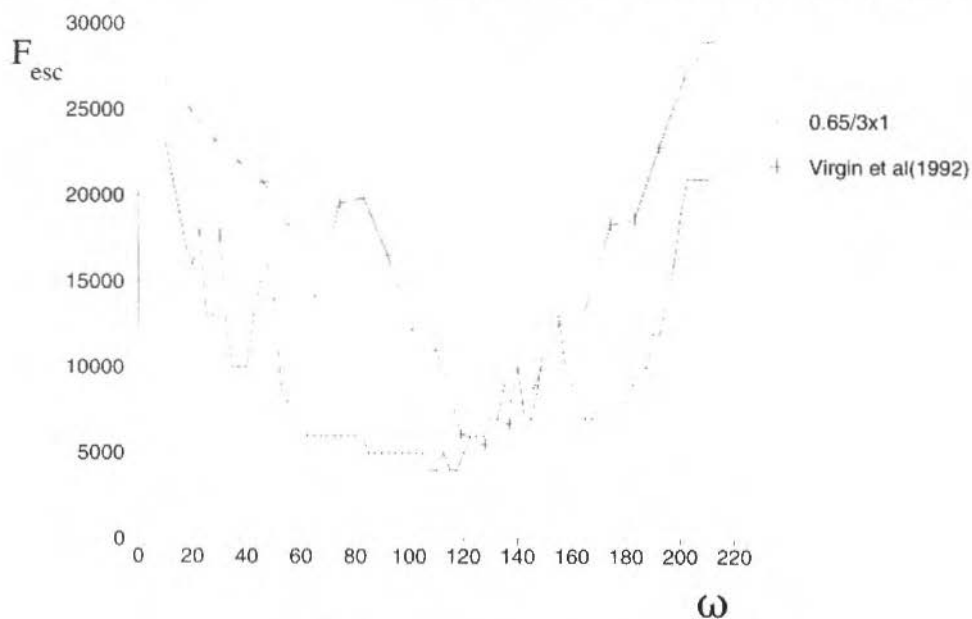


Fig. 11 Boundaries of safe motion for Eq. 5

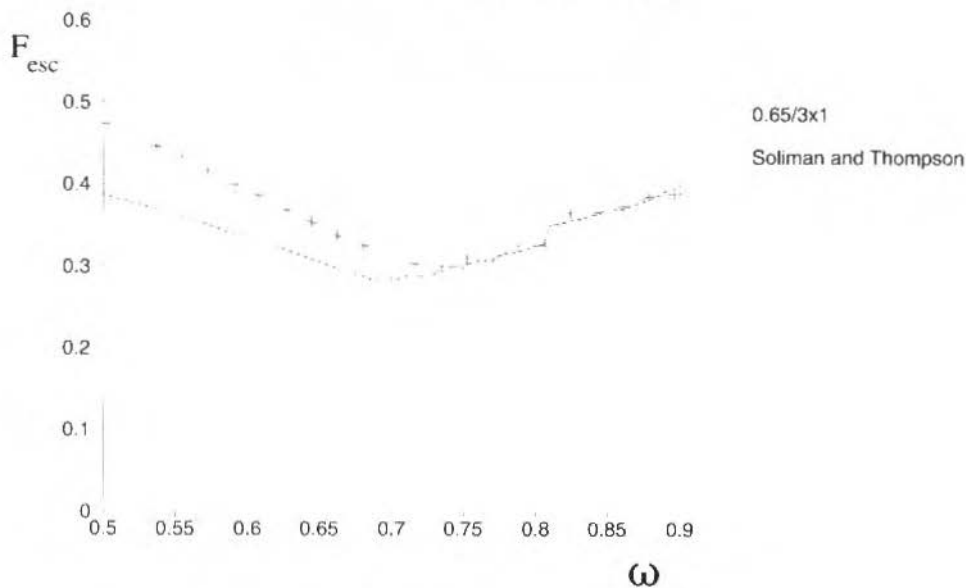


Fig. 12 Boundaries of safe motion for Eq. 6

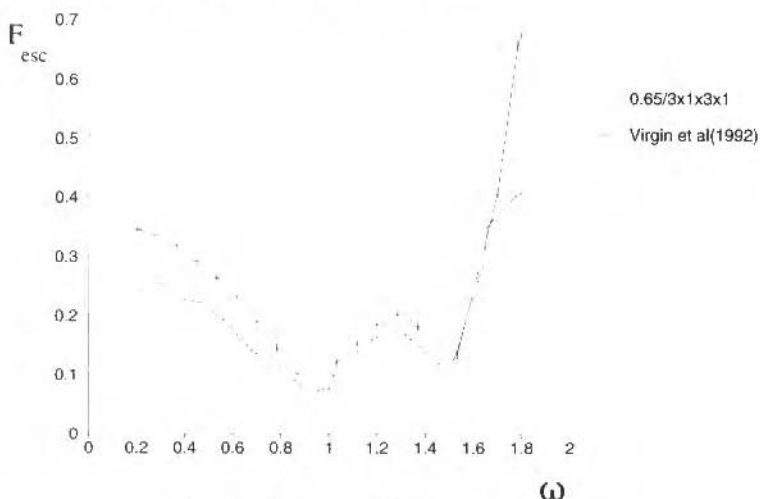


Fig. 13 Boundaries of safe motion for Eq. 7

The fact that significantly lower values of amplitude for escape can be obtained if we use starting points other than the minimum of the potential well signals to a possibly different process of safe basin erosion that may be operating at far-from-resonance conditions. This is a consequence of the fact that if a swift basin erosion process is in operation little difference is to be found between escape predictions from any starting point inside the original (i.e. unforced) safe basin.

Conclusions

We have described a simple and robust method of a coarse grid-of-starts to estimate boundaries of safe motion in the control parameter space of periodically forced nonlinear oscillators. One- and two-degree-of-freedom mathematical models of mechanical oscillators have been used in numerical sensitivity studies in which we have investigated the influence of the main parameters defining a grid of starts.

We have also performed a comparison between this method and results from the recent international literature. This comparison reveals good agreement between our results and those obtained by other researchers. The comparison also indicates that estimates of safe boundaries based on a single starting point, the stable minimum of potential energy, can be non-conservative, in the sense of overestimating minimum amplitudes of excitation that can lead to transient escape in far-from-resonance conditions.

The method presented here is devised as a straightforward yet effective procedure to generate a first estimate of regions of safe operation for forced nonlinear oscillators. Differently from other methods based on the use of large grids-of-starts, this method has been developed with special attention to experimental verification. The method can be implemented on personal computers of modest resources, and the predictions directly compared with experimental data. Also, it is not limited to the parameters of frequency and amplitude of forcing here investigated. On the contrary, any set of parameters can be chosen for analysis, and the corresponding boundaries of safe motion estimated in the control space defined by those parameters.

References

- Bishop, S.R. and de Souza, J.R., 1993. "Transient and steady-state operational limits for ship roll". *App. Mech. Rev.*, vol. 46, No 11, Part 2, pp. S47-S52.
- de Souza, J.R., 1995, "Geometrical methods of nonlinear dynamics in ship capsizing", Ph.D. Thesis, University College London, U.K.
- Kan, M., 1992, "Chaotic capsizing", 20th ITTC Seakeeping Committee Meeting, Osaka.
- Soliman, M.S and Thompson, J.M.T., 1989, "Integrity measures quantifying the erosion of smooth and fractal basins of attraction", *J. Sound and Vibration*, vol. 135, pp. 453-475.
- Soliman, M.S. and Thompson, J.M.T., 1991, "Transient and steady state analysis of capsize phenomena". *App. Ocean Research*, vol. 13, pp. 82-92.

- Thompson, J.M.T., 1989a, "Chaotic phenomena triggering escape from a potential well", Proc. R. Soc. London A, vol. 421, pp. 195-225.
- Thompson, J.M.T., 1989b, "Loss of engineering integrity due to the erosion of absolute and transient basin boundaries", Proceedings IUTAM Symposium 'Nonlinear Dynamics in Engineering Systems, Stuttgart.
- Thompson J.M.T. and de Souza, J.R., 1996, "Suppression of escape by resonant modal interactions: in shell vibration and heave-roll capsize", Proc. R. Soc. London A, vol. 452, pp. 2527-2550.
- Virgin, L.N., Plaut, R.H., and Ching-Chuan, C., 1992, "Prediction of escape from potential well under harmonic excitation", Int. J. Non-Linear Mech., vol. 27, No. 3, pp. 357-365.

Appendix

We collect here in Tables 1 to 3 the numerical details of the simulations used to generate the results of this paper.

Table 1 Numerical details for Fig. 1

Parameters of the Model	$\omega = 0.85 \beta = 0.05$
Parameters of the Grid	$(x_{inf}, x_{sup}, \dot{x}_{inf}, \dot{x}_{sup}) = (-1.2, 1.2, -1.0, 1.0)$ $(N_1, N_2) = (640, 480)$
Numerical Parameters	$\rho = T/80, m = 8, d_{esc} = 1.2$

Table 2 Numerical details for Fig. 2

Parameters of the Model	$\omega = 0.85 \beta = 0.05$
Parameters of the Grid	$(x_{inf}, x_{sup}, \dot{x}_{inf}, \dot{x}_{sup}) = (-1.2, 1.2, -1.0, 1.0)$ $(N_1, N_2) = (640, 480)$
Numerical Parameters	$\rho = T/80, m = 8, d_{esc} = 1.2$

Table 3 Main features of selected systems

Feature → Equation ↓	Reference	Parameters	Starting Points	Maximum Transient Duration	Escape Criterion
(3)	Soliman and Thompson (1991)	$\beta = 0.1$	$x = \dot{x} = 0$	32 T	$x \geq 20$
(3)	Virgin et al. (1992)	$\beta = 0.1$	$x = \dot{x} = 0$	30 T	$x > 1$
(4)	Virgin et al. (1992)	$\beta = 0.1$	$x = \dot{x} = 0$	30 T	$ x > 1$
(4)	Kan (1992)	$\beta = 0.04455$	$x = \dot{x} = 0$	20 T	$ x > 2$
(5)	Virgin et al. (1992)	$\beta = 0.1$ $\omega_0 = 139.93$ $\alpha_2 = 4132.7$ $\alpha_3 = 194.82$	$\dot{x} = \ddot{x} = 0$	30 T	$x < -7.143$
(6)	Soliman and Thompson (1991)	$\beta_1 = 0.0555$ $\beta_2 = 0.1659$ $c_1 = 0.2227$ $c_3 = -0.0694$ $c_5 = -0.0131$	$x = \dot{x} = 0$	16 T	$ x > 1.57$
(7)	Virgin et al (1992)	$\beta = 0.1$	$x_1 = x_2 = \dot{x}_1 = \dot{x}_2 = 0$	30 T	$\sqrt{x_1^2 + x_2^2} > 0.90$

On the Effect of Temperature in Non-Linear Dynamics of an Elasto-Plastic Oscillator With Isotropic Hardening

Marcelo Amorim Savi

Instituto Militar de Engenharia
Departamento de Engenharia Mecânica e de Materiais
22.290.270 Rio de Janeiro, RJ Brazil
savi@epq.lme.eb.br

Pedro Manuel Calas Lopes Pacheco

CEFET-RJ
Departamento de Engenharia Mecânica
20.271.110 Rio de Janeiro, RJ Brasil
calas@cefet-rj.br

Abstract

This contribution presents a dynamical analysis of an elasto-plastic oscillator where the thermomechanical coupling is considered. A constitutive model, used to describe the restitution force of the oscillator, is presented. Isotropic hardening is considered. The operator split technique is used to develop a numerical procedure. An integrator scheme associated with the return mapping algorithm is used to solve the equations of motion. Numerical simulations show that the effect of thermomechanical coupling may produce an unstable response.

Keywords: *Non-linear Dynamics, Elasto-plasticity, Modeling and Simulation.*

Introduction

The elasto-plastic behavior describes the deformation mechanisms of most metals and alloys at room temperature. The theories of elasticity and plasticity are both based on experimental studies of stress-strain relations in polycrystalline aggregate under simple load conditions. Hardening effect represents the way of how plastic strains modify the yield surface. It is a common situation and has many different ways to occur, depending specifically on the material considered. There are many idealized models to describe the hardening effect. A great number of situations involving cyclic loadings can be properly represented by isotropic hardening which corresponds to an uniform expansion of the yield surface (Lemaitre and Chaboche, 1990).

The hypothesis of isothermal process is usually adopted in dynamical analysis of metallic structures. For metallic components subjected to plastic cyclic loadings, however, part of plastic work is transformed into heat, resulting in a temperature rise which can affect substantially the mechanical behavior.

A feedback phenomenon can be promoted by the thermomechanical coupling. The heat generated by the mechanical process causes the increase of temperature which promotes the mechanical strength decrease. As a consequence, the amplitude of plastic strains tends to grow which causes a greater temperature rise and so on. This behavior only happens for some special conditions where an unstable behavior is expected.

This contribution reports a dynamic analysis of an elasto-plastic oscillator where the thermomechanical coupling is considered. The restitution force of the oscillator is considered by a constitutive model with internal variables where the coupling effects are introduced. Isotropic hardening is considered. A numerical method is developed using an implicit integration scheme associated with the return mapping algorithm. Operator split technique is used. Some numerical simulations are presented for forced vibrations and show that the isothermal hypothesis may be inadequate to describe some situations where cyclic inelastic deformations are involved.

Anisothermal Elasto-Plastic Model

A constitutive model to describe the elasto-plastic behavior is considered assuming an additive decomposition, *i.e.*, the total displacement x may be splitted into an elastic part, x^e , and a plastic part, x^p . Including temperature effects in the model, the force-displacement relation is given by the following equation:

$$p = K[(x - x^p) - \alpha_t L(\theta - \theta_0)] \quad (1)$$

where K is a stiffness parameter, α_t the thermal expansion coefficient, L is the total length, θ the absolute temperature and θ_0 the initial temperature of the elasto-plastic element.

The isotropic hardening is described by introducing an internal variable, α , referred to as *internal hardening variable*. A simple evolution equation for this variable considers that the hardening is linear in the amount of plastic flow, x^p and independent of the sign of this flow, *sign*(x^p) (Simo, 1994). This may be expressed by,

$$\dot{\alpha} = |\dot{x}^p| \quad (2)$$

Experimental observations establish that the plastic displacement has the following evolution equation (Simo, 1994):

$$\dot{x}^p = \dot{\gamma} L \text{sign}(p) \quad (3)$$

where $\dot{\gamma}$ represents the rate at which plastic deformation takes place and is called plasticity multiplier.

The elastic region is defined by the plasticity function (Simo and Miehe, 1992):

$$h(p, \alpha, \theta) = |p| - y(\alpha, \theta) \quad (4)$$

where

$$y(\alpha, \theta) = S \left[y_0 + (y_\infty - y_0) \left(1 - e^{-\frac{\delta \alpha}{L}} \right) + h_\alpha \frac{\alpha}{L} \right] \left[1 - h_\theta (\theta - \theta_{ref}) \right] \quad (5)$$

and y_0 , y_∞ , h_α , h_θ and δ are material parameters, θ_{ref} is a reference temperature associated with the initial temperature, θ_0 , and S the cross section area of the elasto-plastic element of the oscillator. The form of this hardening function shows that increasing the internal hardening variable causes elastic domain expansion, while increases in temperature causes the shrinkage of this domain.

The irreversible nature of plastic flow is represented by means of the *Kuhn-Tucker conditions* (Luengerger, 1973). Another constraint must be satisfied when $h(p, \alpha, \theta) = 0$. It is referred as *consistency condition* (Simo, 1994). These conditions are presented as follows:

$$\dot{\gamma} \geq 0$$

$$\dot{\gamma} h(p, \alpha, \theta) = 0 \quad (6)$$

$$\dot{\gamma} h(p, \alpha, \theta) = 0 \quad \text{if} \quad h(p, \alpha, \theta) = 0$$

Disregarding the source term, the energy equation can be written as (Pacheco, 1994):

$$\rho c_e \dot{\theta} = \frac{\chi p \dot{x}^p}{L S} - \frac{h_c S_p}{S} (\theta - \theta_0) \quad (7)$$

where ρ is the density, c_e the specific heat, h_c the convection parameter from the traditional hypothesis of fins and S_p the cross section perimeter of the elasto-plastic element of the oscillator. The first term on

the right side of the energy equation is called the internal thermomechanical coupling and is associated with the internal dissipation of the mechanical process. The empirical parameter χ is called heat conversion factor and indicates the amount of plastic power that is converted into heat (Pacheco, 1994).

Elasto-Plastic Oscillator

Considering a single degree of freedom oscillator with mass m and an external linear viscous dissipation parameter c , the balance of linear momentum is given by the equation,

$$m\ddot{x} + c\dot{x} + p(x, x^p, \alpha, \theta) = f(t), \quad (8)$$

where $p(x, x^p, \alpha, \theta)$ is the elasto-plastic restitution force of the oscillator and $f(t)$ is an external force.

Defining the variables $v = \dot{x}$ and $\omega_0^2 = K/m$, the following non-dimensional variables are used,

$$\tau = \omega_0 t; \quad \Omega = \omega / \omega_0; \quad P = p / (E S); \quad F = f / (E S);$$

$$X = x / L; \quad X^p = x^p / L; \quad V = v / (\omega_0 L); \quad A = \alpha / L; \quad T = \theta / \theta_{ref}; \quad (9)$$

where E is a material parameter. Considering $\mathbf{X} = (X, V, X^p, A, T)$, the equations of motion are like $\dot{\mathbf{X}} = \mathbf{F}(\mathbf{X}, \tau)$, $\mathbf{X} \in \mathfrak{R}^5$, associated with complementary conditions (6). Hence, assuming a periodic excitation $F(\tau) = F_0 \sin(\Omega\tau)$, it is possible to write the following equations of motion:

$$\dot{X} = V$$

$$\dot{V} = F_0 \sin(\Omega\tau) - c_0 V - (X - X^p) + A_T (T - I)$$

$$\dot{X}^p = \dot{\gamma} \text{sign}(P)$$

$$\dot{A} = \dot{\gamma} \quad (10)$$

$$\dot{T} = \varphi P \dot{X}^p - \xi(T - I)$$

$$h(P, A, T) = |P| - Y(A, T)$$

where

$$c_0 = \frac{c}{m \omega_0}$$

$$A_T = \alpha_r \theta_{ref}$$

$$\varphi = \frac{\chi E}{\rho c_e \theta_{ref}}$$

$$\xi = \frac{h_c S_p}{\rho c_e \omega_0 S}$$

$$\text{and } Y(A, T) = \frac{y(\alpha, \theta)}{ES} = \left[Y_0 + (Y_\infty - Y_0)(1 - e^{-\delta A}) + H_A A \right] [1 - H_T(T - I)] \quad (11)$$

$$\text{with } Y_0 = \frac{y_0}{E} ; Y_\infty = \frac{y_\infty}{E} ; H_A = \frac{h_\alpha}{E} ; H_T = h_\theta \theta_{ref}$$

Numerical Procedure

The numerical solution procedure here proposed, uses the operator split technique (Chorin et al., 1978; Ortiz, Pinsky and Taylor, 1983; Marchuk, 1975) to make the partition of the space of variables in two parts. One part is the phase plane and includes the variables (X, V) and the other one is the internal variables and temperature space and includes (X^c, A, T) . With this split, it is possible to develop a solution procedure by considering an iterative process where each part is treated separately.

The time integration of equations of motion on the phase plane can be done by any integration scheme, since the variables X^c , A and T are considered as known parameters. As a first trial, an elastic predictor step is assumed, where the value of X^c , A and T cannot vary from the previous time instant. The next step of the solution procedure consists in evaluating the feasibility of the trial state. Hence, the *return mapping algorithm* is considered (Simo and Taylor, 1985). Then it is necessary to return to phase plane equations and recalculate the pair (X, V) using the new values of the parameters X^c , A and T . This procedure must be repeated until it converges. This situation occurs when the difference between the actual and trial state reaches a prescribed tolerance.

Return Mapping Algorithm

At this point, a trial state (X_{n+1}, V_{n+1}) is known. This is considered as an input for the return mapping algorithm. A trial state is defined by considering an elastic predictor step, which is written as follows:

$$P_{n+1}^{trial} = (X_{n+1} - X_n^p) - \Lambda_T(T_n - I) \quad (12)$$

$$(X_{n+1}^p)^{trial} = X_n^p \quad (13)$$

$$A_{n+1}^{trial} = A_n \quad (14)$$

$$T_{n+1}^{trial} = T_n \quad (15)$$

$$h_{n+1}^{trial} = \left| P_{n+1}^{trial} \right| - Y(A_{n+1}^{trial}, T_{n+1}^{trial}) \quad (16)$$

If $h_{n+1}^{trial} \leq 0$, it means that the state is on the elastic domain and the trial state is the actual one.

Otherwise, if $h_{n+1}^{trial} > 0$, we are outside the elastic domain and a plastic step must be considered. This step is associated with the determination of the increment of plasticity multiplier ($\Delta\gamma$) on the time instant t_{n+1} , when the plasticity function $h(p, \alpha, \theta)$ must vanish. Using an implicit Euler algorithm to discretize the evolution Eqs. (1-3,7), the plastic step can be written as follows:

$$P_{n+1} = P_{n+1}^{trial} - \text{sign}(P_{n+1}^{trial}) (1 + \Lambda_T \varphi P_{n+1}^{trial}) \Delta\gamma + \Lambda_T \xi (T_{n+1}^{trial} - 1) \Delta\tau \quad (17)$$

$$X_{n+1}^p = (X_{n+1}^p)^{trial} + \text{sign}(P_{n+1}^{trial}) \Delta\gamma \quad (18)$$

$$A_{n+1} = A_{n+1}^{trial} + \Delta\gamma \quad (19)$$

$$T_{n+1} = T_{n+1}^{trial} + \varphi |P_{n+1}^{trial}| \Delta\gamma - \xi (T_{n+1}^{trial} - 1) \Delta\tau \quad (20)$$

$$\Delta\gamma = \frac{h_{n+1}^{trial} - [M_T - \Lambda_T \text{sign}(P_{n+1}^{trial})] \xi (T_{n+1}^{trial} - 1) \Delta\tau}{1 + \Lambda_T \varphi P_{n+1}^{trial} + M_A - M_T \varphi |P_{n+1}^{trial}|} \quad (21)$$

where

$$M_A = [1 - H_T (T_{n+1}^{trial} - 1)] \left[(Y_\infty - Y_0) \delta e^{-\delta A_{n+1}^{trial}} + H_A \right] \quad (22)$$

$$M_T = H_T \left[Y_0 + (Y_\infty - Y_0) (1 - e^{-\delta A_{n+1}^{trial}}) + H_A A_{n+1}^{trial} \right] \quad (23)$$

A recursive procedure is used to obtain the increment of plasticity multiplier. This process is repeated until this increment reaches a prescribed tolerance to guarantee the convergence to the yield surface. In spite of the strong non-linearities introduced by the thermomechanical coupling, the proposed return mapping algorithm treats the coupled mechanical and thermal equations simultaneously, which permits the use of relatively large time steps.

Numerical Simulations

This section presents some numerical simulations of the behavior of the elasto-plastic oscillator using the proposed procedure. Forced vibrations are considered. All simulations use the parameters presented in Table 1 (Simo and Miehe, 1992). Time steps less than $\Delta\tau = 2\pi / 800\Omega$ present a good convergence.

Table 1 Parameters of the Oscillator.

Y_0	2.143×10^{-3}
Y_{∞}	3.405×10^{-3}
H_A	6.152×10^{-4}
H_T	6.826×10^{-6}
χ	0.90
Λ_T	2.930×10^{-3}
δ	16.93
c_0	2000
φ	1.800×10^2
ξ	1.098×10^{-6}

A feedback phenomenon can be observed for some special conditions where an unstable behavior is expected. The thermomechanical coupling causes an increase in temperature which promotes mechanical strength decrease. As a consequence, the amplitude of plastic strains tends to grow causing a greater temperature rise and so on. It is important to identify these conditions because wrong predictions can be made and unexpected failures may occur if the thermomechanical effect is not included in the model.

Hence, we are interested to obtain the regions where some qualitative changes on dynamical system behavior occur as a consequence of parameter variations. That is, we are looking for possible bifurcations on the dynamical behavior of the oscillator.

A bifurcation analysis of the problem is now in focus. The variation of two different parameters are important to be considered: Driving force amplitude, F_0 , and frequency, Ω . A bifurcation diagram represents variations of stroboscopically sampled values of some variable under the slow quasi-static increase of the parameter in question (F_0 or Ω).

Figure 1 presents the bifurcation diagram showing the plastic displacement under the variation of driving force amplitude. Two different frequencies are considered: $\Omega = 0.1$ and $\Omega = 0.6$. The variables are sampled at $1/4$ of the period for the last 200 cycles of a 1000 cycles simulation. A driving force amplitude which causes a stable response is associated with only one point on the diagram. On the other hand, an amplitude associated with many points, represents an unstable response.

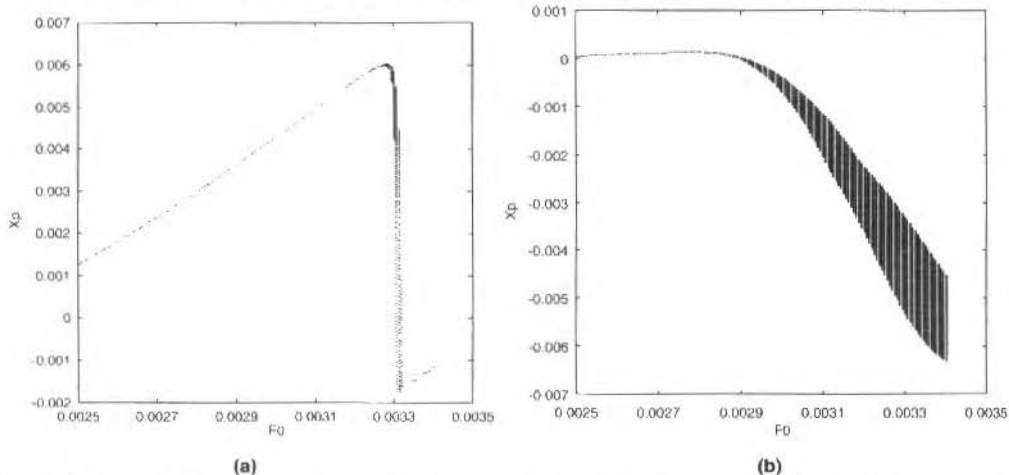


Fig. 1 Bifurcation diagram showing the plastic displacement under the variation of the driving force amplitude for (a) $\Omega = 0.1$ and (b) $\Omega = 0.6$.

Figure 2 presents the bifurcation diagram showing the plastic displacement under the variation of driving force frequency. Two different amplitudes are considered: $F_0 = 3.1e-3$ and $F_0 = 3.3e-3$. Again, the variables are sampled at $1/4$ of the period for the last 200 cycles of a 1000 cycles simulation. Frequency values associated with only one point are representative of stable responses while many points are associated unstable responses.

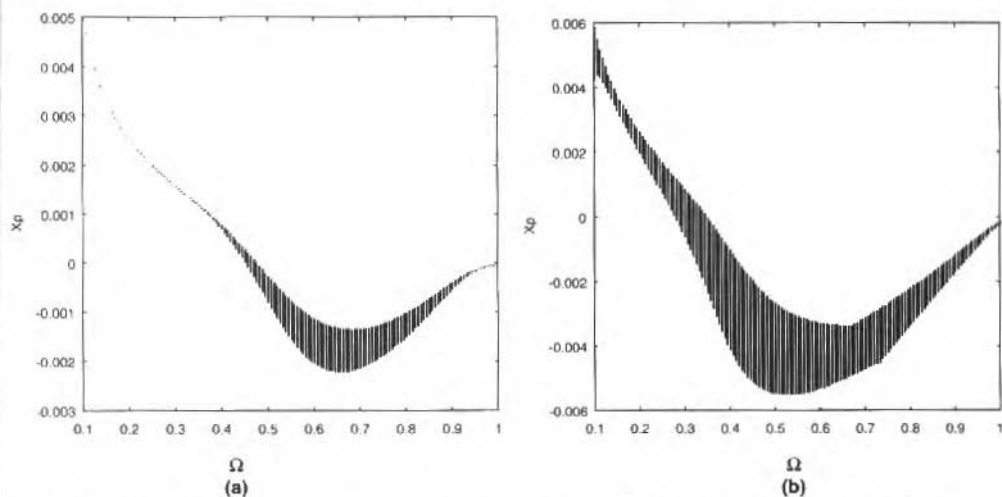


Fig. 2 Bifurcation diagram showing the plastic displacement under the variation of the driving force frequency for (a) $F_0 = 3.1e-3$ and (b) $F_0 = 3.3e-3$.

Now, some particular values of parameters F_0 and Ω are considered. First, consider $F_0 = 3.1e-3$. For this amplitude, $\Omega = 0.1$ corresponds to a stable response while $\Omega = 0.6$ is associated with an unstable behavior. This agrees with the behavior shown in Fig. 1-2. Figure 3 shows the plastic displacement time history. Fig. 3a shows the response for $\Omega = 0.1$ while Fig. 3b shows the response for $\Omega = 0.6$. Figure 4 shows the plastic displacement time history for $F_0 = 3.3e-3$ and the frequencies $\Omega = 0.1$ and $\Omega = 0.6$. Now, both situations present unstable responses, as indicated by Fig. 1-2.

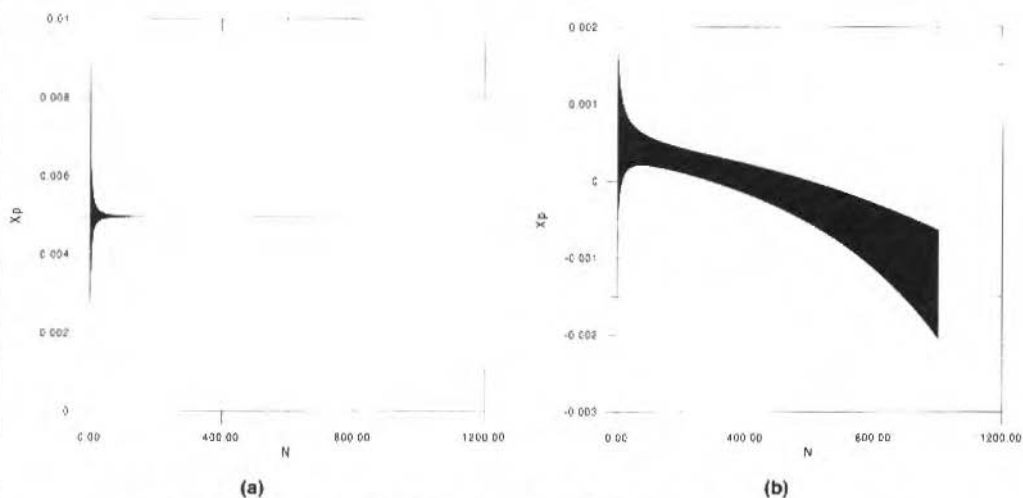


Fig. 3 Plastic displacement time history. (a) $F_0 = 3.1e-3$ and $\Omega = 0.1$; (b) $F_0 = 3.1e-3$ and $\Omega = 0.6$.

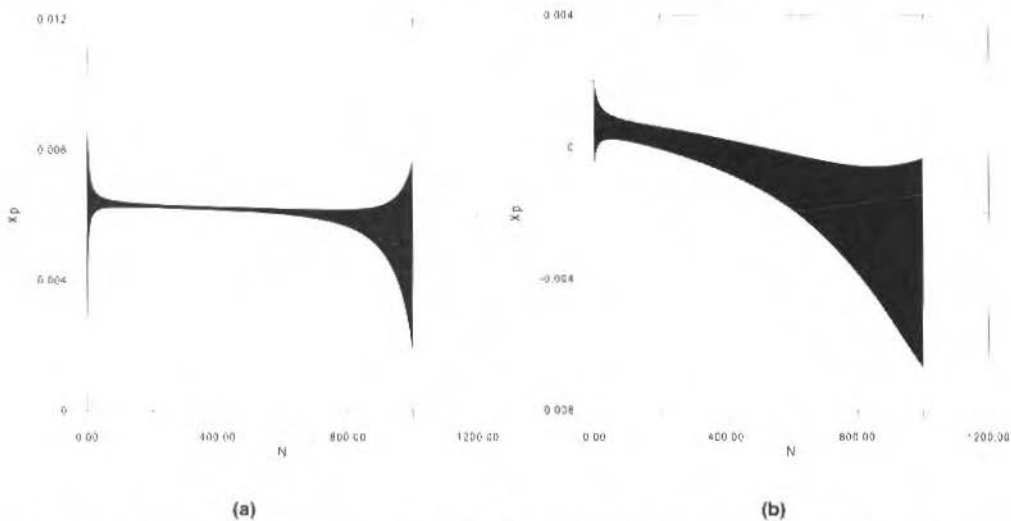


Fig. 4 Plastic displacement time history. (a) $F_0 = 3.3e-3$ and $\Omega = 0.1$; (b) $F_0 = 3.3e-3$ and $\Omega = 0.6$.

Figure 5 shows temperature, T , and yield function, Y , evolution for different pairs (F_0, Ω) . For the situations where an unstable response is present, anisothermal model predicts a continuous increase in temperature values which causes a decrease in the values of yield function. On the other hand, when a stable response is observed, the temperature and the yield function remain constant, after a short transient.

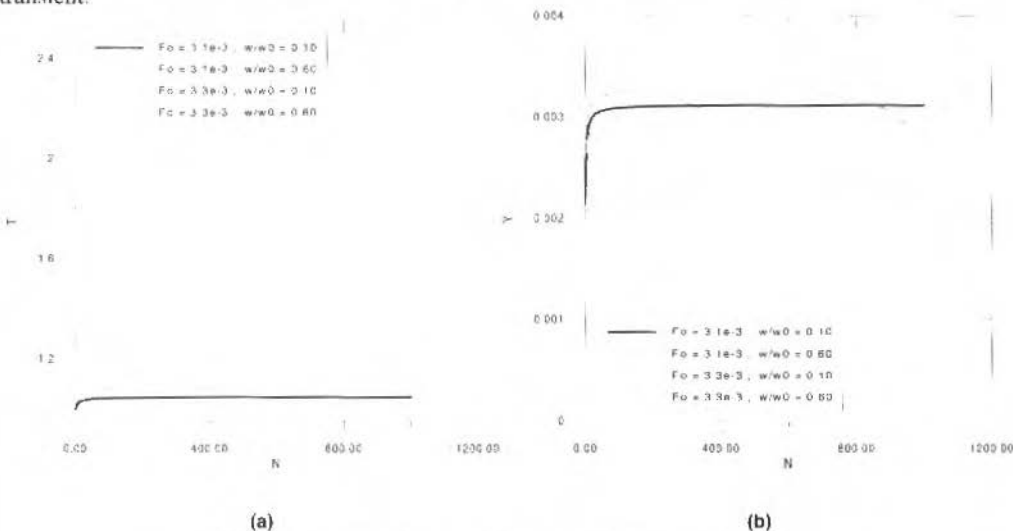


Fig. 5 (a) Temperature evolution; (b) Yield function evolution.

Let us consider a situation where an unstable behavior is expected, say $F_0 = 3.3e-3$ and $\Omega = 0.1$. Figure 6 presents the time history of the other variables of the problem, that is, total displacement, velocity, internal hardening variable and elasto-plastic restitution force. The internal hardening variable, A , evolution presents three distinct regions (Fig. 6c). On the initial region, the variable increases quickly. Then a second region is reached, and a smooth increase occurs. The third region presents a high rate growth. This last region is associated with unstable response. Similar behavior is presented by the temperature (Fig. 5a). Looking at the other variables (Fig. 6a,b,d), it is possible to identify the last region, where the amplitudes begin to vary considerably. Total displacement and velocity tends to

increase (Fig. 6a,b), while the restitution force tends to decrease (Fig. 6d). It is also possible to see that the average values do not vary significantly.

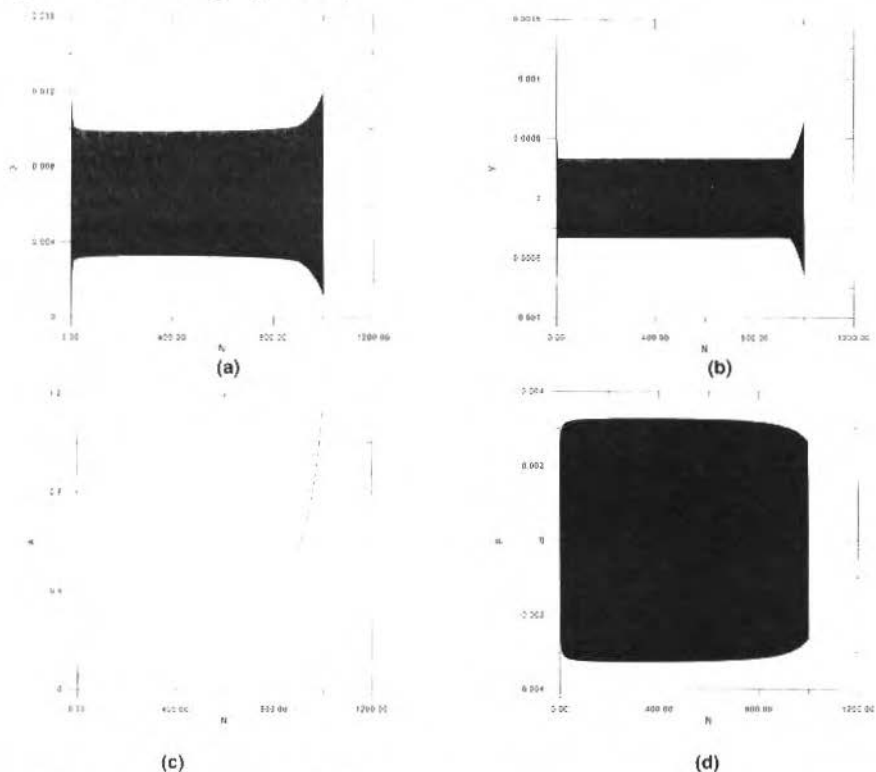


Fig. 6 (a) Total displacement evolution ; (b) Velocity evolution ; (c) Internal hardening variable evolution ; (d) Elasto-plastic restitution force evolution.

In the forthcoming analysis, some examples are considered in order to compare the isothermal and the anisothermal models. Figure 7 presents the total and plastic displacement evolutions, predicted by the isothermal model, when $F_0 = 3.3e-3$ and $\Omega = 0.1$. This Figure allows one to see that the isothermal model predicts a stable response while the anisothermal model predicts an unstable one, as shown in Fig. 4a.

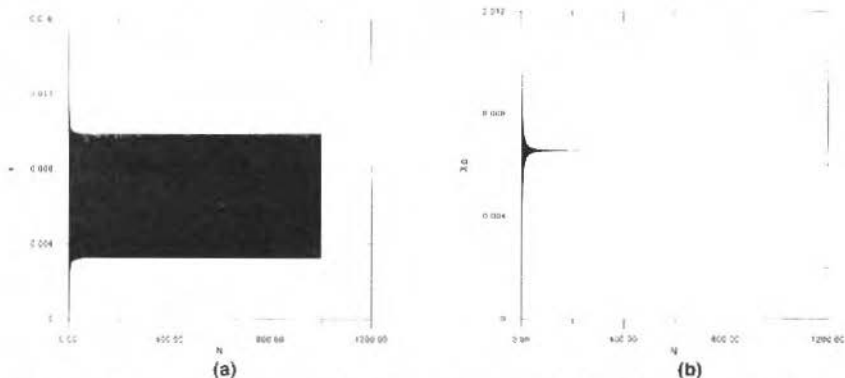


Fig. 7 (a) Total displacement ; (b) Plastic displacement evolution for the isothermal model.

Figure 8 shows the evolution of the internal hardening variable and the yield function for the two models. The unstable response observed in the anisothermal model can be associated to an increasing

evolution of the internal hardening variable (Fig. 8a) and to a softening behavior of the yield function (Fig. 8b). On the other hand, the stable response observed in the isothermal model is associated to a constant temperature causing a monotonically increasing evolution of both variables, followed by a stabilization.

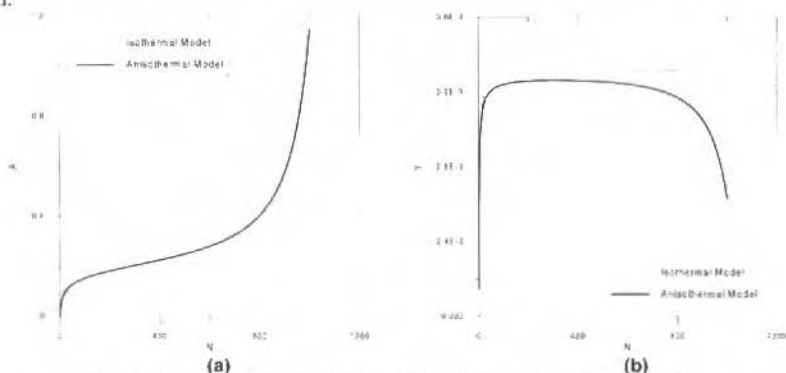


Fig. 8: (a) Isotropic hardening evolution; (b) Yield function evolution.

Figure 9 presents a comparison between the phase plane orbits on the last loading cycle for some of the preceding examples. Again, it is possible to observe the differences between the two models. Isothermal model predict orbits that remain the same when an elastic behavior is reached. On the other hand, when the unstable response is present, the anisothermal model predict a progressive expansion of the orbits (Fig. 9b,c,d). When a stable response is present, both models present the same behavior (Fig. 9a).

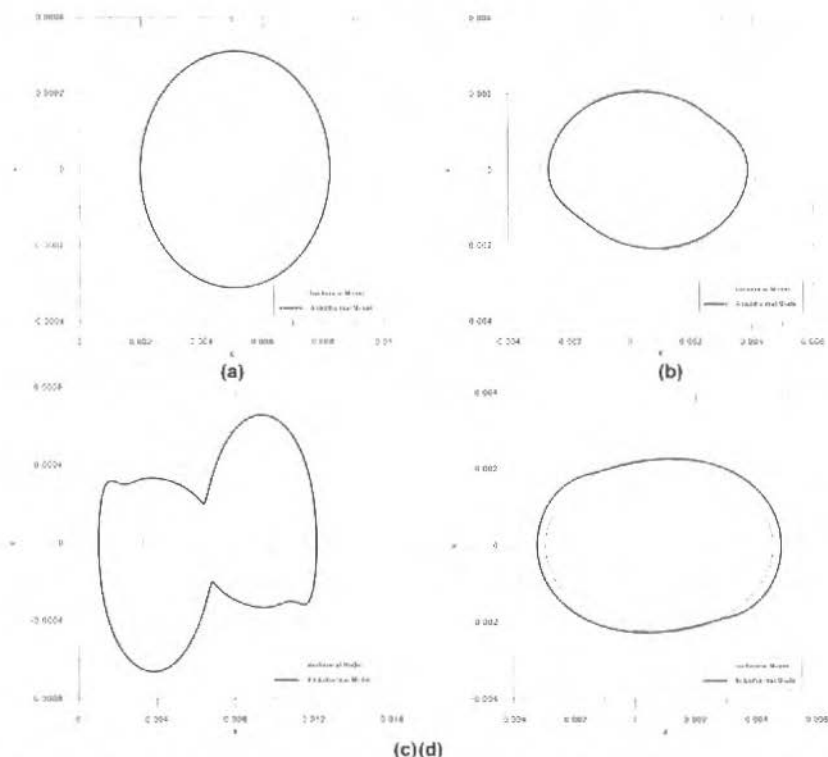


Fig. 9 Phase plane orbits predicted by isothermal and anisothermal models. (a) $F_0 = 3.1e-3$ and $\Omega = 0.1$; (b) $F_0 = 3.1e-3$ and $\Omega = 0.6$; (c) $F_0 = 3.3e-3$ and $\Omega = 0.1$; (d) $F_0 = 3.3e-3$ and $\Omega = 0.6$.

Conclusions

This contribution reports a dynamical analysis of an elasto-plastic oscillator where the thermomechanical coupling is considered. A constitutive model with isotropic hardening is presented. Operator split technique is used for the numerical solution. A numerical method is developed using an implicit integration scheme associated with the return mapping algorithm. The proposed return mapping algorithm treats the coupled mechanical and thermal equations simultaneously, which permits the use of relatively large time steps. Some numerical simulations show that the isothermal model, where thermomechanical coupling is not considered, tends to present an elastic stabilized response. On the other side, the numerical results obtained with the anisothermal model may present an unstable behavior to some special values of the parameters.

References

- Chorin, A., Hughes, T.J.R., McCracken, M.F. and Marsden, J.E., 1978, "Product Formulas and Numerical Algorithms", *Commun. Pure Appl. Math.*, 31, pp.205-256.
- Lemaitre, J. and Chaboche, J.L., 1990, "*Mechanics of Solids Materials*", Cambridge Univ. Press.
- Luenberger, D.G. (1973), "*Introduction to Linear and Nonlinear Programming*". Reading, Addison-Wesley.
- Marchuck, G.L., 1975, "*Methods of Numerical Analysis*". Springer-Verlag.
- Ortiz, M., Pinsky, P.M. and Taylor, R.L., 1983, "Operator Split Methods for the Numerical Solution of the Elastoplastic Dynamic Problem", *Computer Methods Appl. Mech. Eng.*, 39, pp.137-157.
- Pacheco, P.M.C.L., 1994, "*Analysis of the Thermomechanical Coupling in Elasto-viscoplastic Materials*". Doctoral Thesis, Dept. of Mechanical Engineering, PUC-Rio (in portuguese).
- Simo, J.C., 1994, "*Topics on the Numerical Analysis and Simulation of Plasticity*", Handbook of Numerical Analysis.
- Simo, J.C. and Miehe, C., 1992, "On the Coupled Thermomechanical Treatment of Necking Problems via Finite Element Methods", *J. of Appl. Methods in Eng.*, 33, pp.869-883.

A Time Dependent Adaptive Finite Element Method

Karl-Heinz Elmer
Hans Günther Natke

Universität Hannover
Curt-Risch-Institut
D-30167 Hannover, Germany
prof.natke@mbox.cri.uni-hannover.de

Abstract

The complexity of many realistic problems in transient dynamics requires very large systems. Reliable numerical FE-solutions with high accuracy need models with many degrees of freedom and many time steps. So time dependent adaptive FE-methods are developed to optimize the mesh and minimize the computational costs.

The moving wave front is used for a broad time dependent mesh refinement, based on intensity vectors and the speed of wave propagation (intensity indicator), several time steps in advance. The a-posteriori Zienkiewicz-Zhu error indicator controls the adaptive mesh refinement. An implicit-explicit algorithm for direct time integration is based upon operator splitting and mesh partitions. The algorithm avoids subcycling and uses the same time step for a coarse mesh and the local refined mesh.

Keywords: Adaptive FEM, Transient Dynamics

Introduction

Structural dynamic and vibration problems of continuous elastic systems are characterized by the assumption of 'standing waves' between the boundaries of the finite system. There is a local exchange of strain energy and kinetic energy. The dynamic response is a superposition of natural modes of the finite system with a location-dependent and a time-dependent term (Natke, 1989). Purely elastic behaviour of material means that the stress depends only on the local strain at each point of space and time, and total energy as the sum of kinetic and strain energy is conserved. Visco-elastic behaviour means that the total energy is no longer conserved but dissipated, and vibrations of systems with such material behaviour are damped.

On the other hand, wave propagation problems are characterized by the transport of energy through motions of particles about an equilibrium position. A local disturbance of a solid is radiated by traveling waves, and energy is transmitted into other parts of the finite or infinite continuous system, as is well-known from physical experience (Achenbach, 1980). Since the radiation leads to a distribution of energy over the whole system, traveling waves die away through radiation conditions in infinite systems, scattering and material damping.

In finite systems, traveling waves are reflected at the boundaries of the system. This leads to standing waves and to vibrations in finite systems as a superposition of waves traveling in the opposite propagation direction.

The wave equation thus describes not only transient wave propagation problems but all kinds of structural dynamic and vibration problems too.

The complexity of many realistic problems in transient dynamics requires very large numerical systems and finite element models. Nonlinear problems, three-dimensional problems, transient dynamic problems with a broad frequency range and wave propagation problems take up a large amount of computational time. To obtain reliable numerical solutions of transient dynamic problems in the time domain with high accuracy it is necessary to use models with many degrees of freedom and many time steps on high-performance computers.

Fast algorithms and programs for dynamic problems have to be developed to make efficient use of the new hardware features, to optimize time dependent finite element models and to minimize the computational time.

The idea of this paper is to apply the Zienkiewicz-Zhu error estimator (Zienkiewicz and Zhu, 1987) to wave propagation problems with h-adaptive time dependent FE-methods.

As local mesh refinement and system setup after each time step is very expensive, a method is developed to estimate all regions that are to be refined several time steps in advance. Then the a-posteriori Zienkiewicz-Zhu error estimator is only used to control if the refinement has been sufficient

or not. Knowing the expected direction of the energy flow from intensity vectors, the moving wave front allows a broad time dependent mesh refinement several time steps in advance.

Because of the high accuracy and small demand on computational time explicit time integration is used for all elements of the coarse mesh. To avoid subcycling on vector- and parallel-computers all parts of the mesh with local mesh refinement and a Courant-number larger than 1 are treated implicitly with the same time step using an implicit-explicit algorithm.

Adaptive FEM

The local approximation errors of a FE-solution can be described with the numerical approximation \hat{u} of the exact displacement vector u :

$$e_u = u - \hat{u} \quad (1)$$

or in terms of stresses:

$$e_\sigma = \sigma - \hat{\sigma} \quad (2)$$

The energy norm of the error is an integral scalar quantity of the domain Ω and is defined for elasticity problems in stresses as:

$$\|e\| = \left[\int_{\Omega} (\sigma - \hat{\sigma})^T D^{-1} (\sigma - \hat{\sigma}) d\Omega \right]^{1/2} \quad (3)$$

with the elasticity matrix D . This error is related to the strain energy of the problem. The approximation errors decrease as the size of the subdivision of the FE-mesh gets smaller with the so called h-refinement.

As in most cases the exact solutions of σ are not known, the error estimation after Zienkiewicz and Zhu (1987) uses an improved approximation $\hat{\sigma}^*$ (f.e. by averaging of discontinuous stresses $\hat{\sigma}$) and the errors in stresses are estimated errors:

$$e_\sigma = \sigma^* - \hat{\sigma} \quad (4)$$

In an optimal mesh the distribution of the local energy norm error $\|e\|_i$ of any element i should be equal between all elements. To achieve this each element i of the m elements is to be refined, if the local error $\|e\|_i$ is not smaller than the desired average error e_m :

$$\|e\|_i < \eta \left(\frac{\|\hat{\sigma}\|^2 + \|e\|^2}{m} \right)^{1/2} = e_m \quad (5)$$

with the desired relative percentage error η of the energy norm and the relation:

$$\|e\|^2 = \sum_{i=1}^m \|e\|_i^2 \quad (6)$$

In dynamic problems the total error of the problem consists of the error of the potential energy and the error of the kinetic energy.

$$E = E_p + E_k \quad (7)$$

An error estimate for semidiscrete hyperbolic problems is given in Hughes (1989) and Strang and Fix (1973). The exact displacement vector \mathbf{u} of an elliptic boundary value problem is a smooth function of class H^r with r square integrable generalized derivatives. The approximation \mathbf{u}^h yields an approximation error where

$$\|e\|_m \leq \|u - u^h\|_m \leq c \cdot h^\alpha \|u\|_r \quad (8)$$

denotes the error estimate of the elliptic boundary-value problem.

The factor c is a constant independent of \mathbf{u} and h , $\alpha = \min(k+1-m, r-m)$, k is the degree of the complete polynomial appearing in the element shape functions, m is the order of the highest derivatives appearing in the energy expression and h is the diameter of the largest element in the mesh as a scalar, characterizing the refinement of the finite element mesh. The norm $\|u\|_r$ is the H^r norm:

$$\|u\|_r = (u, u)_r^{\frac{1}{2}} \quad (9)$$

using the H^r inner product

$$(u, v)_r = \int_{\Omega} (u_i v_i + u_{i,j} v_{i,j} + u_{i,j,k} v_{i,j,k} + \dots) d\Omega < \infty$$

The error expression describes the convergence of \mathbf{u}^h to \mathbf{u} in the H^m norm as $h \rightarrow 0$. The error estimate for semidiscrete hyperbolic problems is based on the error of the total energy.

The expression

$$E(u, \dot{u}) = \frac{1}{2} [(\dot{u}, \rho \dot{u}) + a(u, u)] \quad (11)$$

denotes the total energy of the problem where (\cdot, \cdot) is a linearform and $a(\cdot, \cdot)$ is a symmetric bilinearform. The square root of E defines a norm equivalent to the $H^m \times L_2$ norm for hyperbolic problems of order $2m$. So the norm of the energy error is:

$$E(e(t), \dot{e}(t))^2 \leq c \{ h^\nu [\|u(0)\|_{k+l} + \|u(t)\|_{k+l}] + h^\mu [\|\dot{u}(0)\|_{k+l} + \|\dot{u}(t)\|_{k+l}] \int_0^t \|\ddot{u}(\tau)\|_{k+l} d\tau \} \quad (12)$$

For each fixed t , the terms in square brackets are bounded according to the inner product definition. Thus $E(e(t), \dot{e}(t))^{1/2} \rightarrow 0$ as the mesh size $h \rightarrow 0$ in a refined FE-mesh.

The term with h^μ concerns to the kinetic energy. Because $\nu < \mu$ and $m = 1$ for the hyperbolic wave propagation problems the term h^μ of the kinetic energy is one order smaller than h^ν of the potential energy. Thus the rate of convergence of the total energy is ν and mainly dependent on the potential energy in the case of mesh refinements.

Therefore the Zienkiewicz-Zhu error estimator is also applicable to hyperbolic problems with time dependent adaptive mesh refinement.

Intensity Indicator

As most of the computational time is wasted with mesh refinement procedures and expensive system setup, a method is developed (Elmer, 1996) to estimate all elements and regions that are to be refined, several time steps in advance. The expected direction of the energy flow and the propagation of

the different kind of waves in 2- and 3-dimensional systems can be described by intensity vectors and the moving wave front can be used for a broad time dependent mesh refinement in advance.

The intensity of a wave field shows the transport of energy per time and area. The intensity vector gives informations about the local change of energy and the direction of energy flow.

The total energy E of a domain Ω consists of the potential energy E_p and the kinetic energy E_k :

$$E = E_p + E_k \quad (13)$$

with the potential energy

$$E_p = \frac{1}{2} \int_{\Omega} c_{ijkl} u_{i,j} u_{k,l} d\Omega, \quad (14)$$

the kinetic energy

$$E_k = \frac{1}{2} \int_{\Omega} \rho \dot{u}_i \dot{u}_i d\Omega, \quad (15)$$

and the elastic tensor c_{ijkl} (Achenbach, 1980) the power of the wave front is:

$$\frac{\partial E}{\partial t} = \int_{\Omega} (\dot{t} \dot{u}_i \dot{u}_i + c_{ijkl} \dot{u}_{i,j} \dot{u}_{k,l}) d\Omega \quad (16)$$

Together with the fundamental equation:

$$\rho \ddot{u}_i = \sigma_{ij,j} = \sigma_{ji,j} \quad (17)$$

and Hooke's law

$$c_{ijkl} u_{l,k} = \sigma_{ij} = \sigma_{ji} \quad (18)$$

the equation (16) yields:

$$\frac{\partial E}{\partial t} = \int_{\Omega} (\sigma_{ij,j} \dot{u}_i + \sigma_{ij} \dot{u}_{i,j}) d\Omega \quad (19)$$

$$= \int_{\Omega} (\sigma_{ij} \dot{u}_i)_{,j} d\Omega \quad (20)$$

With the definition (Elmer, 1996) of the component I_j of the intensity vector \mathbf{I} :

$$I_j = -\sigma_{ij} \dot{u}_i \quad (21)$$

it follows

$$\frac{\partial E}{\partial t} = - \int_{\Omega} I_{j,j} d\Omega \quad (22)$$

In the case of stationary processes it is usual to use mean values of time averages. For transient dynamic problems and wave propagation problems it is more suitable to use the instantaneous intensity vector.

The intensity components I_x , I_y and I_z of element k of a 3-dimensional FE-model are:

$$\begin{bmatrix} I_x \\ I_y \\ I_z \end{bmatrix}_k = - \begin{bmatrix} \sigma_x & \tau_{xy} & \tau_{xz} \\ \tau_{yx} & \sigma_y & \tau_{yz} \\ \tau_{zx} & \tau_{zy} & \sigma_z \end{bmatrix}_k \cdot \begin{bmatrix} \dot{u}_x \\ \dot{u}_y \\ \dot{u}_z \end{bmatrix}_k \quad (23)$$

In the x-direction this is:

$$I_x^k = - (\sigma_x \dot{u}_x + \tau_{xy} \dot{u}_y + \tau_{xz} \dot{u}_z)_k \quad (24)$$

These intensity components describe the direction of the instantaneous energy flow of each element.

The wave front propagates in this direction in the next time steps and also the zone with mesh refinements. This allows to estimate the zone with all elements that are to be refined several time steps in advance. With the maximum wave propagation velocity c_L

$$c_L = \sqrt{\frac{E(1-\nu)}{\rho(1-\nu-2\nu^2)}} \quad (25)$$

the propagation of the refinement zone is

$$s_n = c_L \cdot n_{step} \cdot \Delta t \quad (26)$$

The a-posteriori Zienkiewicz-Zhu error indicator is only used to control if the refinement is sufficient or not. This does not lead to optimized FE-meshes, like meshes of adaptive FE-methods for static problems, but it saves a lot of computational time, if the estimated mesh is sufficient for several time steps.

A broad time dependent mesh refinement for several time steps is more efficient than several steps of mesh refinement.

Time Integration

Starting with a coarse reference mesh and a time step based upon the maximum frequency of the load spectrum, explicit time integration is used because of high accuracy and only small amount on computational time.

After every time step the Zienkiewicz-Zhu error indicator leads to local mesh refinement and an optimized FE-mesh with an equal distribution of the energy norm between all elements. Refined parts of the mesh with small elements and the Courant-number larger than 1 are to be treated with a smaller time step to keep numerical stability of the solution. As implicit time integration with the possibility of larger time steps avoids subcycling an implicit-explicit algorithm is used based upon operator splitting and mesh partitions.

The algorithm (Hughes, 1989) allows part of the mesh with local mesh refinement to be treated implicitly with the Newmark method and part of the original coarse mesh to be treated explicitly with a predictor-corrector method. This avoids unefficient subcycling on vector- and parallel-computers (Elmer, 1996).

The solution of the initial value problem of the semidiscrete equation of motion

$$M\ddot{u} + C\dot{u} + Ku = F \quad (27)$$

of finite element procedures is the displacement $\mathbf{u} = \mathbf{u}(t)$ that fulfills the differential equation and the initial conditions.

Time integration procedures only consider the differential equation at discrete times t_n with the approximations \mathbf{u}_n , \mathbf{v}_n and \mathbf{a}_n for the functions $\mathbf{u}(t)$, $\dot{\mathbf{u}}(t_n)$ and $\ddot{\mathbf{u}}(t_n)$ and an approximation error depending on the difference procedure (Natge, 1989).

The new solution at the time step t_{n+1} is:

$$M\mathbf{a}_{n+1} + C\mathbf{v}_{n+1} + K\mathbf{u}_{n+1} = \mathbf{F}_{n+1} \quad (28)$$

The unknown acceleration \mathbf{a}_{n+1} of the implicit scheme results from the solution of the equation

$$(M + \gamma\Delta t C + \beta\Delta t^2 K)\mathbf{a}_{n+1} = \mathbf{F}_{n+1} - C\tilde{\mathbf{v}}_{n+1} - K\tilde{\mathbf{u}}_{n+1} \quad (29)$$

with the predictor terms $\tilde{\mathbf{u}}_{n+1}$ and $\tilde{\mathbf{v}}_{n+1}$. The unknown velocity \mathbf{v}_{n+1} and displacement \mathbf{u}_{n+1} are calculated after this with a corrector step.

For $\beta = 0$ and $\gamma = 1/2$ the Newmark predictor-corrector scheme becomes an explicit scheme identical to the central difference method with the temporally discrete equation of motion

$$M\mathbf{a}_{n+1} + C\tilde{\mathbf{v}}_{n+1} + K\tilde{\mathbf{u}}_{n+1} = \mathbf{F}_{n+1}$$

with the diagonal matrix \mathbf{M} .

As long as \mathbf{M} is diagonal, \mathbf{a}_{n+1} may be determined from this without solving equations, and a corrector step is inapplicable.

The implementation of the Newmark method as an implicit-explicit scheme allows part of the mesh to be treated implicitly and part to be treated explicitly (Hughes, 1989). This has considerable practical advantages in that 'stiff' subdomains of large finite element models can be treated economically with an implicit integrator if the Courant number is larger than 1. When using the implicit-explicit method the elements of a finite element model are divided into two groups: the implicit elements and the explicit elements. The system matrices contain explicit and implicit groups with the equation of motion

$$M\mathbf{a}_{n+1} + C^I\mathbf{v}_{n+1} + C^E\tilde{\mathbf{v}}_{n+1} + K^I\mathbf{u}_{n+1} + K^E\tilde{\mathbf{u}}_{n+1} = \mathbf{F}_{n+1} \quad (31)$$

where the implicit arrays multiply corrector values, whereas explicit arrays multiply predictor values.

It is an advantage especially on high-performance computers like vector- and parallel-computers to use the same time step for the whole system without subcycling. On vector-computers subcycling means additional calculations on a part of the whole mesh with short vector length and on parallel-computers domain decomposition with local subcycling and data dependency is not very efficient.

Example

A local disturbance within a continuous system causes dilatational waves (P-waves) and equivoluminal shear waves (S-waves), which separate according to their different propagation velocity $c_p \neq c_s$. The propagation velocity c_p of P-waves is

$$c_p = \sqrt{\frac{\lambda + 2\mu}{\rho}} \quad (32)$$

with the Lamé constants

$$\lambda = \frac{\nu E}{(1 + \nu)(1 - 2\nu)} \quad (33)$$

$$\mu = \frac{E}{2(1 + \nu)} = G \quad (34)$$

and the propagation velocity c_s of shear waves is

$$c_s = \sqrt{\frac{\mu}{\rho}} \quad (35)$$

Both kind of waves, the P-wave and the S-wave, are body waves and have to be considered in order to satisfy the boundary conditions of the plane surface or interface. Normal stresses and shear stresses vanish at the free surface and produce another kind of wave, the Rayleigh wave (R-wave), whose activity is confined to the neighbourhood of a free surface. The Rayleigh wave has the smallest amplitude decay with the distance of propagation and is the most important wave in soil dynamic problems like earthquake engineering and vibration control.

The soil dynamic problem simulates the propagation of mechanical waves induced by a transient pulse load of $P = 2.5\text{kN}$ of 0.05s duration on the elastic half plane. The following numerical values are adopted for the material constants of the problem:

$$E = 1 \cdot 10^8 \text{ N/m}^2$$

$$\nu = 0.4$$

$$\rho = 1.9 \cdot 10^3 \text{ kg/m}^3$$

$$c_p = 336\text{m/s}$$

$$c_s = 137\text{m/s}$$

The system has a rectangular excavation that influences the propagation of the different kind of waves. The FE-mesh covers a section of $100 \cdot 50\text{m}$. Adaptive mesh refinement is used every 10 time steps in advance with the intensity indicator, and a-posteriori with the Zienkiewicz-Zhu error indicator.

The initial FE-model is a coarse mesh of 289 nodes and 515 isoparametric elements. The energy norm error is set to be less than 15 % for all time steps. In accordance with the critical time step the time increment Δt used in the explicit time integration procedure must obey the following formula

$$\Delta t \leq \frac{\min \Delta l}{c_p} \quad (36)$$

with the minimum mesh size Δl of the coarse mesh and is set to 0.001s . Figure 1 shows the time dependent adaptive mesh after 50 time steps with 643 nodes and 1,191 elements with refined elements

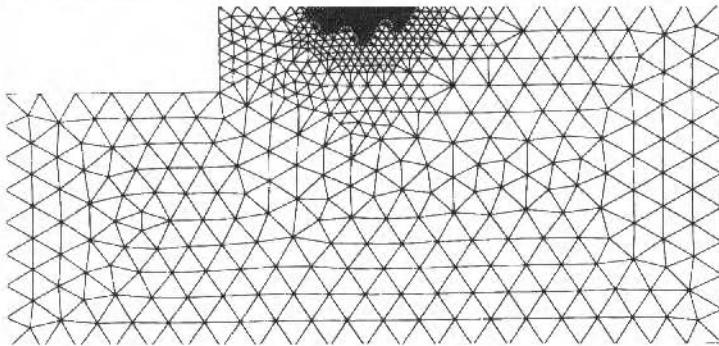


Fig. 1 Adaptive mesh refinement near the point of load after 50 time steps with 643 nodes and 1,191 elements below the driving point of the load. After 200 time steps the adaptive FE-system shows 3,021 nodes and 5,896 elements in Fig. 2 with refined regions, mainly due to the Rayleigh waves and the shear

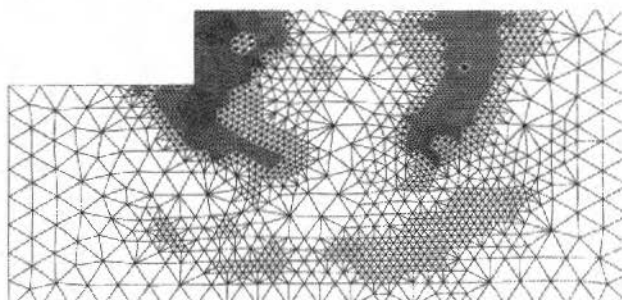


Fig. 2 Adaptive mesh refinement after 200 time steps with 3,021 nodes and 5,896 elements

waves. The instantaneous intensity vectors of Fig. 3 visualize the energy flow at that time with the

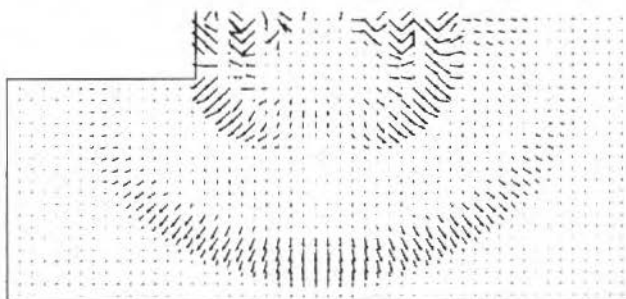
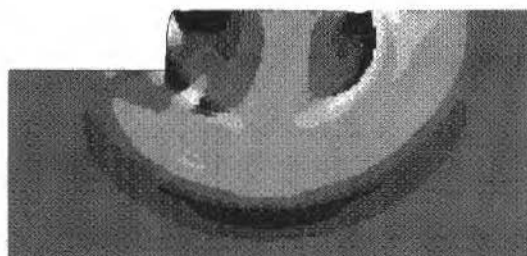


Fig. 3 Energy flow with intensity vectors after 200 time steps

influence of the dilatational wave, the shear wave and the Rayleigh waves below the surface. The simulation in Fig 4 and the reflections at the excavation shows the amplitudes of principal stresses with respect to the sign.



-11. 0. 11.

Fig. 4 Principal stresses with respect to the sign in N/m^2

It is obvious that this adaptive FE-method with a-priori intensity indicator after every 10 time steps does not lead to optimized FE-meshes with an equal distribution of the discretization error but it is a very efficient solution method if the estimated mesh is sufficient for several time steps. The demand on CPU-time and on storage depends on the number of degrees of freedom of the system.

The costs of the adaptive solution compared to a solution of a full refined system (=100 %) depends on the number of intermediate time steps between the steps of mesh refinement. Figure 5 shows that adaptive mesh refinement after each time step is inefficient but leads to optimal meshes.

There is a minimum of CPU-time in this example when using about 5 intermediate time steps with only 3,021 nodes instead of 7,803 of a conventional solution.

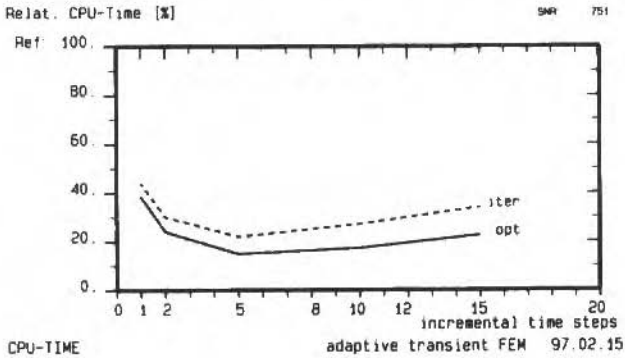


Fig. 5 CPU-time of the adaptive solution is down to 15 % of a conventional solution

Acknowledgments

The work was supported by the German Research Society DFG.

References

- Achenbach, J.D., 1980. "Wave Propagation in Elastic Solids", North-Holland Publishing Company, Amsterdam, New York, Oxford.
- Elmer, K.-H., 1996. "Optimierung numerischer FE-Modelle zur Simulation der Wellenausbreitung mit Vektor- und Parallelrechnern (Optimization of Numerical FE-Models for Simulating Wave Propagation on Vector and Parallel Computers)", DFG-Report NA 139/17-2, Curt-Risch-Institut, Hannover.
- Hughes, T.J.R., 1989. "The Finite Element Method", Prentice-Hall, Englewood Cliffs, N.J.
- Natke, H.G., 1989. "Baudynamik", B.G. Teubner, Stuttgart.
- Strang, G. and G.J.Fix., 1973, "An Analysis of the Finite Element Methods, Prentice-Hall", Englewood Cliffs, N.J.
- Zienkiewicz, O.C. and J.Z. Zhu, 1987, "A Simple Error Estimator and Adaptive Procedure for Practical Engineering Analysis", Int. J. Numer. Methods Eng., 24, 333-357.

On the Application of Flight Simulation to the Investigation of Helicopter Accidents

Olympio A. F. Mello

Instituto de Aeronáutica e Espaço
Centro Técnico Aeroespacial
12228-904 São José dos Campos, SP Brazil
oamello@iae.cta.br

Abstract

Two applications of flight simulation to the investigation of helicopter accidents are presented. In the first, an accident with typical tail rotor loss characteristics is considered. The investigation board worked on two hypotheses, namely tail rotor shaft failure and pilot's loss of pedal control after he suddenly increased the collective pitch near the ground and delayed applying pedals as needed. A simulation was conducted using simple models of yaw dynamics and tail rotor aerodynamics, and results indicated that pedal control would still be available even with a three second pilot delay in applying the pedals, therefore the hypothesis of loss of pedal control was discarded. In the second application, a helicopter accident at sea in which the aircraft wreck had not been recovered is considered. In that case, the investigation board had to rely on information from the Cockpit Voice/Flight Data Recorder (CVFDR) and a video recorded by an undersea robot. The most significant information obtained from the FDR were extremely high vibrations in all three axes, at a frequency associated with the first harmonic of main rotor rotational speed. The investigation was directed towards several hypotheses associated with main rotor blade and assemblies that might explain the vibrations. A simulation program based on an existing general helicopter flight simulation code was developed and simulations were conducted for the assumed blade failure hypotheses. Results indicated that the excessive accelerations were consistent with the loss of a large rotating mass, due to blade fracture near the root. In both applications, simulation provided substantial grounds for the investigation boards to establish the most probable causes for the accidents.

Keywords: Helicopter, Aeronautical Accident, Flight Simulation, Flight Dynamics.

Introduction

When investigating helicopter accidents - or any aeronautical accident - it is not unusual to come to questions that can only be answered by flight simulation. However, in many cases these simulations are not straightforward, as simulation programs are not often developed with the capability to simulate failure hypotheses, which may vary widely.

In this paper, two examples of application of simulation programs to the investigation of helicopter accidents are presented. In the first case, an accident with typical tail rotor loss characteristics occurred, but the tail rotor blades left marks on the ground which suggested that the tail rotor was still spinning. This evidence raised an alternate possibility that the accident might have occurred due to the pilot's delay in applying pedals during the flare maneuver. In order to investigate both hypotheses, a very simple model was developed to simulate yaw dynamics and tail rotor rotational speed decrease after tail rotor shaft failure.

In the second application, a helicopter had crashed on the sea surface after suffering excessive vibrations. Only the flight data and cockpit voice recorders were retrieved, and the investigators had to rely on simulation to establish possible causes for the accident. For this investigation, a more detailed simulation code, based on an existing program, was developed in order to simulate several hypotheses associated with failures in the main rotor blades and assemblies.

Tail Rotor Loss

After a helicopter accident¹ with typical tail rotor loss characteristics, it was suggested that the accident might have occurred due to pilot's loss of pedal control after he suddenly increased the collective pitch near the ground and delayed applying pedals as needed. This possibility was apparently supported by marks left on the ground indicating that the tail rotor was still spinning when it hit the

¹ Specific accident details, such as date and aircraft, are not given in order to preserve investigation confidentiality.

ground. The investigation board established two working hypotheses, namely loss of pedal control due to excessive pilot delay and loss of tail rotor due to shaft failure.

In order to investigate the first hypothesis, a numerical simulation of aircraft yaw dynamics without loss of tail rotor rotational speed was performed. In order to investigate the second hypothesis, a numerical simulation of aircraft yaw dynamics coupled with tail rotor blade rotation dynamics was performed. In both cases, the helicopter was assumed trimmed in hover with main rotor torque at 45%. The sudden increase in collective pitch was modeled by a corresponding sudden increase in main rotor torque from 45% to 95%, applied during a one second ramp, after which the torque remained constant at 95%. For the second hypothesis, it was assumed that shaft failure occurred at the same time the increase in collective pitch started.

For the simulation of both hypotheses, simple models of the aircraft yaw dynamics and tail rotor aerodynamics were used. In the tail rotor loss case, a model for blade rotation dynamics was also used. These models will be discussed next.

Simulation Model

The yaw equation of motion was obtained by considering main rotor torque, aircraft yaw inertia, tail rotor thrust and vertical empennage drag. Fig. 1 illustrates the conventions used here.

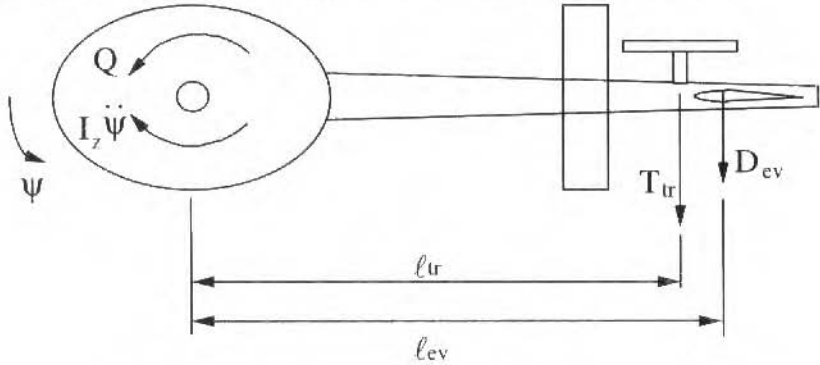


Fig. 1 Contributing Forces and Moments for Yaw Dynamics

The governing equation for yaw dynamics used here is:

$$Q_{mr} - I_z \ddot{\psi} - T_{tr} \ell_{tr} - D_{ev} \ell_{ev} = 0 \quad (1)$$

where $Q_{mr} = Q_{mr}(t)$ is the main rotor torque, I_z is the helicopter yaw moment of inertia with respect to the main rotor axis, ψ is the yaw angle, $T_v = T_v(\psi)$ is the tail rotor thrust, l_v is the distance between the main and tail rotor axes, $D_{ev} = D_{ev}(\psi)$ is the vertical empennage drag and l_v is the distance between the vertical empennage center of pressure and the main rotor axis. Note that, in the above equation, fuselage drag has been neglected, as the main contribution in terms of yaw moment is due to the vertical empennage drag.

As mentioned above, the helicopter was assumed initially trimmed in hover with main rotor torque at 45%. The sudden increase in collective pitch was modeled by a corresponding sudden increase in main rotor torque from 45% to 95%, applied during a one second ramp, after which the torque remained constant at 95%.

If the pilot increases collective pitch without adjusting the pedals accordingly, the helicopter enters yaw motion due to low tail rotor thrust. In this condition, the tail rotor operates in a way similar to a main rotor in descent. The treatment presented here uses this analogy. An equivalent "vertical" rotor velocity (positive when rotor is climbing) due to the yaw movement is $V = -l_r \dot{\psi}$.

The tail rotor operating regime in this equivalent descent depends on this equivalent "vertical" velocity. It may be normal operating state, vortex ring/turbulent wake state or windmill brake state (Gessow and Myers, 1952). The state in which the tail rotor operates may be established from the ratio

V/v_h , where v_h is the induced velocity in "hover", which corresponds here to the induced velocity for zero yaw speed, given by:

$$v_h = \Omega_{tr} R_{tr} \sqrt{\frac{C_{Ttr}}{2}} \quad (2)$$

where Ω_{tr} is the tail rotor angular velocity, R_{tr} is the tail rotor radius and C_{Ttr} is the tail rotor thrust coefficient. The tail rotor operating state is established as follows:

- (a) if $V/v_h \geq -1$, normal operating state;
- (b) if $-2 < V/v_h < -1$, vortex ring/turbulent wake state;
- (c) if $V/v_h \leq -2$, windmill brake state.

For all tail rotor operating states, a blade element approach is used. The blade is divided into sections (elements), for which aerodynamic forces are calculated and summed up to yield tail rotor thrust and thrust coefficient. In order to compute lift and drag coefficients, the induced velocity v_i at a given section is needed. The computation of this velocity has to be performed in a specific manner for each operating state. For normal operating state, combined momentum and blade element theories give:

$$\lambda = \left(\frac{\lambda_c}{2} \frac{\sigma a}{16} \right) + \sqrt{\left(\frac{\lambda_c}{2} \frac{\sigma a}{16} \right)^2 + \frac{\sigma a \theta_{tr} r}{8}} \quad (3)$$

where $\lambda = (V + v_i) / \Omega_{tr} R_{tr}$ is the total inflow ratio, $\lambda_c = V / \Omega_{tr} R_{tr}$ is the climb inflow ratio, $\sigma = N_{btr} c_r / \pi R_{tr}$ is the solidity ratio, a is the mean blade section lift curve slope, N_{btr} is the number of blades, c_r is the chord, θ_{tr} is the pitch angle and r is the section radial location. From Eq. (3) and the definition of λ , v_i may be obtained:

$$v_i = \lambda_i \Omega_{tr} R_{tr} = (\lambda - \lambda_c) \Omega_{tr} R_{tr} \quad (4)$$

where λ_i is the induced inflow ratio. For vortex ring/turbulent wake state, no theory yields a simple expression for the mean induced velocity. Therefore, the following empirical formula (Johnson, 1980) is used:

$$v_i = v_h \left(\frac{V}{v_h} \right) \left[0.373 \left(\frac{V}{v_h} \right)^2 - 1.991 \right] \quad (5)$$

For windmill break state, momentum theory gives the mean induced velocity as:

$$v_i = -\frac{V}{2} \sqrt{\left(\frac{V}{2} \right)^2 - v_h^2} \quad (6)$$

Once the induced velocity is computed using either Eqs. (4), (5) or (6), depending on the tail rotor operating state, one may obtain the induced angle at a given element $\phi = \tan^{-1} (U_P / U_T)$, where $U_P = V + v_i$ is the velocity normal to the blade and $U_T = \Omega_{tr} r$ is the velocity tangential to the blade. The blade effective angle of attack is then given by $\alpha = \theta_{tr} - \phi$.

Section lift (c_l) and drag (c_d) coefficients are obtained from experimental data (Sadler, 1972). From these coefficients, blade element lift, drag and the resulting contribution to normal force may be computed:

$$dF_z = (c_l \cos \phi - c_d \sin \phi) \frac{\rho U^2 c_r}{2} dr \quad (7)$$

where $U = \sqrt{U_T^2 + U_P^2}$ is the total blade section velocity and ρ is the air density. Integration of these contributions along the blade gives the total blade normal force and consequently tail rotor thrust and thrust coefficient:

$$T_{Tr} = N_b F_z = N_b \int_{r_{Tr}}^{R_{Tr}} dF_z \quad (8)$$

$$C_{T_{Tr}} = \frac{T_{Tr}}{\rho \pi R_{Tr}^2 (\Omega_{Tr} R_{Tr})^2} \quad (9)$$

where r_{Tr} is the blade root cut-out.

In the computation of tail rotor thrust, the blade pitch is required. The pitch is set by the pilot pedal control. Here, it is assumed that the helicopter is initially at trim in hover, with the pedal adjusted to compensate for main rotor torque at 45%, as described previously. In this investigation, the pilot is assumed to have delayed applying the pedals for a time t_0 . After this delay, the pitch would be increased from the initial value θ_{i0} to the maximum pitch $\theta_{i_{max}}$, during a one second ramp, after which the pitch remained constant.

The initial and maximum pitch are determined from the tail rotor thrust which is needed to compensate the initial torque $Q_{mr_0} - Q_{mr_{45\%}}$ and the maximum torque $Q_{mr_{max}}$, respectively. The thrust needed to compensate a given torque Q_{mr} is $T_{Tr} = Q_{mr} / l_{Tr}$ and the thrust coefficient corresponding to this thrust is computed from the definition of C_T , Eq. (9). The tail rotor pitch is found from the following expression, derived from combined blade element and momentum theories (Johnson, 1980):

$$\theta_{Tr} = \frac{6C_{T_{Tr}}}{\sigma a} + \frac{3}{2} \sqrt{\frac{C_{T_{Tr}}}{2}} \quad (10)$$

For the purposes of this investigation, the vertical empennage is represented by a plate in stagnation flow. The vertical drag is therefore given by:

$$D_{ev} = \frac{1}{2} \rho V_{ev}^2 A_{ev} c_{D_{ev}} \quad (11)$$

where V_{ev} is the velocity normal to the empennage, A_{ev} is the vertical empennage area and $c_{D_{ev}}$ is the plate drag coefficient, estimated to be 1.2 (ESDU, 1978).

For tail rotor loss simulations, the blade rotational equation of motion is also needed. Neglecting transmission and shaft friction, the contributing moments are blade inertia and tail rotor torque due to aerodynamic forces. Thus the equation for tail rotor angular velocity Ω_{Tr} is:

$$I_{b_{Tr}} \dot{\Omega}_{Tr} + Q_{Tr} = 0 \quad (12)$$

where $I_{b_{Tr}}$ is the blade moment of inertia with respect to the tail rotor axis and Q_{Tr} is the tail rotor torque, obtained from integration of blade element contributions:

$$Q_{Tr} = N_b \int_0^{R_{Tr}} (c_d \cos \phi + c_t \sin \phi) \frac{\rho U^2 c_{lr}}{2} r dr \quad (13)$$

For simulations without loss of tail rotor rotational speed, Eq. (1) is integrated in time using a standard fourth-order Runge-Kutta scheme (Beyer, 1987). For simulations with loss of rotational speed, both Eqs. (1) and (12) are integrated simultaneously using the same scheme.

Simulation Results

The simulated yaw motion for the hypothesis of constant tail rotor rotational speed, i.e., no shaft failure, is presented in Fig. 2. In this Figure, three simulations are shown. The first two correspond to pilot delays of 2 and 3 seconds, respectively, in applying the pedals after collective pitch increase. In these simulations, pedals were applied in a one-second ramp. The third simulation corresponds to no pilot pedal adjustment after collective pitch increase. It is clear from these simulations that even after a three-second delay the pilot is able to adjust the aircraft heading before making a complete turn. Actual pilot delays depend on the disturbance (Kuchnel, 1960) and typically do not exceed 0.25 sec. (Ashkenas and McRuer, 1962; Pedreiro, 1989). Actual time required to apply full controls would take well less than one second (Pedreiro, 1989; Etkin, 1982). The pilot delays assumed here are much higher than what might be expected and therefore the hypothesis of loss of directional control due to pilot delay is discarded.

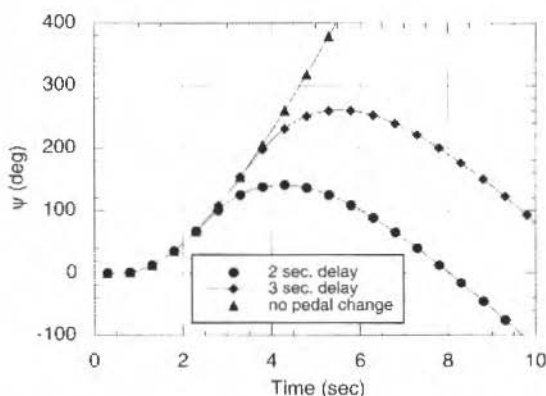


Fig. 2 Yaw Motion without Loss of Tail Rotor

The simulated yaw motion for the hypothesis of loss of tail rotor rotational speed due to shaft failure is presented in Fig. 3. In this Figure, three simulations are shown. The first corresponds to a pilot delay of 2 seconds in applying the pedals after collective pitch increase. The second simulation corresponds to no pilot pedal adjustment after collective pitch increase. The third simulation corresponds to no collective pitch increase or pedal change. Tail rotor rotational speeds for these simulations are presented in Fig. 4.

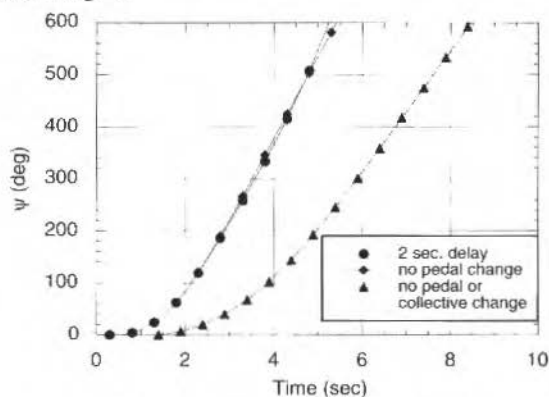


Fig. 3 Yaw Motion after Tail Rotor Shaft Failure

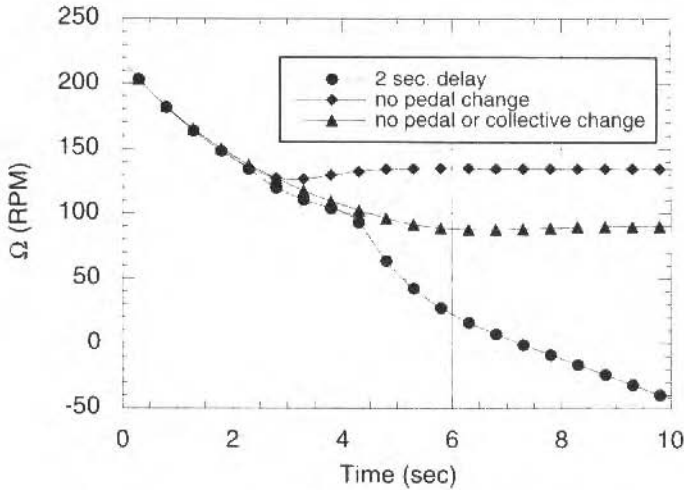


Fig. 4 Tail Rotor Rotational Speed after Tail Rotor Shaft Failure

From these simulations it is seen that shaft failure quickly causes loss of directional control, as expected. However, if the pedals are not applied the rotational speed eventually reaches a constant value, as the tail rotor enters an autorotative regime in vortex ring/turbulent wake state. If pedals are fully applied, the tail rotor enters windmill brake state and the rotational speed decreases. This implies that the rotational speed on impact depends on when and to what extent the pedals are applied. Therefore, even with loss of tail rotor shaft, it would be possible for the tail rotor to hit the ground at a range of rotational speeds which could account for the marks left on the ground. This result provided the investigators with evidence to support the hypothesis of tail rotor shaft failure.

Main Rotor Blade Failure

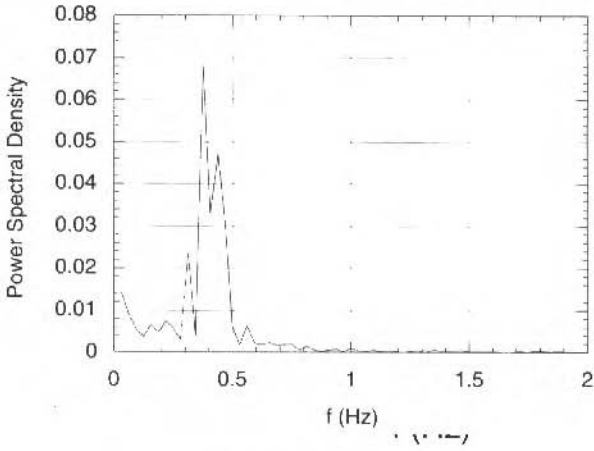
In this accident, a helicopter² was on its way to an offshore oil rig. A sudden bang was heard, the aircraft started suffering from excessive vibrations and the crew lost control of the aircraft, which crashed on the sea surface.

An initial attempt to retrieve the wreck was unsuccessful, but the combined Flight Data Recorder (FDR) / Cockpit Voice Recorder (CVR) was recovered. A video showing the wreck was recorded by an undersea robot.

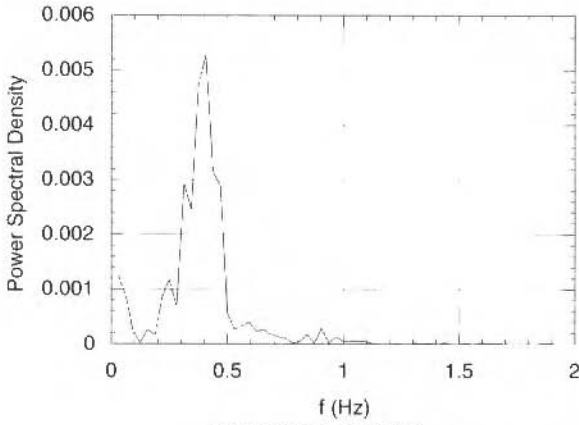
Although some channels were apparently defective, among those the lateral cyclic position, the FDR proved to be an essential contribution to this particular investigation. Most significant were the extremely high vibrations in all three axes, most notably a ± 1 g longitudinal vibration and a ± 0.4 g lateral vibration.

Spectral analysis of the FDR acceleration data is shown in Fig. 5. From this Figure, normal vibrations appear to be associated with a 3.6 Hz frequency, very close to the main rotor rotational speed (3.43 Hz in this case). Longitudinal and lateral vibrations appear to be associated with a 0.4 Hz frequency. However, while the normal accelerations were sampled at 8 Hz, which allows identification of frequencies up to 4 Hz, longitudinal and lateral accelerations were sampled at 4 Hz, which allows spectral analysis up to 2 Hz only. For this reason, the signal was aliased and the peak at 0.4 Hz actually represents phenomena associated with the difference $4 \text{ Hz} - 0.4 \text{ Hz} = 3.6 \text{ Hz}$, which is the same frequency identified by spectral analysis of the normal accelerations.

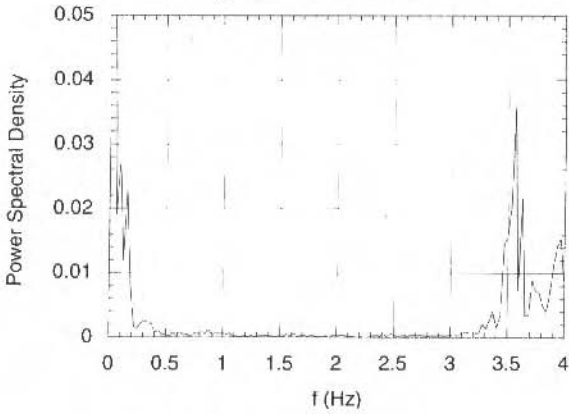
² Specific accident details, such as date and aircraft, are not given in order to preserve investigation confidentiality



(a) Longitudinal acceleration



(b) Lateral acceleration



(c) Normal acceleration

Fig. 5 Power Spectral Density of FDR-recorded Accelerations

From these considerations, it was found that the vibrations were associated with the first harmonic of main rotor rotational speed.

As mentioned before, the aircraft wreck had not been recovered for rotor head and blade material analysis. However, the undersea video allowed the investigators to identify some possible failure hypotheses, all related with main rotor blades and assemblies. These hypotheses were:

1. Total loss of one blade;
2. Blade spar fractured near the root;
3. Blade spar fractured near the tip;
4. Loss of balancing block near the tip
5. Loss of portions of some blade sections aft of the spar (trailing edge pockets);
6. Loss of one lag damper;
7. Loss of one pitch link;
8. Damaged pitch link, resulting in excessive slack.

Simulation Methodology

Since the aircraft wreck was not available for analysis, simulation of the failure hypotheses was essential in the determination of the most probable cause. The helicopter manufacturer conducted their own simulations of hypotheses nos. 3, 6 and 7 using an aeroelastic code not coupled with flight dynamics. These simulations pointed to hypothesis no. 3 as the most probable. However, the vibration levels resulting from the simulations were still substantially lower than the levels recorded by the FDR. The manufacturer suggested that this might be due to the absence of aircraft motion in the simulation.

In order to provide a more consistent basis for determination of the most probable cause, a simulation program based on an existing general helicopter flight simulation code (Howlett, 1981) was developed. In this method, the aircraft has six degrees of freedom and the rotor blades have three rigid body degrees of freedom - flapping, lagging and pitching. A blade element method is used, in which the aerodynamic coefficients are computed from simple algebraic equations based on experimental airfoil data. A first-order dynamic inflow model (Peters and HaQuang, 1988) is incorporated for computation of rotor wake downwash, (Mello, 1994). Section forces are integrated along the blade and summed up to yield main rotor forces and moments. These are added to fuselage, tail rotor and vertical and horizontal stabilizer forces and moments, so that total aircraft forces and moments can be obtained. From these, aircraft accelerations are found and integration of the equations of motion is performed. Details of the basic simulation method are available elsewhere (Howlett, 1981) and therefore are not presented here.

Simulation of blade failure hypotheses is conducted by appropriate modification of blade force computation. For the simulations presented here, the helicopter is initially trimmed. After a specified time (0.25 sec.), one of the failure hypotheses under investigation is introduced, as follows:

- Loss of blade or portion of the blade (hypotheses 1 to 4): Contributions of lost sections to blade inertial and aerodynamic forces are eliminated;
- Loss of trailing edge pockets (hypothesis 5): Contribution of lost parts to blade inertial forces are eliminated; aerodynamic coefficients of affected sections are modified to represent reduction in lift - assumed 30% - and increase in drag - assumed 100%;
- Loss of one lag damper (hypothesis 6): Force due to lag damper is eliminated;
- Loss of pitch link or slack (hypotheses 7 and 8): The pitch link is modeled by a torsional spring (Johnson, 1980); when it fails the moment due to this spring is eliminated. If there is some slack, the spring is effective only when the difference between the control pitch and the actual pitch is greater than the specified slack.

Simulations were conducted for all the above hypotheses in three modes: In the first, the helicopter was not allowed to move. This case was simulated so that the results could be compared with the simulations conducted by the manufacturer. In the second mode, the helicopter was allowed to move freely in space, with the controls held fixed to the trim positions. In the third mode, the helicopter was free to move, but the control positions were input during the simulation according to the positions registered in the FDR, except for the lateral cyclic, for which the FDR register was inoperative.

Simulation Results

A substantial amount of results was generated in this investigation, since eight failure hypotheses and three simulation modes were considered. Only some representative results are shown here.

Simulated and registered accelerations for hypothesis no. 2 (blade fractured near the root) for the free aircraft, pilot-in-the-loop simulation mode, are shown in Fig. 6. Results for hypothesis no. 1 (total blade loss) are very similar and are not shown for brevity. From these results, it may be seen that these hypotheses would cause vibrations consistent with the FDR data. It should be recalled that the flight-recorded data were sampled at a frequency lower than the rotational frequency, hence the noticeable aliasing.

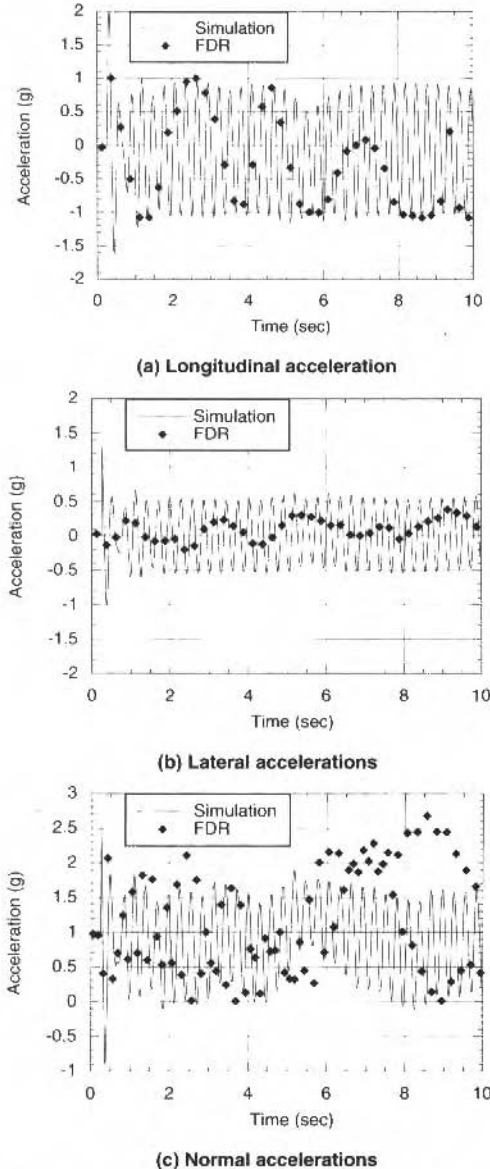


Fig. 6 Simulated and registered accelerations for hypothesis no. 2 (blade fractured near the root), pilot in the loop.

Simulated and registered accelerations for hypotheses nos. 3 (blade fractured near the tip), 6 (loss of lag damper) and 7 (loss of one pitch link) for the free aircraft, pilot-in-the-loop simulation mode, are shown in Figs. 7 through 9, respectively. It may be seen that these hypotheses would cause significantly lower vibrations than recorded. The other hypotheses under investigation - for which the results are not shown here - cause even lower vibrations.

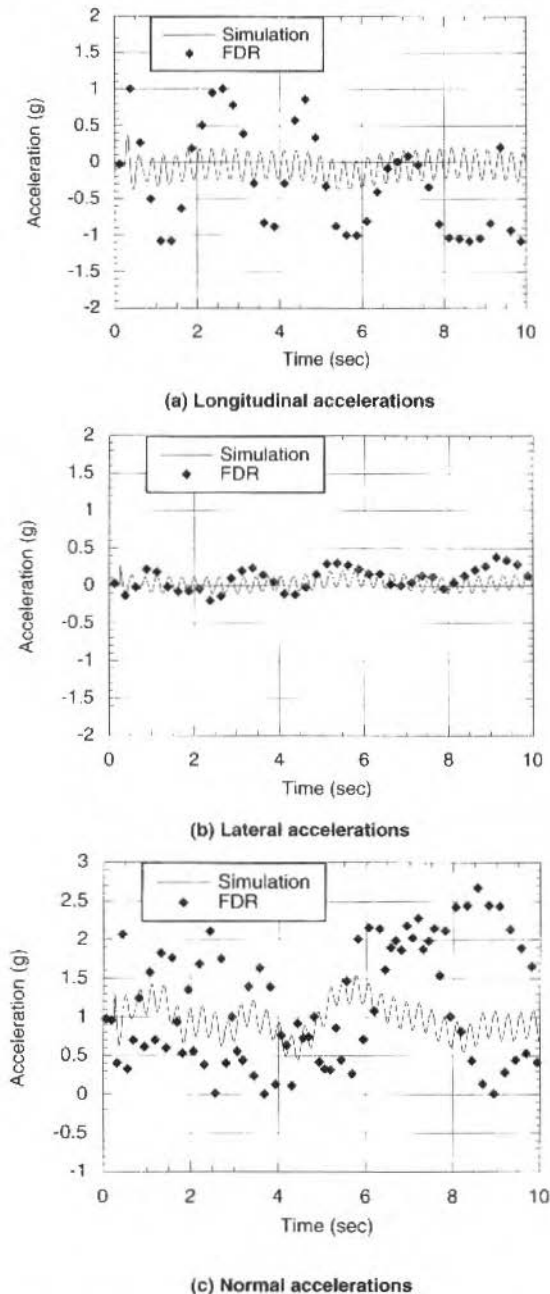


Fig. 7 Simulated and registered accelerations for hypothesis no. 3 (blade fractured near the tip), pilot in the loop.

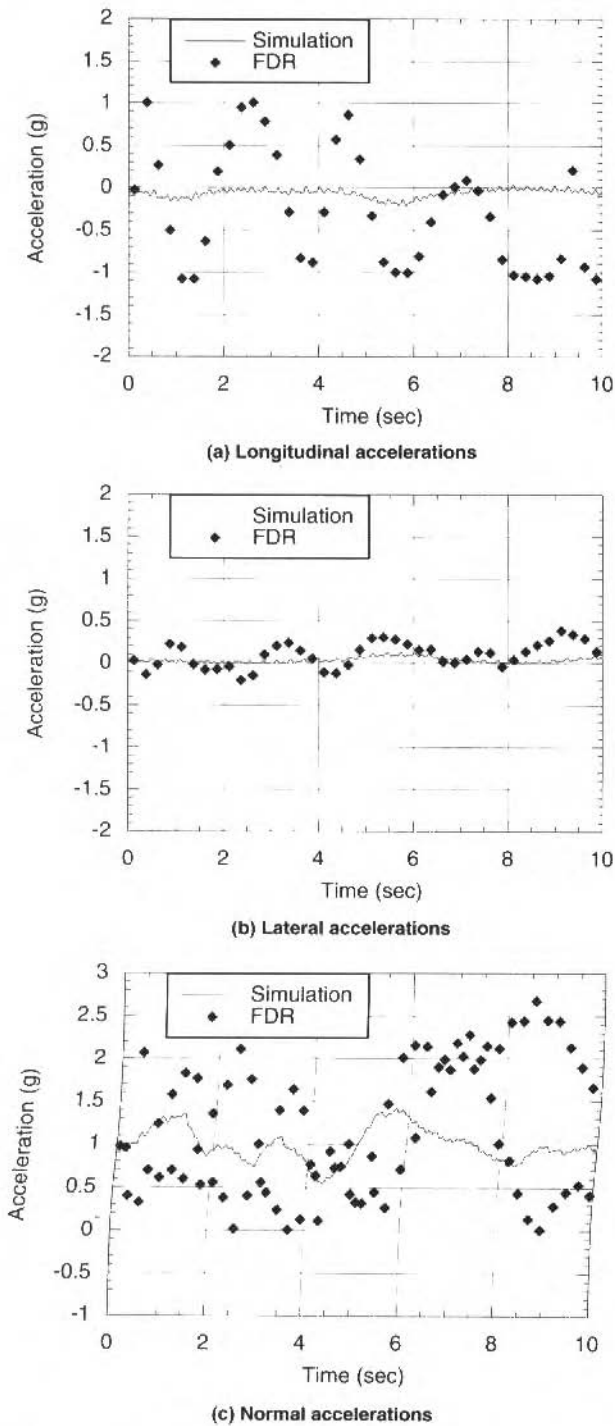
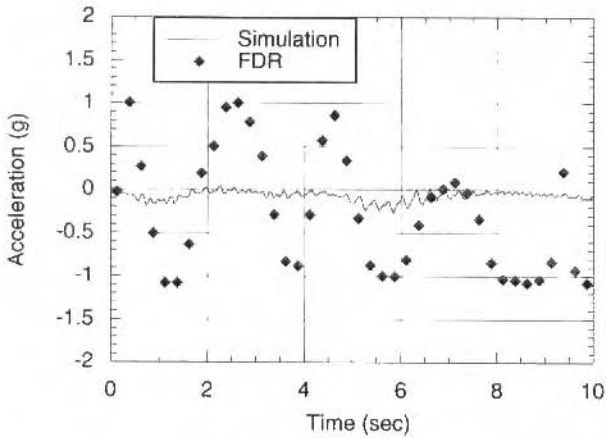
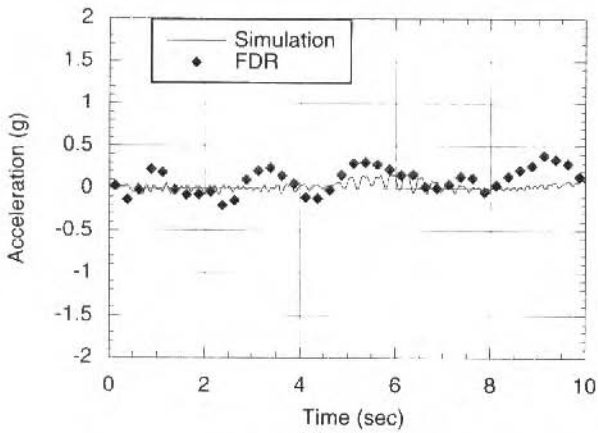


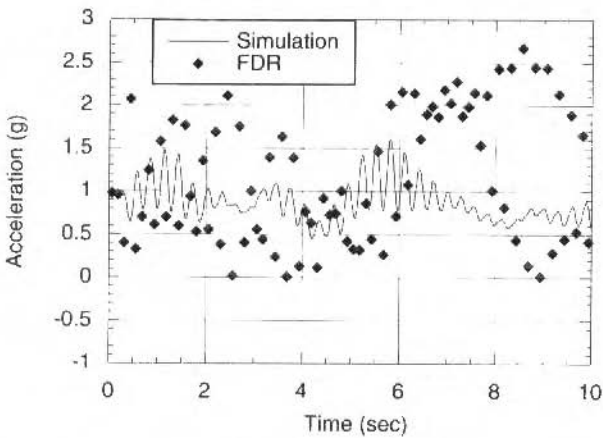
Fig. 8 Simulated and registered accelerations for hypothesis no. 6 (loss of one lag damper), pilot in the loop.



(a) Longitudinal accelerations



(b) Lateral accelerations



(c) Normal accelerations

Fig. 9 Simulated and registered accelerations for hypothesis no. 7 (loss of one pitch link), pilot in the loop.

In order to illustrate in what extent aircraft motion induced higher levels of acceleration, simulated and registered accelerations for hypothesis no. 2, fixed aircraft, pilot-out-of-the-loop simulation mode are presented in Fig. 10. By comparison between this Figure and Fig. 6, it may be seen that introduction of aircraft motion affects significantly only normal accelerations, while longitudinal and lateral accelerations are not affected much. Therefore, a fixed-aircraft simulation could still provide a good indication of probable causes for this accident.

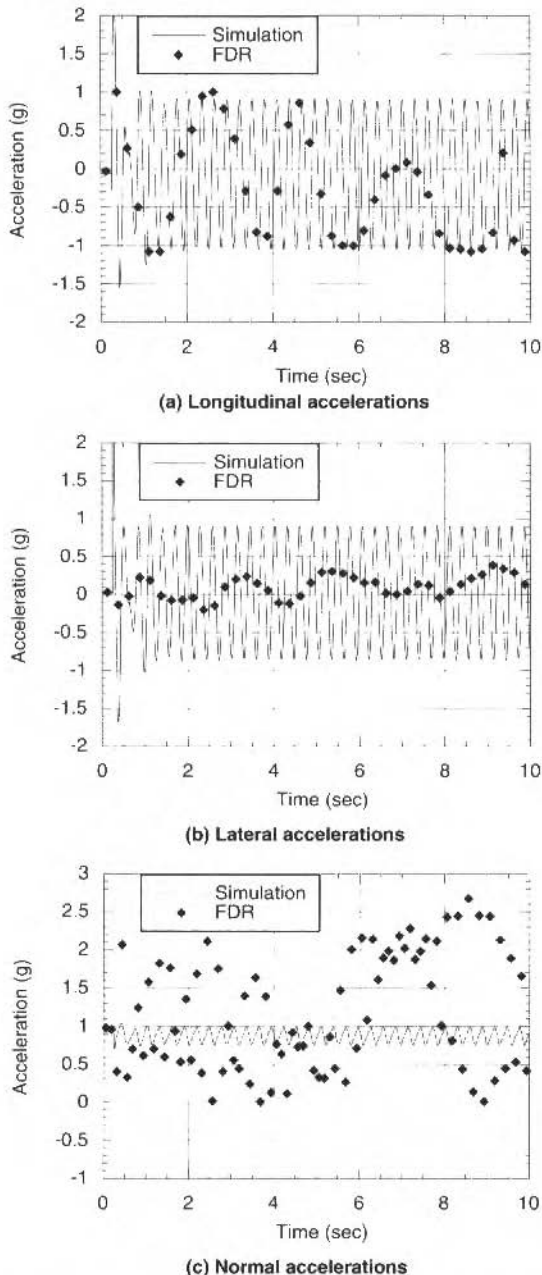


Fig.10 Simulated and registered accelerations for hypothesis no. 2 (blade fractured near the root), pilot out of the loop, aircraft fixed in space.

Although the unavailability of lateral cyclic register in the FDR was a serious handicap in the pilot-in-the-loop simulations, acceleration levels were quite consistent with those recorded. However, aircraft attitude could not be correctly simulated. This is illustrated in Fig. 11, where aircraft pitch attitude as simulated for hypothesis no. 2, pilot-in-the-loop mode, is compared with FDR-registered attitudes. This was due to the fact that the lateral cyclic was held constant during these simulations. Nevertheless, the trends in aircraft response are consistent. Since aircraft motion was found not to affect substantially longitudinal and lateral accelerations, these discrepancies are not relevant with respect to characterization of vibration levels for the different hypotheses considered here.

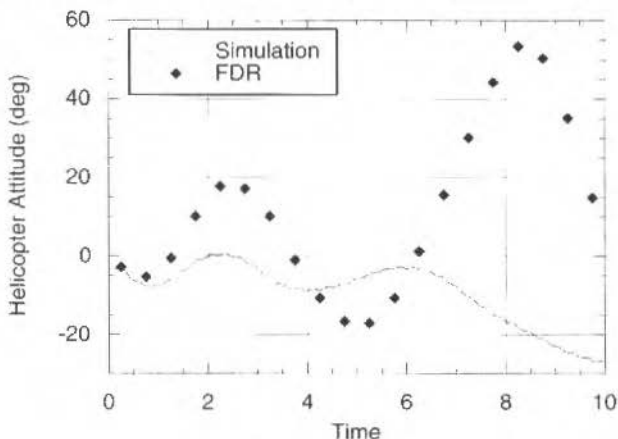


Fig. 11 Simulated and registered aircraft attitudes for hypothesis no. 2 (blade fractured near the root), pilot in the loop

Overall, these results indicated that the excessive accelerations were consistent with the loss of a large rotating mass, as in hypotheses nos. 1 and 2. Therefore, the simulation provided substantial grounds for the investigation board to establish these hypotheses as the most probable causes and to discard the other hypotheses.

Concluding Remarks

Two applications of flight simulation to the investigation of helicopter accidents were presented. In the first application, simulations of yaw dynamics with and without tail rotor loss were carried out in order to determine if loss of pedal control due to pilot's delay could be the cause of an accident with loss of directional control, and if the tail rotor could still be spinning when it hit the ground in case of tail rotor shaft failure. The results indicated that pedal control would still be available even with a three second pilot delay in applying the pedals, therefore the hypothesis of loss of pedal control was discarded. The simulation also indicated that the rotor blade could have hit the ground within a range of rotational speeds after tail rotor shaft failure, which could account for the marks on the ground, therefore maintaining the hypothesis of tail rotor loss.

In the second application, a numerical simulation of helicopter flight after several blade failure hypotheses has been conducted. Because in that case the aircraft wreck had not been recovered, simulation was essential to the investigation board in establishing the most probable cause of the accident. Simulations were conducted with and without the pilot in the loop, and for the latter, with and without aircraft movement in space. Longitudinal and lateral acceleration levels for these different simulation modes did not differ substantially, therefore simulation without aircraft movement or pilot control was sufficient for characterization of the effects of blade failure. Simulated accelerations indicated that the excessive accelerations were consistent with the loss of a large rotating mass, either due to total blade loss or blade fracture near the root. Simulated aircraft attitude changes did not compare well with FDR-recorded data, probably due to the unavailability of lateral cyclic positions.

In both applications, the simulations conducted here allowed clear characterization of the hypotheses under investigation, therefore the goal of providing the investigators with substantial grounds for establishing the most probable causes was attained.

References

- Ashkenas, I.L., and McRuer, D.T., 1962, "A Theory of Handling Qualities Derived from Pilot-Vehicle System Considerations", *Aerospace Engineering*, Vol. 21, no. 2, pp. 60-61,83-102.
- Beyer, W.H. (editor), 1987, "CRC Standard Mathematical Tables", 28th ed., CRC, Boca Raton, Florida.
- ESDU - Engineering Sciences Data Unit, 1978, "Fluid Forces, Pressures and Moments on Rectangular Blocks", In: "ESDU Aeronautical Series, Aerodynamic Sub-Series, Vol. 4b - Aerodynamics of Bodies, Controls and Flaps", Item No. 71016, with Amendments A to C, Engineering Sciences Data Unit, London.
- Etkin, B., 1982, "Dynamics of Flight - Stability and Control", 2nd ed., John Wiley & Sons, New York.
- Gessow, A., and Myers, G.C., Jr., 1952, "Aerodynamics of the Helicopter", Frederick Ungar. Reprint, College Park Press, College Park, Maryland, 1985.
- Hoerner, S.F., 1965, "Fluid-Dynamic Drag", Published by the Author, Brick Town, New Jersey.
- Howlett, J.J., 1981, "UH-60A Black Hawk Engineering Simulation Program: Volume 1 - Mathematical Model", NASA CR-166309, Moffett Field, California.
- Johnson, W., 1980, "Helicopter Theory", Princeton University Press, Princeton, New Jersey.
- Kuehnel, H.A., 1960, "In-Flight Measurement of the Time Required for a Pilot to Respond to an Aircraft Disturbance", NASA TN D-221, Washington, DC.
- Mello, O.A.F., 1994, "Numerical Simulation of Helicopter / Ship Airwake Interactions", Progress Report submitted to Naval Air Warfare Center, School of Aerospace Engineering, Georgia Institute of Technology, Atlanta.
- Pedreiro, N., 1989, "Aplicação de um Modelo Matemático do Piloto Humano na Estimativa da Qualidade de Voo" (Application of a Mathematical Model of the Human Pilot in the Estimation of Flight Qualities), M.S. Thesis, Instituto Tecnológico de Aeronáutica, São José dos Campos, Brazil (in Portuguese).
- Peters, D.A., and HaQuang, N., 1988, "Dynamic Inflow for Practical Applications", *Journal of the American Helicopter Society*, pp. 64-68.
- Sadler, S.G., 1972, "Main Rotor Free Wake Geometry Effects on Blade Air Loads and Response for Helicopters in Steady Maneuvers; Vol. I: Theoretical Formulation and Analysis of Results", NASA CR-2110, Washington, DC.

Detecting Faults in Cooling Coils of Air-Handling Units - Part I : The Method and Some Simulation Results

Newton Maruyama

Universidade de São Paulo
Escola Politécnica
Departamento de Engenharia Mecânica
05508-900 São Paulo, SP Brazil
maruyama@usp.br

Abstract

Building Energy Management and Control systems have contributed to the reduction of energy use without affecting the occupant's comfort, however, the inability to provide early detection and compensation of faults in air-handling units has not provided extra energy saving. For further improvement of reliability, safety and performance, an early detection and diagnosis of faults is of great interest. A fault detection method which uses static neuro-fuzzy models to describe the correct operation of the plant is proposed to detect faults in cooling coils of air-handling units. Abnormal operation of the plant is detected when residuals exceed a variable threshold value which accounts for modelling errors, noisy measurements and unmodelled disturbances. Simulation results are presented for both whole operating space and typical operation data of air-handling units to demonstrate the capabilities of the proposed scheme.

Keywords: Fault Detection, Neuro-Fuzzy Modelling, Air-Handling Units.

Introduction

Over the past two decades model-based methods of Fault Detection and Diagnosis (FDD) have achieved significant results (Frank 1990, Patton, Frank and Clark 1989). The methods for model-based FDD are based on analytical redundancy which includes methods like parity equations, diagnostic observers and Kalman filtering. Because very accurate mathematical description of systems are rarely available, these methods must incorporate some form of robustness against uncertainties, i.e., they must be insensitive to modelling errors, unmodelled disturbances and measurement noise which in practice are always present and could be a source of false alarms. Robust FDD methods have been reported (Ding and Frank 1991). However, these model-based methods can work only for systems that are information rich i.e.: these systems are linear or linearizable; approximate physical models or semi-physical models can be obtained; sensor measurements are complete (all variables necessary for the model are measured), accurate and recorded at frequencies much higher than the process fluctuations; and uncertainties can be somehow modelled.

Here, instead of information rich systems, the focus is on FDD for a system that has high uncertainty: cooling coils of air-handling units. Recently, there has been a great interest on developing Fault Detection and Diagnosis for Heating, Ventilating and Air-Conditioning systems (HVAC) (Hyvärinem and Kärki 1996). Analytical models are in practice hardly available for this class of system, therefore it might be more natural to consider methods based on either pattern recognition (Himmelblau 1978) or knowledge based approaches (McDowell, Kramer and Davis 1991). In recent years, Artificial Neural Networks (ANNs) have arisen as a method that can be used to perform pattern recognition and therefore for FDD (Sorsa, Koivo and Koivisto 1991). Fuzzy models have also been used for fault detection and diagnosis in uncertain systems. They have the advantage of more easily incorporate the expert knowledge available about the system. Fuzzy models may assume many different forms and can be used in qualitative model-based, pattern recognition and knowledge-based methods (Ulieru 1993, Dexter 1995).

In this work, a new fault detection method using neuro-fuzzy models is proposed for cooling coils of air-handling units. The cooling coils of air-handling units and the difficulties with the modelling task of cooling coils are presented. The dependence on operating conditions for fault detection in cooling coils which limits the performance of FDD methods are discussed. Simulations results are presented for both whole operating space and typical HVAC operation data. Some conclusions about the method are given. The companion article (Maruyama 1997a) discusses the practical problems which arise with the

implementation of the method and illustrates with an example. Related results has been presented in (Maruyama, Benouarets and Dexter 1996b, Maruyama, Benouarets and Dexter 1996a) and the method is extensively discussed in (Maruyama 1997b).

The Cooling Coils of Air-Handling Units

Figure 1 illustrates an schematic diagram of a cooling coil subsystem. The main components are a combined heat exchanger and a three port valve with actuator. The physical characteristics of the

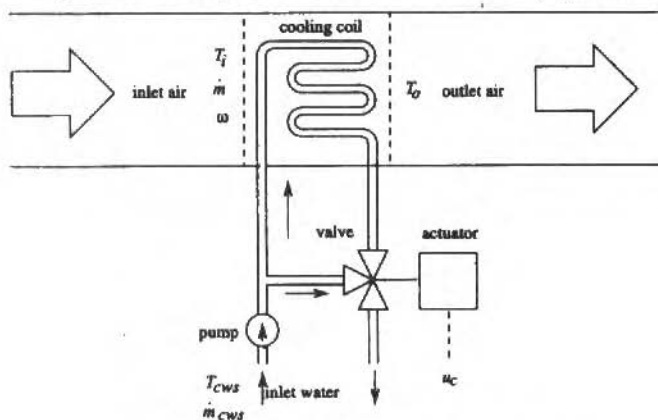


Fig. 1 Schematic diagram of a cooling coil sub-system.

cooling coil depends on the material of the tubes and many geometric features. The cooling coils studied here are one of the sub-systems of Heating, Ventilating and Air-Conditioning systems as illustrated in Fig. 2.

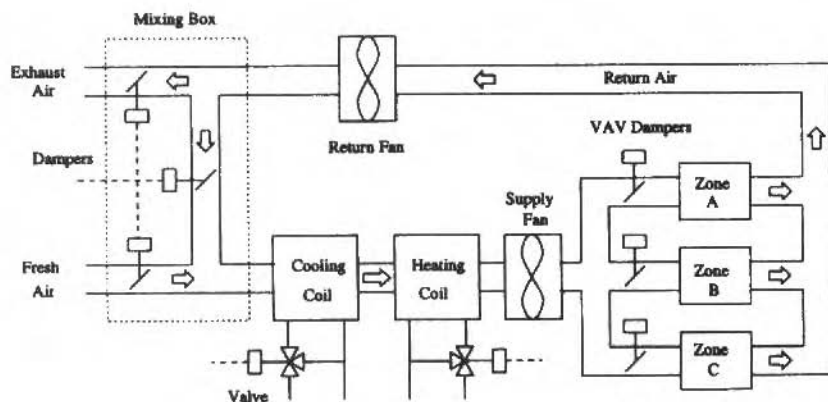


Fig. 2 Schematic diagram of an HVAC system.

The main variables are:

1. inlet air temperature T_i ($^{\circ}\text{C}$),
2. outlet air temperature T_o ($^{\circ}\text{C}$),
3. valve control signal u_c

4. air mass flow rate \dot{m} (Kg/s),
5. humidity ratio ω (Kg of vapor/Kg of dry air),
6. chilled water supply mass flow rate \dot{m}_{cws} (Kg/s),
7. chilled water supply temperature T_{cws} .

Figure 3 illustrates a typical location of sensors in a cooling coil sub-system.

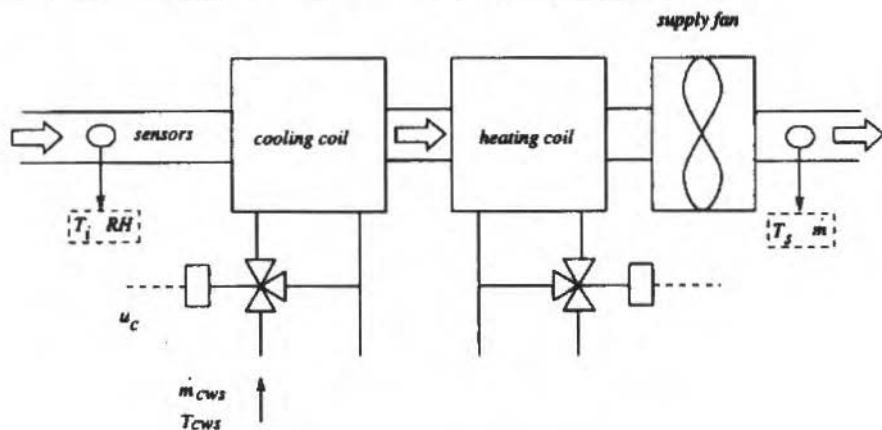


Fig. 3 Location of the sensors.

The air enters the coil itself at temperature T_i and is cooled by the chilled water as it flows through the heat exchanger. The air leaves the coil with a temperature given by T_o . The input-output relationship of the coil can be expressed as:

$$T_o = f(T_i, \dot{m}, u_c, \omega, \dot{m}_{cws}, T_{cws}) \quad (1)$$

The valve control signal controls the chilled water supply flow rate. If the valve is closed ($u_c = 0$) the air is not cooled. If the valve is open ($u_c > 0$) the air is cooled and the value of the outlet temperature T_o depends not only on the state of the cooling coil given by the valve control signal u_c , the chilled water supply mass flow rate \dot{m}_{cws} , and the chilled water supply temperature T_{cws} , but on the state of the inlet air given by the inlet air temperature T_i , the air mass flow rate \dot{m} , and the humidity ratio ω .

Developing a model for the cooling coil in an air-handling unit is not an easy task. The sources of uncertainty that are related to the modelling and testing of cooling coils are:

- the chilled water supply temperature T_{cws} and the chilled water supply flow rate \dot{m}_{cws} are usually not measured. Usually, both variables T_{cws} and \dot{m}_{cws} are assumed to be constant but in practice they can have some fluctuations. The outlet temperature T_o is particularly sensitive to fluctuations of these variables;
- measurements reflects only the state of the air in the neighbourhood of the sensor and not for the whole section of the duct;
- the outlet air temperature T_o is not usually measured. The supplied air temperature T_i is measured instead. In this case, T_o must be estimated from T_i or one must design a model that includes the other subsystems;
- the humidity ratio ω is not usually measured directly, the relative humidity RH is measured instead. Using T_i and RH it is possible to calculate approximately the dew point temperature T_{dew} that is correlated to ω in addition to the local pressure;

- during normal operation, the data collected is not complete enough to build a parametric or non-parametric model;
- during normal operation, the frequency contents of input signals of cooling coils are not complete enough to build a model that can be reliable at all possible frequencies;
- test signals for identification can not be easily generated as the state of the inlet air depends most on weather conditions.

Some mathematical models of cooling coils have been developed (Ding, Eppe, Lebrun and Wasacz 1990) for simulation programs of HVAC systems. These are usually complex models that rely on iterative solutions. Due to their complexity, these models are only suitable for off-line simulation of HVAC systems. Less complex models must be developed before on-line fault detection can be viable. Some physical models have been developed for FDD purposes (Salsbury, Haves and Wright 1995, Haves, Salsbury and Wright 1996), however, the nonlinear characteristics of these physical models make them very sensitive to the training data and large estimation errors can arise if training data is scarce.

The Most Common Faults in Cooling Coils Are:

1. leaky valve: for example, water leakage resulting from wear to the plug or seat of the valve;
2. fouled coil: for example, water-side fouling as a result of the build-up scale inside the tubes of the coil;
3. temperature sensor offset: for example, due to drifting of parameters.

These faults usually introduce changes in the static and dynamic behaviour of the cooling coil that can be detected as differences in the output variable T_c . For fault detection purposes, it is desirable to design an accurate dynamic model for correct operation. Faults may be then detected by comparing the predicted output given by the model against the measured data from the actual plant.

The Proposed Fault Detection Scheme

Figure 4 shows a schematic diagram of the fault detection scheme. The measurements of input and output signals are first pre-processed using a moving average filter and a transient detector. Residuals are then generated by comparing the output of the plant with the predicted output of a static neuro-fuzzy model of correct operation. Abnormal operation is detected when the residuals at steady-state points, exceed a threshold value which varies with the operating point, so as to take account of the modelling errors, measurement noise and unmodelled disturbances. An alarm is generated if the model indicates the presence of a fault.

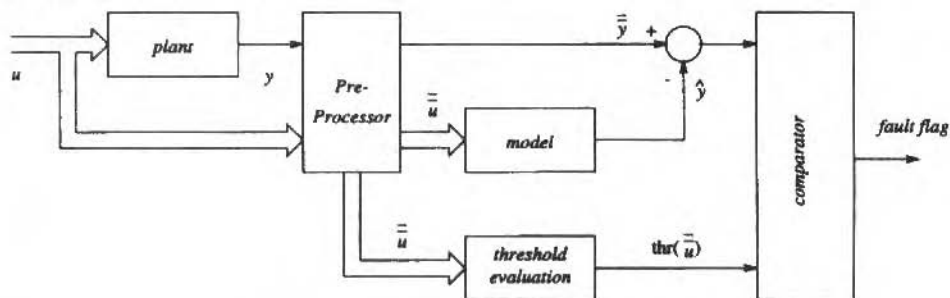


Fig. 4 Block diagram of the fault detection scheme.

The pre-processor generates moving average values of the inputs $\bar{u}(t)$ and the outputs $\bar{y}(t)$ of the system.

The comparator block compares the average measured outputs $\bar{y}(t)$ with the predicted output $\hat{y}(t)$ of the static neuro-fuzzy model which uses the average values $\bar{u}(t)$ as its inputs. The comparator sets a fault flag whenever residuals exceed the corresponding threshold value:

$$|\hat{y}(t) - \bar{y}(t)| > \text{thr}(\bar{u}). \quad (2)$$

The Static Neuro-Fuzzy Model

A neuro-fuzzy system is a modelling approach that performs a $X \subset \mathfrak{R}^n \rightarrow \mathfrak{R}$, where X is the input domain. The model can be interpreted as a rulebase comprising of Q fuzzy production rules of the following form:

$$\text{Rule}_q: \text{IF } x_1 \text{ is } A_1^q \text{ AND } x_2 \text{ is } A_2^q \text{ AND } \dots \text{ AND } x_n \text{ is } A_n^q \text{ THEN } y \text{ is } w_q,$$

where $q = 1, 2, \dots, Q$, x_i ($i = 1, 2, \dots, n$) are the inputs variables, y is the output variable, A_i^q are linguistic terms defined by membership functions $\phi_{A_i^q}(x_i)$ and w_q is a scalar value associated with the output variable. For each \underline{x} the output $y = h(\underline{x})$ can be calculated as (Brown and Harris 1994):

$$h(\underline{x}) = \frac{\sum_{q=1}^Q w_q \phi_q(\underline{x})}{\sum_{q=1}^Q \phi_q(\underline{x})}, \quad (3)$$

where $h: X \subset \mathfrak{R}^n \rightarrow \mathfrak{R}$, $\underline{x} = (x_1, \dots, x_1, \dots, x_n)^T \in X$, $\phi_q(\underline{x}) = \prod_{i=1}^n \phi_{A_i^q}(x_i)$ is a multidimensional membership function.

A static neuro-fuzzy model is chosen here because the most common faults change the steady-state behaviour of the cooling coils and significant steady-state information is available during operation of the system as demonstrated in (Maruyama 1997b). The presence of steady-state information about the operation of a cooling coil occurs because the excitation signals has very low frequency when compared with the dominant time constant of the plant. The use of static models reduces significantly the complexity of the model and consequently the amount of training data that is required to estimate the parameters of the model.

The Pre-Processor

In order to use static neuro-fuzzy models for fault detection, a steady-state detector must be designed to select the portions of the input-output signals that are quasi-stationary, i.e., are sufficiently close to steady-state. The procedure can be summarized by the following steps:

The raw data from each sensor is passed through a low-pass filter which performs a moving average calculation to remove high frequency noise. For each one of the input and output variables, z , the moving average at time t is calculated as,

$$\bar{z}(t) = \frac{\sum_{k=t-N_{w_f}+1}^t Z(k)}{N_{w_f}}, \quad (4)$$

for $t = N_{w_f}, 2N_{w_f}, \dots$ where N_{w_f} is the number of samples in the window length Fig. 5.

The filtered data is then processed to obtain a measure of the activity or functional variation. The average activity is calculated as,

$$\bar{a}_z(t) = \frac{1}{N_{w_1} T} \sum_{k=t-N_{w_2}+2}^t |\bar{z}(k) - \bar{z}(k-1)|, \quad (5)$$

where N_{w_2} is the size of the window, which may be different from N_{w_1} , and T is the sampling time interval.

The activity measure is then compared with a threshold in order to decide whether the system is in steady-state or not. A threshold for the activity is defined based on the acceptable error when a static model is used for predictions with non steady-state data. The following threshold is adopted (Maruyama 1997b):

$$\varepsilon_z(t) = \frac{\xi \bar{\bar{z}}(t)}{\tau_D}, \quad (6)$$

where

$$\bar{\bar{z}}(t) = \frac{\sum_{k=t-N_{w_2}+1}^t \bar{z}(R)}{N_{w_2}}, \quad (7)$$

and ξ is the acceptable relative prediction error for the static model and τ_D is dominant time constant of the system. If $\bar{a}_z(t) < \varepsilon_z(t)$ for all input and output variables simultaneously then the system is considered to be in steady-state at time t .

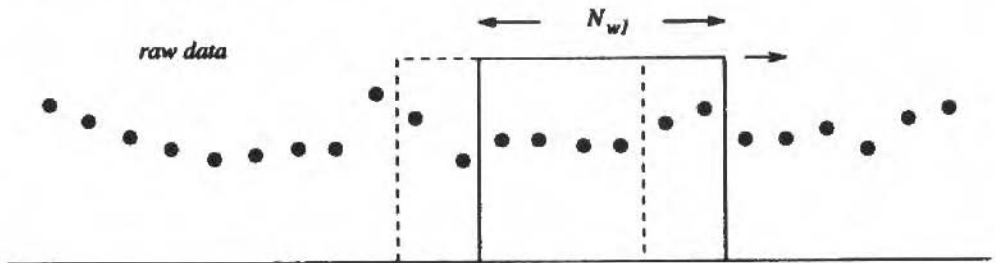


Fig. 5 Moving window.

Threshold Evaluation

The selection of suitable thresholds for the model is a key step in any fault detection scheme. Thresholds must take into account modelling errors, unmodelled disturbances and measurement noise. In this particular scheme, some of the noise and unmodelled disturbances is filtered out by the pre-processor module.

A common procedure is to set a fixed threshold for the whole operating space. The occurrence of a fault is signified by a residual which surpasses the threshold value. A large threshold reduces the sensitivity to faults, and only large faults can be detected. On the other hand, if the threshold is too small, the rate of false alarms can be very high. Another approach is to select adaptive or variable thresholds (Frank 1992). The idea of variable thresholds was introduced to compensate for the

uncertainties of the model which make the residual vary even when there are no faults in the system. The change in the residuals, especially for large variations in operating points, can be large enough to cause false alarms if fixed threshold is used. A fixed threshold could be used in the case of static neuro-fuzzy models. However the performance of the fault detection scheme can be enhanced by employing a variable threshold. Hence, a new method of threshold evaluation was designed, which attempts to take advantage of the structure of the model, and the data available during the learning process.

The threshold in each part of the operating space is evaluated using the following expression:

$$thr(\underline{x}) = \frac{\sum_{q=1}^Q thr_q \phi_q(\underline{x})}{\sum_{q=1}^Q \phi_q(\underline{x})}, \quad (8)$$

where \underline{x} is the input vector, thr_q are local thresholds associated with each basis function $\phi_q(\underline{x})$.

The functions $\phi_q(\underline{x}), q=1, \dots, N$, are the basis functions used to define the neuro-fuzzy model.

Here, thr_q is calculated as:

$$thr_q = thra_q + thro_q, \quad (9)$$

where $thra_q$ is the component calculated using the available training data, and can be understood as an estimate of the maximum approximation error in each region (though a significant amount of data must be available for this estimate to be precise). The other component, $thro_q$, is a fixed value that reflects the uncertainty arising in the estimation of $thra_q$ from the lack of data, the noise and unmodelled disturbances that can corrupt the training data, and the noise and unmodelled disturbances that can arise during operation of the system. Here, the following procedure is used to calculate the maximum approximation errors (Maruyama et al. 1996a):

$$thra_q = \left\{ \max \left\{ e_i = \left| \hat{y}_i - y_i \right| \mid i=1, \dots, N \mid \phi_q(\underline{x}_i) > 0 \right\} \right\}, \quad (10)$$

for the training data $D = \{(\underline{x}_i, y_i), i = 1, \dots, N\}$, and where \hat{y}_i is the predicted value. In this work, the main focus is the approximation errors which arise due to the finite complexity of neuro-fuzzy models. Noise and unmodelled disturbances are considered in the companion article (Maruyama 1997a).

The Dependence on Operating Point Conditions for Fault Detection in Cooling Coils

In cooling coils, the detection of faults depends on operating point conditions. In the case of leakage, for example, the percentage of the typical operating space in which the fault can be detected (POSFD) is limited to regions where the valve control signal u_v is zero or close to zero. In this case, the operating space in which the fault can be detected is small and this affects the performance of any fault detection and diagnosis scheme.

The dependence on operating point conditions for detection of the most common faults in cooling coils can be analysed by calculating the percentage of the typical operating points at which the fault can be detected, i.e., the percentage of the typical operating points where the observed behaviour, when a

fault is present, is different from that of correct operation. The differences are detected by calculating the residuals between the data for correct operation and data for a faulty operation. Suppose that the set of points $D^c = \{(\underline{x}_i, y_i^c \mid i = 1, \dots, N)\}$ represents correct operation and the set $D^f = \{(\underline{x}_i, y_i^f \mid i = 1, \dots, N)\}$ represents a faulty operation. The residuals $r(\underline{x}_i)$ are calculated as:

$$r(\underline{x}_i) = |y_i^c - y_i^f| \quad (11)$$

If the residual $r(\underline{x}_i)$ is larger than a threshold δ , the data sets are considered to be different at that particular operating point \underline{x}_i . The percentage of the operating space at which a particular fault can be detected is then determined for the whole operating points \underline{x}_i ($i = 1, \dots, N$). In the following, data are generated by simulation using the HVACSIM+ program (Clark 1985), for the same cooling coil, for correct operation, and for different sizes of valve leakage and water-side fouling. The outlet air temperature T_o is calculated for all combinations of the input values. The data must be equally spaced for the statistics to reflect the percentage of the operating space. Table 1 summarizes the results for two different sizes of valve leakage, for two different sizes of water-side fouling and four different values of the threshold δ .

As expected, for valve leakage the percentage POSFD is small (only 15.23% for 3% leakage with $\delta = 0.5^\circ\text{C}$). For water-side fouling the POSFD is significantly larger when compared to valve leakage for any threshold δ . If the size of the fault increases, the POSFD also increases. Specially for valve leakage there is a significant increase in the POSFD when the size of leakage increases from 3% to 5% for both $\delta = 0.5^\circ\text{C}$ and $\delta = 1.0^\circ\text{C}$. If the threshold δ increases the POSFD decreases. If the modelling errors are large and the fault detector can only detect differences larger than 1.0°C there is a significant reduction of the POSFD specially for water-side fouling which can be as low as 25.66% for 0.5mm water-side fouling. For $\delta = 0.1^\circ\text{C}$, which is a realistic lower limit for a detectable residual, the probability of detecting the fault for 3% and 5% valve leakage are still below 50%. This emphasizes the fact that, when there is valve leakage, the cooling coil behaves correctly for most of the operating points.

Table 1 Percentage of the operating space where faults can be detected for different thresholds δ .

Fault	$\delta = 0.1^\circ\text{C}$	$\delta = 0.2^\circ\text{C}$	$\delta = 0.5^\circ\text{C}$	$\delta = 1.0^\circ\text{C}$
3% valve leakage (%)	27.71	23.89	15.23	8.85
5% valve leakage (%)	42.54	27.67	21.84	14.68
0.5mm water-side fouling (%)	88.59	82.49	60.13	25.66
1.0mm water-side fouling (%)	91.93	89.10	78.13	58.72

Measuring the Performance Over the Whole Operating Space

In order to measure the performance of a particular fault detector scheme over the whole operating space, a comparison with a perfect fault detector (PERFFD) is made. A perfect fault detector is defined here as the one which for a set of data points $D = \{(\underline{x}_i, y_i), i = 1, \dots, N\}$, gives an answer based on the distance $r(\underline{x}_i) = |y_i^c - y_i|$ where y_i^c ($i = 1, \dots, N$) are perfect predictions of the correct operation of the plant. A perfect fault detector with a threshold δ can be defined and a data set of correct operation $D^c = \{(\underline{x}_i, y_i^c \mid i = 1, \dots, N)\}$ used for prediction purposes, as in the earlier section. To calculate these statistics for each operating point \underline{x}_i , the output from the fault detection scheme under test is compared with the perfect fault detector. The performance is measured by estimating and comparing the estimated probability of false alarms P_{FA} and the estimated probability of detection P_{FD} of both fault detectors. The estimated probability of false alarms is determined using the correct operation data set and is given by:

$$P_{FA} = \frac{N_I^c}{N} \times 100\% \quad (12)$$

where N_i^C is the number of points at which the fault detector sets the alarm when it is tested with correct operation data. N is the total number of test points in the operating space. The estimated probability of detection is given by the same equation but it is calculated for the faulty data sets:

$$P_{FD} = \frac{N_i^F}{N} \times 100\%, \quad (13)$$

where N_i^F is the number of points at which the fault detector sets the alarm when it is tested with faulty operation data

The fact that faults like valve leakage and water-side fouling are not observable over the whole operating space introduces not only the possibility of a fault not being detected at some operating points by the designed fault detector (FDNF), when the PERFFD can detect it, but also a possibility of the fault being detected by the FDNF at some operating points when the PERFFD can not detect it. In both cases, the cause is either modelling errors or inadequacies in the method used to estimate the threshold. From this point of view it maybe useful to calculate other performance indices that reflect the estimated probability of correct classification. The following classification indices are calculated for this purpose:

1. the estimated probability of operating points correctly classified as correct operation:

$$P_{00} = \frac{N_{00}}{N} \times 100\%, \quad (14)$$

where N_{00} is the number of operating points at which both fault detectors do not set their alarms; and there is no fault present.

2. the estimated probability of operating points incorrectly classified as faulty operation:

$$P_{01} = \frac{N_{01}}{N} \times 100\%, \quad (15)$$

where N_{01} is the number of operating points at which the PERFFD does not set the alarm and the FDNF does set the alarm; and there is no fault present.

3. the estimated probability of operating points incorrectly classified as correct operation:

$$P_{10} = \frac{N_{10}}{N} \times 100\%, \quad (16)$$

where N_{10} is the number of operating points at which the PERFD sets the alarm and the FDNF does not set the alarm; and there is a fault present.

4. the estimated probability of operating points correctly classified as faulty:

$$P_{11} = \frac{N_{11}}{N} \times 100\%, \quad (17)$$

where the N_{11} is the number of operating points at which both the PERFD and the FDNF set their alarms; and there is a fault present.

The correctly classified operating points of the FDNF are reflected by P_{00} and P_{11} and the incorrectly classified operating points are reflected by P_{01} and P_{10} . From Equations 14-17 it can be seen that P_{FA} but $P_{01} = P_{01} + P_{11}$ therefore the estimated performance can be misleading if P_{01} is large.

Test Results Over the Whole Operating Space

In this section, test results obtained with the HVACSIM+ (Clark 1985) simulation program are presented. The examples in this section address the following issues: the capabilities of the fault detection scheme in detecting different types of faults which can occur in the cooling coil; the sensitivity of the fault detection scheme to the sizes of the faults and the advantages of using variable thresholds.

Results are presented for the case when the cooling coil is dry, i.e., when the humidity ratio of the inlet air ω is very low. In this situation, the outlet air temperature T_o depends on three variables: the valve control signal u_v , the air mass flow rate \dot{m} and the inlet air temperature T_i . The simulated humidity ratio ω , the chilled water supply temperature T_{cws} and the chilled water mass flow rate \dot{m}_{cws} are kept constant. Since the aim of this work is to demonstrate the capabilities of the fault detection scheme, the humidity ratio ω is held constant at 0.004kg/kg to reduce the complexity of the models. A static neuro-fuzzy model is generated to describe the correct operation of the cooling coil and the supply fan. In this way, it is possible to avoid using the outlet air temperature T_o , which will not usually be measured in practice (see Fig. 3), and to use the supply air temperature T_i instead. This model is represented by the following equation:

$$T_o = f(u_v, \dot{m}, T_i) \quad (18)$$

The fault detector is tested using data collected when the coil is working correctly, when the valve is leaky, when the coil is fouled, and when there is an offset on the output of the supply air temperature sensor. The neuro-fuzzy model, training data and test data are generated as follows:

- Training data is generated for the following combination of input values:

$$u_v = \{0.0, 0.02, 0.05, 0.1, 0.15, 0.2, 0.3, 0.4, 0.5, 0.6, 0.7, 0.8, 0.9, 1.0\},$$

$$\dot{m} = \{2.0, 2.5, 3.0, 3.5, 4.0, 4.5, 5.0, 5.5, 6.0, 6.5, 7.0, 7.5, 8.0\},$$

$$T_i = \{16.0, 18.0, 20.0, 22.0, 24.0, 26.0, 28.0, 30.0, 32.0\}.$$

The total number of data points is 1638.

- The test data is generated equally spaced as in the earlier section.
- The structure of the model is defined by the following input knots¹:

$$u_v = \{0.0, 0.1, 0.5, 1.0\},$$

$$\dot{m} = \{2.0, 4.0, 6.0, 8.0\},$$

$$T_i = \{16.0, 21.33, 26.67, 32.0\}.$$

The static model has 64 rules. The basis functions for the input variables, are chosen to be triangular (B-spline basis functions of order 2). They are presented in Fig. 6.

- the thresholds are calculated using Eqs. 8 and 9. thra_o is calculated using Equation 10 and thro_o is set to zero for all of the rules.

¹ For a lattice defined by B-spline basis functions of order 2, the knots corresponds to points where the basis function assumes its maximum value.

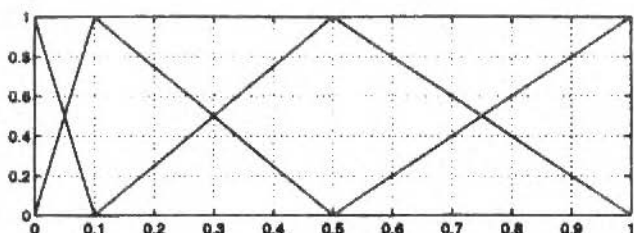
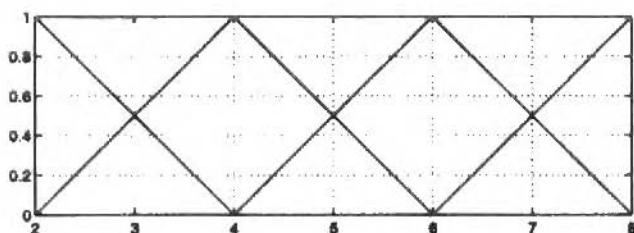
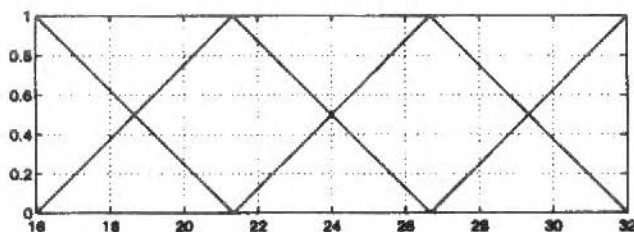
(a) basis functions for μ_c .(b) basis functions for m .(c) basis functions for T_i .

Fig. 6 Basis functions.

The estimated probability of false alarms and estimated probability of detection are calculated for the perfect fault detector (PERFFD) and the fault detector with neuro-fuzzy model and variable threshold (FDNFV). The threshold δ for the perfect fault detector is chosen as $\delta = 0.5^\circ\text{C}$ which is a reasonable detectable residual for the FDNFV. Table 2 summarizes the results for correct data set and for different types of faults: 3% and 5% valve leakage, 0.5mm and 1.0mm water-side fouling. The estimated probability of false alarms and the estimated probability of detection for both PERFFD and FDNFV will be denominated respectively as P_{FA}^r , P_{FD}^r , P_{FA}^N , and P_{FD}^N . The estimated probability of false alarms of the PERFFD P_{FA}^r is 0.00%, as expected, but the FDNFV has a very small P_{FA}^N . However, for faulty test data sets the FDNFV has a considerably smaller P_{FD} . For 3% valve leakage for example the P_{FD}^r is 65.36% larger than P_{FD}^N . From Table 2 is also possible to conclude that the estimated probability of detection P_{FD} increases with the increase of the size of the fault.

The advantage of using variable thresholds is shown here through a comparison between the fault detector using a neuro-fuzzy model and a variable threshold (FDNFV) and two fault detectors using the same neuro-fuzzy model structure but with a fixed threshold (FDNFF) one with $\delta = 0.5^\circ\text{C}$ and the other with $\delta = 1.5^\circ\text{C}$. The test data sets are the same as in the earlier section. Table 3 summarizes the result.

Table 2 Performance indices for different types and sizes of faults – P_{FA} and P_{FD}

Model	Type of operation	P_{FA}	P_{FD}
PERFFD $\delta = 0.5^\circ\text{C}$	correct	0.00%	-
	3% valve leakage	-	15.23%
	5% valve leakage	-	21.80%
	0.5mm water-side fouling	-	60.13%
	1.0mm water-side fouling	-	78.39%
FDNFV	correct	0.04%	-
	3% valve leakage	-	9.21%
	5% valve leakage	-	15.62%
	0.5mm water-side fouling	-	44.94%
	1.0mm water-side fouling	-	67.73%

As pointed out in the earlier section the probability of fault detection P_{FD} can be given by $P_{FD} = P_{D1} + P_{D2}$, so large P_{D1} can give a false impression about the performance of the fault detector. In Table 3 it is noted that the FDNFF with $\delta = 0.5^\circ\text{C}$ has larger values of P_{D1} , which is undesirable, and P_{D2} when compared to the FDNFV, however, the FDNFF with $\delta = 1.5^\circ\text{C}$ has smaller values of P_{D1} but also smaller values of P_{D2} , indicating a poor performance. Specially for water-side fouling the value of P_{D2} is very small when compared to FDNFV. These observations prove the advantage of using variable threshold schemes.

Table 3 Comparing variable and fixed thresholds schemes.

Model	Type of operation	P_{D1}	P_{D2}	P_{FD}	P_{FA}
FDNFV	correct	99.96%	0.04%	0.00%	0.00%
	3% valve leakage	84.45%	0.31%	6.34%	8.89%
	5% valve leakage	76.94%	1.26%	7.44%	14.36%
	0.5mm water-side fouling	35.42%	4.45%	19.63%	40.50%
	1.0mm water-side fouling	19.44%	2.16%	12.84%	65.56%
FDNFF $\delta = 0.5^\circ\text{C}$	correct	94.21%	5.79%	0.00%	0.00%
	3% valve leakage	78.87%	5.90%	3.90%	11.33%
	5% valve leakage	70.60%	7.60%	1.97%	19.83%
	0.5mm water-side fouling	31.52%	8.34%	5.86%	54.27%
	1.0mm water-side fouling	17.67%	3.94%	3.11%	75.29%
FDNFF $\delta = 0.5^\circ\text{C}$	correct	99.96%	0.04%	0.00%	0.00%
	3% valve leakage	84.77%	0.00%	9.29%	5.94%
	5% valve leakage	78.12%	0.08%	12.91%	8.89%
	0.5mm water-side fouling	39.75%	0.12%	53.95%	6.18%
	1.0mm water-side fouling	21.57%	0.04%	38.76%	39.63%

Measuring the Performance Based on Typical HVAC Operation Data

When calculating the performance for typical HVAC operation data the estimated probability of false alarms and the estimated probability of detection is a measure of the estimated probability of steady-state data points detected as faulty during the operation of the HVAC system and not the estimated probability of points over the whole operating space. In this case, the estimated probability of false alarms is given by:

$$P_{FA}^* = \frac{N_I^C}{N_{SS}} \times 100\% \quad (19)$$

where N_i^c is the number of steady-state operating points classified as faulty, when tested with correct operation data, and N_{ss} is the total number of steady-state operating points. Similarly, the estimated probability of detection is given by:

$$P_{FD}^* = \frac{N_i^F}{N_{ss}} \times 100\%, \quad (20)$$

where N_i^F is the number of steady-state operating points classified as faulty when tested with faulty operation data.

Due to the dependence on operating point conditions both the estimated probability of false alarms P_{FA}^* and the estimated probability of detection P_{FD}^* do not reflect the actual performance. Because steady-state points are not distributed uniformly. However, these statistics are the only ones which can be generated during on-line operation.

Test Results for Typical HVAC Operation Data

In the following, the use of the method is illustrated using simulation results for typical HVAC operation data. The test data are generated by simulating a detailed air-conditioning system (Fig. 2) using the HVACSIM+ simulation program (Clark 1985). The dynamics of sensors and actuators are modelled but measurement noise and unmodelled disturbances are not considered. Figure 3 illustrates where the measurements are taken. As a sensor for measuring the humidity ratio ω is usually not available, a relative humidity RH sensor is used instead. Both dry operation of the coil and wet operation of the coil are considered.

The model used for these results is the same as in Section 6. All fault detection results consist of three plots of the following variables:

1. A data validation flag which assumes the value 0 when the input data is related to an operating point which can be represented by the model, and assumes the value 1 otherwise;
2. A fault flag that assumes the value 0 when no fault is detected, and assumes the value 1 when a fault is detected;
3. The absolute residual and the detection threshold.

The test data used in the experiments, and the corresponding fault detection results are illustrated in Figs 7-8. In all plots, steady-state conditions are indicated by circles. The tuning parameters of the steady-state detector are the following:

$$N_{wf} = 0,$$

$$N_{w2} = 30,$$

$$\tau_D = 200s$$

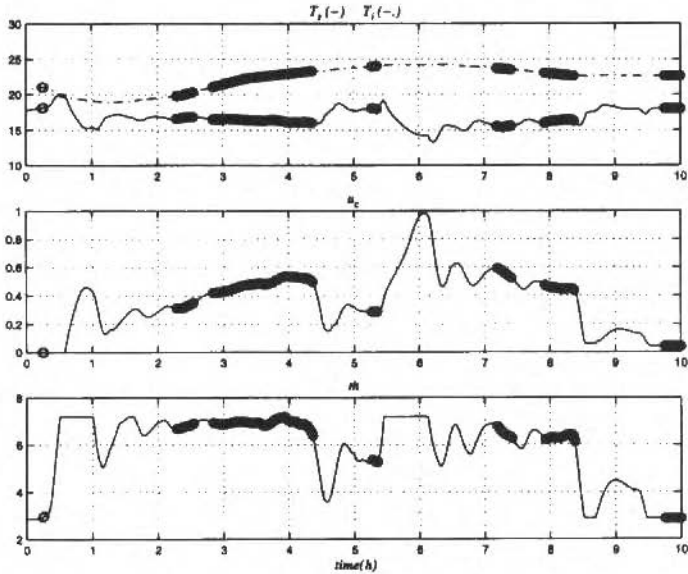
$$\xi = 0.03.$$

N_{wf} can be set to zero because the simulated test data are noise free. This selection of parameters allows reasonable amount of detected steady-state points which are truly in steady-state.

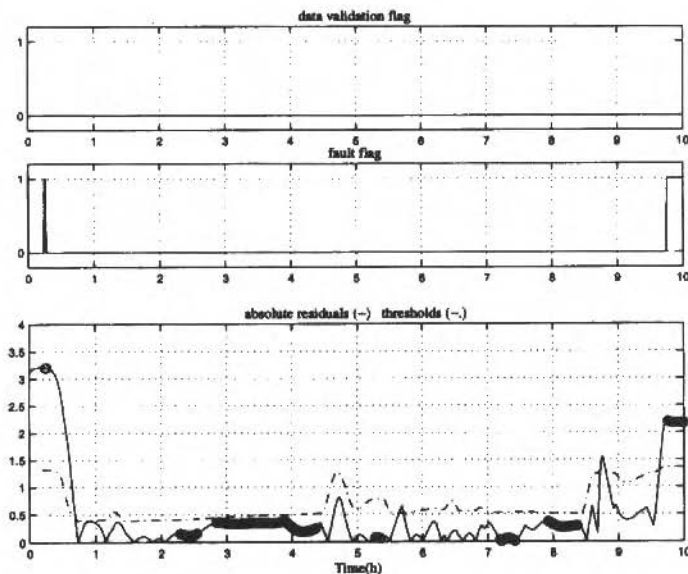
- 3% leaking valve: Fig. 7(a) illustrates the test data for 3% leaking valve and 7(b) illustrates the fault detection results. The estimated probability of detection is $P_{FD}^* = 10.17\%$.

- 0.5mm water-side fouling: Fig. 8(a) illustrates the test data for 0.5mm water-side fouling and 8(b) illustrates the fault detection results. The estimated probability of detection is $P_{FD}^* = 81.72\%$.

The tests demonstrate the capabilities of the proposed fault detection scheme in detecting different type of faults in cooling coils using test data which represent typical operation data of air-handling units.

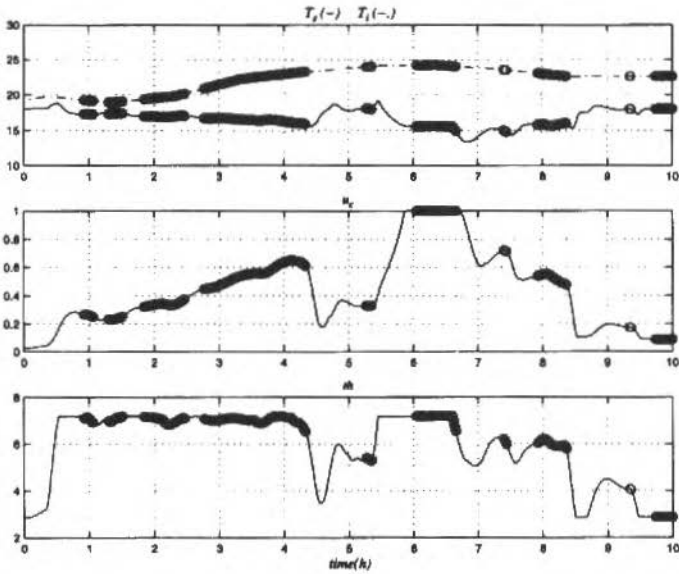


(a) Test data.

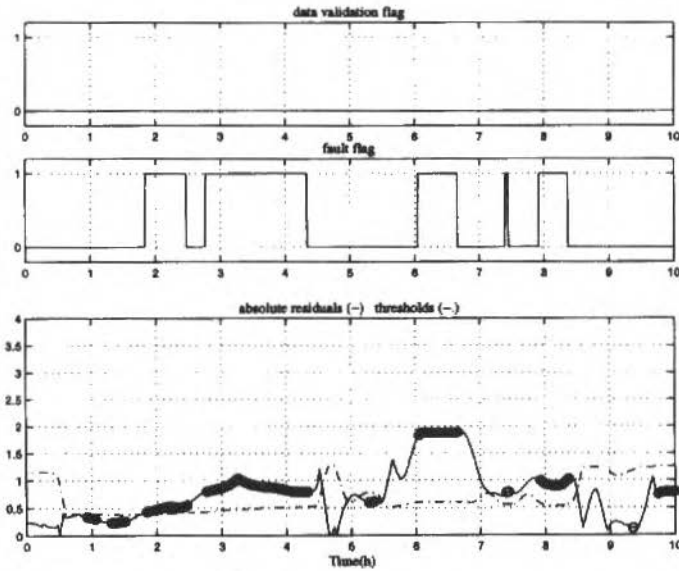


(b) Fault detection results.

Fig. 7 3% leaking valve operation.



(a) Test data.



(b) Fault detection results.

Fig. 8 0.5mm water-side fouling.

Conclusions

A fault detection method which uses static neuro-fuzzy models to describe the correct operation of the plant has been proposed to detect faults in cooling coils of air-handling units. Abnormal operation

of the plant is detected when residuals at steady-state points exceed a variable threshold value which account for modelling errors, noisy measurements and unmodelled disturbances.

The capabilities of the fault detection scheme and the advantage of using a variable threshold instead of fixed threshold have been demonstrated. The results of tests on a simulated cooling coil have highlighted the dependence of the results on operating conditions. Such a dependence explains, why, for some test data, the fault detection scheme can have a very small value of the estimated probability of detection. It has been shown that the only consistent performance indices are those that are based on comparisons with an ideal model-based detector over the whole operating space. However, in practice, the estimated probability of false alarms and the estimated probability of detection must be obtained from typical operation data. These estimates can be misleading since they are highly dependent on test conditions.

It has been demonstrated that the fault detection scheme can detect different types of faults which are common in cooling coils. An increase in the size of the faults results in larger residuals at many operating points and, in all cases, the larger residuals lead to an increase in the estimated probability of detection.

It has been shown that neurofuzzy models with low complexity can be used for fault detection, though the approximation errors and thresholds may become large as the models become less complex (Maruyama 1997b). In such cases, the sensitivity is reduced and it may not be possible to detect small faults.

Acknowledgments

The author would like to thank Dr. Arthur Dexter (Department of Engineering Science, University of Oxford) for the discussions and advice which lead to this work. This research was partially supported by the Conselho Nacional de Desenvolvimento Científico e Tecnológico (CNPq), grant no. 200234/92-7.

References

- Brown, M. and Harris, C.: 1994, "Neurofuzzy adaptive modelling and control", Prentice-Hall.
- Clark, D. R.: 1985, "HVACSIM+ building systems and equipment simulation program reference manual", U.S. Department of Commerce.
- Dexter, A. L.: 1995, "Fuzzy model-based fault diagnosis", IEE Proceedings, Pt. D 142(6), 545-550.
- Ding, X., Eppe, J., Lebrun, J. and Wasacz, M.: 1990, "Cooling coil models to be used in transient and/or wet regimes. theoretical analysis and experimental validation, Proceedings of the international conference of system simulation in buildings", Liege, Belgium, pp. 405-437.
- Ding, X. and Frank, P.: 1991, "Frequency domain approach and threshold selector for robust model-based fault detection and isolation", Preprints of IFAC Symposium SAFEPROCESS'91, Vol. 1, Baden-Baden, FRG, pp. 307-312.
- Frank, P.: 1992, "Robust model-based fault detection in dynamic systems, IFAC symposium on-line fault detection in the chemical process industries", Newark, Delaware, pp.1-13.
- Frank, P. M.: 1990, "Fault diagnosis in dynamic systems using analytical and knowledge-based redundancy - a survey and some new results", Automatica 26(3), 459-474.
- Haves, P., Salisbury, T. and Wright, J.: 1996, "Condition monitoring in hvac subsystems using first principles models", ASHRAE Transactions 102(Pt. 1).
- Himmelblau, D.: 1978, "Fault detection and diagnosis in chemical and petrochemical processes", Elsevier, Amsterdam.
- Hyvärinen, J. and Kärki, S., Eds., "Building optimisation and fault diagnosis source book", IEA Annex 25, Technical Research Centre of Finland, Espoo, Finland.
- Maruyama, N.: 1997a, "Detecting faults in cooling coils - part II - the issues of practical implementation", Submitted to Revista Brasileira de Ciências Mecânicas.
- Maruyama, N.: 1997b, "Fault detection in uncertain systems using neuro-fuzzy modelling", PhD thesis, Department of Engineering Science, University of Oxford.
- Maruyama, N., Benouarets, M. and Dexter, A.: 1996a, "Fuzzy model based fault detection", XI Congresso Brasileiro de Automatica, Vol. 1, SBA, São Paulo, Brazil, pp. 305-310.

- Maruyama, N., Benouarets, M. and Dexter, A.: 1996b, "Fuzzy model-based fault detection and diagnosis", 13th IFAC World Congress, Vol. N. IFAC, San Francisco, USA, pp. 121-126.
- McDowell, J., Kramer, M. and Davis, J.: 1991, "Knowledge-based diagnosis in process engineering", IEEE Expert (6), 65-67.
- Patton, R., Frank, P. and Clark, R. (eds): 1989, "Fault diagnosis in dynamic systems, theory and applications", Prentice-Hall.
- Salsbury, T., Haves, P. and Wright, J.: 1995, "A fault detection and diagnosis method based on first principles models and expert rules", Proceedings of Tsinghua HVAC-95, Beijing, PRC.
- Sorsa, T., Koivo, H. N. and Koivisto, H.: 1991, "Neural networks in process fault diagnosis", IEEE Transactions on Systems, Man and Cybernetics 21(4), 815-825.
- Ullieru, M.: 1993, "Processing fault-trees by approximate reasoning in solving the technical diagnostic problem", 12th IFAC World Congress, Sydney, Australia, pp. 221-224.

Detecting Faults in Cooling Coils of Air-Handling Units - Part II : The Issues of Practical Implementation

Newton Maruyama

Universidade de São Paulo
Escola Politécnica
Departamento de Engenharia Mecânica
05508-900 São Paulo, SP Barzil
maruyama@usp.br

Abstract

Building Energy Management and Control systems have contributed to the reduction of energy use without affecting the occupant's comfort, however, the inability to provide early detection and compensation of faults in air-handling units has not provided extra energy saving. For further improvement of reliability, safety and performance, an early detection and diagnosis of faults is of great interest. A fault detection method which uses static neuro-fuzzy models to describe the correct operation of the plant is proposed to detect faults in cooling coils of air-handling units. Abnormal operation of the plant is detected when residuals exceed a variable threshold value which accounts for modelling errors, noisy measurements and unmodelled disturbances. This work points out, the major issues when designing fault detectors in cooling coils of air-handling units based on neuro-fuzzy models. A methodology is proposed which tries to overcome the drawbacks of neuro-fuzzy models and the intrinsic difficulties of modelling cooling coils. An example is presented using an actual plant. Comments on the method and its performance are given.

Keywords: Fault Detection, Neuro-Fuzzy Modelling, Air-Handling Units.

Introduction

In the companion paper (Maruyama 1997a), a new fault detection method for cooling coils of air-handling units which uses static neuro-fuzzy models has been introduced. The cooling coils of air-handling units can be classified as information poor systems (Howell 1994) where an accurate analytical model is difficult to produce, the data available for training a black-box model are incomplete, and measurements are sparse and of poor quality. Therefore, these systems are characterized by the presence of high uncertainty.

The companion paper has presented some simulation results for both whole operating space and typical operation data of air-handling units to demonstrate the capabilities of the proposed fault detection scheme. The major focus of this paper, on the contrary, is to point out which are the major issues which arises in a practical implementation. Firstly, the characteristics of neuro-fuzzy models and their major limitations are presented. The proposed fault detection method is briefly reviewed. Then, a methodology is proposed which tries to overcome the drawbacks of neuro-fuzzy models and the intrinsic difficulties of modelling cooling coils. An example of the modelling process and some fault detection experiments using an actual plant is presented. Comments on the method and its performance are presented.

Neuro-Fuzzy Modelling

A neuro-fuzzy system is a modelling approach that performs a mapping $X \subset \mathcal{R}^n \rightarrow \mathcal{R}$, where X is the input domain. The model can be interpreted as a rulebase comprising of Q fuzzy production rules of the following form:

$$\text{Rule } q: \text{IF } x_1 \text{ is } A_1^q \text{ AND } x_2 \text{ is } A_2^q \text{ AND } \dots \text{ AND } x_n \text{ is } A_n^q \text{ THEN } y \text{ is } w_q.$$

where $q = 1, 2, \dots, Q$, x_i ($i = 1, 2, \dots, n$) are the inputs variables, y is the output variable, A_i^q are linguistic

terms defined by membership functions $\phi_{A_i^q}(x_i)$ and w_q is a scalar value associated with the output variable. For each \underline{x} , the output $y = h(\underline{x})$ can be calculated as:

$$h(\underline{x}) = \frac{\sum_{q=1}^Q w_q \phi_q(\underline{x})}{\sum_{q=1}^Q \phi_q(\underline{x})} \quad (1)$$

where $h: X \subset \mathcal{R}^n \rightarrow \mathcal{R}, \underline{x} = (x_1, \dots, x_1, \dots, x_n)^T \in X$, $\phi_q(\underline{x}) = \prod_{i=1}^n \phi_{A_i^q}(x_i)$ is a multidimensional membership function.

Equation 1 can be rewritten as:

$$h(\underline{x}) = \sum_{q=1}^Q w_q \phi_q^*(\underline{x}) \quad (2)$$

where

$$\phi_q^*(\underline{x}) = \frac{\phi_q(\underline{x})}{\sum_{q=1}^Q \phi_q(\underline{x})}$$

are normalised multidimensional functions. The resultant equation is the general form for a class of neural networks known as Associative Memory Networks (AMNs) that includes neuro-fuzzy models, B-spline networks, Cerebellar Model Articulation Controller (CMAC), which are lattice networks, and Radial Basis Functions (RBF) (Brown and Harris 1994). In the context of associative memory networks $\phi^*(\underline{x})$ are called basis functions and parameters w_q are called weights. The equivalence between neuro-fuzzy models and AMNs means that the learning algorithms and the mathematical analysis of the AMNs can also be used for neuro-fuzzy models. This means also that they share the same drawbacks. The main issue is that the number of basis functions and the associated amount of training data required grow exponentially as the number of input variables grows linearly. This property is known as curse of dimensionality (Bellman 1961) and it limits the use of these models to low dimensional problems.

Learning from Examples: The Limitations of Estimators Designed with Neuro-Fuzzy Models

Estimators designed with neuro-fuzzy models have intrinsic limitations due to their finite representational capacity and the use of a finite training data set. These limitations are responsible for the generalization errors of the model, when it is used with data that was not presented during the learning process. Geman et al. (1992) use the bias/variance error decomposition to analyse the learning process of feedforward networks. This result is quite general and can be extended to other approximation techniques such as neuro-fuzzy models. The main aspects of this result are summarized here in order to highlight the importance of model structure selection and representative training data.

Given a data set $D = \{(\underline{x}_i, y_i), i = 1, \dots, N\}$, where \underline{x} is the independent variable and y is the response, obtained by sampling N times the set $X \times Y$ according to a probability distribution $P(\underline{x}, y)$. An estimator will be any function $h: X \rightarrow Y$ where the parameters are estimated using D .

The mean squared error of the estimator h is given by the functional:

$$I[h] = E\left[(y - h(\underline{x}))^2 \right] \quad (3)$$

$$= \int_{X \times Y} P(\underline{x}, y) (y - h(\underline{x}))^2 d\underline{x} dy \quad (4)$$

defined as the expected risk.

The expected risk can be decomposed in two parts:

$$I[h] = E\left\{h_o(\underline{x}) - h(\underline{x})\right\}^2 + E\left\{y - h_o(\underline{x})\right\}^2 \quad (5)$$

where $h_o(\underline{x})$ is the regression function $h_o(\underline{x}) = E\{y|\underline{x}\}$.

From Eq. 5, it is possible to conclude that $h_o(\underline{x})$ minimizes the expected risk and is therefore the best estimator, since $h_o(\underline{x})$ is an unbiased estimate. The second term of Eq. 5 is the variance of y and cannot be influenced by the design of the estimator $h(\underline{x})$.

In practice, $P(\underline{x}, y)$ is unknown and $I[h]$ cannot be evaluated. Because only the training data set D is provided, the expected risk must be approximated by the empirical risk:

$$I_{emp}[h] = \frac{1}{N} \sum_{i=1}^N (y_i - h(\underline{x}_i))^2 \quad (6)$$

The problem of finding a regressor h that minimizes the empirical risk is ill-posed because an infinite number of solutions may exist. To avoid this, we must consider a family of parametric functions for the estimators. Neuro-fuzzy models with Q rules will be chosen and represented by $\hat{h}_{Q,N}(\underline{x})$. The index N means that the parameters were estimated using a set D with N elements.

The error between the regression function $h_o(\underline{x})$ and the estimator $\hat{h}_{Q,N}(\underline{x})$ will be called the generalization error:

$$E_D \left\{ h_o(\underline{x}) - \hat{h}_{Q,N}(\underline{x}) \right\}^2$$

where E_D represents expectation over the ensemble of all possible D .

The generalization error can be decomposed in two parts, named bias and variance (Geman et al. 1992):

$$E_D \left[\left(h_o(\underline{x}) - \hat{h}_{Q,N}(\underline{x}) \right)^2 \right] = \underbrace{\left[\bar{h}_{Q,N}(\underline{x}) - h_o(\underline{x}) \right]^2}_{(\text{BIAS})^2} + \underbrace{\frac{1}{n} \sum_{j=1}^n \left[h_{Q,N}^j(\underline{x}) - \bar{h}_{Q,N}(\underline{x}) \right]^2}_{\text{VARIANCE}}$$

where n is the number of estimators in the population and $\bar{h}_{Q,N}(\underline{x})$ is defined by:

$$\bar{h}_{Q,N}(\underline{x}) = \frac{1}{n} \sum_{j=1}^n h_{Q,N}^j(\underline{x}) \quad (7)$$

Each estimator $h_{Q,N}^j(\underline{x})$ is supposed to be designed with an independent training data set D^j . The bias measures the extent to which the average (over all sets) of the neuro-fuzzy models differ from the desired function $h_o(\underline{x})$, and the variance measures the extent to which the network function $h_{Q,N}(\underline{x})$ is sensitive to the particular choice of data set.

The number of rules Q represent the power of approximation (or hypothesis complexity) of the hypothesis class: if Q increases, the power of approximation increases. The bias and variance, and therefore the generalization error, depend on the complexity. The fundamental trade-off, known as the bias/variance dilemma, is that as complexity increases, bias decreases and variance increases; as complexity decreases, bias increases and variance decreases. Therefore, the empirical risk can never be made zero.

Training Data Issues

The first step for the learning process is to collect representative training data. For many pattern recognition problems using neural or fuzzy approaches, like fingerprint recognition, collecting training data may be a straightforward task. For identification of a non-linear dynamic process, collecting training data is usually a very difficult task.

The only way to identify a very accurate neuro-fuzzy model is to collect training data that covers, the whole input subspace, $X \subset \mathfrak{R}^n$ where the prediction is desired. For this purpose, the first step is to choose an appropriate input excitation signal $\underline{u}(t)$ for the plant or for the simulation that represents the behaviour of the system.

In the case of dynamic models, the vector of input, \underline{x} , to the neuro-fuzzy model, is related with the past time information of the input $\underline{u}(t)$ and the output $y(t)$ of the system, for example, if a first-order model is used:

$$\underline{x} = [y(t-1) \underline{u}(t-1)]^T$$

To cover the entire sub-space $X \subset \mathfrak{R}^n$, it is necessary to drive the output $y(t)$ in a range of the input space using just the input $\underline{u}(t)$. The presence of past values of the output of the system, $y(t)$, as neuro-fuzzy model inputs constitutes a major concern because some values of $y(t)$ can be very difficult to reach. In practice, training data will be always incomplete so prior knowledge plays a major role. In the case of static models, past values of inputs and outputs are not used. In general, the inputs of the system are used as model inputs:

$$\underline{x} = \underline{u}(t)$$

In this case, uniform training data can be generated in an open-loop configuration for the whole input sub-space, if inputs of the system $\underline{u}(t)$ can be arbitrarily selected.

The Fault Detection Scheme

Figure 1 shows a schematic diagram of the fault detection scheme. The fault detector uses a static neuro-fuzzy model of correct operation to generate residuals. Abnormal operation is detected when the residuals, generated by comparing the measured output of the actual plant with that predicted by the model, exceed a threshold value which varies with the operating point, so as to take account of the modelling errors.

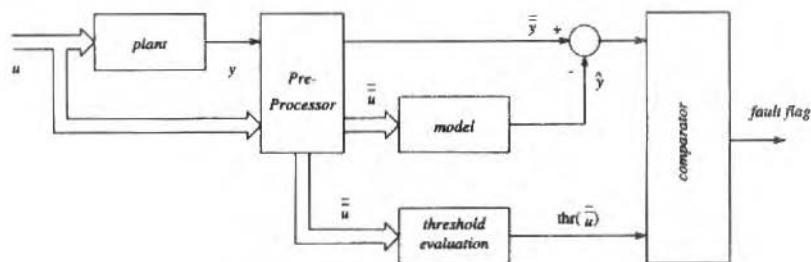


Fig 1 The fault detection scheme.

Threshold Evaluation

The threshold in each part of the operating space is evaluated using the following expression,

$$thr(\underline{x}) = \frac{\sum_{q=1}^Q thr_q \phi_q(\underline{x})}{\sum_{q=1}^Q \phi_q(\underline{x})}, \quad (8)$$

where \underline{x} is the input vector of the model ($\underline{x} = \bar{\underline{u}}$ in Fig. 1). The local threshold thr_q must be calculated adequately considering uncertainties, modelling errors and unmodelled disturbances.

Here, thr_q is calculated as:

$$thr_q = thra_q + thro_q, \quad (9)$$

where $thra_q$ is the component calculated using the available training data, and can be understood as an estimate of the maximum approximation error in each region. Significant amount of data must be available for this estimate to be precise. The other component, $thro_q$, is a fixed value that reflects the uncertainty arising in the estimation of $thra_q$ from the lack of data, the noise and unmodelled disturbances that can corrupt the training data, and the noise and unmodelled disturbances that can arise during operation

The component $thra_q$ is calculated as (Maruyama et al. 1996a):

$$thra_q = \left\{ \max_i \left\{ e_i = \left| \hat{y}_i - y_i \right| \mid i=1, \dots, N \mid \phi_q(\underline{x}_i) > 0 \right\} \right\}, \quad (10)$$

for the training data $D = \{(\underline{x}_i, y_i), i=1, \dots, N\}$ and where \hat{y}_i is the predicted value.

Preprocessor

The preprocessor consists of a moving average filter and a transient detector (see the companion paper (Maruyama 1997a)). The filter removes any high frequency measurement noise and short-term variations caused by unmodelled disturbances, so that the underlying longer term variations in the state of the system may be observed. The transient detector calculates the average activity of each of the measured variables, over a rectangular window, to locate those sections of the data where the system is near enough to steady-state for a static model to be used for prediction. \bar{y} is the average measured output and $\bar{\underline{u}}$ is the average measured input vector.

Comparator

This block compares the average measured outputs, $\bar{y}(t)$ with the predicted output $\hat{y}(t)$ given by each neuro-fuzzy model with the average values as inputs, i.e., $\hat{y}(t) = h(\bar{\underline{u}})$. The comparator sets a fault flag whenever residuals exceed the threshold value,

$$\left| \hat{y}(t) - \bar{y}(t) \right| > thr(\bar{\underline{u}}) \quad (11)$$

The Proposed Methodology

In the following, a methodology to design fault detectors of cooling coils which uses neuro-fuzzy models is proposed. As the modelling of cooling coils presents intrinsic difficulties due to the strong dependence on training data these are the main issues addressed.

Static Models of Cooling Coils

As already pointed, during normal operation the frequency contents of input signals of cooling coils are not complete enough to build a model that can be reliable at all possible frequencies. In fact the

frequencies of input signals are very low and there is always a significant amount of points in near steady-state during operation. As the most common faults of cooling coils introduce changes in steady-state behaviour, static neuro-fuzzy models can be used to detect faults. This implies in neuro-fuzzy models with lower complexity and by consequence less training data is required. The effects of any loss of accuracy during transients can be avoided by using a transient detector to eliminate those portions of data which cannot be represented adequately by a static model.

Normalised Models of Cooling Coils

Most of the models of cooling coils do not use the chilled water supply flow rate \dot{m}_{cws} and temperature T_{cws} as these are not usually measured. They are made constant in the model. Therefore the model in this case can be represented by:

$$T_o = f(T_i, \dot{m}, u_c, \omega), \quad (12)$$

where: T_o is the outlet temperature, \dot{m} is the air mass flow rate, u_c valve control signal and ω is the humidity ratio.

An alternative model of the cooling coil, which reduces the number of inputs from four to three, makes use of variables normalised with the design parameters of the plant (Dexter and Benouarets 1995a). This model can be represented by:

$$\alpha = h(u_c, W, \dot{m}_n), \quad (13)$$

where:

$$\alpha = \frac{(T_i - T_o)}{(T_i - T_{cws})}, \quad (14)$$

is called the air-side approach. T_i is the inlet air temperature, T_o is the outlet air temperature, T_{cws} is the chilled water supply temperature and,

$$W = \frac{(T_o - T_{dew})}{\Delta}, \quad (15)$$

is called wetness condition. T_{dew} is the dew-point temperature and Δ is a user selected parameter whose value accounts for the uncertainty in assessing the wetness of the coil:

$$\dot{m}_n = \frac{(\dot{m} - \dot{m}_{min})}{(\dot{m}_{max} - \dot{m}_{min})}, \quad (16)$$

is the normalised air mass flow rate where \dot{m} is the air mass flow rate, and \dot{m}_{min} and \dot{m}_{max} are respectively the minimum and the maximum design air mass flow rates. The use of the chilled water supply temperature, T_{cws} , in the normalisation allows the model to be used for different values of T_{cws} . The training data for these models is generated using the same method as before, and converted into normalised variables using Eqs. 14-16. The use of a normalised model also contributes to reduce the complexity of the model and therefore the requirements of training data.

One disadvantage is that the training data is incomplete for some regions due to the use of the outlet temperature T_o to generate the input variables.

The Modelling Process

The parameters of the neuro-fuzzy models can only be estimated if representative training data covering the whole operating space of the actual plant is available. Representative training data can

usually only be generated by simulations because the inputs to the simulations can be chosen arbitrarily. However, the training data generated by simulations is sensitive to model mismatch. For the cooling coil, representative training data from plant operation is particularly difficult to obtain under normal operating conditions because some of the inputs are related to weather conditions. Also, the data may be corrupted by noise and unmodelled disturbances.

The solution for this problem is to fuse the partial data from the real plant with the prior knowledge provided by a generic model. This is achieved by initialising the weights of a specific model with the values of the weights of the generic model and then updating them with partial data from the correctly operating actual plant. Methods based on Least Squares algorithms has been proposed to combine prior knowledge and partial training data (Maruyama 1997). The resultant model is an enhanced model with characteristics close to the actual plant at operating conditions where training data recorded from the actual plant is available. In regions where no data from the actual plant is available, the model has characteristics inherited from the generic model. Using this method, the model can be continuously updated and its behaviour will tend to that of the actual plant as more steady-state data representing correct operation are recorded.

Generic fuzzy models are useful in situations where there is insufficient information to design an accurate model of a particular plant (Maruyama et al. 1996, Dexter and Benouarets 1995a). The idea is to develop a model which can represent the behaviour of not just one plant but a class of plants. This is achieved using training data generated by a set of different plants. If a generic model is used to characterise a small class, then the design parameters of the different plants used to generate the training data must be very similar. However, if a large class is required then design parameters of the different plants must be chosen that are different enough to guarantee that the model is sufficiently generic. Since a least-squares algorithm is used for training, this type of generic model can be viewed as an average model of all of the plants in the class.

Since the detection threshold must take into account the prediction errors associated with all of the plants in the class, the value of the threshold must be large enough to ensure that the prediction errors are within the thresholds for all of training data from each of the individual plants. A safety factor can be introduced if it is unclear whether the class includes the actual plant under test. The use of a neurofuzzy model to represent an entire class of plants may result in larger approximation errors and larger thresholds. The sensitivity of the associated fault detector will therefore be directly related to the size of the class.

An Application of the Modelling Process to Cooling Coils

In this section, the modelling process is applied to a cooling coil in an air-conditioning evaluation rig. The air-conditioning evaluation rig is a full-scale test facility at the Building Research Establishment (BRE), Garston, U.K. The design of the rig is typical of a commercial air-conditioning plant and the rig was commissioned by building services engineers to meet industrial standards. A schematic diagram of the air-conditioning rig is given in Fig. 2.

The available measurements are:

- T_s : supply air temperature ($^{\circ}\text{C}$),
- m : air mass flow rate (kg/s),
- T_f : fresh air temperature ($^{\circ}\text{C}$),
- T_r : return air temperature ($^{\circ}\text{C}$),
- RH_s : supply air relative humidity (%),
- u_c : control signal,
- RH_{mix} : mixed air relative humidity (%),
- T_{mix} : mixed air temperature ($^{\circ}\text{C}$),

- u_d : damper control signal,
- T_{cws} : chilled water supply temperature ($^{\circ}\text{C}$).

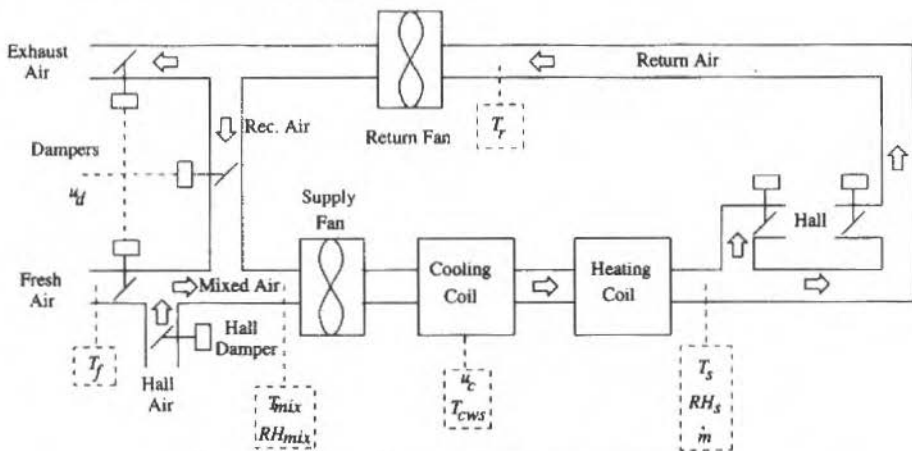


Fig. 2 Schematic diagram of the BRE air-conditioning evaluation rig.

The air-conditioning rig was interfaced to a building emulator program which simulates six $3\text{ m} \times 4\text{ m}$ rooms with internal gains of 25 W/m^2 when unoccupied and 70 W/m^2 when occupied. The simulated solar gains used in the emulator were recorded on a September day with significant cloud cover (low load) and on a cloudless July day (high load). The return air in the test facility is reheated to reflect the air temperature in the simulated room. The test data used in the following experiments were recorded by the BRE staff during the Summer of 1995. For generic neuro-fuzzy models of cooling coils, the normalised model introduced in a later section is adopted. The measured variables are normalised by the following design parameters: chilled water supply temperature T_{cws} , minimum air mass flow rate \dot{m}_{min} and maximum air mass flow rate \dot{m}_{max} . These parameters are called normalisation parameters. For cooling coils, there are many other design parameters like the coil duty, water mass flow rate, valve capacity, etc. that are chosen according to current design practice.

The first step is to produce simulations of suitable plant designs, which generates the data for the generic model. The plant designs must be chosen in order to try to guarantee that the behaviour of the actual plant is within the class of design chosen. Complete information about the design of the actual cooling coil was not available for the plant considered here. The following information is known about the actual plant:

- the chilled water supply temperature T_{cws} fluctuates between approximately 7.0°C and 9.0°C ,
- the maximum air flow rate \dot{m} is approximately 2.5 kg/s ,
- the chilled water flow rate \dot{m}_{cws} is approximately 1.5 kg/s ,
- the duct cross section is $1.2\text{ m} \times 1.2\text{ m}$
- the design specifications are: inlet air temperature $T_i = 21.7^{\circ}\text{C}$, inlet humidity ratio $\omega_i = 0.0078\text{ kg/kg}$, the outlet air temperature $T_o = 8.9^{\circ}\text{C}$, outlet humidity ratio $\omega_o = 0.0071\text{ kg/s}$, chilled water supply temperature $T_{cws} = 8.0^{\circ}\text{C}$, maximum air flow rate $\dot{m} = 2.5\text{ kg/s}$.

Four plants are chosen to design the generic model. One of the plants is based on manufacturer's design data, which means that all parameters of the plant are known, and the others are based on design specifications, which means that only the information about a nominal condition which characterizes the behaviour of the coil is known. The main design specifications of a cooling coil are the following: the inlet air temperature T_i , the inlet humidity ratio ω_i , the outlet air temperature T_o , the outlet humidity ratio ω_o , the maximum air flow rate \dot{m} , the chilled water supply temperature T_{cws} and the face area of the coil A_f . Usually, manufacturers generate design data based on design specifications. The design data

for the plants, for which only design specifications are known, are generated using software developed at Loughborough University (Wright 1994). The chosen plants are the following:

- plant 1 is a cooling coil based on the design specifications for the actual plant. The design specification cited above plus the coil dimensions = 1.2m x 1.2m are used to generate the design parameters of the coil.
- plant 2 is a cooling coil based on the manufacturer's design data for the cooling coil of a small scale experimental air-handling unit at Oxford University.
- plant 3 is a cooling coil based on the design specifications of a cooling coil in the air-handling unit of a commercial office building. The design specifications are: $T_i=23.7^\circ\text{C}$, $\omega_i=0.0091\text{kg/kg}$, $T_o=11.0^\circ\text{C}$, $\omega_o=0.0075\text{kg/s}$, $\dot{m}=3.46\text{kg/s}$, $T_{cws}=5.5^\circ\text{C}$, coil dimensions = 1.02m x 1.0m.
- plant 4 is a cooling coil based on the design specifications for a cooling coil in the air-handling unit of a multi-storey building situated in the City of London. $T_i=24.5^\circ\text{C}$, $\omega_i=0.0088\text{kg/kg}$, $T_o=12.0^\circ\text{C}$, $\omega_o=0.0072\text{kg/kg}$, $\dot{m}=4.2\text{kg/s}$, $T_{cws}=7.0^\circ\text{C}$, coil dimensions = 1.05m x 1.0m.

The main design parameters of the plants are summarized in Table 1. Although the coils are very different in terms of coil duty, air flow rate, water flow rate and height, their behaviour when the air is dry, i.e. with the inlet humidity ratio $\omega = 0.004$, is very similar. However, their behaviour differs when the air is saturated because they have very different design specifications for dehumidification. This ensures more variability for regions where the wetness condition W is negative and reduces the chances of the real plant of being outside the class of coils described by the generic model.

Table 1: Main design parameters of the cooling coil sub-systems.

Design	Plant 1	Plant 2	Plant3	Plant 4
Coil duty (kw)	36.1	5.0	61.4	64.7
Air flow rate (kg/s)	2.5	0.3	3.5	4.2
Chilled water supply temp. ($^\circ\text{C}$)	8.0	5.0	5.5	7.0
Water flow rate (kg/s)	1.5	0.2	2.6	3.4
N ^o of rows	11	10	7	8
Height of coil (m)	1.2	0.3	1.02	1.05
N ^o of circuits	9	2	17	20
Valve capacity (m^3/h)	5.06	1.99	20.19	23.77
Coil resistance (0.001kg.m)	50.59	266.97	3.25	2.31

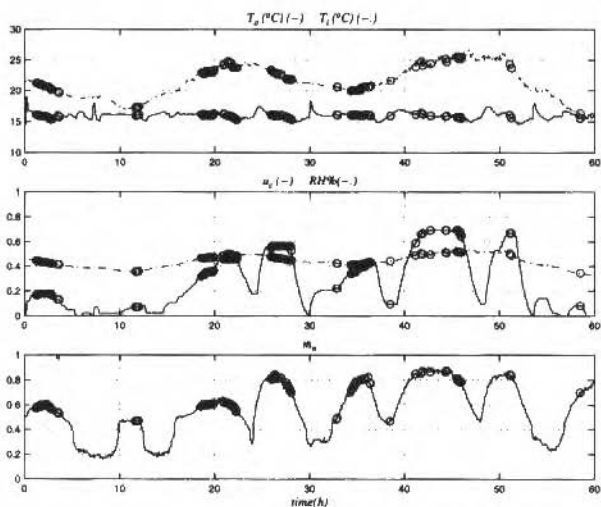
The normalisation parameters for the four plants and the actual plant are summarized in Table 2. \dot{m}_{min} for all plants correspond to 14% of the design air mass flow rate and \dot{m}_{max} correspond to 110% of the design air mass flow rate. The values of \dot{m}_{min} and \dot{m}_{max} are based on the observed values for the air-flow rate during operation of the actual plant. The uncertainty factor, Δ , used to calculate the wetness condition is chosen to be 5°C . With these design parameters simulations are produced using the HVACSIM+ (Clark 1985) program.

Table 2: Normalisation parameters.

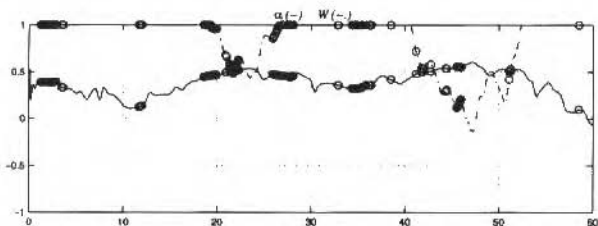
	Plant 1	Plant 2	Plant 3	Plant 4	Actual plant
\dot{m}_{min} (kg/s)	0.350	0.042	0.588	0.490	0.350
\dot{m}_{max} (kg/s)	2.750	0.330	4.620	3.850	2.750
T_{cws} ($^\circ\text{C}$)	8.0	5.0	5.5	7.0	8.0

To produce the enhanced model a set of actual data recorded from the rig and corresponding to correct operation are used as training data. The correct data set corresponds to 60 hours of operation. Measurements were recorded every 60s which resulted in a total of 3600 data points. The measurements are filtered and a transient detector is used to select the steady-state points. The variations in T_{cws} are treated as unmodelled disturbances.

Figure 3(a) illustrates the variables after the correct data set is filtered with a moving average filter with a window length of $N_{w,j}=5$ and Fig. 3(b) illustrates the correspondent normalised variables.



(a) filtered values with $N_{w1} = 5$ and normalised air mass flow rate m_n .
 (o) Correspond to steady-state values.



(b) Test data - normalised variables. Filtered values with $N_{w2} = 30$. (o)
 Correspond to steady-state values.

Fig 3 Correct operation - Data Set 1.

Steady-state points are indicated by circles. The outlet air temperature are estimated from the supply air temperature T_s :

$$\hat{T}_o = T_s \quad (17)$$

This is based on the assumption that the heating coil is always off when the air is being cooled. The cooling coil inlet air temperature T_i is estimated from the measured mixed air temperature T_{mix} using a linear model, to approximate the rise of temperature across the fan:

$$\hat{T}_i = T_{mix} + 0.167 \dot{m} + 0.667, \quad (18)$$

where \dot{m} is the air mass flow rate. The parameters of this equation were estimated by simulating a typical fan. The measurements of the mixed air temperature T_{mix} (see Fig. 2) are usually not very precise because the air, whose temperature is being measured, is a stratified mixture of outside air and recirculated air from the rooms. The dew point temperature T_{dew} is estimated using the following equation (Croome and Roberts 1981):

$$T_{dew} = \frac{4030.0(T_i + 235.0)}{4030.0 - (T_i + 235.0) \log(RH)} - 235.0, \quad (19)$$

with the estimate of \hat{T}_i and the estimate of the inlet air relative humidity \hat{RH} . The inlet air relative humidity RH is estimated from the mixed air relative humidity RH_{mix} :

$$\hat{RH} = RH_{mix} \quad (20)$$

For the same reasons as T_{mix} , the RH_{mix} can also be unreliable.

The steady-state detector uses the following parameters (see the companion paper (Maruyama 1997a)):

$$N_{w1} = 5, \quad (21)$$

$$N_{w2} = 30, \quad (22)$$

$$\tau_D = 200s, \quad (23)$$

$$\xi = 0.01. \quad (24)$$

where N_{w1} is the window length of the moving average filter; N_{w2} is the window length for the average activity calculation; τ_D is the dominant time constant of the plant and ξ is the relative prediction error.

The measurement noise is reasonably small for all measured variables therefore the value of the window length N_{w1} does not need to be very large. Because there are clearly some measurement errors problems the use of a small relative prediction error ξ (0.01) is chosen which guarantees that the detected steady-state points are more likely to be truly in steady-state.

The structure of the model is defined by the following input knots:

$$u_n = \{0.0, 0.1, 0.5, 1.0\}, \quad (25)$$

$$W = \{-1.0, -0.5, 0.0, 0.5, 1.0\}, \quad (26)$$

$$\dot{m}_n = \{0.0, 0.5, 1.0\}. \quad (27)$$

resulting in 60 rules. The basis functions for the input variables are chosen to be triangular.

The steady-state points are normalised and a modified RLS algorithm (Yoon and Clarke 1994) is used to train the network.

The improvement of the performance when trained with Data Set 1 can be observed by monitoring the prediction errors of the generic model and the enhanced model using the mean-squared error defined by:

$$I = \frac{\sum_{i=1}^{N_{ss}} (\hat{\alpha}_i - \alpha_i)^2}{N_{ss}} \quad (28)$$

where $\hat{\alpha}_i = h(\underline{x}_i)$ is the predicted air-side approach for the input \underline{x}_i and α_i is the calculated air-side approach based on measured variables and N_{ss} is the number of steady-state points. Table 3 summarizes the results. It should be noted that there is a significant improvement in the performance for the enhanced model trained using Data Set 1.

Table 3 The mean squared error for the generic and enhanced models.

	Generic Model	Enhanced Model
I	0.0320	0.0054

Calculation of the Thresholds

Here the thresholds are calculated considering all possible factors which can generate false alarms in practice. The following assumptions are made when calculating the threshold for the experiments described here:

- the measurement errors due to noise and other sensor inaccuracies are significantly minimized by the use of the pre-processor module;
- the only significant unmodelled disturbances are those due to variations in the chilled water supply temperature T_{cws} . It is considered that fluctuations on m_{cws} are not significant.

The thresholds are calculated as follows:

1. For the regions where the weights of the enhanced model are inherited from the generic model the thresholds are calculated using Eq. 9 with thra_q given by Eq. 10 and the additional uncertainty component thra_q is chosen to be 0.1. The data used to estimate thresholds is the same as that used to train the generic model.
2. For the regions of the model where weights are estimated using steady-state data from the actual plant, thresholds is calculated using Eq. 9 with thra_q given by Eq. 10 and the additional uncertainty component thra_q is chosen to be 0.05. The component thra_q is chosen smaller because it is assumed that modelling errors are reduced after training.

Fault Detection Experiments

It is intended in this section to demonstrate that the fault detection scheme proposed can detect faults in a real plant without having a detailed knowledge about the plant. In order to assess the performance of the fault detection method some experiments are conducted with a fault detector based on the enhanced neuro-fuzzy model. The test data for correct and faulty operations were recorded from the BRE rig (see Fig. 2). The following faults were introduced artificially:

- **leaky valve:** the Building Energy Management System (BEMS) software controlling the valve action was modified so as to cause a 2°C drop in the supply temperature T , when the valve is commanded to be fully closed and the air mass flow rate is at its maximum value. This is equivalent to the imposition of a minimum water flow rate when the control valve signal u_c is below a pre-defined value u_c^m ;
- **supply air temperature sensor offset:** the BEMS software was modified to add an offset of 2°C to the value measured by the supply air temperature sensor;

In the following, the tests with typical operation data are presented for correct operation, leaky valve and temperature sensor offset.

Test 1 - Correct operation Fig. 4(a) illustrates the test data (Data Set 2) when the coil is operating correctly but conditions are different to those observed in the Data Set 1. The normalised variables are plotted. Fig. 4(b) shows the fault detection results. A data validation flag indicates if an operating point is covered by the model, and a fault detection flag indicates if there is a fault. For this case, no false alarms are detected.

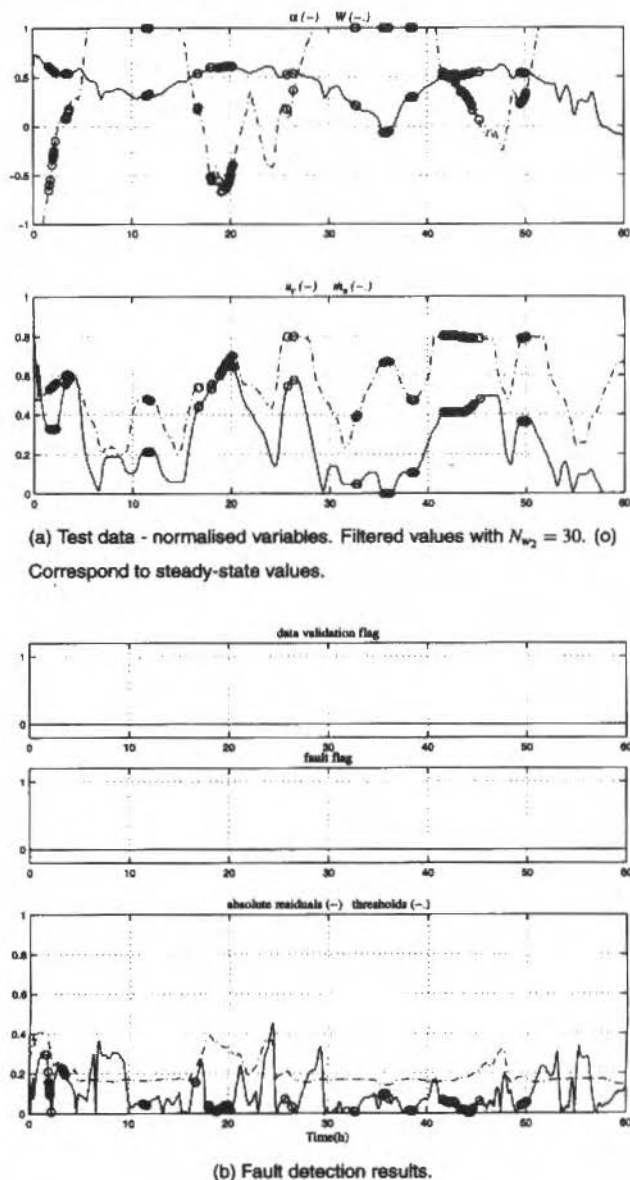
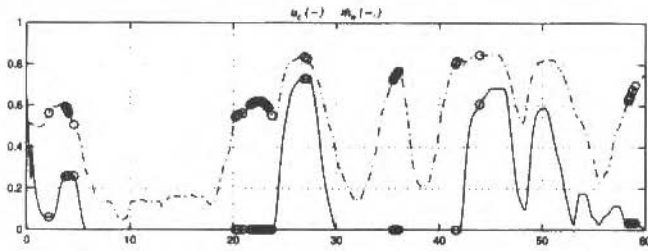
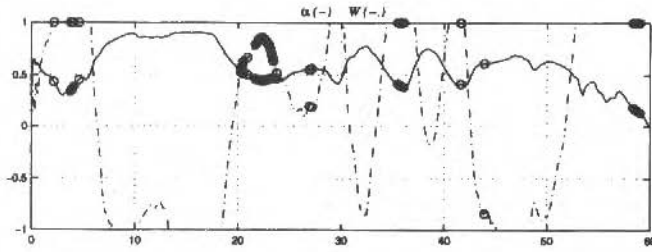


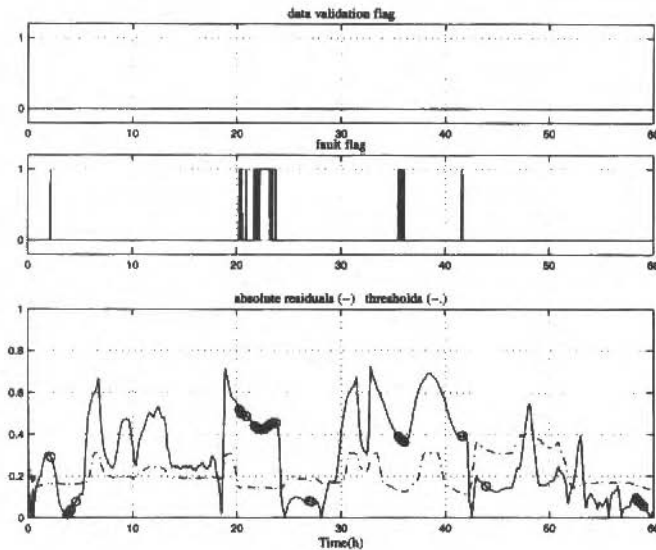
Fig. 4 Correct operation - Data Set 2.

Test 2 - Leaky valve Fig. 5(a) shows the test data when the coil has a leaky valve. Fig. 5(b) illustrates the fault detection results. The valve in this experiment is closed for long periods of

time, which is the optimal condition to detect leakage, and the fault is detected successfully during four different periods:



(a) Test data - normalised air mass flow rate. Filtered values with $N_{w_2} = 30$. (c) Correspond to steady-state values.



(b) Fault detection results.

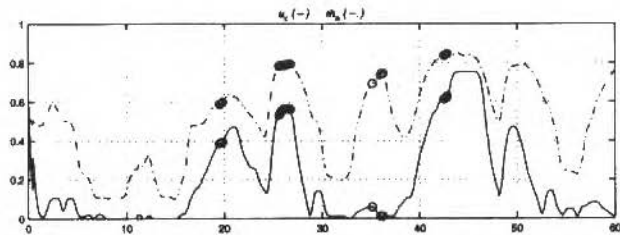
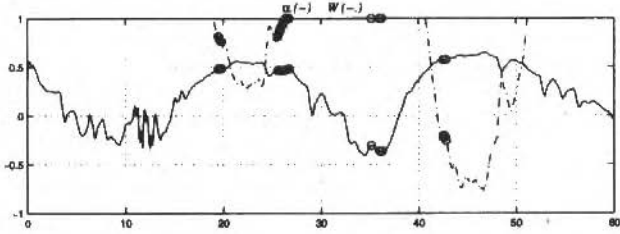
Fig. 5 Leaky valve.

1. Around $t = 2.0\text{h}$ when $u_e = 0.05$,
2. During the interval $[20.0\text{h}, 25.0\text{h}]$ when $u_e = 0.0$,
3. Around $t = 35.0\text{h}$ when $u_e = 0.0$,

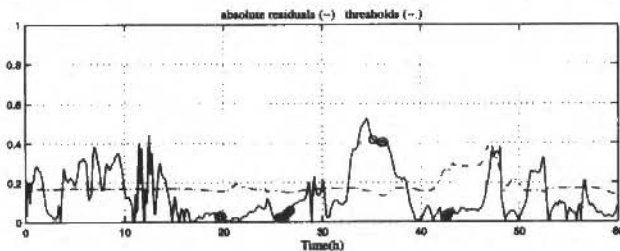
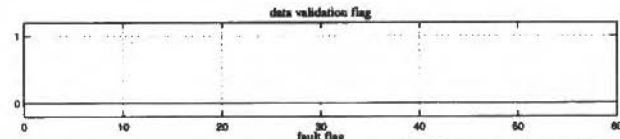
4. Around $t = 42.0\text{h}$ when $u_c = 0.0$.

The fault was set-up so as to provide a drop of 2.0°C when $u_c = 0.0$ although the values of the air-side approach α when the fault is detected suggest that the drop of temperature is much larger. During the interval $[t = 20.0\text{h}, t = 25\text{h}]$ the drop of temperature is around 8.0°C and around $t = 35.0\text{h}$ is around 5.0°C . These larger drops in temperature are more likely to be caused by the way the fault is designed. Also, it is known that during the last twelve hours the coil operates correctly and as expected it is observed that the fault detector generates correct results even when $u_c \approx 0.0$.

Test 3 - Temperature Sensor Offset Fig. 6(a) shows the test data when there is an offset in the output from the supply air temperature sensor. Figure 6(b) illustrates the fault detection results.



(a) Test data - normalised air mass flow rate. Filtered values with $N_{w_2} = 30$. (c) Correspond to steady-state values.



(b) Fault detection results.

Fig. 6 Sensor offset operation.

As the offset is present during the whole test, the fault should be detected at all of the steady-state points. However, the fault is only detected for $t = 37.0h$. So, the fault is only detected when the conditions are favourable (i.e. with small values T , which gives larger differences for α). For the other steady-state points, the scheme is not sensitive enough to detect the fault.

The main problem of the tests with typical operation data is the measuring of performance. This difficulty arises mainly due to dependence of the detection of faults on operating point conditions. One could think of calculating the probability of fault detection using the number of detected points divided by the total number of steady-state points, which might be the only statistics which can be generated in practice, however, this can be misleading because steady-state points are not distributed uniformly, and large values of this probability could be due to a large percentage of particular operating points where faults can be detected easily. The best way to assess the performance of the fault detector would be to have sets of data for correct and faulty operation which cover the whole operating space of the actual cooling coil. In this case, the designed fault detector could be compared with a perfect fault detector over the whole operating space. When testing for typical HVAC operation data it should be possible to determine what is the cause (modelling errors or unmodelled disturbances and measurement errors) of success or failure for each operating point by comparing with the answer of the test with the perfect fault detector. However, this is not possible in practice. In (Maruyama 1997) other fault detection tests with typical HVAC operation are presented together with a comparison with other methods.

Concluding Remarks

A new modelling process has been described for use in situations where there is insufficient training data to generate an accurate model of the actual plant. First, a generic model is generated based on simulations of a set of plants which defines a class. Then, the generic model is updated, using a modified RLS algorithm, with data recorded from the actual plant. The resultant model is an enhanced model with characteristics close to the actual plant in regions where real training data are available, and inherits characteristics from the generic model in regions where there is no training data provided by the actual plant. The enhanced model can be updated continuously and its behaviour will tend to that of the actual plant as more data representing correct operation are recorded.

The experiments in this chapter have shown that the fault detection scheme proposed can detect faults in a real plant without having a detailed knowledge about the plant. Even though the performance is less than ideal the proposed fault detection method may be the only realistic alternative in many real systems since complete design data are rarely available and training data from the plant under test are seldom complete.

Acknowledgments

The author would like to thank Dr. Arthur Dexter (Department of Engineering Science, University of Oxford) for the discussions and advice which lead to this work. This research was partially supported by the Conselho Nacional de Desenvolvimento Científico e Tecnológico (CNPq), grant no. 200234/92-7.

References

- Bellman, R.E., 1961. "Adaptive control process". Princeton University Press.
- Brown, M. and Harris, C.J., 1994. "Neurofuzzy adaptive modelling and control". Prentice-Hall.
- Clark, Daniel R., 1985. "HVACSIM + building systems and equipments simulation program reference manual". U.S. Department of Commerce.
- Croome, D. J. and Roberts, B.M., 1981. "Air conditioning and ventilation of buildings". Pergamon Press.
- Dexter, A.L. and Benouarets, M., 1995a, "Generic modeling of hvac plant for fault diagnosis". In: 4th IBPSA Int. Conference, Madison, Wisconsin, USA.
- Geman, S., E Bienenstock and Doursat, R., 1992, "Neural networks and the bias/variance dilemma. Neural Computation" 4, 1-58.
- Howell, J., 1994, "Model-based fault detection in information poor plants. Automatica 30(6), 929-943.
- Maruyama, N., 1997a. "Detecting faults in cooling coils - part - the method and some simulation results". Submitted to Revista Brasileira de Ciências Mecânicas.

- Maruyama, N., 1997b, "Fault detection in uncertain systems using neuro-fuzzy modelling". PhD thesis. Department of Engineering Science, University of Oxford.
- Maruyama, N., M Benouarets and Dexter, A.L., 1996a, "Fuzzy model based fault detection". In: XI Congresso Brasileiro de Automatica. Vol. 1. SBA, São Paulo, Brasil. pp. 305-310.
- Maruyama, N., M Benouarets and Dexter, A.L., 1996b, "Fuzzy model-based fault detection and diagnosis". In: 13th IFAC World Congress. Vol. N. IFAC. San Francisco, USA. pp. 121-126.
- Wright, J.A., 1994, "Private communication", Department of Civil and Building Engineering, Loughborough University.
- Yoon, T.-W. and Clark D.W., 1994, "Towards robust adaptive predictive control In: Advances in model-based predictive control" (D.W. Clark, Ed.). pp. 402-414. Oxford University Press. Oxford, U.K.

Controle da Espessura de Saída de Tiras Laminadas Utilizando a Lógica Nebulosa

Control of Rolled Strips Thickness Using Fuzzy Logic

Regina Fátima Gibson Gonçalves

Horacio Helman

Universidade Federal de Minas Gerais

Faculdade de Engenharia

Departamento de Engenharia Metalúrgica

30160-030 Belo Horizonte, MG Brazil

hhelman@demet.ufmg.br

Abstract

The thickness of a rolled strip, which must remain within very close limits, is one of the critical parameters in the characterization of its quality. The process of controlling this thickness frequently requires actions which may affect other important characteristics of the strip, such as profile and shape. Two control procedures are commonly used for this purpose, one on the screw-down mechanism and the other on the strip front or back tensions. One or the other may be more adequate, depending on the operational conditions. These control actions have been normally determined and executed in correspondence with the variation of only one of the parameters of the process. In the present work, a method is developed based on the application of fuzzy logic, which allows for the calculation of suitable control actions to adjust the final thickness of the strip, considering the simultaneous variation of any two operational parameters of the process.

Keywords: Strip Rolling, Gage Control, Fuzzy Logic.

Introdução

O mercado consumidor de tiras laminadas vem se tornando cada vez mais exigente em relação à qualidade do produto. Um dos parâmetros que definem esta qualidade é a espessura de saída da tira (h_s). As ações de controle desta espessura podem provocar alterações em outros aspectos importantes, tais como a planicidade e a forma, já que a espessura de saída está diretamente associada ao valor da carga de laminação. Em Helman (1988) são apresentados modelos teóricos para o cálculo dessa carga e analisados os fatores que podem alterar a espessura de saída em uma dada operação. Ribeiro (1990) analisa as causas que podem comprometer a planicidade de tiras laminadas. Batista (1994) apresenta uma discussão dos aspectos que influenciam o coroamento e a planicidade das tiras laminadas a frio.

Várias técnicas de projeto de controladores têm sido empregadas para solucionar o problema do controle da geometria das tiras laminadas a frio: Hasegawa e Taki (1991) desenvolveram um sistema de controle de forma para a laminação a frio de tiras, baseado na lógica nebulosa; Hattori et al. (1992) utilizam um algoritmo de controle nebuloso aliado a uma rede neural para realizar o controle de planicidade no processo de laminação a frio; Denti e Helman (1995a e 1995b) e Denti et al. (1996) apresentam um método de controle da espessura de saída de tiras laminadas a frio, desenvolvido a partir de modelos teóricos, que permite a consideração da variação simultânea de dois parâmetros; Feldmann (1997) apresenta modelos matemáticos para a simulação e o controle de sistemas modernos de laminação de planos, com o objetivo de estimar a maneira pela qual alterações no projeto podem influenciar a produtividade e a qualidade do produto.

Nomenclatura

A e B = coeficientes da equação de Lüdwick, para o cálculo da tensão de escoamento (kgf/mm^2) (adimensional)
 h_i = espessura de entrada (mm)
 h_f = espessura de saída (mm)

g = abertura dos cilindros (mm)
M = módulo de rigidez do laminador (t/mm)
P (t) = carga de laminação
 t_f = tensão a frente (kgf/mm^2)
 t_r = tensão a ré (kgf/mm^2)
 Δh_i = variação da espessura de entrada (%)

Δt = variação da tensão a ré (%)
 $\Delta \mu$ = variação do coeficiente de atrito (%)
 $\Delta \sigma$ = variação da tensão de escoamento (%)
 ϵ = deformação verdadeira (%)
 σ = tensão de escoamento (kgf/mm^2)

O processo de laminação

A espessura de saída de tiras laminadas (h_f) é maior do que a abertura dos cilindros (g), devido à ocorrência de deformações elásticas na própria tira, que são recuperadas após sua saída do laminador, e no laminador, que se deforma quando submetido às cargas de laminação (P). Como, em geral, os valores dessas cargas são elevados, a deformação do laminador é significativa e envolve todos os seus componentes, isto é, estrutura, cilindros, mancais, etc. Esta deformação se traduz em um acréscimo na abertura dos cilindros, e se relaciona com a carga de laminação através de um parâmetro denominado "módulo de rigidez do laminador" (M). Para determinadas condições operacionais, é aceitável supor que este módulo de rigidez seja constante. Neste caso, representando graficamente a relação "carga-deformação" do laminador, para uma dada abertura dos cilindros, obtém-se uma reta, $h_f = g + P/M$, normalmente conhecida como "reta de carga".

O valor da carga de laminação é determinado por diversos parâmetros operacionais relacionados à tira, ao processo e ao laminador. Fixando todos os outros parâmetros, a carga de laminação dependerá apenas da espessura de saída. Pode-se representar esta relação por uma curva "carga-espessura final da tira", normalmente conhecida como "curva de operação".

As duas linhas mencionadas acima, traçadas em um mesmo gráfico, formam o "diagrama de operação", representado na Fig. 1. No ponto de interseção das curvas tem-se o "ponto de operação", ou seja, o par de valores carga de laminação (P) e espessura de saída (h_f) para uma determinada abertura dos cilindros (g).

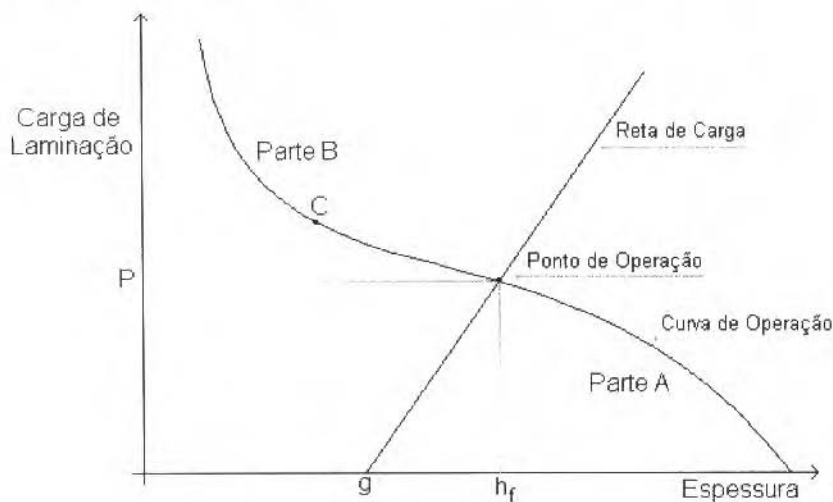


Fig. 1 Diagrama de operação

Outro aspecto a ser considerado no processo de produção está relacionado à forma da tira. Tanto a pressão desenvolvida na laminação como a dissipação do calor gerado na operação não são uniformes ao longo da largura da tira. Como resultado destas não-uniformidades, a tira é deformada diferentemente ao longo de sua largura, o que pode comprometer sua planicidade e gerar tensões residuais.

Controle da espessura de saída

Se acontecer uma variação de algum dos parâmetros de processo, a curva de operação será alterada. Nestas condições, se for mantido o posicionamento dos cilindros, a reta de carga não será modificada. Conseqüentemente, haverá um novo ponto de operação e, portanto, uma nova espessura de saída. Para se manter as dimensões originais, é necessária a determinação da ação que deverá ser executada para a

correção da espessura. Na prática podem ser adotados dois procedimentos de controle: alterar a separação entre os cilindros do laminador, dando origem a uma nova reta de carga (ajuste pela abertura), ou variar as tensões a que fica submetida a tira à entrada (tensão a ré) e/ou à saída do laminador (tensão a frente), introduzindo modificações na curva de operação, no sentido de recuperar o ponto de operação original (ajuste pelas tensões a frente e/ou a ré).

O ajuste pela abertura provoca uma variação na carga de laminação, com conseqüentes alterações no perfil transversal da tira. É possível ainda que esta operação aumente a carga até valores inadmissíveis sob o ponto de vista do laminador, por exceder a capacidade dos motores de acionamento ou o valor da carga de laminação máxima tolerável. Além do mais, há situações em que ajustes da abertura não serão suficientes para alterar a deformação plástica sofrida pela tira, mas modificarão apenas sua deformação elástica.

A modificação da curva de operação também apresenta limitações, pois as tensões não podem ser diminuídas ou aumentadas em qualquer proporção, devido à possibilidade de levar a condições impróprias de operação, tais como torque negativo, ângulo neutro fora do arco de contato, ou até mesmo provocar o rompimento da tira. Além disto, como a relação entre as tensões a frente e a ré e a carga de laminação não são lineares, pode-se estar operando em condições nas quais a correção de espessura por meio de variações nas tensões não seja viável.

Para se decidir entre uma ou outra forma de correção, deve-se levar em conta, entre outros fatores, os efeitos sobre a geometria do produto. Denti et al. (1996) mostraram que o controle por meio do ajuste da abertura é o mais simples, porém provoca alguns efeitos negativos sobre a forma da tira; o controle por meio do ajuste da tensão a frente apresenta algumas limitações e dificuldades adicionais em comparação ao primeiro, mas é o que menos compromete a forma do produto. O controle pela tensão a ré apresenta as mesmas limitações e dificuldades de implementação que o da tensão a frente, além de ser mais prejudicial à forma do produto, não sendo, portanto, usualmente empregado.

A determinação de uma ação de controle quantificada de modo a restabelecer o valor original da espessura de saída, após uma alteração da mesma, apresenta alguns complicadores, já que não há uma relação matemática simples entre as ações e os resultados obtidos. Por exemplo, no caso do ajuste pela tensão a frente, a determinação do valor de tensão que possibilita a correção desejada requer complicados cálculos, caso se deseje utilizar modelos mais elaborados para o cálculo da carga.

Descrição do método de controle proposto

A solução para o problema de correção da espessura de saída de tiras laminadas, frente a alterações dos parâmetros de processo, consiste na determinação do novo valor necessário da abertura dos cilindros ou do novo valor de tensão a frente, conforme o caso. A maioria dos métodos de controle encontrados na literatura apresenta a limitação de considerar a variação de apenas um dos parâmetros de processo de cada vez.

Neste trabalho é apresentada uma generalização do método de solução proposto em Gonçalves e Helman (1996), incluindo a possibilidade de se considerar a variação simultânea de dois parâmetros, desenvolvido com base na metodologia de projeto de controladores nebulosos apresentada por Gomide e Gudwin (1994).

O projeto pode ser esquematizado nas seguintes etapas: construção do modelo nebuloso, transformação dos valores numéricos das variáveis de entrada em valores lingüísticos, determinação do conjunto de regras de controle, avaliação das regras, transformação da ação nebulosa de controle em uma ação executável (valor numérico).

Na construção do modelo nebuloso, cada variável do processo deve ser representada em conjuntos nebulosos, dentro de seu domínio. No problema em questão, estas variáveis representam as variações dos seguintes parâmetros: espessura de entrada da tira, condições de lubrificação do processo (traduzidas em termos de um coeficiente de atrito), tensão de escoamento do material da tira à entrada do laminador e tensão a ré aplicada. A variação da tensão a frente não foi considerada como uma variável de entrada, apesar de ser também um fator que pode provocar alterações na espessura de saída, porque será eventualmente utilizada como ação de controle.

Em seguida, são escolhidas as leis de definição das funções de pertinência e criada uma variável nebulosa que represente semanticamente o conceito associado. Verifica-se que esta etapa é uma das mais críticas no que diz respeito ao sucesso do controlador. Um dos parâmetros de particular importância é o número de conjuntos nebulosos. O universo de discurso de cada variável foi definido com base em valores típicos apresentados em Bryant (1973). Foram escolhidos conjuntos nebulosos de forma triangular, em número ímpar, uniformemente distribuídos em todo o universo de discurso, para representar cada variável.

Na Figura 2 é apresentado um exemplo de representação da variação da espessura de entrada (Δh_i) em valor lingüístico: o universo de discurso corresponde à amplitude da faixa de variação esperada (-10% a +10% de h_i) e foram definidas cinco funções de pertinência triangulares e uniformemente espaçadas.

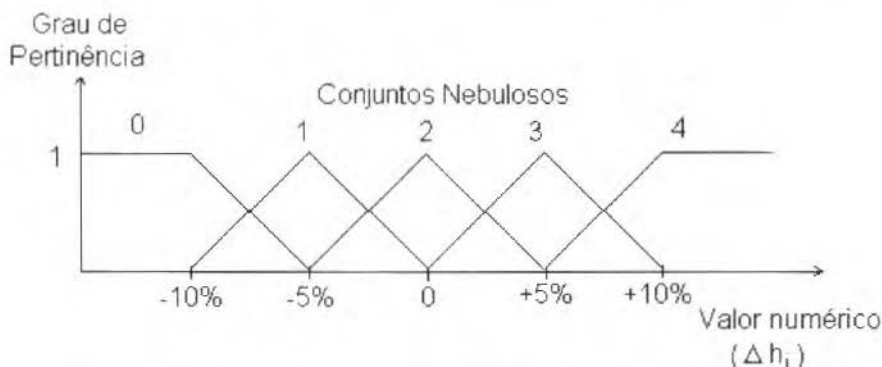


Fig. 2 Exemplo de representação de uma variável em conjuntos nebulosos

Em seguida as variáveis de entrada são transformadas em variáveis nebulosas. O passo seguinte consiste em se escrever as regras que ligam os valores das entradas às propriedades de saída do modelo. Estas regras são escritas em uma linguagem natural, com uma sintaxe do tipo:

Se <proposição nebulosa> então <proposição nebulosa>.

onde as proposições nebulosas são da forma " x é Y " ou " x não é Y ", sendo x uma variável escalar e Y um conjunto nebuloso associado à variável. Um grupo de regras deste tipo forma uma memória associativa nebulosa.

Infelizmente, não há uma orientação geral que possa ser seguida em todas as aplicações, quando se trata da definição dos conjuntos nebulosos e da escolha das regras de controle. Uma das vantagens do método proposto é que necessita-se apenas escolher os números de funções de pertinência para a representação das variáveis de entrada e das ações de controle, sendo a transformação das grandezas numéricas em valores lingüísticos e a escolha das regras executadas automaticamente. Podem ser experimentadas facilmente várias combinações desses números, para que se escolha a que mais se adapte ao problema em questão.

Quando é considerado um conjunto de valores de entrada, cada uma das regras cuja premissa seja pelo menos parcialmente verdadeira será executada. Os resultados das diversas regras devem ser combinados entre si segundo um critério previamente escolhido. Neste caso, foi adotada a composição max-min apresentada em Klir e Folger (1988).

O resultado da aplicação das regras é uma ação de controle representada por um conjunto nebuloso de saída, ou seja, um procedimento descrito em forma lingüística. Este deverá ser convertido em uma ação de controle executável, representada por uma variável solução definida. A parte final da criação do modelo nebuloso básico consiste na escolha do método de se realizar esta conversão. Neste trabalho optou-se pelo método centróide de "defuzzification", apresentado em Klir e Folger (1988).

Uma vez que o projeto do controlador nebuloso esteja construído, começa o processo de simulação e o ciclo inicial de testes. Nesta etapa, o modelo é comparado com casos conhecidos, para validação de seus resultados. Se os resultados não forem os desejados, são feitas modificações, seja na descrição do sistema nebuloso ou nos mapeamentos codificados das regras.

Seleção do procedimento de controle

A curva de operação, apresentada na Fig. 1, pode ser aproximada e qualitativamente dividida em duas partes: uma região quase linear (Parte A) e uma região não-linear (Parte B). Enquanto o ponto de operação se situa na parte A, é possível controlar a espessura de saída agindo-se sobre a abertura dos cilindros. Já na parte B, em razão da curvatura, este mecanismo de controle pode, em alguns casos, tornar-se ineficiente. A posição do ponto C, que separa ambas as partes, depende das características mecânicas do laminador e da sensibilidade dos instrumentos da operação.

No presente trabalho, a escolha de um dos procedimentos de controle é feita em função da localização do ponto de operação: se o mesmo estiver na região quase linear da curva de operação, será escolhida a correção pelo ajuste da abertura dos cilindros. Caso contrário, será escolhida a correção pelo ajuste da tensão a frente. Esta escolha é baseada no fato de que, como o ajuste da abertura dos cilindros é muito mais simples que o ajuste da tensão a frente, esse procedimento de controle deverá ser utilizado sempre que possível.

Aplicação do método proposto

O método desenvolvido foi instrumentado em microcomputador, para a variação simultânea de até dois parâmetros.

Foi elaborado um programa que analisa a variação da carga de laminação em relação à amplitude da perturbação detectada, a fim de encaminhar o controle para o ajuste da abertura dos cilindros ou da tensão a frente (Gonçalves e Helman, s. d.). A partir dos números de conjuntos nebulosos, o programa representa os parâmetros variáveis em valores lingüísticos, escolhe pontos para determinar correções na abertura dos cilindros ou no valor da tensão a frente, utilizando modelos teóricos, e, a seguir, com os valores obtidos propõe um conjunto de regras para o controlador. A partir daí, são simuladas variações dos parâmetros e determinadas as ações adequadas para corrigir as espessuras de saída. Na Fig. 3 é apresentado um fluxograma simplificado do programa.

No programa desenvolvido, os números de funções de pertinência estão limitados a onze, para a representação dos parâmetros variáveis, e a 25, no caso da representação da ação de controle.

Verifica-se que a correção pelo ajuste da tensão a frente apresenta limitações que dependem entre outros fatores do valor da tensão nominal a frente adotado. O programa permite que se escolha automaticamente a tensão nominal a frente que reduza ao máximo as limitações do método. Esta operação aumenta consideravelmente o tempo de processamento.

Como uma maneira de validação do método proposto, cada procedimento de controle foi testado separadamente. A subrotina que determina as correções via ajuste da tensão a frente foi utilizada com os dados dos exemplos apresentados em Denti e Helman (1995a), tendo sido obtidos resultados satisfatórios. Por exemplo, na simulação da laminação de uma tira de aço, cuja tensão de escoamento em estado plano de deformações foi aproximada por uma equação de Lüdwick ($\sigma = A + B\epsilon^m$) com $A = 9,634 \text{ kgf/mm}^2$, $B = 75,166 \text{ kgf/mm}^2$ e $m = 0,2967$, foi considerada uma variação do coeficiente de atrito de 0,1 para 0,112 combinada com uma variação da tensão de escoamento na entrada de 9,634 para 10,405 kgf/mm^2 . A espessura de saída teve sua variação corrigida para 2,499 mm (sendo observado um erro de 0,016% da espessura nominal de saída) na citada referência e foi corrigida pelo método proposto para 2,501 mm (o que corresponde a um erro de 0,021%). Os mesmos dados foram utilizados com a subrotina que determina a correção pelo ajuste da abertura, tendo sido obtidos resultados também satisfatórios (erro de 0,015% para esse mesmo exemplo).

Ambas as subrotinas foram utilizados em vários outros exemplos. Em cada um deles foram aplicados os dois procedimentos de controle, independentemente da localização do ponto de operação, para que os métodos pudessem ser comparados com resultados encontrados na literatura.

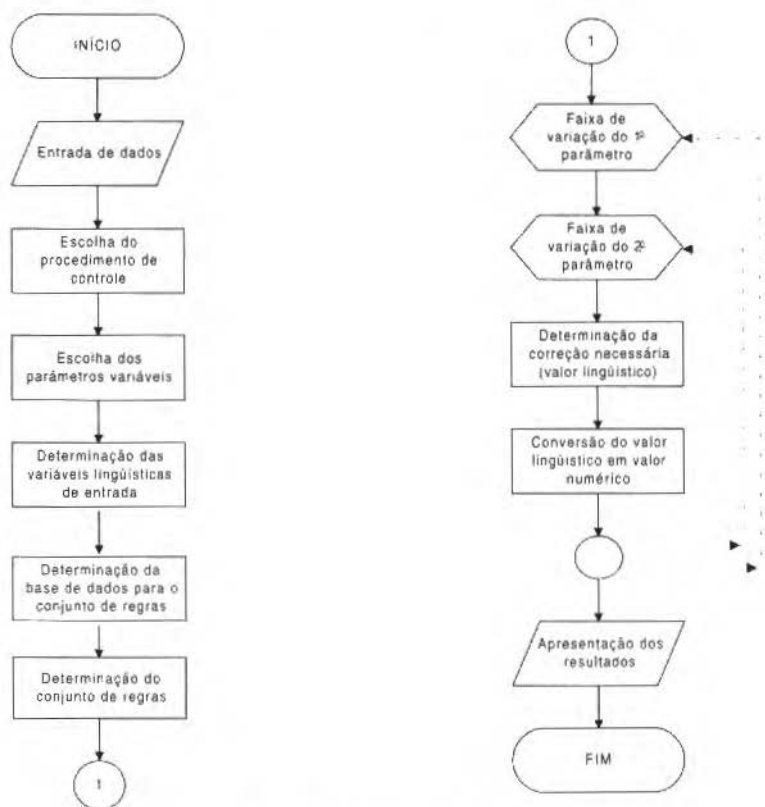


Fig. 3 Fluxograma simplificado

Análise dos resultados

O programa apresenta os resultados indicando as variações dos parâmetros, a correção necessária (novo valor para a abertura dos cilindros ou para a tensão a frente, dependendo do procedimento de controle adotado), a espessura de saída e o erro que ocorreria se não fosse feita nenhuma correção, a espessura de saída obtida após a correção e o erro associado. Inicialmente é gerada uma tabela com 121 combinações de variações dos parâmetros. Após a tabela são informados: o erro máximo em valor absoluto e a média dos valores absolutos dos erros associados. A seguir, pode-se entrar com outros valores de variações dos parâmetros.

A título de exemplo, são apresentados os resultados correspondentes a uma tira de aço com 500 mm de largura, espessura inicial de 3 mm, espessura nominal de saída de 2 mm, sendo laminada com tensão a frente de 20 kgf/mm² e tensão a ré correspondente a 30% da tensão de escoamento à entrada do laminador, cujos cilindros de trabalho têm 100 mm de raio e módulo de rigidez de 500 t/mm. A velocidade de laminação considerada foi de 50 m/min e o coeficiente de atrito adotado foi de 0,1. A tensão de escoamento do material da tira foi aproximada pela mesma equação de Ludwick utilizada no item "Aplicação do método proposto".

Foi simulada a variação simultânea da espessura de entrada (Δh_1) e da tensão de escoamento ($\Delta \sigma$), ambas em uma faixa de -10% a +10% de seus valores nominais, tendo sido escolhidos os valores 15 e 25 para os números de conjuntos nebulosos.

Os resultados obtidos estão apresentados em forma de gráficos, com os seguintes eixos: variação percentual da tensão de escoamento do material da tira em relação ao valor nominal desta tensão ($\Delta\sigma$), variação percentual da espessura de entrada em relação ao valor da espessura nominal de entrada (Δh_1) e erros observados, expressos em percentagem da espessura nominal de saída.

Para ilustrar a maneira pela qual o programa fornece os resultados, são apresentadas duas tabelas, uma para cada subrotina.

Na Figura 4 é mostrado o gráfico do erro na espessura de saída decorrente das alterações dos parâmetros, sem nenhuma correção. Os erros formam um plano inclinado. Reduções em relação a valores nominais, tanto de h_1 como de σ , têm como efeito uma diminuição da espessura de saída. Portanto, os maiores erros estão naturalmente associados às máximas variações destes dois parâmetros: o maior erro positivo (5,779%) corresponde a $\Delta h_1 = +10\%$ e $\Delta\sigma = +10\%$; o erro negativo maior em valor absoluto (-6,295%) corresponde a $\Delta h_1 = -10\%$ e $\Delta\sigma = -10\%$. Há situações em que o efeito da variação de um dos parâmetros tende a ser compensado pela variação do outro, reduzindo o erro associado a valores insignificantes (pontos de interseção do plano dos erros com o plano erro = 0). Pode-se observar que o efeito da espessura de entrada é mais marcante que o da tensão de escoamento.

As espessuras de saída corrigidas e os erros associados estão apresentados na Tabela 1 e nos gráficos das Figs. 5 e 6, para a correção pelo ajuste da tensão a frente, e na Tabela 2 e gráfico da Fig. 7, para a correção pelo ajuste da abertura.

Nas tabelas mencionadas, as espessuras de entrada e as tensões de escoamento estão expressas em termos de suas variações percentuais em relação aos valores nominais, as espessuras de saída antes e após a correção estão dadas em milímetros e os erros respectivos estão expressos em percentagem da espessura nominal de saída.

Nas figuras nota-se que, com a correção, os erros passam a formar superfícies que oscilam em torno do plano de erro nulo, não apresentando tendências nítidas de crescimento em nenhuma direção, em toda a região de aplicabilidade de cada método.

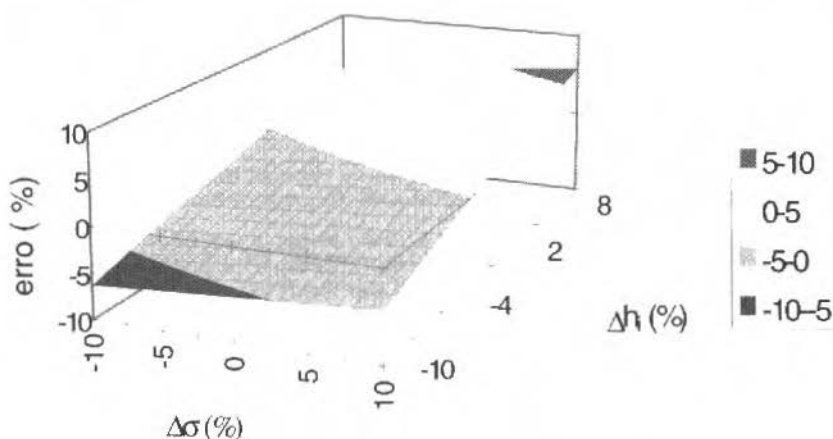


Fig. 4 Erro na espessura de saída, sem correção

A Figura 5 corresponde a resultados obtidos sem otimização da tensão nominal a frente. Neste caso, a aplicabilidade do método limita-se a variações da espessura de entrada na faixa de -3,5% a +10% de seu valor nominal, com a tensão de escoamento variando na faixa de -1% a +10% de seu valor nominal. O erro negativo máximo em valor absoluto verificado foi de -0,427%, que ocorreu para: $\Delta h_1 = 0,65\%$ com $\Delta\sigma = +5,28\%$ e o maior erro positivo foi de 0,385%, para $\Delta h_1 = +0,65\%$ com $\Delta\sigma = +6,67\%$. A média dos valores absolutos dos erros foi de 0,102%.

A Figura 6 apresenta os resultados obtidos para a correção da espessura, já com a tensão nominal a frente otimizada: 40 kgf/mm^2 . Este valor foi determinado automaticamente pelo programa e permite a correção da espessura de saída para variações dos parâmetros em toda a faixa pretendida, ou seja, de -10% a +10% dos valores nominais da espessura de entrada e da tensão de escoamento. Neste caso, o erro negativo máximo em valor absoluto (-0,631%) ocorreu para $\Delta h_1 = 3\%$ com $\Delta\sigma = 6\%$ e o erro positivo máximo (0,869%) ocorreu para $\Delta h_1 = 1\%$ com $\Delta\sigma = 0$. A média dos valores absolutos dos erros foi 0,174% da espessura nominal de saída.

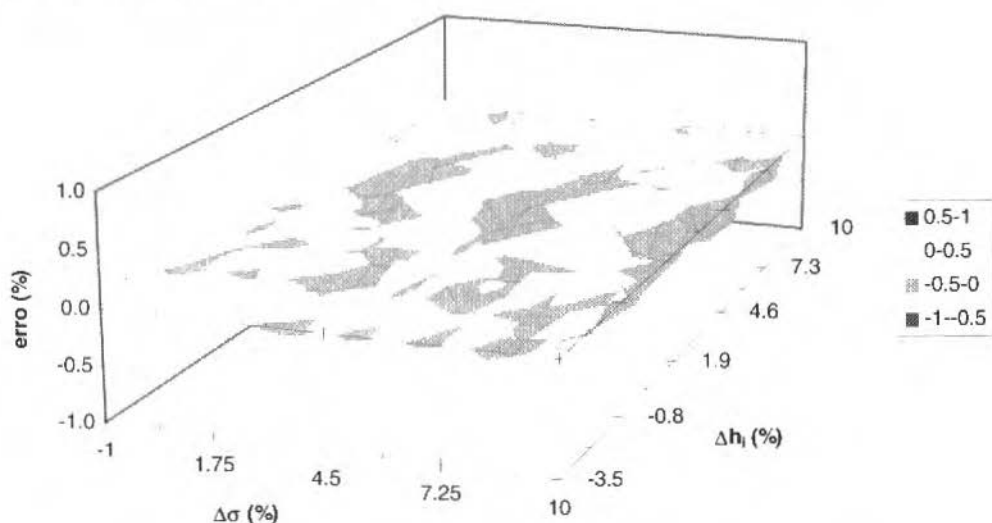


Fig. 5 Erro na espessura de saída corrigida pela tensão a frente, sem otimização da tensão nominal a frente

Pode-se observar que, embora os erros sejam um pouco maiores que na situação anterior, nesta forma foi possível executar satisfatoriamente a ação de controle na totalidade do domínio de variação desejado.

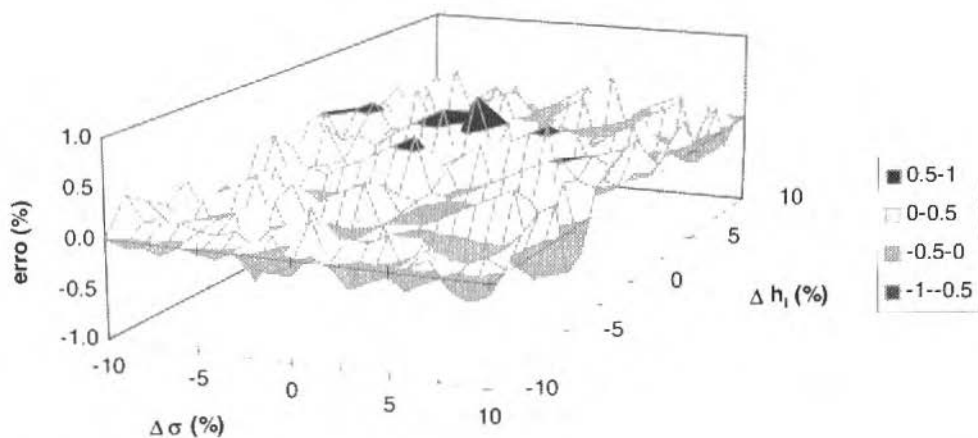


Fig. 6 Erro na espessura de saída corrigida pela tensão a frente, com a otimização da tensão nominal a frente

Para otimizar a tensão a frente e gerar uma tabela de resultados com 121 combinações de valores dos parâmetros, o tempo de processamento foi de 475 s, contra um tempo de 59 s sem a otimização. Nestes tempos de processamento incluem-se as representações das variáveis em conjuntos nebulosos e a determinação das regras de controle. Para ilustrar a saída da subrotina que calcula a correção pelo ajuste da tensão a frente, alguns resultados são apresentados na Tabela 1.

Tabela 1 Correção pelo ajuste da tensão a frente, com a otimização do valor nominal

Δh_i (%)	$\Delta\sigma$ (%)	t (kgf/mm ²)	h_i (s/corr) (mm)	erro (s/corr) (%)	h_i (corrigida) (mm)	erro (corrigido) (%)
-10,0	-10,0	8,7	1,871	-6,466	2,000	0,000
-5,0	-5,0	29,6	1,937	-3,157	2,003	0,133
0,0	0,0	40,0	2,000	0,000	2,000	0,000
5,0	5,0	47,1	2,061	3,025	1,997	-0,129
10,0	10,0	52,2	2,119	5,931	2,000	0,001

A Figura 7 mostra os resultados obtidos com a subrotina que determina correções da espessura de saída pelo ajuste da abertura dos cilindros. Verifica-se que o erro negativo máximo em valor absoluto (-0,678%) ocorreu para $\Delta h_i = -7\%$ com $\Delta\sigma = -1\%$ e o maior erro positivo (0,679%) ocorreu para $\Delta h_i = 3\%$ com $\Delta\sigma = -9\%$. A média dos valores absolutos dos erros foi de 0,142%. Neste caso, o tempo de processamento foi de 15 s, incluindo-se o tempo para a representação das variáveis em conjuntos nebulosos, a determinação do conjunto de regras e o cálculo dos resultados de uma tabela com 121 combinações de valores dos parâmetros. A redução do tempo de processamento em comparação com o tempo gasto na correção pela tensão a frente deve-se a uma redução significativa dos cálculos teóricos necessários à obtenção dos conjuntos nebulosos e dos conjuntos de regras deste método em relação ao anterior.

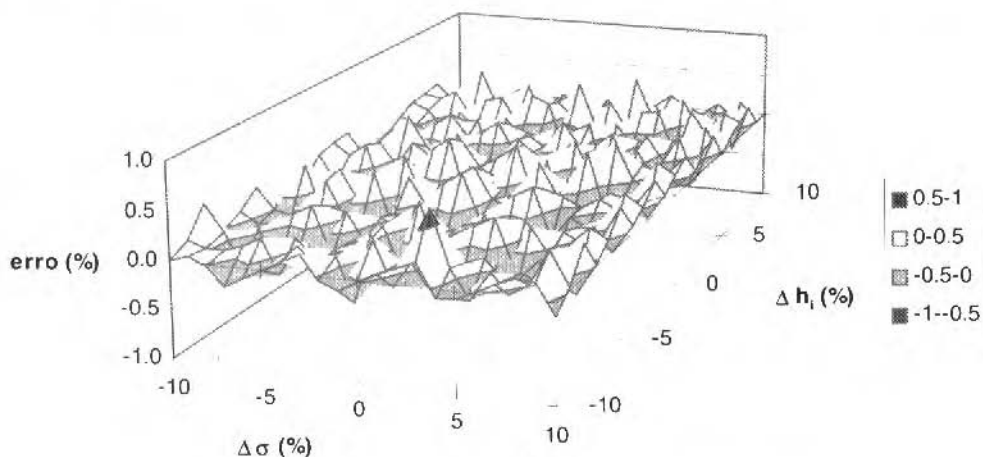


Fig. 7 Erro na espessura de saída corrigida pela abertura dos cilindros

Para ilustrar a saída de resultados da subrotina que calcula a correção pelo ajuste da abertura dos cilindros, são apresentados alguns resultados na Tabela 2.

A utilização do programa em vários outros exemplos mostrou que as superfícies de erro mantiveram sua forma oscilante em torno do plano de erro nulo. Entretanto, a relação entre os números de funções de pertinência escolhidos para representar as variáveis de entrada e as ações de controle afeta significativamente a precisão dos resultados, aumentando ou reduzindo tanto a amplitude das oscilações quanto a média dos valores absolutos dos erros associados. Por exemplo, houve um caso em que o erro na espessura de saída corrigida variou de 1,794% do valor esperado, com a adoção de 7 e 11 funções de pertinência para representar respectivamente os parâmetros variáveis e as ações de controle, para 0,256% desse mesmo valor, com a adoção de 11 e 25 funções.

Tabela 2 Correção pelo ajuste da abertura dos cilindros

Δh_i (%)	$\Delta \sigma$ (%)	Abertura (mm)	h_i (s/corr) (mm)	erro (s/corr) (%)	h_i (corrigida) (mm)	erro (corrigido) (%)
-10.0	-10.0	1.644	1.874	-6.295	2.000	0.000
-5.0	-5.0	1.581	1.938	-3.078	2.001	0.069
0.0	0.0	1.519	2.000	0.000	2.000	0.000
5.0	5.0	1.461	2.059	2.950	2.001	0.060
10.0	10.0	1.403	2.116	5.779	2.000	0.000

Conclusões

O método proposto mostrou-se satisfatório para o controle do processo.

Os resultados obtidos em vários exemplos mostraram a importância de uma escolha adequada dos conjuntos nebulosos. O programa torna esta escolha simples, uma vez que facilita a experimentação de várias representações em busca da melhor delas. No caso da correção pelo ajuste da tensão a frente, a escolha do valor nominal para esta tensão é um fator decisivo na aplicabilidade do método. O programa pode determinar automaticamente o melhor valor (do ponto de vista da correção da espessura de saída) para esta tensão.

Os métodos de correção propostos reduziram em até dez vezes os erros percentuais associados à espessura de saída, em relação aos erros sem nenhuma correção, mostrando-se sempre inferiores às tolerâncias utilizadas na prática industrial (ver ACESITA). Tais resultados permitem enfrentar com segurança os crescentes níveis de exigência na qualidade dimensional dos produtos laminados.

No exemplo apresentado, o método de correção pelo ajuste da abertura conduziu a erros ligeiramente menores que o método de correção pelo ajuste da tensão a frente, com o valor nominal otimizado desta tensão. Entretanto, esta conclusão não pode ser generalizada: há situações em que um dos métodos torna-se sensivelmente mais eficiente que o outro, podendo chegar até a casos em que apenas um deles seja viável. Deve-se, pois, analisar as condições de cada operação para se escolher o método mais apropriado. Esta escolha pode ser realizada automaticamente levando em conta também outros aspectos importantes relacionados à qualidade do produto, além do critério baseado unicamente na localização do ponto de operação ora proposto (Gonçalves e Helman, s. d.).

Referências

- Acesita. Catálogo de produtos, Norma ACESITA (ASTM).
- Batista, J. C., 1994, "Modelo matemático para o controle da planicidade de chapas de aço inoxidável laminadas a frio". Belo Horizonte: Escola de Engenharia da UFMG. (Dissertação, Mestrado em Engenharia Metalúrgica).
- Bryant, G. F., 1973, "Automation of tandem mills. London: The Iron And Steel Institute". 412p.
- Denti Filho, J. e Helman, H., 1995a, "Simulação dos efeitos da tensão a frente como ação de controle da espessura de saída na laminação de tiras". In: Congresso Anual da ABM, 50, São Pedro.
- Denti Filho, J. e Helman, H., 1995b, "Um método computacional para a simulação dos efeitos da tensão a frente como ação de controle da espessura de saída na laminação de tiras". In: CILAMCE- Congresso Ibero Latino Americano sobre Métodos Computacionais para Engenharia, 16, Curitiba, PR, Brasil. Anais... v.1, p.863-70.
- Denti Filho, J., Helman, H., Baptista, E., 1996, "Strip rolling process simulation and exit thickness control actions - A Review". In: lasted International Conference on Modelling and Simulation, Pittsburgh, Pennsylvania, USA. Proceedings, p.227-230.
- Feldmann, F., 1997, "Mathematical models for simulation and control in flat rolling mills". MPT International, p.90-97.
- Gomide, F. A. C., Gudwin, R. R., 1994, "Modelagem, controle, sistemas e lógica fuzzy". SBA Controle & Automação, v.4, n.3., pp. 97-115.
- Gonçalves, R. F. G., "Otimização de seqüências de passes no processo de laminação". Belo Horizonte: Escola de Engenharia da UFMG. s. n. t. (Tese, Doutorado em Engenharia Metalúrgica, em andamento).
- Gonçalves, R. F. G. e Helman, H., 1996, "Aplicação da lógica nebulosa (fuzzy) à correção da espessura de saída na laminação a frio de tiras". In: Congresso Anual da ABM, 51, Porto Alegre. Anais... v.3, p.413-426.
- Gonçalves, R. F. G. e Helman, H. "Técnica para a otimização da laminação de produtos planos". A ser publicado.

- Hasegawa, A., Taki, F., 1991 "Development of fuzzy set theory-based shape control system for cold strip mill". Nippon Steel Technical Report, Tokyo, n.49, p.59-62.
- Hattori, S., Nakajima, M., Katayama, Y., 1992, "Fuzzy control algorithm and neural networks for flatness control of a cold rolling process". Hitachi Review, v.41, n.1, p.31-38.
- Helman, H., 1988, "Fundamentos da laminação de produtos planos". São Paulo: ABM, 396p.
- Klir, G. T. e Folger, T. A., 1988, "Fuzzy sets, uncertainty, and information". London: Prentice-Hall International, 355p.
- Ribeiro, L. A. de M., 1990. "Estudo das causas que afetam a planicidade de tiras laminadas a frio". Belo Horizonte: Escola de Engenharia da UFMG, 100p. (Dissertação. Mestrado em Engenharia Metalúrgica).

Automatic Process for the Determination of Modal Supersets of Residual Flexibilities Used in The Modal Synthesis Method

Paulo Roberto Gardel Kurka
Cleudmar Amaral de Araújo

Universidade Estadual de Campinas
Faculdade de Engenharia Mecânica
Departamento de Projeto Mecânico
13083-970 Campinas, SP Brazil

Abstract

The work presents an automatic process for the selection of modes of substructures with the purpose of building the superset of a residual flexibility model. This superset is used in the modal synthesis method for the experimental analysis of large structures. The qualitative indication of modes to be eliminated in a substructure plays an important role in the precision of the synthesis process. Actual mode elimination techniques are based on arbitrary user decisions which could lead to the extinction of modes which would have an important contribution to the synthesis of the complete structure. The technique is applied here for systems without damping. Such a technique relies on a relative weighting of the modes of the substructures, based on Euclidian norm calculations.

Keywords : Modal Synthesis, Modal Supersets, Residual Flexibility, Identification, Experimental Analysis.

Introduction

The modal synthesis method is a convenient procedure for the modelling of large structures due to the modularity approach used. In such a methodology, the complete system is divided in different substructures whose reduced modal models are grouped and synthesized in order to yield the eigenvalues and eigenvectors of the larger system.

From Hurthy's 1965 original work about modal synthesis many different substructuring methods have been devised: Hintz, 1975; Craig, 1977; Craig and Chang, 1977; Hurty et al, 1971; Craig, 1981; Macneal, 1971; Rubin, 1975; Arruda and Santos, 1993. The work by Craig, 1987, which presents a review of the most important methods, shows that modal synthesis methods can be singled out in the way they force compatibility conditions in the assembling of the equilibrium equations and the assembling of modal supersets which can include static and/or normal modes.

In recent experimental analysis works, Craig (1987) and Duarte (1994) stress that the best modal superset is that of the residual flexibility, which is comprised of the kept normal modes and normal residual flexibility modes which are calculated from modes deleted from the system's original modal base. The referred authors found that the inclusion of residual flexibility modes in the modal base brings as a consequence an improvement to the precision of the numerical results obtained. One of the problems associated with this procedure however is the correct choice of the modes to be deleted from the modal base of each substructure. If the choice is not correctly performed, the modal base obtained for the extended structure might not be in good agreement with the expected results. This is due to the fact that the deleted mode might have had a higher level of deflection energy in its boundary than in its internal coordinates. This fact may yield a final synthesis with reduced sensitivity which will have an undesired influence to the precision of the model obtained.

The present work develops a process for automatic elimination of the modes of substructures in order to yield an optimized residual flexibility modal base. A modal base weighting factor is introduced which is based on the L2 norm (Kreyszig, 1993).

Component Mode Synthesis

Modal synthesis methods can be classified according to the chosen modal supersets as well as the different substructure coupling techniques used. The analysis presented here considers, for the sake of simplicity, a freely vibrating undamped system. The method developed in this work is similar to Craig and Chang's, 1977 which also considers freely vibrating undamped substructures.

Manuscript received: April 1996, revised July 1998. Technical Editor: Agenor de Toledo Fleury.

Two components (a) and (b) are coupled together via a common interface, forming a global structure, according to Fig. 1. The rigid body modes of the free-free condition of each component are considered to be imbedded in their normal modal matrices.

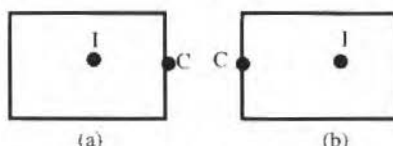


Fig. 1 Substructures (a) and (b) : I - Internal coordinates , C - Boundary coordinates.

The equation of movement of each substructure can be written considering its internal and coupling degrees of freedom:

$$\begin{bmatrix} m_{ii} & m_{ic} \\ m_{ci} & m_{cc} \end{bmatrix} \begin{Bmatrix} \ddot{u}_i \\ \ddot{u}_c \end{Bmatrix} + \begin{bmatrix} k_{ii} & k_{ic} \\ k_{ci} & k_{cc} \end{bmatrix} \begin{Bmatrix} u_i \\ u_c \end{Bmatrix} = \begin{Bmatrix} f_i \\ f_c \end{Bmatrix} \quad (1)$$

Normal modes are obtained from the solution of the eigenproblem associated to (1):

$$\{ [K] - \omega_j^2 [M] \} \{ \Phi \}_j = \{ 0 \}. \quad (2)$$

Normal modes form a vector base matrix Φ which has the following orthogonality properties:

$$\begin{aligned} \Phi^T [M] \Phi &= I \\ \Phi^T [K] \Phi &= \Lambda, \end{aligned} \quad (3)$$

where

$$\Lambda = \begin{bmatrix} \omega_1^2 & & & \\ & \omega_2^2 & & \\ & & \ddots & \\ & & & \omega_n^2 \end{bmatrix}. \quad (4)$$

Nomenclature

C_{dd} = Submatrix of dependent restriction	u = Physical coordinates	i = Relative to the internal nodes
C_{dk} = Submatrix of independent restriction	Z_f = Boundary residual flexibility	c = Relative to the boundary nodes
\bar{f} = Relative nodes force vector	ω = Natural Frequencies	r = Relative to the rigid body modes
F = Force vector	μ = Subst. generalized mass matrix	n = Relative to the normal modes
G = Flexibility matrix	α = Subst. generalized mass matrix	f = Relative to the residual flex. modes
G_f = Residual flexibility matrix	Φ = Normal modes	k = Relative to the kept normal modes
I = Identity matrix	Φ_{dc} = Deleted modes relative to boundary	d = Relative to the deleted normal modes
K = Substructure stiffness matrix	$\bar{\Phi}_k$ = Kept modes	j = Relative to (j) mode
\bar{K} = Synthesized system stiffness	Φ_f = Residual flexibilitie modes	
\bar{M} = Substructure mass matrix	Ψ = Residual flexibility superset.	Superscript
\bar{M} = Synthesized system's mass matrix	$\bar{\Psi}$ = Inverse residual flexibility superset.	T = Transpose matrix
p = Modal coordinates synthesized	P = Relative weight matrix	-1 = Inverse matrix
q = Modal coordinates (substructure)	Φ_d = Extracted normal modes	.. = First ordem derivate
R = General restrictions matrix	Λ = Eigenvalues matrix	.. = Second ordem derivate
S = Equilibrium matrix	Subscript	a = Substructure first
		b = Substructure second
		+ = Pseudo inverse matrix

The normal modes can be separated into the categories of flexible and rigid. Rigid modes are those associated to null eigenvalues. Equation (3) can be rewritten in terms of the flexible and rigid partitions of matrix Φ :

$$\begin{bmatrix} \Phi_r^T \\ \Phi_n^T \end{bmatrix} K \begin{bmatrix} \Phi_r \\ \Phi_n \end{bmatrix} = \begin{bmatrix} \Lambda_r & \\ & \Lambda_n \end{bmatrix} \quad (5)$$

where subscripts "r" and "n" represent association to rigid and non-rigid modes.

The Flexibility matrix is defined as:

$$\{G\} = \{K^{-1}\} = \Phi_n \Lambda_n^{-1} \Phi_n^T \quad (6)$$

where

$$\Lambda_n^{-1} = \begin{bmatrix} \ddots & & \\ & \frac{1}{\omega_i^2} & \\ & & \ddots \end{bmatrix}$$

A selection of "d" modes from Φ_n and d elements from the diagonal matrix Λ_n form the residual flexibility matrix:

$$G_f = \Phi_d \Lambda_d^{-1} \Phi_d^T \quad (7)$$

where subscript "d" denotes the submatrices extracted from Φ_n and Λ_n

The residual flexibility matrix might be multiplied by a restriction matrix f_c defined as:

$$f_c = \begin{bmatrix} 0 \\ I_c \end{bmatrix} \quad (8)$$

where I_c is an identity matrix associated to the coupling degrees of freedom yielding the residual flexibility matrix

$$\Phi_f = G_f f_c \quad (9)$$

A residual flexibility superset is thus defined from the residual flexibility matrix, rigid modes and kept flexible modes:

$$\Psi = \begin{bmatrix} \Phi_f \\ \Phi_r \\ \Phi_k \end{bmatrix} = \begin{bmatrix} \Phi_f & \bar{\Phi}_k \end{bmatrix} \quad (10)$$

where Φ_k are the complementary modes to Φ_d with regards to Φ_n and $\bar{\Phi}_k$ are the combination that kept flexible modes and the rigid bodies modes.

The modal residual flexibility superset defined in the previous equation may be used to define the modal model of each component substructure:

$$\begin{aligned} \mu \ddot{q} + \alpha q &= \Psi^T F \\ \mu &= \Psi^T M \Psi \\ \alpha &= \Psi^T K \Psi \end{aligned} \quad (11)$$

where,

$$\mu = \begin{bmatrix} \mu_f & 0 \\ 0 & I_k \end{bmatrix} \quad \alpha = \begin{bmatrix} Z_f & 0 \\ 0 & \Lambda_k \end{bmatrix} \quad (12)$$

$$Z_f = \Phi_f^T K \Phi_f = \Phi_{dc} (\Lambda_d)^{-1} \Phi_{dc}^T$$

$$\mu_f = \Phi_f^T M \Phi_f = \Phi_{dc} (\Lambda_d)^{-2} \Phi_{dc}^T$$

$$q = \begin{bmatrix} q_f \\ q_k \end{bmatrix}$$

Observation of the previous equations show that the mass and stiffness matrices can be obtained from the modal residual flexibility and the kept normal modes. Such a particular behaviour make this modal superset attractive for experimental analysis purposes. A structure's modal base can be identified through time (Gomes, 1996) or frequency (Santos, 1993) domain modal analysis. The connection of substructures is obtained from compatibility restrictions and interface force conditions:

$$u_c^a - u_c^b = 0$$

$$f_c^a + f_c^b = 0 \quad (13)$$

The equations of motion can be expressed in modal coordinates as:

$$\mu_f \ddot{q}_f + Z_f q_f = \Phi_f^T F$$

$$I_k \ddot{q}_k + \Lambda_k q_k = \bar{\Phi}_k^T F \quad (14)$$

The modal coordinates response, relative to the residual flexibility modes, can be approximated by a pseudo-static response. Such a response can be written, ignoring the acceleration terms, as:

$$Z_f q_f = \Phi_f^T F \quad (15)$$

where,

$$F = \begin{bmatrix} 0 \\ e_c \end{bmatrix}$$

with $e_c^T = [I \ I \ \dots \ I]$. Manipulation of Eqs. (12) and (15) leads to:

$$\Phi_{dc} (\Lambda_d)^{-1} \Phi_{dc}^T (q_f - e_c) = 0 \quad (16)$$

The first term of equation (16) is non-singular, implying that:

$$q_f = e_c \quad (17)$$

The compatibility conditions can then be written as:

$$\begin{aligned} u_c^a - u_c^b &= 0 \\ q_f^a + q_f^b &= 0 \end{aligned} \quad (18)$$

The modal coordinates vector for each substructure can be separated in residual flexibility and kept normal modes:

$$\bar{q} = \begin{Bmatrix} q_f^a \\ q_f^b \\ q_k^a \\ q_k^b \end{Bmatrix} \quad (19)$$

Equations (18) and (19) lead to:

$$\begin{aligned} u_c^a - u_c^b &= \begin{bmatrix} \Phi_f^a & -\Phi_f^b & \bar{\Phi}_k^a & -\bar{\Phi}_k^b \end{bmatrix} \bar{q} = 0 \\ q_f^a + q_f^b &= [I \quad I \quad 0 \quad 0] \bar{q} = 0 \end{aligned} \quad (20)$$

The restriction matrix [R] can thus be written as:

$$R = \begin{bmatrix} C_{dd} & C_{dk} \end{bmatrix} = \begin{bmatrix} \Phi_f^a & -\Phi_f^b & \bar{\Phi}_k^a & -\bar{\Phi}_k^b \\ I & I & 0 & 0 \end{bmatrix} \bar{q} = 0 \quad (21)$$

It can be said from the previous equations that the general restrictions matrix [S] can be written as:

$$\begin{aligned} S &= \begin{bmatrix} -C_{dd}^{-1} C_{dk} \\ I_k \end{bmatrix} \\ \bar{q} &= S \quad p \\ p &= \begin{bmatrix} q_k^a \\ q_k^b \end{bmatrix} \end{aligned} \quad (22)$$

The displacements equation can be written in terms of the general restrictions matrix:

$$\bar{M} \ddot{p} + \bar{K} p = 0 \quad (23)$$

where, $\bar{K} = S^T \alpha S$

The eigenvalues associated to Eq. (23) are the modal base of the original system.

Selection of the Residual Flexibility Modes

Modal synthesis methods that use the residual flexibility modal superset have the user to define which modes are to be removed from the modal base. In this case, even when sufficient number of modes are kept for the base representation there is always the risk that important modes would be deleted, that otherwise would have been important in the construction of the original system. It can be seen from equation (2) that the modal base coordinates vector is related to the physical coordinates vector of each substructure, through the inverse of the modal matrix. It is thus possible to observe that the inverse modal matrix provides a weighting of the internal and boundary physical coordinates in the

expression of the degrees of freedom of the modal coordinates. A selection criterion for the modes to be deleted could be thus based on the influence of the boundary physical coordinates on each individual mode. Strong candidates for elimination will be those modes which receive the greatest influence from the boundary physical coordinates. This is due to the fact that, in assembling the superstructure, the boundary degrees of freedom of each substructure are necessary and directly subjected to new conditions imposed by the coupling. The interior degrees of freedom, by their time, will suffer the effects of coupling only in an indirect way. Keeping the modes which possess a greater influence from the internal degrees of freedom represents the maintenance of the least uncertainty information of the modal base which will belong to the superstructure.

Defining a Criteria for Mode Elimination

A criteria has been defined for verifying the influence of the boundary degrees of freedom in the modal base. The physical coordinates of a substructure can be written as:

$$u = \Psi q, \quad \begin{Bmatrix} u_i \\ u_c \end{Bmatrix} = \begin{bmatrix} \Psi_i \\ \Psi_c \end{bmatrix} q \quad (24)$$

The modal coordinates can be rewritten as:

$$q = \begin{bmatrix} \bar{\Psi}_i^T & \bar{\Psi}_c^T \end{bmatrix} \begin{Bmatrix} u_i \\ u_c \end{Bmatrix} \quad (25)$$

where $\bar{\Psi}_i^T$ and $\bar{\Psi}_c^T$ are partitions of the inverse of $\begin{bmatrix} \Psi_i \\ \Psi_c \end{bmatrix}$. Such partitions refer to the internal

and boundary regions of the physical coordinates. The second parcel of equation (25) weights the values of the boundary u_c in the composition of the modal coordinates q_m . The relative weight between the two parcels of the modal base can be specified using the Euclidian norm (Kreyszig, 1993). Such a weight can be defined for a particular mode as:

$$P_j = \frac{\sqrt{\bar{\Psi}_{1j}^2 + \bar{\Psi}_{2j}^2 + \dots + \bar{\Psi}_{cj}^2}}{\sqrt{\Psi_{1j}^2 + \Psi_{2j}^2 + \dots + \Psi_{ij}^2}} \quad (26)$$

where $\bar{\Psi}_{cj}^2$ e $\bar{\Psi}_{ij}^2$ are generic elements of row "j" of partitions that inverses modal matrices relatives the boundary coordinates and the internal coordinates, respectively. A search along m modes will thus indicate those which have a higher influence from boundary conditions. Those are candidate modes for deletion, according to the proposed criterion. The number of modes to be deleted on the modal base of each substructure is a user decision. The modes to be deleted, according to such a decision, are those with the largest weights defined according to equation (26).

Numerical Results

A Fortran code (Program STRUCT) has been written for performing modal synthesis, according to the theory described. Eigenproblems are solved from Eispack (1976) routines and data input is made from ASCII data files. The program allows for automatic mode elimination according to the user given number of modes to be deleted. A numerical example has been used to illustrate the performance of the code and the mode elimination criterion. Such an example is similar to the one presented by Santos (1993), without considering damping effects. The discretized system is shown in Fig. 2, which is comprised of two linked substructures. The first substructure has two internal and one boundary coordinate. The second substructure has three internal and one boundary coordinate.

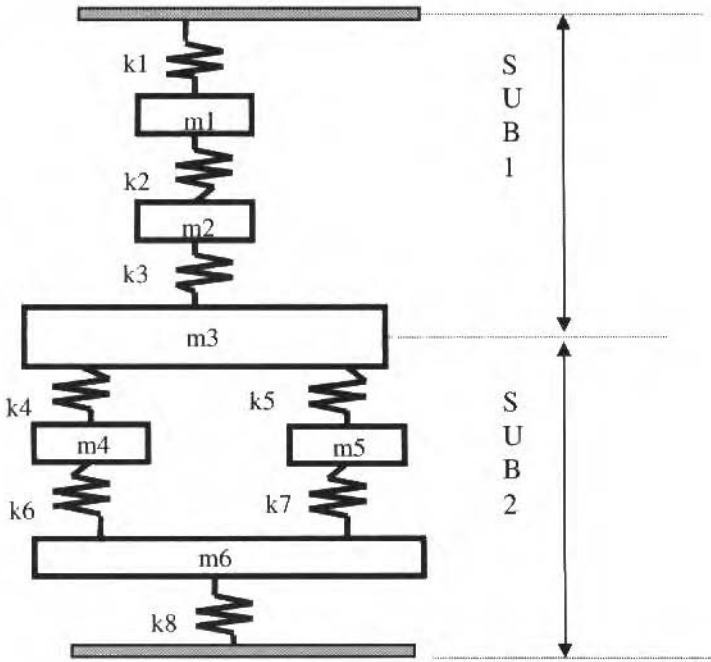


Fig. 2 Discret system

Each station has one degree of freedom and the physical parameters are:

$$m_1 = 10 \text{ kg} , m_2 = 10 \text{ kg} , m_3 = 10 \text{ kg} , m_4 = 10 \text{ kg} , m_5 = 10 \text{ kg} , m_6 = 10 \text{ kg}$$

$$k_1 = 10000 \text{ N/m} , k_2 = 10000 \text{ N/m} , k_3 = 20000 \text{ N/m} , k_4 = 20000 \text{ N/m} , k_5 = 12000 \text{ N/m} ,$$

$$k_6 = 10000 \text{ N/m} , k_7 = 15000 \text{ N/m} , k_8 = 20000 \text{ N/m}$$

The physical coordinate vector for the substructures are:

$$\begin{aligned}
 u_1 &= \left\{ u^1 \quad u^2 \quad u^3 \right\}^T \\
 u_2 &= \left\{ u^4 \quad u^5 \quad u^6 \quad u^3 \right\}^T
 \end{aligned}
 \tag{27}$$

Tables 1 and 2 show, respectively, eigenvalues and eigenvectors for substructures 1 and 2. In those tables are also displayed the calculated relative weights for each mode. If two modes are to be kept in substructure 1 and three modes in substructure 2, then the program indicates that the second mode of substructure 1 and the fourth mode of substructure 2 should be extracted. Such an indication is based on their

Table 1 Eigenvalues and eigenvectors of substructure 1

Mode	1	2	3
Eigenvalue(rd/s)	208.71	2000.00	4791.29
	- 0.11042	0.28288	- 0.08843
Eigenvector	- 0.19777	0.00002	0.24686
	- 0.22066	- 0.14136	- 0.17655
Weight	0.97	0.50	0.67

Table 2 Eigenvalues and Eigenvectors of substructure 2

Mode	1	2	3	4
Eigenvalue(rd/s)	317.67	2540.43	4261.04	6280.83
	0.15621	-0.23506	-0.55675	-0.13162
Eigenvector	0.17615	0.16925	0.13333	-0.15034
	0.09784	-0.09368	0.20859	0.19496
	0.18707	0.08560	-0.18871	0.14855
Weight	0.73	0.28	0.74	0.53

calculated relative weights. Table 3 shows the eigen information of the complete structure without

Table 3 Eigenvalues and mass-normalized eigenvectors of the global system.

Mode	1	2	3	4	5	6
Eigenvalue(rd/s)	270.9	1453.7	2398.0	3153.1	4561.7	5962.5
	0.0769	-0.2354	-0.1326	-0.1216	-0.0780	0.0148
	0.1329	-0.1286	0.0528	0.1402	0.1998	-0.0585
	0.1430	0.0183	0.0822	0.0501	-0.1170	0.0792
Eigenvector	0.1149	0.1190	-0.2140	0.0872	-0.0431	-0.1318
	0.1311	0.0781	0.0922	-0.2203	0.0556	-0.1288
	0.0718	0.0843	-0.1088	-0.0664	0.1472	0.2233

using components modal synthesis. Tables 4 to 7 present eigen information of synthesized systems, for combinations which yield the four highest MAC values.

Table 4 Eigenvalues and Eigenvectors of the synthesized system - criterion selected elimination of the 2nd mode of substructure 1 and 4th mode of substructure 2.

Identified Mode	1	2	4	5	6
Eigenvalue (rd/s)	270.9	1465.0	3105.0	4562.0	5962.0
	0.0741	-0.6308	-0.1423	-0.0790	0.0142
	0.1282	-0.3737	0.1366	0.1988	-0.0630
	0.1378	0.0285	0.0640	-0.1156	0.0861
Eigenvector	-0.1109	0.4057	0.0300	-0.0462	-0.1452
	0.1264	0.1836	-0.1753	0.0577	-0.1363
	0.0690	0.2690	-0.0831	0.1453	0.2388
MAC	1.000	0.9889	0.9393	0.9998	0.9998

Table 5 Eigenvalues and Eigenvectors of the synthesized system - elimination of the 1st mode of substructure 1 and 1st mode of substructure 2

Identified Mode	2	3	4	5	6
Eigenvalue (rd/s)	1425.0	2394.0	3137.0	4561.0	5961.0
	-0.6159	-0.2827	-0.1566	-0.0789	-0.0138
	-0.3797	0.1214	0.1926	0.2055	0.0493
	-0.0137	0.1869	0.0780	-0.1179	-0.0708
Eigenvector	0.2557	-0.4368	0.1309	-0.0423	0.1117
	0.1467	0.2039	-0.2767	0.0593	0.1088
	0.1854	-0.2220	-0.0758	0.1521	-0.1948
MAC	0.9808	0.9984	0.9953	0.9998	0.9997

Table 6 Eigenvalues and Eigenvectors of the synthesized system - elimination of the 2nd mode of substructure 1 and 2nd mode of substructure 2

Identified Mode	1	2	3	4	5
Eigenvalue (rd/s)	273.2	1494.0	2410.0	3241.0	4575.0
	0.5662	-0.2961	-0.1267	-0.0999	-0.0190
	0.9797	-0.1511	0.0524	0.1251	0.0489
	1.0539	0.0331	0.0793	0.0358	-0.0289
Eigenvector	0.8860	0.1258	-0.2205	0.0856	-0.0070
	1.0089	0.0717	0.1114	-0.1650	0.0151
	0.5118	0.1209	-0.1251	-0.0987	0.0288
MAC	0.9994	0.9900	0.9945	0.9650	0.9887

Table 7 Eigenvalues and Eigenvectors of the synthesized system - elimination of the 3rd mode of substructure 1 and 4th mode of substructure 2.

Identified Mode	1	2	3	4	5
Eigenvalue (rd/s)	270.9	1454.0	2398.0	3162.0	4728.0
	0.0691	-0.2348	-0.1151	-0.2007	-0.2057
	0.1195	-0.1268	0.0444	0.2205	0.4979
Eigenvector	0.1285	0.0173	0.0729	0.1001	-0.2384
	0.1034	0.1192	-0.1881	0.1387	-0.2486
	0.1178	0.0786	0.0798	-0.3893	0.0110
	0.0644	0.0828	-0.0940	-0.1029	0.6242
MAC	1.000	0.9999	0.9999	0.9965	0.8824

Table 8 displays MAC^{*} values for the synthesized systems, considering different combinations of deleted modes.

Table 8 Correlation between the original modal base and synthesized system's modal base for all combinations of extracted modes.

Extracted Modes sub1.sub2	1,1	1,2	1,3	1,4	2,1	2,2	2,3	2,4	3,1	3,2	3,3	3,4
MAC [*]	.995	.942	.869	.988	.837	.986	.892	.909	.931	.783	.600	.976

MAC^{*} - Modal Assurance Criterion, (Ewins, 1984)

The value of MAC describes the correlation between synthesized and modal base vectors. If the value MAC is near unity, then better the correlation of the values. The MAC number can be defined as:

$$MAC_{j(s,x)} = \frac{(\phi_x^T \cdot \phi_s)^2}{(\phi_x^T \cdot \phi_x) \cdot (\phi_s^T \cdot \phi_s)} \quad (28)$$

$$\overline{MAC} = \frac{\sum_{j=1}^m MAC_{j(s,x)}}{m}$$

Terms with x in equation (28) represent values from the original system and terms with p represent synthesized values.

Discussion of Results and Conclusion

The work proposes a component modal synthesis procedure to be used in experimental modelling. The simulation shows that a good approximation to the system's eigenbase can be obtained through the synthesis process (table 4 to 7).

The number of kept modes is within the recommended (Duarte, 1994) least 70 %, for each substructure. The modal elimination criterion yields good results as to the synthesis of the system's modal base. MAC values obtained using the criterion are amongst the best possible combination results. Such an information can be compared to other combination results in Table 8. The modal elimination selection criterion is but an indicator of efficient synthesis possibility. It may not lead always to the synthesis with the smallest relative error among all the synthesized modes.

Further validation of the technique requires extensive tests, including experimental measurements where the identified modal base comes from less than ideal system information and is heavily contaminated by noise. The proposed method is to be integrated with time domain modal base identification algorithms (Kurka and Bazán, 1992).

References

- Arruda, J. R. F., Santos, J. M. C., 1993, "Experimental Estimation of Mechanical Joint Parameters Using Frequency Response Functions and Modal Parameters", 11 th. Int. Conf. on Modal Analysis IMAC, 1502-1507.
- Craig, Jr., R. R., 1977, "Methods of Component Mode Synthesis", Shock And Vib. Dig., 9(11), 3-10.
- Craig, Jr., R. R. and Chang, C. J., 1977, "On the Use of Attachment Modes in Substructure Coupling for Dynamic Analysis", AIAA/ASME 18th Struct., B, 89-99.
- Craig, Jr., R. R., 1987, "A Review of Time-Domain and Frequency-Domain Component Mode Synthesis Methods", J. of Modal Analysis, 59-72.
- Duarte, M. A. V., 1994, "Ajuste de Modelos de Dinâmicos de Estruturas com Não Linearidades Concentradas", Doctoral thesis, Unicamp - Campinas.
- Ewins, D. J., 1994, "Modal Testing: Theory and Practice", John Wiley & Sons, New York.
- Hintz, R. M., 1975, "Analytical Methods in Component Modal Synthesis", AIAA J., 13(8), 1007 - 1016.
- Hurty, W. C., 1965, "Dynamic Analysis of Structural Systems Using Component Modes", AIAA J., 3(4), 678 - 685.
- Hurty, W. C., Collins, J. D., Hart, G. C., 1971, "Dynamic Analysis of Large Structures by Modal Synthesis Techniques", J. Computers & Struct., 1(4), 535-563.
- Kreyszig, E., 1993, "Advanced Engineering Mathematics", John Wiley & Sons, Inc., 7a. ed..
- Kurka, P. R. G., e Bazán, F. S. V., 1992, "Regularization Techniques in the Time Domain Modal Parameter Identification", 17th International Seminar on Modal Analysis, Catholic University of Leuven, Belgium, p. 221 - 225.
- Lecture Notes in Computer Science, 1976. "Matrix Eigensystem Routines - EISPACK Guide", Springer-Verlag, 2nd Edition, Vol. 6.
- Macneal, R. H., 1971, "A Hybrid Method of Component Mode Synthesis", Computers and Struct., 1(4), 581-601.
- Rubin, S., 1975, "Improved Component-Mode Representation for Structural Dynamic Analysis", AIAA J., 13(8), 995-1006.
- Santos, J. M. C., 1993, "Ajuste de Modelos de Estruturas Acopladas por Juntas Mecânicas Usando Funções de Resposta em Frequência e Síntese Modal de Componentes", Doctoral thesis, Unicamp - Campinas.

Errata

Paper: "Comparison of Implicit Approximate Factorization Algorithms in the Solution of the Navier-Stokes Equations"

Journal: VOL. XX, No.3, September 1998

- Page 353 – Main Author Correct Adress:

Edisson Sávio Góes Maciel
 ITA – Instituto Tecnológico de Aeronáutica
 Centro Técnico Aeroespacial
 12228-900 São José dos Campos, SP Brazil
 msg@aer.ita.cta.br

ViDa 98 - Danômetro Visual para Automatizar o Projeto à Fadiga Sob Carregamentos Complexos

ViDa 98 - Visual Damagemeter To Automate the Fatigue Design Under Complex Loading

Marco Antonio Meggiolaro¹

Jaime Tupiassú Pinho de Castro

Departamento de Engenharia Mecânica PUC-Rio

22453-900 Rio de Janeiro, RJ, Brazil

meggi@mit.edu

jcastro@mec.puc-rio.br

Abstract

A powerful language named **ViDa 98** was developed to automate all the methods traditionally used in mechanical design to calculate the fatigue damage caused by complex loading: SN , HW (for welded structures) and eN to predict crack initiation, and da/dN for studying plane and 2D crack propagation based on Fracture Mechanics concepts, considering load sequence effects. It has a friendly graphical interface and runs in a Windows environment. Among a number of similar features, can be highlighted: several intelligent data banks, two rain-flow counters and a race-track filter, generators of corrected hysteresis loops and 2D crack fronts, importation and adjustment of experimental data, an equation interpreter and a complete help file, which includes an online advanced course on fatigue. Moreover, its damage models introduce various non-trivial innovations, and the interface language can be English or Portuguese.

Keywords: Fatigue, Life Prediction, Complex Loading.

Resumo

Uma poderosa linguagem chamada **ViDa 98** foi desenvolvida para automatizar todos os métodos tradicionalmente usados no projeto mecânico à fadiga sob carregamentos complexos: SN , HW (para estruturas soldadas) e eN para prever a iniciação da trinca, e da/dN para estudar a propagação das trincas planas e 2D usando conceitos da Mecânica da Fratura, considerando os efeitos de seqüência do carregamento. Entre outras ferramentas similares, todas com uma interface gráfica amigável que roda num ambiente Windows, destacam-se: vários bancos de dados inteligentes, dois contadores rain-flow e um filtro race-track, geradores de laços de histerese elastoplástica corrigidos e de frentes de trincas 2D, importação e ajuste de dados experimentais, um interpretador de equações e um completo arquivo de ajuda, que inclui um curso avançado em fadiga. Além disto, seus modelos de dano introduzem diversas inovações não-triviais, e a língua da interface pode ser português ou inglês.

Palavras-Chaves: Fadiga, Carregamentos Complexos, Previsão de Vida.

Introdução

Fadiga é o tipo de falha mecânica caracterizada pela geração e/ou propagação paulatina de uma trinca, causada primariamente pela aplicação repetida de carregamentos variáveis. Estes fenômenos são progressivos, cumulativos e localizados.

A geração das trincas geralmente ocorre a partir de entalhes, e depende primariamente da gama das tensões $\Delta\sigma$ ou deformações $\Delta\epsilon$ locais, atuantes nos pontos mais solicitados da peça. Para efeito de dimensionamento, $\Delta\sigma$ e $\Delta\epsilon$ são quantificados num volume grande em relação aos parâmetros microestruturais do material (e.g., o tamanho de grão em metais). Quando as solicitações cíclicas são pequenas ($\Delta\sigma$ macroscopicamente elástica), o fenômeno é muito influenciado pelos detalhes do material, do acabamento superficial, do gradiente das tensões e do estado de tensões residuais atuantes na raiz do entalhe. A resistência à iniciação de uma trinca por fadiga tende a aumentar com a resistência à ruptura S_{11} , com a melhoria do acabamento superficial, com o aumento do gradiente de tensões e com a presença de tensões residuais compressivas. Estes detalhes são menos importantes quando as cargas

¹ Atualmente no Mech Eng Dept., M.I.T.

alternadas são grandes, e a componente plástica de $\Delta\epsilon$ não é desprezível frente à elástica. Neste caso, é a ductilidade do material o principal parâmetro controlador da resistência à fadiga.

Trincas grandes (maiores que alguns tamanhos de grão) têm a sua taxa de propagação por fadiga, da/dN , controlada primariamente pela gama do fator de intensidade de tensões ΔK . Entretanto, esta taxa é muito influenciada por outros parâmetros (e.g., pela microestrutura e pelas cargas médias) quando ΔK é baixo (próximo do limiar de propagação ΔK_{th}) ou alto (com K_{max} próximo da tenacidade do material K_{IC}).

Os métodos tradicionais de dimensionamento mecânico à iniciação de uma trinca por fadiga são o SN e o ϵN . Estruturas soldadas são em geral dimensionadas por uma variação do método SN, segundo procedimentos de institutos de soldagem como o IIW ou a AWS. Para quantificar a propagação das trincas usa-se normalmente o chamado método da/dN , baseado em conceitos da Mecânica da Fratura.

Para automatizar as rotinas de projeto de *todos* estes métodos, foi desenvolvida uma poderosa linguagem chamada **vida 98**, de **Danômetro Visual**, versão 98. Ela roda em ambiente Windows, possui uma interface gráfica intuitiva e amigável e é particularmente útil para tratar o caso de carregamentos complexos, considerando efeitos de seqüência entre os eventos do carregamento, tanto na iniciação como na propagação de trincas 1D e 2D. De interesse para este trabalho são as diversas inovações que tiveram que ser desenvolvidas e implementadas nos vários métodos de dimensionamento à fadiga, para que se pudesse garantir a confiabilidade e aumentar a velocidade dos cálculos, e as diversas melhorias em relação às versões iniciais do programa, descritas em Meggiolaro e Castro 95 e 96. Dentre elas, destacam-se:

- a introdução do conceito da contagem *rain-flow* ordenada;
- a consideração do efeito de sobrecargas elastoplásticas no método SN;
- uma série de correções na metodologia ϵN tradicional, para garantir a previsão de laços de histerese fisicamente admissíveis nos entalhes;
- modelos de propagação de trincas planas e 2D de velocidade e precisão ajustável, pela divisão do fator de intensidade de tensões em duas partes, carregamento e geometria, que podem ser atualizadas a taxas diferentes;
- modelos para descrever efeitos de seqüência na propagação de trincas, como retardos após sobrecargas;
- banco de dados inteligente com propriedades de materiais hierarquizadas (o programa *estima* valores coerentes na ausência de propriedades medidas, reconhecendo-os como diferentes dos valores experimentais);
- a *forma* das diversas telas gráficas, que usam informações visuais claras e notações tradicionais e intuitivas, para eliminar do processo de projeto qualquer programação.

Filosofia da Linguagem

O **vida 98** inclui todos os métodos do projeto tradicional à fadiga (Anderson 95, Bannantine et al. 90, Barson e Rolfe 87, Broek 88, Dowling 93, Farahmand 97, Fuchs e Stephens 80, Hertzberg 89, Juvinal 67, Rice 88, Shigley e Mischke 89, por exemplo). O seu objetivo primário é tornar o projeto à fadiga um processo equivalente a editar um texto num processador moderno de alto nível (e é por isto que as vezes prefere-se chama-lo de *linguagem* e não de *programa*). Todos os métodos de projeto requerem informações em seis áreas complementares de igual importância (Fig. 1):

- **Dimensões Geométricas** (incluindo principalmente a dos entalhes e das trincas, caso presentes).
- **Cargas de Serviço** (devem ser medidas não estimadas, pois influenciam diretamente as previsões).
- **Propriedades dos Materiais** (também devem ser preferencialmente medidas, pela mesma razão).
- **Análise de Tensões** (nos pontos críticos, para prever a iniciação das trincas).
- **Análise das Trincas** (para prever a sua propagação).
- **Análise do Acúmulo de Dano** (p.ex. modelo de Wöhler-Goodman-Miner no método SN).

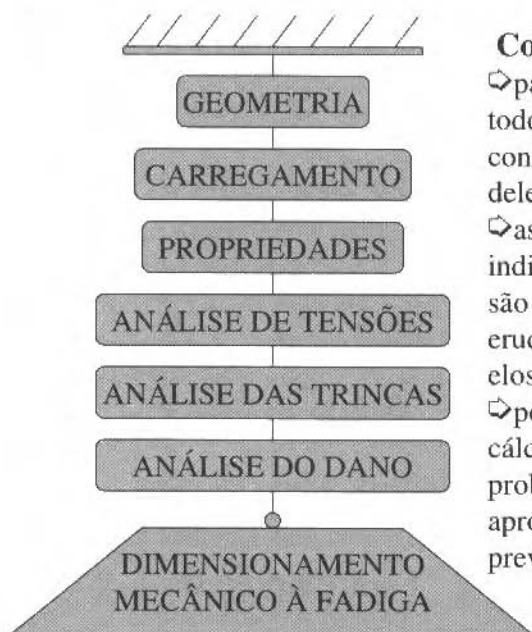


Fig. 1 A corrente do projeto à fadiga, e os diversos elos nos quais o processo pode ser dividido.

Note-se que a precisão das previsões é controlada pelo elo *menos* preciso desta corrente, logo não adianta sofisticar os modelos de análise de tensões, de trincas e de acúmulo de dano (que dependem de erudição acadêmica), se os outros elos (que dependem de informações experimentais) não forem igualmente bem conhecidos. A qualidade dos modelos de cálculo *não* substitui as informações experimentais indispensáveis nas aplicações práticas. Por outro lado, deve-se também reconhecer que modelos de cálculos incorretos simplesmente *não* geram previsões adequadas sobre a vida da peça, mesmo que se disponha de dados experimentais confiáveis sobre os três primeiros elos.

Por isto, os objetivos deste programa foram especificados tanto sob o ponto de vista do projetista mecânico quanto do pesquisador acadêmico, de forma a obter-se uma ferramenta precisa, atualizada e fácil de usar, visando:

- Apresentar uma interface gráfica clara, amigável e intuitiva.
- Calcular corretamente o dano à fadiga por todos os métodos tradicionais de projeto, incluindo todas as sofisticações necessárias para maximizar a acurácia dos cálculos.
- Dar ao usuário total controle sobre todas as opções de cálculo
- Incluir um completo arquivo de ajuda com todas as informações necessárias sobre o funcionamento, desempenho numérico e embasamento teórico de todos os modelos de cálculo.
- Minimizar o tempo de cálculo, usando opções de filtragem e algoritmos numéricos eficientes.
- Incluir todos os bancos de dados necessários às rotinas de projeto.
- Permitir a fácil expansibilidade de todos os bancos de dados.
- Gerar relatórios gráficos e numéricos facilmente imprimíveis e exportáveis.

Entrada de Dados

A tela de entrada do programa é ilustrada na Fig. 2. Sua aparência é a usual no ambiente Windows, e na sua parte superior apresenta cinco opções geradoras de menus. A opção **Arquivo** serve para carregar ou ativar:

Corrente do Projeto à Fadiga

- ↳ para otimizar o projeto à fadiga, todos os elos devem ter precisão e confiabilidade similares: o *pior* deles controla a qualidade
- ↳ as informações experimentais indispensáveis aos 3 primeiros *não* são supridas sofisticando-se (pela erudição acadêmica) os 3 últimos elos da corrente
- ↳ por outro lado, *só* modelos de cálculo que descrevam a física do problema de forma *correta* e apropriada podem gerar boas previsões de vida à fadiga!

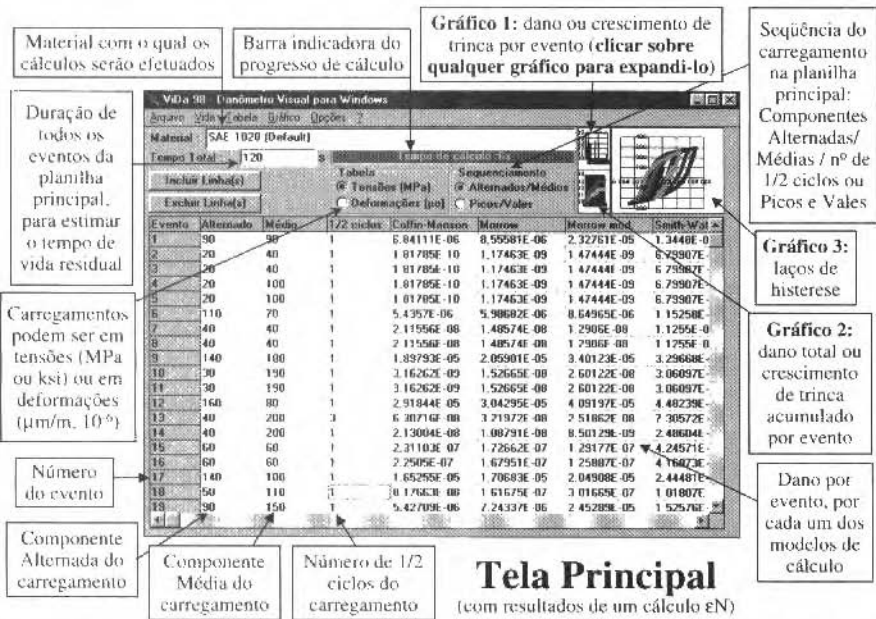


Fig. 2 Tela principal do VIDA 98 no modo de saída, com a planilha mostrando os resultados de um cálculo eN. Notar a complexidade dos carregamentos, os diversos modelos de cálculo disponíveis e o gráfico dos laços de histerese corrigidos.

- as histórias do carregamento,
- o cálculo de tensões equivalentes ou de rosetas,
- a filtragem do carregamento,
- a contagem *rain-flow*,
- o cadastro de propriedades de materiais, e
- os cadastros dos fatores de concentração de tensão K_t , dos fatores de intensidade de tensão K_I , ou das equações de propagação de trincas.

As cargas podem ser especificadas em tensão ou em deformação, e o usuário pode escolher o SI ou o sistema inglês para as unidades. A história do carregamento pode ser dada (i) por sua seqüência ordenada de picos e vales, (ii) pela seqüência equivalente de cargas médias, alternadas e número de reversões (ou 1/2 ciclos), ou (iii) por um histograma. A informação pode ser manualmente digitada ou importada de listas ordenadas com extensão .csv, inclusive as geradas experimentalmente ou numa planilha tipo Excel. A ordem dos carregamentos seqüenciais é preservada. No caso das cargas médias e alternadas, é claro que a amplitude σ_a ou ϵ_a tem que ser um número positivo, enquanto que a média σ_m ou ϵ_m pode ser compressiva ou trativa, já que nos cálculos são reconhecidas as diferenças entre seus efeitos na vida à fadiga.

Há opções de filtragem do carregamento em amplitude segundo um patamar ajustável, seguindo a idéia do método *race-track* (Nelson e Fuchs 77), e de contagem de ciclos, segundo os métodos *rain-flow* tradicional (Dowling 93, p.ex.) e seqüenciado, explicado abaixo. Para que se possa visualizar a história do carregamento, o programa desenha a seqüência dos picos e vales, e também os carregamentos filtrados.

A filtragem em amplitude é muito útil para diminuir o esforço computacional nos cálculos de dano à fadiga, mas deve ser usada com cuidado porque *despreza* carregamentos, o que é um procedimento intrinsecamente *não* conservativo. Uma boa regra é limitar o patamar de corte ao valor do limite de fadiga na carga média em questão, já que solicitações menores que este valor não causam dano à peça (Castro et al. 94).

Para evitar que a contagem *rain-flow* seja tratada como qualquer estatística, perdendo as informações de seqüência, há também a opção de ordena-la mantendo a localização de seus picos, uma nova idéia explicada na Fig. 3. A contagem *rain-flow* seqüenciada contabiliza o efeito dos

carregamentos no momento em que eles ocorrem (e não *antes* de sua ocorrência, como no método tradicional), sem acrescentar qualquer dificuldade de monta ao algoritmo de contagem.

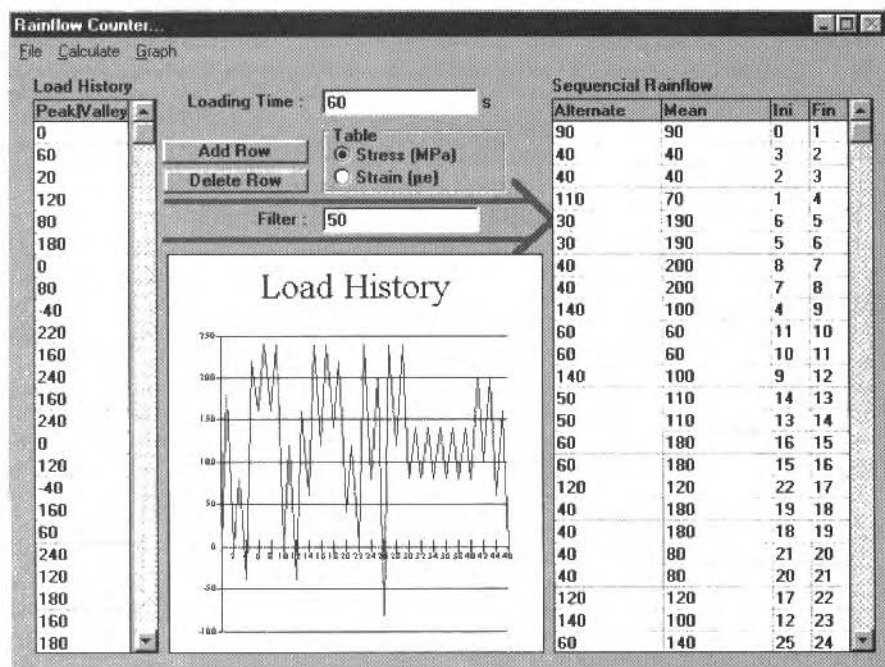


Fig. 3 Contagem rain-flow sequencial. Notar que, ao contrário da contagem tradicional, este método não antecipa os carregamentos, minimizando assim os efeitos de sequência. Notar também que, como o ViDa 98 permite a escolha da língua da interface, esta tela está em inglês.

Todos os cadastros são facilmente editáveis e expansíveis. Os cadastros de K_I , K_f e de curvas da/dN podem ser editados através de um interpretador de fórmulas matemáticas com sintaxe padrão Basic, sendo fácil ampliá-los, por exemplo, com informações contidas nas referências tradicionais (Peterson 74, Hardy e Malik 92 ou Tada et al. 85).

É na opção *Arquivo* que também se escolhe qual o material da peça. O programa fornece um banco de dados inteligente e hierarquizado (que já conta com propriedades de centenas de materiais diferentes), o qual pode ser facilmente expandido sem limites de armazenamento. Com este banco de dados pode-se:

- Selecionar materiais ordenando-os por uma ou mais propriedades (e.g., pode-se listar os materiais com resistência ao escoamento S_Y entre 500 e 700MPa e tenacidade K_C maior que 100MPa \sqrt{m}).
- Gerar os gráficos SN, ϵN , da/dN vs. ΔK , e $\sigma \epsilon$ real (monotônico e cíclico), com *zoom* e eixos ajustáveis (basta *clique* sobre os gráficos para expandi-los, e pode-se imprimi-los diretamente).
- Ajustar tabelas de pontos experimentais, com geração dos gráficos e cálculo das propriedades correspondentes.
- Completar as tabelas de propriedades, *estimando* as não fornecidas (os números estimados aparecem em vermelho, para diferenciá-los dos valores medidos). As regras usadas nesta estimativa podem ser modificadas pelo usuário.
- Ajustar manualmente qualquer das propriedades, para verificar sua influência nos cálculos.
- Remeter as propriedades para os modelos de cálculo.

A opção seguinte da tela inicial do programa chama-se *Vida*, e é sua parte mais importante, pois inclui *todas* as metodologias tradicionais de projeto à fadiga, *em toda a sua complexidade*. Estes métodos são:

Método SN

O método SN correlaciona o trincamento por fadiga de *qualquer* peça complexa com o de pequenos corpos de prova (CP), que tenham a mesma *resistência* que o *ponto crítico* da peça (em geral a raiz de um entalhe), e que sejam submetidos à mesma *história de tensões* $\Delta\sigma$ que o solicita em serviço. Desta forma, a rotina de projeto é:

1. Avaliar a resistência à fadiga do ponto crítico da peça.
2. Calcular a história de tensões nele induzida pelo carregamento real.
3. Quantificar o dano acumulado pelos diversos eventos do carregamento.

Este método só deve ser aplicado aos $\Delta\sigma$ macroscopicamente elásticos, logo às longas vidas de iniciação (ao contrário do ϵN , o SN não considera de forma explícita os efeitos elastoplásticos cíclicos eventualmente presentes nas raízes dos entalhes e, como aquele, não reconhece a presença de trincas). Entretanto, o SN é computacionalmente muito mais rápido que o ϵN , conta com um vasto banco de dados e muita experiência acumulada, e pode ser usado confiavelmente talvez na maioria dos casos práticos de dimensionamento mecânico.

No **VIDA 98** o cálculo do número de ciclos necessários para iniciação de uma trinca segundo o método SN segue as idéias consagradas pelo uso em projeto mecânico, e inclui algumas melhorias não-usuais interessantes, como o reconhecimento do efeito das tensões residuais causadas por sobrecargas elastoplásticas, conforme explicado abaixo. A tela deste método está ilustrada na Fig. 4.

The screenshot shows the 'Calcular Vida (SN)' window with several input fields and a graph. The graph plots $\log(S_f)$ vs $\log(N_f)$ with a curve labeled 'Curva S-N (MPa x cycl)'. A secondary window, 'Curva de Dano Personalizada', is open, showing parameters for a 'PUC' curve, including 'Exp. Tensão Alternada' (1.5), 'Exp. Tensão Média' (1), and 'Resistência Referência' (441 MPa). The main window also displays material properties like S_f (220.5 MPa), k_a (9.42E-01), k_b (9.26E-01), k_c (1.00E+00), k_d (1.00E+00), and k_e (1.00E+00). The 'Curva S-N' section has options for 'Automática', 'b-S-N', and 'b-c-N', with 'b' set to 5.53E-00 and 'c' to 5.71E-07. The 'Critério de falha' is set to 'Miner', and the 'Número de pontos' is 40. The 'Tela SN' label is at the bottom right.

Fig. 4 Tela SN do VIDA 98, mostrando as principais opções de cálculo disponíveis.

Notar o gráfico dos diversos diagramas SaSm, e a opção de cálculo dos efeitos elastoplásticos causados por sobrecargas.

Como a história dos carregamentos disponível pode incluir ou não o efeito dos entalhes (neste caso os carregamentos são chamados nominais), há um banco de dados com fatores de concentração de tensões K_t para diversas geometrias (Fig. 5), que o usuário pode expandir usando o interpretador de equações do programa. O valor de K_t pode ser modificado pela sensibilidade ao entalhe q e transformado em $K_f = 1 + q(K_t - 1)$, para multiplicar os carregamentos nominais e calcular as tensões causadoras do trincamento por fadiga (q também é calculável pelo programa, em função da resistência à

ruptura do material e do raio do entalhe). Pode-se optar por aplicar ou não o efeito da concentração de tensões sobre a componente média do carregamento.

Para prever a resistência da peça à fadiga, primeiro a curva de Wöhler padrão do material (estimada pelo programa, caso não haja um conjunto de resultados experimentais confiáveis) é modificada pelos fatores de acabamento superficial, tamanho, forma de carregamento, etc., característicos do ponto mais solicitado da peça, seguindo especificamente as equações propostas por Shigley (89). Todos os fatores são calculados automaticamente, mas podem ser modificados pelo usuário, que também pode desprezar o limite de fadiga S_e para os aços, mantendo ou modificando a inclinação da curva SN a partir de uma vida de referência.

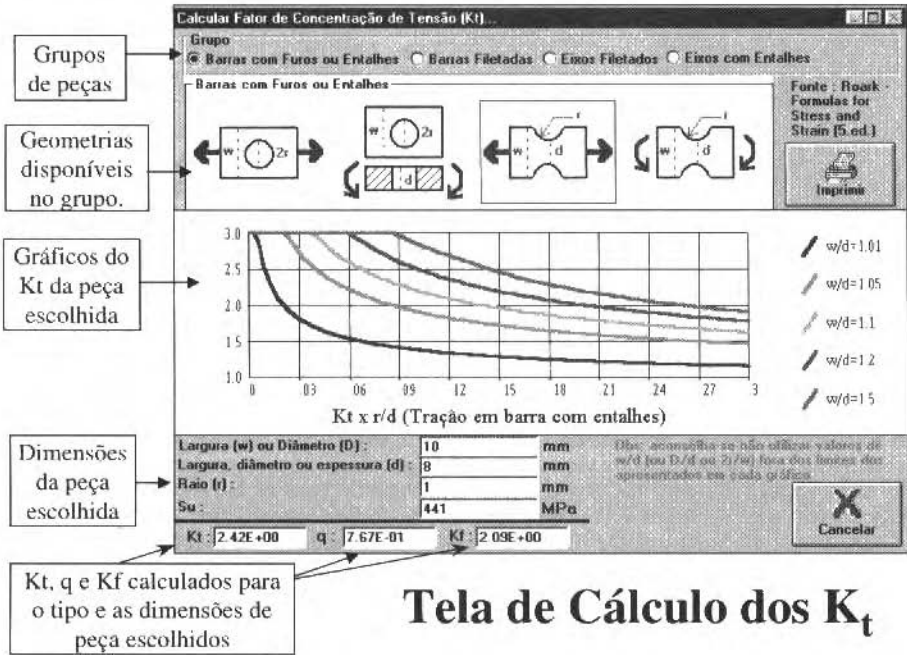


Fig. 5 Tela de cálculo dos fatores de concentração de tensões K_t de entalhes típicos.

O efeito das cargas médias é quantificado por diversas regras ou “diagramas $S_a S_m$ ” (que são o lugar geométrico das combinações $\sigma_a \sigma_m$ que causam o mesmo dano à fadiga), como Goodman, Gerber, Soderberg e elíptica (da qual as outras três são casos particulares):

$$\left(\frac{\sigma_a}{S_a}\right)^r + \left(\frac{\sigma_m}{S_m}\right)^s = 1 \quad (1)$$

O usuário pode especificar os parâmetros da regra elíptica, definindo a resistência à carga média S_m e os expoentes r e s (Castro 79). A resistência à carga alternada $S_a(N)$ é calculada diretamente da curva de Wöhler da peça, se $S_a > S_e$: $S_a = (c/N)^b$. A parte correspondente à carga média compressiva pode ser considerada de duas formas nos diversos diagramas $S_a S_m$: ou desprezando seu efeito (fazendo $\sigma_m = 0$ quando σ_m for negativo), ou usando uma percentagem ajustável da inclinação da curva de Goodman, para quantificar seu benefício.

O dano à fadiga d é definido pela razão entre os números de ciclos aplicado, n , e o que causaria falha, N : $d = n/N$. No caso de carregamentos complexos, o i -ésimo 1/2 ciclo (contado pelo método *rain-flow*) pode ter componentes alternadas e médias $\sigma_{a_i} \cdot \sigma_{m_i}$, e o dano causado por este evento é $d_i = 1/2N_i$.

(N_i é a vida à fadiga que a peça teria sob um carregamento simples, onde estas componentes não variassem). Para calcular d_i , o programa calcula primeiro a tensão totalmente alternada σ_{ai} equivalente ao carregamento $\sigma_{ai} \cdot \sigma_{mi}$ por cada uma das regras $S_a S_m$, e depois a vida N_i correspondente, usando Wöhler:

$$\sigma'_{ai} = \frac{\sigma_{ai}}{\left[1 - \left(\frac{\sigma_{mi}}{S_m} \right)^s \right]^{1/r}} \quad \therefore \quad N_i = \frac{c}{(\sigma'_{ai})^b} \Rightarrow d_i = \frac{(\sigma'_{ai})^b}{2 \cdot c} \quad (2)$$

O dano é acumulado a cada evento do carregamento, e falha é definida pelo seu somatório: $\sum d_i = \alpha$, onde α é especificável pelo usuário.

Além destas rotinas de cálculo, que podem ser chamadas de tradicionais, o programa inclui uma opção não-usual no método SN: a consideração das tensões residuais devidas a gradientes de deformação plástica, causados por sobrecargas esporádicas superpostas a um carregamento de outra forma elástico, aproveitando a informação da *ordem* dos carregamentos. Ao reconhecer algum evento que provoque tensões maiores que a resistência ao escoamento S_Y (localmente na raiz do entalhe), o programa pode aplicar apenas neste 1/2 ciclo a metodologia eN (detalhada mais abaixo) para calcular a tensão residual resultante do descarregamento desta sobrecarga, e passar a somá-la à componente média dos ciclos subsequentes.

A grande vantagem desta opção é acumular o dano reconhecendo o principal efeito de seqüência do carregamento, eliminando assim (pelo menos parcialmente) a principal desvantagem da regra de Miner. Também não se perde muito da vantagem computacional, pois o método SN é aplicado a todos os ciclos elásticos do carregamento antes e após a sobrecarga.

A saída numérica é na forma de uma planilha que inclui o dano por evento, segundo cada uma das regras $S_a S_m$, o dano acumulado e a vida residual prevista. Além disto, o programa gera gráficos de dano versus evento para cada uma das curvas $S_a S_m$, e também desenha os laços de histerese elastoplástica correspondentes aos eventos de sobrecarga, quando esta opção é especificada.

A função de cada um dos botões da diversas telas do programa é descrita num completo arquivo de ajuda, e todos os detalhes dos vários modelos de cálculo são explicados num curso avançado de fadiga incluído no manual visual do programa. Por fim, os usuários menos experientes podem optar por usar a versão simplificada do método SN, onde o dano é calculado sem que seja necessário especificar as várias opções de modelagem discutidas acima.

Projeto de Estruturas Soldadas

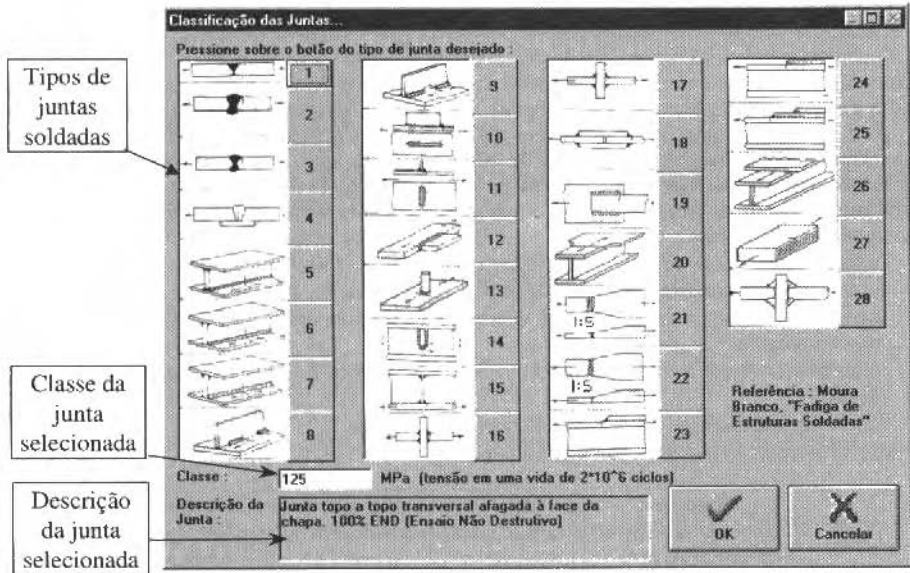
O projeto à fadiga de estruturas soldadas é um sub-conjunto do método SN particularmente simples, e baseia-se em testes feitos em estruturas e não em pequenos CPs soldados (devido principalmente às tensões residuais de soldagem e às características geométricas dos filetes mais longos, como tamanho e distribuição dos poros e inclusões).

A metodologia normalizada por órgãos como o IIW - International Institute of Welding, a AWS - American Welding Society, etc., é baseada em apenas duas premissas simples, assumindo que a resistência de uma junta estrutural soldada (executada segundo padrões de controle de qualidade industriais em aço estrutural ao C ou C-Mn) depende apenas de dois fatores (Moura Branco et al., 87):

- da geometria ou do tipo da junta, que é classificada em diversas classes como as ilustradas na Fig. 6 (que são as normalizadas pelo IIW); e
- da gama do carregamento nominal $\Delta\sigma$.

Note-se que esta metodologia tem duas diferenças importantes em relação ao método SN, pois ela *não depende*:

- do material de base (para as normas não importa, do ponto de vista de resistência à fadiga, se a chapa soldada é de aço A36 ou de SAR-60, mesmo que o S_Y deste seja mais que o dobro daquele), e
- da carga média aplicada na estrutura.



Tela das Classes de Juntas Soldadas

Fig. 6 Tela do cálculo da vida à fadiga de juntas soldadas, segundo o método do IIW.

Os diversos detalhes de soldagem são divididos em classes de resistência cuja notação varia entre as diversas organizações normalizadoras. No IIW estas classes são denominadas pelo valor da gama de tensões $\Delta\sigma$ em MPa que o detalhe de soldagem pode suportar com uma vida mínima à fadiga de $2 \cdot 10^6$ ciclos, dentro de uma confiabilidade de 95%.

O **ViDa 98** reconhece todas as classes de juntas normalizadas pelo IIW, e permite que o usuário escolha entre as diversas opções da norma (como o expoente da curva de Wöhler 3.0 ou 3.5, e a existência ou não de um limite de fadiga em $5 \cdot 10^6$ ciclos). Do ponto de vista computacional, o projeto à fadiga de estruturas soldadas é bem mais simples que o SN tradicional, pois não é necessário calcular a tensão σ_{ai} equivalente à combinação $(\sigma_{ai}, \sigma_{mi})$ do i -ésimo carregamento aplicado à peça. A insensibilidade à carga média σ_{mi} também facilita muito a identificação do patamar de filtragem de amplitude mais adequado ao problema. Uma interessante aplicação prática desta simplificação é discutida em Castro et al. (94), onde se estuda um caso real de previsão da vida residual de reparos soldados em pontes rolantes.

Vale a pena comentar esta aparente insensibilidade das estruturas soldadas à carga média, o que a primeira vista parece um contra-senso, já que as tensões residuais de soldagem são tão altas que frequentemente ultrapassam as resistências ao escoamento tanto do material de base quanto do depositado. Mas, exatamente por isto, a superposição do carregamento externo às já muito altas tensões residuais só pode induzir uma pequena *variação* das cargas médias atuantes nos cordões de solda. Na realidade, o efeito das grandes tensões residuais reflete-se na baixa resistência à fadiga intrínseca das juntas soldadas: os piores detalhes - os da classe 45 - só toleram uma amplitude de carregamento que é cerca de 5% da resistência à ruptura dos aços *menos* resistentes, enquanto que os melhores - as juntas de topo esmerilhadas da classe 125 - têm uma resistência à fadiga só 2.8 vezes maior do que isto.

Método eN:

O método eN correlaciona o *trincamento* por fadiga de *qualquer* peça com o de pequenos CPs, que sejam submetidos à mesma *história de deformações* $\Delta\epsilon$ e que tenham a mesma *resistência* que o *ponto crítico* da peça. Eventos *elastoplásticos* induzidos pelo carregamento no ponto crítico *são* quantificados. Desta forma, a rotina de projeto, similar à do método SN, é:

1. Avaliar a resistência à fadiga do ponto crítico da peça.
2. Calcular a história de deformações nele induzida pelo carregamento real.
3. Quantificar o dano acumulado pelos diversos eventos do carregamento.

Como no caso do método SN, o eN também só se aplica ao dimensionamento à fadiga de peças *não* trincadas mas, por quantificar explicitamente as deformações plásticas cíclicas macroscópicas, pode ser usado para prever qualquer vida (o eN *tem* que ser usado em vez do SN quando o problema for o dimensionamento à fadiga oligocíclica ou de baixa ciclagem, isto é, quando a gama das deformações plásticas $\Delta\epsilon_p$ atuantes na raiz do entalhe for da mesma ordem ou maior que as elásticas $\Delta\epsilon_e$, mas este método também *pode* ser usado para o dimensionamento às vidas longas). Esta modelagem requer quatro tipos de informação:

- uma relação $\Delta\sigma/\Delta\epsilon$, para descrever o laço de histerese elasto-plástica na raiz do entalhe,
- uma regra de concentração de deformações (como a de Neuber ou a Linear), para correlacionar as tensões nominais $\Delta\sigma_n$ aplicadas sobre a peça com as deformações $\Delta\epsilon$ por elas induzidas na raiz do entalhe,
- uma relação entre a gama de deformações $\Delta\epsilon$ e a vida à fadiga N, como a regra de Coffin-Manson, e
- uma regra de acúmulo de dano, como a regra de Miner.

A tela de entrada do método eN é mostrada na Fig. 7.

The screenshot shows the 'Calcular Vida (eN)' window with several input fields and options. The main window is divided into several sections:

- Inputs:**
 - Acabamento superficial do ponto crítico da peça: Retificado
 - Título do cálculo: Flexão
 - Diâmetro da peça: 15 mm
 - Resistência à ruptura: 441 MPa
 - Temperatura de trabalho: 20 °C
 - Fatores de modificação da curva SN: $k_a: 0.2205$, $k_b: 9.42E-01$, $k_c: 9.26E-01$, $k_d: 1.00E+00$, $k_e: 1.00E+00$
 - Constantes da curva eN: $C_f: 9.36E+02$ MPa, $C_s: 4.10E-01$, $b: 1.29E-01$, $c: -5.10E-01$
 - Crítério de falha segundo a regra de Miner: $\Sigma n_i/N_i = \alpha$ (α normalmente = 1)
 - Fator de concentração de tensões: $K_t: 2.50E+00$
- Options:**
 - Concentração de Deformações (valores nominais elásticos): Efeito Linear ($K_e = K_t$) Sistema de Neuber ($K_e K_a = K_t^2$)
 - Considerar Cotovelo da Curva S-N
 - Traçar Laços de Histerese
 - Carregar Laços (altamente recomendado)
 - Desenhar Curva S e Cíclica sobre os Laços
 - Rainflow nas Deformações
 - Filtro Amplitude: 0 ao 200
 - Definir Laços a Traçar: Inicial: 100, Final: 200
 - Pts. cálculo: 40
 - Pts. plotagem: 20
- Plot:** A graph showing 'Curva e-N (reversões)' with a plot of stress vs. strain.
- Buttons:** OK and Cancelar.

Annotations around the screenshot explain various features:

- Usar Neuber ou a regra Linear para quantificar o Efeito do K_t nos cálculos eN
- Reconhecer o limite de fadiga
- Desenhar laços de histerese
- Corrigir cálculos eN para gerar laços corretos
- Contar (rainflow) as deformações calculadas, após filtragem de amplitude

Tela eN

Fig. 7 Tela eN do VIDA 98, mostrando as diversas opções de cálculo disponíveis. Notar os botões de correção dos laços e de contagem *rain-flow* das deformações calculadas, propostas que são discutidas no texto e que são indispensáveis para que se possa obter previsões fisicamente corretas.

Este é um método moderno, corroborado por instituições tradicionais como a SAE (Rice 88), mas que tem certas idiosincrasias relativamente pouco conhecidas, e que devem ser respeitadas sob pena de graves insucessos. Por isto foi necessário desenvolver uma série de procedimentos alternativos para que o VIDA 98 efetuasse adequadamente os cálculos eN, conforme resumido a seguir.

A metodologia eN clássica trabalha com tensões e deformações reais, usa relações σ/ϵ tipo Ramberg-Osgood e considera o amolecimento ou endurecimento cíclico do material, mas não o seu

transiente a partir do comportamento monotônico, assumindo uma equação única para o laço de histerese expressa por:

$$\epsilon_u = \frac{\Delta\epsilon_e}{2} + \frac{\Delta\epsilon_p}{2} = \frac{\Delta\sigma}{2E} + \left(\frac{\Delta\sigma}{2K'} \right)^{1/n'} \quad (3)$$

onde E é o módulo de Young, enquanto K' e n' são o coeficiente e o expoente de encruamento da curva $\sigma\epsilon$ cíclica estabilizada. No caso onde as tensões nominais sejam elásticas, pode-se escrever a regra de concentração de deformações de Neuber como:

$$K_t^2 = \frac{\Delta\sigma \cdot \Delta\epsilon \cdot E}{\Delta\sigma_n^2} \quad (4)$$

onde $\Delta\sigma$ e $\Delta\epsilon$ são as gamas de tensão e deformação atuantes na raiz do entalhe, e $\Delta\sigma_n$ a tensão nominal atuante (em relação à qual é definido o valor de K_t). A relação entre a amplitude das deformações atuantes na raiz do entalhe e a vida à fadiga é geralmente dada pela regra de Coffin-Manson, expressa por:

$$\frac{\Delta\epsilon}{2} = \frac{\sigma'_f}{E} (2N)^b + \epsilon'_f (2N)^c \quad (5)$$

onde σ'_f , ϵ'_f , b e c são constantes do material.

Há vasto suporte experimental para justificar o uso das simplificações do método ϵN no caso do dimensionamento à fadiga sob carregamentos simples, mas em geral a literatura *não* reconhece explicitamente a fundamental importância do estado inicial da peça e da ordem do carregamento no caso de carregamentos complexos.

A forma tradicional de se projetar pelo método ϵN nestes casos tem sido calcular o dano d_i provocado pelas n_i reversões do i -ésimo carregamento nominal $\Delta\sigma_{n_i}$ (contadas pelo método *rain-flow*, como se os diversos ciclos do carregamento fossem independentes), e usar a regra de Miner para acumular o dano $d_i = n_i/2N_i$, sendo N_i o número de ciclos que a peça duraria se somente o carregamento $\Delta\sigma_{n_i}$ estivesse atuando. Para carregamentos nominais elásticos, este método tradicional pode ser resumido por:

(i) Dado o i -ésimo evento do carregamento $\Delta\sigma_{n_i}$, calcula-se a tensão $\Delta\sigma_i$ induzida na raiz do entalhe:

$$\left(K_t \Delta\sigma_{n_i} \right)^2 = \Delta\sigma_i \cdot \left(\Delta\sigma_i + 2E \cdot \left(\frac{\Delta\sigma_i}{2K'} \right)^{1/n'} \right) \quad (6)$$

(ii) A seguir calcula-se a deformação $\Delta\epsilon_i$ causada por $\Delta\sigma_i$, e os correspondentes N_i e d_i :

$$\frac{\Delta\sigma_i}{E} + 2 \cdot \left(\frac{\Delta\sigma_i}{2K'} \right)^{1/n'} = \Delta\epsilon_i = \frac{2\sigma'_f}{E} (2N_i)^b + 2\epsilon'_f (2N_i)^c \Rightarrow d_i = \frac{n_i}{2N_i} \quad (7)$$

Estas equações não são inversíveis, logo o uso do método ϵN é computacionalmente trabalhoso, o que explica (mas não justifica) a pouca divulgação dos problemas que o seu uso não criterioso pode acarretar:

A aplicação destas equações à contagem *rain-flow* do carregamento **não** gera previsões de laços de histerese fisicamente admissíveis!

De fato, para garantir a qualidade das previsões é indispensável assegurar primeiro que o modelo de cálculo reproduza os laços de histerese que atuam na raiz do entalhe, para só então calcular o dano por eles provocado. Como os incrementos de deformação plástica *são* dependentes da história, mesmo que a peça seja virgem, que o estado de tensões e deformações residuais seja zero, e que se possa desprezar os transientes de amolecimento ou endurecimento cíclico, ainda assim é necessário distinguir entre o primeiro 1/2 ciclo do carregamento e os subsequentes. O primeiro 1/2 ciclo segue a relação $\sigma \varepsilon$ cíclica $\varepsilon = \sigma/E + (\sigma/K')^{1/n'}$ e não as equações do laço:

$$(K_i \sigma_{ni})^2 = \sigma_i \left[\sigma_i + E \cdot \left(\frac{\sigma_i}{K'} \right)^{1/n'} \right] \quad (8)$$

$$\frac{\sigma_i}{E} + \left(\frac{\sigma_i}{K'} \right)^{1/n'} = \varepsilon_i = \frac{2\sigma'_f}{E} (2N_i)^b + 2\varepsilon'_f (2N_i)^c \Rightarrow d_i = \frac{1}{2N_i} \quad (9)$$

Mas este cuidado indispensável ainda não é suficiente. Como ilustrado na Fig. 8, é também necessário garantir que todos os eventos subsequentes não ultrapassem (i) a curva $\sigma \varepsilon$ cíclica, nem (ii) o envoltório dos laços de histerese. Para isto, deve-se verificar se e quando as deformações previstas pela equação do laço de histerese para cada evento $\Delta\sigma_{ni}$ cruzam a curva $\sigma \varepsilon$ cíclica ou um laço previamente induzido na raiz do entalhe. No caso de cruzamento, deve-se trocar a equação do *i*-ésimo laço a partir da interseção, e passar a seguir a curva $\sigma \varepsilon$ (ou a do laço anterior de maior amplitude) até o fim do carregamento $\Delta\sigma_{ni}$.

Picos e Vales de Deformação

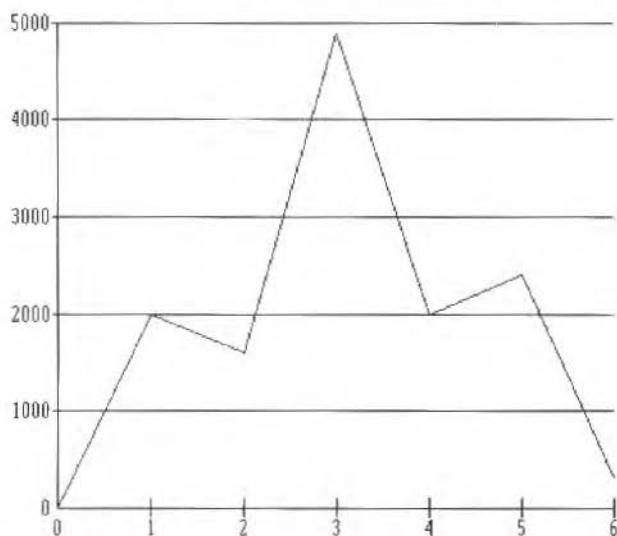


Fig. 8a Carregamento imposto sobre um CP de tração de aço 1020.

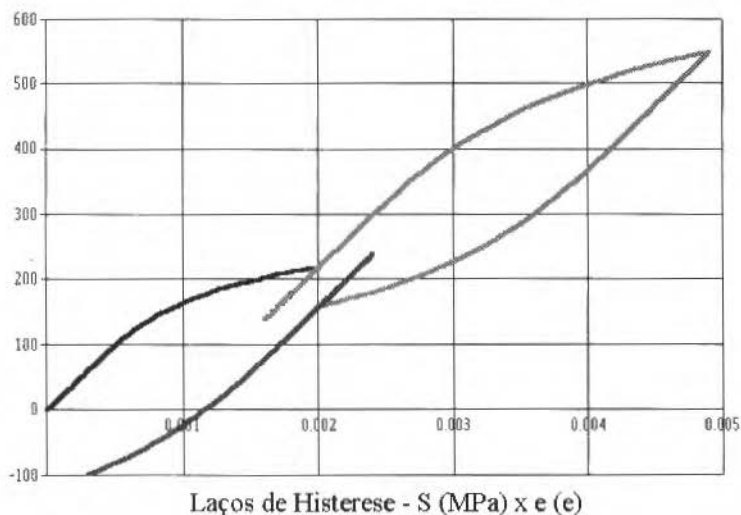


Fig. 8b Laços previstos pelo método eN tradicional.

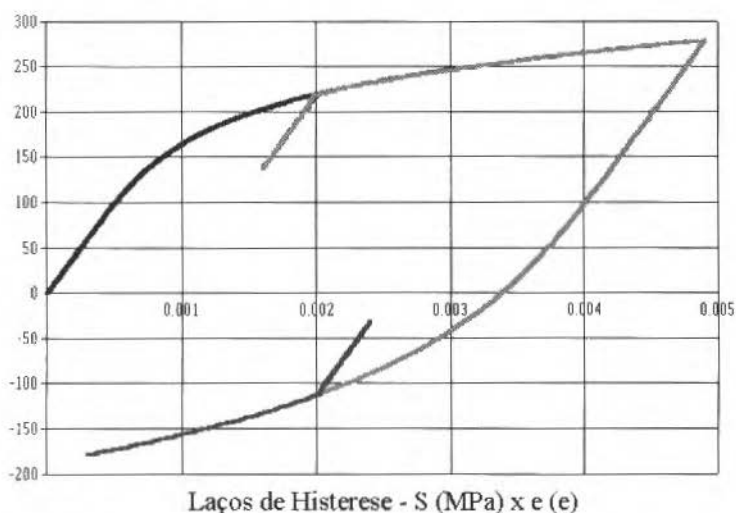


Fig. 8c Laços obtidos após incluir nos cálculos as correções necessárias.

Este passo é complicado, mas é absolutamente indispensável sob pena de gerar previsões (i) fisicamente inadmissíveis, e (ii) possivelmente *não conservativas*. De fato, conforme mostrado na Fig. 8, só se efetuando a troca das equações chega-se ao $\Delta\epsilon_i$ correto, que pode ser *maior* do que aquele que seria previsto pela equação do laço.

Para garantir a precisão dos cálculos, no programa seguem-se todos os procedimentos discutidos acima, além de uma série de outros igualmente importantes que, por limitações de espaço, são detalhados num trabalho complementar específico (Castro e Meggiolaro 98). Além disto o programa:

- desenha a curva eN , plota sobre ela a curva SN tradicional, e permite que se force a componente elástica da deformação a atingir a curva SN no limite,
- permite que se troque a regra de Neuber pela regra linear de concentração de deformações,

- desenha os laços de histerese *devidamente corrigidos* (e também os previstos pelo método tradicional),
- calcula a vida à fadiga não só por Coffin-Manson e pelo método das inclinações universais de Manson, que não consideram a carga média, como também considera os efeitos da componente média do carregamento pelas regras de Morrow, Morrow modificada e Smith-Topper-Watson.
- gera gráficos de dano versus evento para cada um dos modelos de cálculo.

Como no caso SN, também há uma versão simplificada do método ϵN para os usuários menos experientes. E, da mesma forma, a função de cada um dos botões da tela deste método, bem como o embasamento teórico de todas as opções de cálculo, são detalhadamente descritos nos arquivos de ajuda do programa.

Método da/dN:

Este método assume que:

- A trinca é o *ponto crítico* da peça, e pode ser modelada pelos conceitos tradicionais da Mecânica da Fratura.
- A taxa de propagação de trincas da/dN (e também dc/dN, no caso das trincas 2D) depende primariamente da faixa ou gama de variação do fator de intensidade de tensões ΔK .

A tela usada no cálculo do crescimento de trincas 2D por fadiga é mostrada na Fig. 9. A tela do crescimento 1D é similar. Trincas 2D são trincas internas, superficiais ou de canto que se propagam em duas direções, digamos a e c, mudando de forma a cada ciclo do carregamento. Desta forma, estas trincas têm duas taxas de propagação diferentes mas acopladas (isto é, da/dN e dc/dN dependem de a e de c).

Valor de K_C , de ΔK_{th} , e das constantes das regras de Paris e de Elber

Tamanhos iniciais e finais da trinca (estes usados como critério de parada dos cálculos)

Curvas da/dN de Paris, de Elber e de uma terceira equação especificada, usando os valores numéricos listados na tabela de variáveis

Nome da terceira equação da/dN usada nos cálculos

Calcula da/dN para um ΔK especificado

Grava uma nova equação de propagação de trincas

Tabela das variáveis usadas nas equações

Especificação dos gráficos de saída

Parcelas de flexão e tração na carga

Regras da/dN usadas nos cálculos

Considera efeitos de retardo na propagação de trinca (Wheeler para corrigir da/dN ou Wheeler Modificado para ΔK) e especifica a precisão do cálculo numérico

Especifica o uso do modelo ΔK_{rms} para os cálculos, e integra por Simpson

Tela da/dN 2D

Fig. 9 Tela da propagação de trincas 2D. Notar (i) os vários tipos de trincas; (ii) as opções de cálculo ΔK_{rms} e sequencial (no texto chamado de modelo ccc), esta incluindo os efeitos de retardo; (iii) o editor de equações; (iv) as diversas opções dos gráficos de saída; e (v) o gráfico das curvas da/dN, que é alterado quando se mudam as constantes da tabela de variáveis, permitindo assim um fácil ajuste visual das diversas equações.

O método da/dN teve início quando Paris demonstrou convincentemente que é a gama do fator de intensidade de tensões ΔK e não a da tensão $\Delta\sigma$ o parâmetro que controla a propagação das trincas por fadiga, e propôs a famosa regra da/dN = $A \cdot \Delta K^m$, onde A e m são constantes que dependem do material. Entretanto, as curvas da/dN vs. ΔK típicas não são parabólicas, mas têm uma forma sigmoidal característica em log-log, com três fases bem distintas: a fase I, com um limiar de propagação ΔK_{th} e derivada decrescente, a fase II, de derivada constante, e a fase III, de derivada crescente até a fratura, que ocorre quando $K_{max} = K_C$. A regra de Paris só descreve bem a fase II, e pode gerar erros *significativos* nas previsões de vida, pois (i) não reconhece os efeitos da carga média, de ΔK_{th} nem de K_C na taxa da/dN, (ii) é muito conservativa em pequenos ΔK , e (iii) é *não*-conservativa em altos ΔK e em altas cargas médias. Além disto, *a maior parte da vida pode ser consumida ou para propagar trincas pequenas, ou após sobrecargas que retardem a trinca, reduzindo os valores de ΔK até a ordem de ΔK_{th} .*

Por isto, nos cálculos mais precisos, é necessário usar regras mais completas que a de Paris. Dentre estas, a mais simples é a de Elber, da/dN = $A \cdot (\Delta K - \Delta K_{th})^m$, que modela as fases I e II, mas não reconhece os efeitos da carga média (o programa ajusta dados experimentais de propagação de trincas por Paris e por Elber, usando-se mínimos quadrados). Inúmeras outras regras foram e podem ser propostas para descrever mais precisamente a curva da/dN vs. ΔK , como detalhado num trabalho complementar (Castro e Meggiolaro, 97a). Muitas delas estão incluídas num banco de dados, que pode ser expandido através do interpretador de equações. Uma facilidade particularmente útil é o gráfico de propagação mostrado na Fig. 9, no qual se plota, além de Paris e Elber, qualquer regra de propagação escolhida pelo usuário (para se expandir o gráfico, basta *clique* sobre ele). Desta forma se tem uma informação visual imediata sobre a concordância entre as diversas regras (o que permite um rápido ajuste de suas constantes), e pode-se facilmente estudar a sensibilidade das previsões de vida à fadiga aos diversos modelos de propagação.

Pode-se calcular o crescimento da trinca correspondente a um dado carregamento especificado (tensão $\Delta\sigma$; atuando durante n_i ciclos), ou especificar as dimensões iniciais e finais da trinca, caso se queira calcular a vida correspondente. Em todos os casos, o programa automaticamente pára os cálculos e indica o instante da ocorrência se durante o carregamento acontecer (i) fratura por $K_{max} = K_C$, ou (ii) a trinca atingir o tamanho máximo especificado para a trinca final, ou (iii) a peça atingir a resistência à ruptura no ligamento residual, ou (iv) da/dN igualar Imm/ciclo ou o CTOD por ciclo, ou (v) no caso das trincas 2D, quando uma das fronteiras da peça é atingida pela frente da trinca. Desta forma, pode-se usar os valores calculados com a garantia de que o limite de validade dos modelos matemáticos nunca é excedido. Além disto, o programa avisa quando atingir o escoamento do ligamento residual antes que o valor especificado para n_i ou para o tamanho máximo da trinca seja atingido.

No caso das trincas 2D, o programa pode desenhar as frentes de trinca a cada evento especificado pelo usuário, para que se possa acompanhar as mudanças de geometria que ocorrem durante a sua propagação. E também pode plotar gráficos que envolvam qualquer das variáveis calculadas, como variação da forma de trinca a/c, $K_I(a)$, $K_I(c)$, etc., para que se possa estudar todas as nuances do comportamento daquelas trincas, que certamente não é nem simples nem intuitivo. A Figura 10 ilustra o crescimento de uma trinca superficial semi-elíptica, mostrando claramente a mudança de forma observada durante a propagação de trincas 2D. Como todos os gráficos gerados pelo programa são facilmente plotáveis, esta é uma poderosa ferramenta para visualizar e ilustrar os problemas de fadiga.

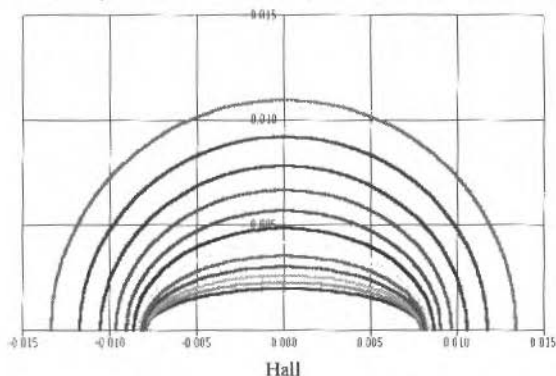


Fig. 10a Previsão do crescimento de uma trinca superficial semi-elíptica, mostrando a mudança da forma da frente da trinca, uma característica do problema 2D.

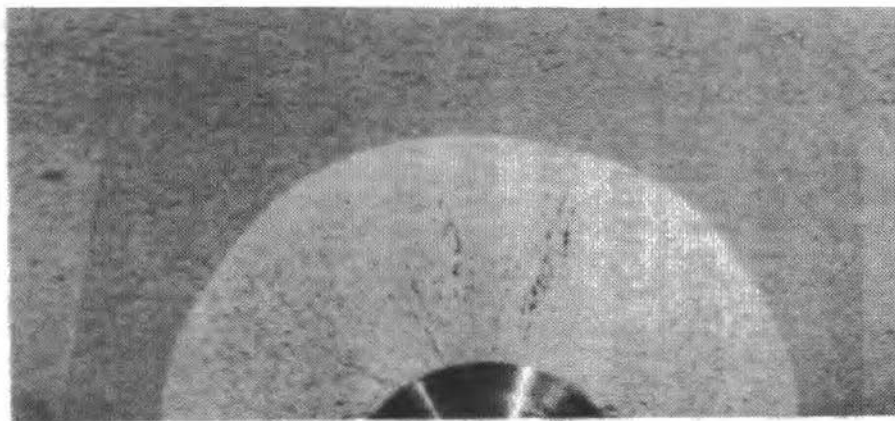


Fig. 10b Trinca superficial mostrando mudanças de forma como as simuladas acima (Broek 89).

Prever o crescimento de trincas sob carregamentos de amplitude constante usando regras mais completas do que a de Paris é uma tarefa (conceitualmente) trivial. No caso geral, a regra de propagação pode depender de ΔK , de ΔK_{th} , de K_C , da carga média (em geral dada por $R = K_{min}/K_{max}$), e de outros parâmetros: $da/dN = F(\Delta K, \Delta K_{th}, K_C, R, \dots)$. Para calcular o número de ciclos que a trinca leva para crescer de um comprimento inicial a_0 até um final a_f , pode-se usar qualquer algoritmo de integração numérica, como Simpson, e.g., para obter:

$$N = \int_{a_0}^{a_f} \frac{da}{F(\Delta K, \Delta K_{th}, K_C, R, \dots)} \quad (10)$$

Mas o problema do crescimento de trincas sob carregamentos complexos não é nada trivial. Mesmo quando se desprezam os efeitos da interação entre os ciclos, como retardos na taxa de propagação induzidos por sobrecargas, implementar um algoritmo numericamente eficiente exige cuidados não desprezíveis. No **vídeo 98** foram implementados dois métodos para tratar este problema: os métodos do crescimento ciclo a ciclo (ccc) e da carga de amplitude constante equivalente (ΔK_{rms}), Barson e Rolfe (87). Este é o mais simples, e substitui o carregamento complexo por um outro de amplitude $\Delta \sigma_{rms}$ constante equivalente, no sentido de causar o mesmo crescimento da trinca. O algoritmo de Hudson (81)

$$\Delta K_{rms} = (\sigma_{max_{rms}} - \sigma_{min_{rms}}) \sqrt{\pi a} \cdot f(a) \quad (11)$$

$$\sigma_{max_{rms}} = \sqrt{\frac{\sum_{i=1}^q (\sigma_{max_i})^2}{q}}, \quad \sigma_{min_{rms}} = \sqrt{\frac{\sum_{i=1}^q (\sigma_{min_i})^2}{q}}, \quad R_{rms} = \frac{\sigma_{min_{rms}}}{\sigma_{max_{rms}}} \quad (12)$$

permite que o carregamento complexo seja tratado como se fosse de amplitude constante (e igual a $\Delta \sigma_{rms}$). Este procedimento foi generalizado para o caso das trincas 2D, seguindo as mesmas idéias detalhadas acima. Como ΔK_{rms} se comporta como uma carga simples, o número de ciclos N que a trinca leva para crescer do comprimento inicial a_0 até o final a_f é dado por:

$$N = \int_{a_0}^{a_f} \frac{da}{F(\Delta K_{rms}, R_{rms}, \Delta K_{th}, K_C, \dots)} = \int_{a_0}^{a_f} \frac{da}{F(a)} \quad (13)$$

Na prática, um carregamento complexo é dado por uma seqüência de picos e vales $\{\sigma_{\max_i}, \sigma_{\min_i}\}$, ou pela seqüência equivalente $\{\sigma_m, \sigma_m, n_i\}$. Para se usar o método ΔK_{rms} deve-se primeiro zerar os σ_{\max_i} e $\sigma_{\min_i} < 0$, para depois calcular $\Delta\sigma_{\text{rms}}$, R_{rms} . Entretanto, há uma série de detalhes que tornam o uso deste modelo menos simples do que aparentam as equações acima. Deve-se notar que:

- O método ΔK_{rms} deveria ser chamado de $\Delta\sigma_{\text{rms}}$, pois ele *não* contabiliza o crescimento da trinca em ΔK_{rms} .
- $\Delta\sigma_{\text{rms}}$ *não* é o valor médio quadrático de σ (se o valor rms de σ fosse usado, cargas de amplitude constante não convergiriam para $\Delta\sigma_{\text{rms}} = \Delta\sigma$, e se os picos e vales negativos não fossem zerados, cargas com $\sigma_m = 0$ não causariam crescimento da trinca).
- O valor ΔK_{rms} de um carregamento complexo é *similar mas não idêntico* a um carregamento simples pois, como toda estatística, ΔK_{rms} não reconhece ordem temporal, e não pode perceber problemas como (i) fratura súbita (basta que *num único* evento o valor de $K_{\max} = K_C$), (ii) qualquer efeito de interação entre os ciclos do carregamento (como *retardos* induzidos por sobrecargas)
- *Não* se pode garantir a inatividade da trinca se $\Delta K_{\text{rms}}(a_0) < \Delta K_{\text{th}}(R_{\text{rms}})$

Estes problemas acentuam-se na implementação do modelo de crescimento 2D. Os detalhes estão discutidos em trabalhos complementares (Castro e Meggiolaro, 97b e Castro et al., 98).

O método ccc quantifica o crescimento da trinca a cada ciclo do carregamento, e é, desta forma, conceitualmente similar ao acúmulo de dano usado na modelagem da geração das trincas por fadiga. Como no caso ΔK_{rms} , a parte negativa dos carregamentos é desconsiderada, já que a trinca não cresce enquanto fechada. Desprezando efeitos de interação entre os diversos eventos de um carregamento complexo, é fácil escrever uma expressão geral para o crescimento da trinca a cada ciclo, segundo qualquer regra de propagação. Sendo $da/dN = F(\Delta K, R, \Delta K_{\text{th}}, K_C, \dots)$, então no i -ésimo $1/2$ ciclo $\Delta\sigma_i$ a trinca cresce de δa_i dado por:

$$\delta a_i = F(\Delta K(\Delta\sigma_i, a_i), R(\Delta\sigma_i, \sigma_{\max_i}), \Delta K_{\text{th}}, K_C, \dots) / 2 \quad (14)$$

As trincas 2D também podem crescer na profundidade e na largura, e tanto $\Delta K(a_i)$ quanto $\Delta K(c_i)$ dependem de a_i e de c_i ao mesmo tempo. Logo, o crescimento δa_i e δc_i nas duas direções é acoplado. Ver os trabalhos complementares já citados acima para detalhes.

Para se efetuar o cálculo do crescimento ciclo a ciclo de um carregamento complexo, deve-se reconhecer primeiro todos os eventos do carregamento. Mas para isto é particularmente importante utilizar a contagem *rain-flow seqüenciada*, como indicado na Fig. 3, pois os efeitos de ordem do carregamento na propagação das trincas são de duas naturezas distintas:

- os de retardo no crescimento subsequente da trinca (efeitos prolongados), e que podem ser causados, e.g., por alteração do fechamento tipo Elber ou por bifurcações da ponta da trinca
- os relacionados com eventos de fratura, que são instantâneos e dependem da relação entre a tenacidade à fratura do material K_C e $K_{\max_i} = \sigma_{\max_i} \sqrt{\pi a_i} f(a_i)$ em cada evento.

Estes últimos são muito mais dramáticos, pois significam a quebra da peça e tem que ser previstos com exatidão. A modificação introduzida na contagem *rain-flow* (que na sua versão original *antecipa* os grandes picos do carregamento em relação ao momento de sua ocorrência) evita que o programa não reconheça um evento de quebra quando os picos de carga ocorrem com a trinca já grande, pois estes só são contabilizados no instante de sua ocorrência e o programa sempre verifica se $K_{\max_i} < K_C$. (A contagem *rain-flow* seqüencial não elimina *todos* os problemas de ordenamento causados pelo método tradicional, mas é certamente uma opção recomendável pois apresenta vantagens sobre e não acrescenta dificuldades ao algoritmo de contagem original).

O algoritmo ccc não é eficiente sob carregamento complexo. Por isto, na sua implementação numérica foram introduzidas opções para diminuir o tempo de computação, como uma (pequena e especificável) percentagem de variação na \sqrt{a} para só então mudar o valor do fator geométrico de ΔK usado nos cálculos.

Como no caso geral $\Delta K = \Delta\sigma\sqrt{\pi a} f(a)$, onde $f(a)$ é um fator que só depende da geometria, pode-se dizer que a gama do fator de intensidade de tensões a cada ciclo do carregamento ΔK_i depende: (i) da variação da tensão naquele ciclo $\Delta\sigma_i$, e (ii) do comprimento da trinca a_i naquele *instante*. Ora, desta

forma ΔK depende de duas variáveis de naturezas diferentes. É claro que $\Delta\sigma_i$ pode em geral variar bastante a cada ciclo quando o carregamento é complexo, mas as trincas *sempre* se propagam muito devagar por fadiga, pois as maiores taxas de crescimento *estável* observadas na prática são da ordem de $\mu\text{m}/\text{ciclo}$, sendo que durante a maioria da vida as taxas são melhor medidas em nm/ciclo . Como em geral as expressões para $f(a)$ podem ser muito complexas mas não apresentam descontinuidades, pode-se tirar proveito da pequena mudança no produto $\sqrt{a}f(a)$ para pequenos incrementos no comprimento da trinca. Desta forma, em vez de se calcular a cada ciclo $\Delta K_i = \Delta\sigma_i \sqrt{(\pi a_i)} f(a_i)$, o que demandaria grande esforço computacional, pode-se manter o produto $\sqrt{a}f(a)$ constante enquanto a \sqrt{a} não variar da (pequena) percentagem especificada pelo usuário do programa.

Efeitos de seqüência podem ser *muito* significativos na propagação das trincas de fadiga (podem *parar* o crescimento da trinca!). Este é um problema complexo, com vários mecanismos envolvidos como, e.g.: (i) alteração do *fechamento* da trinca; (ii) *cegamento* e/ou *bifurcação* da ponta da trinca; (iii) tensões e/ou deformações *residuais*; (iv) *rugosidade* das superfícies da trinca; e (v) *oxidação* das faces da trinca (Suresh, 91). A importância relativa dos diversos mecanismos pode variar dependendo de fatores como tamanho da trinca, microestrutura do material, estado de tensões dominante, meio ambiente, etc. Entretanto, as modelagens tradicionais deste problema baseiam-se apenas na idéia do fechamento induzido por plasticidade, segundo a qual:

- Trincas de fadiga se propagam cortando um material que já foi ciclicamente deformado pela zona plástica que acompanha suas pontas.
- As faces da trinca ficam embutidas num envelope de deformações (plásticas) residuais trativas.
- As trincas de fadiga *comprimem* as suas faces quando completamente descarregadas, e só se abrem aliviando-as de forma progressiva.
- Quanto maior a carga de abertura da trinca, menor o valor efetivo de ΔK : $\Delta K_{\text{ef}} = K_{\text{max}} - K_{\text{ab}}$
- ΔK_{ef} seria o principal controlador da taxa da/dN .
- ΔK_{ef} diminui se a carga de abertura aumentar quando a trinca penetrar na zona plástica hipertrofiada pela sobrecarga, retardando ou até parando o crescimento da trinca.

O programa dispõe de dois modelos para quantificar a interação entre ciclos. O primeiro é o modelo de Wheeler (Broek, 88), segundo o qual se a zona plástica do carregamento estiver embutida na de uma sobrecarga (ver Fig. 11), o retardo depende da distância da fronteira plástica da sobrecarga à ponta da trinca, isto é, se $a_i + ZP_i < a_{\text{sc}} + ZP_{\text{sc}}$, e vale:

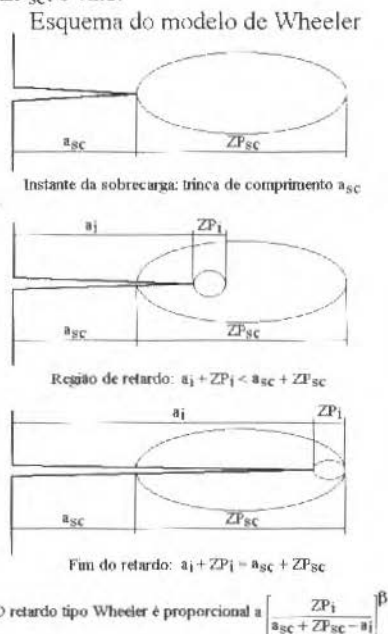


Fig. 11 Esquema da zona de influência dos modelos de retardo tipo Wheeler. No **VIDA 98** pode-se especificar o expoente dos modelos e um limiar de filtragem, abaixo do qual não se consideram os efeitos das sobrecargas (ver detalhes em Castro e Meggiolaro 97b).

$$\left(\frac{da}{dN}\right)_{ret_i} = \left(\frac{da}{dN}\right)_i \cdot \left(\frac{ZP_i}{a_{sc} + ZP_{sc} - a_i}\right)^\beta \quad (15)$$

Este modelo não pode prever a parada das trincas após uma sobrecarga de amplitude suficientemente grande. Por isto, também foi introduzida e implementada uma modificação que aplica o efeito do retardo em ΔK e não em da/dN :

$$\Delta K_{ret}(a_i) = \Delta K(a_i) \cdot \left(\frac{ZP_i}{a_{sc} + ZP_{sc} - a_i}\right)^\gamma \quad (16)$$

Os detalhes destes modelos, bem como de sua implementação numérica, tanto no caso 1D como no 2D, são bastante longos, e estão discutidos num trabalho complementar (Castro e Meggiolaro 97b). Como nos casos SN e ϵN , também há uma versão simplificada do método da/dN para os usuários menos experientes. E, da mesma forma, a função de cada um dos botões da tela deste método, bem como o embasamento teórico de todas as opções de cálculo, são detalhadamente descritos nos arquivos de ajuda do programa.

Conclusões

Um programa chamado **ViDa** foi concebido e desenvolvido para calcular vida à fadiga sob carregamentos complexos por todos os métodos usuais de projeto mecânico, incluindo todas as facilidades que pudessem ser úteis ao projetista, como bancos de dados, inúmeras opções de cálculo, interface amigável, etc. Este programa tem sido compartilhado com pessoal qualificado que queira contribuir para o seu desenvolvimento, e que participe do mini-curso intensivo "Avanços na Automação do Projeto à Fadiga", oferecido pelo Centro de Estudos em Integridade Estrutural - CEIE - da PUC-Rio. A versão 98 deste programa inclui, além das características resumidas no texto, rotinas de cálculo depuradas por três anos de testes intensivos. Por isto, a distribuição do programa para uso acadêmico em Universidades já pode ser discutida diretamente com os autores.

Referências

- Anderson, T.L., 1995. "Fracture Mechanics", CRC.
- Bannantine, J.A.; Comer, J.J. e Handrock, J.L., 1990, "Fundamentals of Metal Fatigue Analysis", Prentice Hall.
- Barson, J.M. e Rolfe, S.T., 1987, "Fracture e Fatigue Control in Structures", Prentice-Hall.
- Broek, D., 1988, "The Practical Use of Fracture Mechanics", Kluwer.
- Castro, J.T.P., 1979, "Um Método Racional Explícito para Projeto de Componentes Mecânicos Sujeitos a Carregamentos Dinâmicos Gerais", Rev. Bras. Ciênc. Mecânicas v.2, n.2, pp71-80.
- Castro, J.T.P.; Freire, J.L.F. e Vieira, R.D., 1994, "Fatigue Life Prediction of Repaired Welded Structures", J.Constructional Steel Research, V.28, pp.187-195.
- Castro, J.T.P. e Meggiolaro, M.A., 1997a, "Uma Nota Sobre a Modelagem da Curva de Propagação de Trincas por Fadiga", submetido à Rev. Bras. Ciênc. Mecânicas.
- Castro, J.T.P. e Meggiolaro, M.A., 1997b, "Uma Nota Sobre a Automação do Cálculo da Propagação de Trincas por Fadiga sob Carregamentos Complexos", submetido à Rev. Bras. Ciênc. Mecânicas.
- Castro, J.T.P.; Giassoni, A. e Kenedi, P.P., 1998, "Propagação por Fadiga de Trincas Superficiais Semi e Quarto-Elipticas em Soldas Molhadas", Rev. Bras. Ciênc. Mecânicas vol.20, n.2, pp.263-269, 98.
- Castro, J.T.P. e Meggiolaro, M.A., 1998, "Alguns Comentários sobre a Automação do Método ϵN para Dimensionamento à Fadiga sob Carregamentos Complexos", a ser publicado na Rev. Bras. Ciências Mecânicas.
- Dowling, N. E., 1993, "Mechanical Behavior of Materials", Prentice-Hall.
- Farahmand, B., 1997, "Fatigue e Fracture Mechanics of High Risk Parts", Chapman e Hall.
- Fuchs, H. O. e Stephens, R.L., 1980, "Metal Fatigue in Engineering", Wiley.
- Hardy, S. J. e Malik, N.H., 1992, "A Survey of Post-Peterson Stress Concentration Factor Data", Int.J.Fatigue v.14, n.3, pp.147-153.
- Hertzberg, R. W., 1989, "Deformation e Fracture Mechanics of Engineering Materials", Wiley.

- Hudson, C. M., 1981, "A Root-Mean-Square Approach for Predicting Fatigue Crack Growth under Random Loading", ASTM STP 748, pp.41-52.
- Juvinall, R. C., 1967, "Stress, Strain e Strength", McGraw-Hill.
- Meggiolaro, M.A. e Castro, J.T.P., 1995, "VIDA - Programa para Previsão de Vida à Fadiga sob Carregamentos Complexos", Anais do III Simpósio de Análise Experimental de Tensões, pp.7-10, ABCM.
- Meggiolaro, M.A. e Castro, J.T.P., 1996, "Desenvolvimentos na Automação do Projeto à Fadiga sob Carregamentos Complexos", II Sem. Mec. Fratura, pp.99-118, ABM.
- Moura Branco, C. et al., 1987, "Fadiga de Estruturas Soldadas", Gulbenkian.
- Nelson, D. V. e Fuchs, H.O., 1977, "Predictions of Cumulative Fatigue Damage Using Condensed Load Histories", in Fatigue Under Complex Loading, SAE.
- Peterson, R. E., 1974, "Stress Concentration Factors", Wiley.
- Rice, R. C., ed., 1988, "Fatigue Design Handbook", SAE.
- Shigley, J. E. e Mischke, C.R., 1989, "Mechanical Engineering Design", McGraw-Hill.
- Suresh, S., 1991, "Fatigue of Materials", Cambridge.
- Tada, H.; Paris, P.C. e Irwin, G.R., 1985, "The Stress Analysis of Cracks Handbook", Paris Prod.

Abstract

Biage, M., 1998, "Analysis of Impedance Probes Behavior Applied to Liquid Film Thickness Measurements", J. of the Braz. Soc. Mechanical Sciences, Vol. 20, No. 4, pp. 486-505.

A study of impedance probes behavior (conductive and capacitive), aimed at liquid film thickness measurement, is presented. Theory, principle of operation, calibration and error sources are discussed. This study was encouraged by the need to find low-cost solutions for problems involving local and instantaneous fluid measurements. The equipment in question can be used to study the liquid-gas interface behavior and related flow instability. Also, results can be used for the development of closure conditions in two-fluid flow modeling. Analysis of the probes dynamic behavior was carried out employing the experimental results obtained for the liquid film flow on a vertical rectangular channel, exposed to a counter-current gas flow. This study confirmed that the probes presented good response in frequency and spatial resolution. In fact, they characterize efficiently the transition process of a concurrent to counter-current flow.

Keywords: Two-phase Flow, Liquid film Thickness, Conductive Probe, Capacitive Probe.

Sodré, J.R. and Yates, D. A., 1998, "A Parametric Study on the Influence of the Spark Plug Position on Combustion, Emissions and Performance of an Engine", J. of the Braz. Soc. Mechanical Sciences, Vol. 20, No. 4, pp. 506-517.

An analytical model has been developed to calculate the flame geometry parameters of a spark ignition engine. The model is based on a disc type combustion chamber. The flame geometry model is part of a computer program that simulates the cycle of spark ignition engines. The model requires the spark plug to be located in the cylinder head, and its position can be anywhere from the center to the corner with the cylinder liner. The effects of the spark plug position on combustion, emissions and performance have been investigated. A parametric analysis has shown that combustion takes shorter periods as the spark plug is closer to the center, for which higher cylinder pressures are attained. The performance parameters were insensitive to the plug position, but lower emission levels were verified when the plug was located in the corner. Experiments carried out on a research engine have provided the basic information to the program to perform the simulations.

Keywords: Internal Combustion Engines, Combustion, Models

Leite, A. P. F., 1998, "Thermodynamic Analysis and Modeling of an Adsorption-Cycle System for Refrigeration from Low-Grade Energy Sources", J. of the Braz. Soc. Mechanical Sciences, Vol. 20, No. 4, pp. 518-531.

A theoretical analysis of an adsorption-cycle, employing low-grade thermal sources, for application to a cooling system is presented. The basic fundamentals of adsorption processes and some considerations about the most commonly used adsorbent-adsorbate pair in refrigeration, the activated carbon-methanol pair, are described. It is established from the analysis of the main isotherms of adsorption that the Dubinin-Astakhov equation as the most suitable equation of state to represent the adsorption of methanol in activated carbon. An expression to calculate the liberated heat from the adsorption process, or the isosteric heat of adsorption, is deduced and aspects related to the kinetics of adsorption are also considered. A thermodynamic analysis of the adsorption cycle has been carried out in order to obtain a simple ratio between condensation temperature and regeneration temperature and to evaluate the coefficient of thermal performance (COP) of an ideal quadri-thermal machine. Finally, the energy equation for an adsorptive bed interacting with other components of a simple effect cooling machine that operates at moderate temperatures is given, and some of their terms are detailed. This theoretical analysis can be applied to an adequate modeling and design of a refrigeration system, based on an adsorption cycle operating from a low-grade energy source.

Keywords: Microporous Media, Adsorption Potential, Isosteric Heat, Adsorption Cooling Cycle.

Silva Neto, A. J., Fordham, M. J., Kiether, W. J. and Sorrel, F. Y., 1998, "Rapid Thermal Processing Furnace With Three Heating Zones", J. of the Braz. Soc. Mechanical Sciences, Vol. 20, No. 4, pp. 532-541.

A new rapid thermal processing (RTP) furnace configuration is described, and the mathematical model, model predictions and experimental results are presented. The ultimate design objective is to achieve uniform wafer temperature distribution throughout the complete heating cycle. It is accomplished as demonstrated by the uniformity of the measured film thickness after polycrystalline silicon deposition. The three-zone RTP system was also designed for operation with thin quartz windows, for minimum window heating.

Keywords: Rapid Thermal Processing, Modeling, Thermal Radiation, Temperature Uniformity.

Pinotti, M. and Braile, D. M., 1998, "Shear Stresses and Turbulent Eddies: The Causes of Mechanical Hemolysis in a Centrifugal Blood Pump", J. of the Braz. Soc. Mechanical Sciences, Vol. 20, No. 4, pp. 542-552 (in Portuguese).

The lack of basic information about the performance of mechanical hemolysis severely affects centrifugal blood pump handling. The present work faced this problem by studying the flow structures and the way hemolytic potential is influenced by them. Two distinct approaches were applied: numerical simulation of a single channel of the pump, in order to understand the interaction of inertial, viscous and pressure forces in different operational situations, and non-invasive measurements of the velocity field to provide a general picture of the flow field as well as the interaction between the flow generated by each channel. Solving the momentum equations, that were written in generalized orthogonal coordinates, using the stress-flux formulation, was the challenge of the numerical method. The computational program was devised by employing the finite volume method and it was implemented in FORTRAN language. The velocity measurements were performed by a laser Doppler anemometer system capable of acquiring and processing two simultaneous orthogonal velocity components. The main contribution of the present study concerns the development of a specific methodology which provides the link between the flow structures and the potential damage to the red blood cells.

Keywords: Laser Doppler Anemometer, Turbulent Flow, Hemolysis, Centrifugal Blood Pump, Bioengineering.

Nohara, B. T., 1998, "An Absorption Algorithm and Its Implementation for Irregular Ocean Waves in a Test Tank", J. of the Braz. Soc. Mechanical Sciences, Vol. 20, No. 4, pp. 553-563.

This paper describes a newly developed absorbing algorithm and its implementation for irregular ocean waves in a test tank. In a tank test, while using a wave maker for determining ocean wave tolerance of floating body structures, as well as ships, there is a problem: reflective waves from the test body or a tank termination disturb the target waves. These reflective waves make test performance undependable, because the test body is exposed to reflective waves along with target waves. An accurate test must keep the test body out of reflective waves. Past studies have made the conditions for complete absorption of regular waves clear. However the conditions for absorption of irregular waves is only partially obtained using hydrodynamic force acting on a wave board. The authors propose a complete absorption algorithm, which utilizes sensing of water surface elevation instead of hydrodynamic force, and its implementation for irregular waves. The authors have obtained good experimental results from this algorithm. Also in this paper, the authors introduce time-frequency analysis, using a short-time Fourier transform technique, for visualizing the state of absorption.

Keywords: Wave Maker, Absorption, Irregular Wave, Short-Time Fourier Transform

Souza Jr., J. R. and Bishop, S. R., 1998, "Boundaries of Safe Motion Through a Coarse Grid-of-Starts", J. of the Braz. Soc. Mechanical Sciences, Vol. 20, No. 4, pp. 564-575.

This paper describes computational methods for the evaluation of safe limits of operation of driven mechanical systems. We define the problem of evaluating the safety of transient and steady-state motions in terms of the escape from a potential well. We then describe a simple, robust method of determining boundaries of safe operation in control space, and we conclude by applying the method to a number of examples.

Keywords: Nonlinear Dynamics, Escape Phenomena, Potential Wells, Nonlinear Oscillators

Savi, M. A. and Pacheco, P. M. C. L., 1998, "On the Effect of Temperature in Non-Linear Dynamics of an Elasto-Plastic Oscillator With Isotropic Hardening", J. of the Braz. Soc. Mechanical Sciences, Vol. 20, No. 4, pp. 576-586.

This contribution presents a dynamical analysis of an elasto-plastic oscillator where the thermomechanical coupling is considered. A constitutive model, used to describe the restitution force of the oscillator, is presented. Isotropic hardening is considered. The operator split technique is used to develop a numerical procedure. An integrator scheme associated with the return mapping algorithm is used to solve the equations of motion. Numerical simulations show that the effect of thermomechanical coupling may produce an unstable response.

Keywords: Non-linear Dynamics, Elasto-plasticity, Modeling and Simulation.

Elmer, K. H. and Natke, H. G., 1998, "A Time Dependent Adaptive Finite Element Method", J. of the Braz. Soc. Mechanical Sciences, Vol. 20, No. 4, pp. 587-595.

The complexity of many realistic problems in transient dynamics requires very large systems. Reliable numerical FE-solutions with high accuracy need models with many degrees of freedom and many time steps. So time dependent adaptive FE-methods are developed to optimize the mesh and minimize the computational costs.

Gonçalves, R. F. G. and Helman, H., 1998, "Control of Rolled Strips Thickness Using Fuzzy Logic", J. of the Braz. Soc. Mechanical Sciences, Vol. 20, No. 4, pp. 645-655 (in Portuguese).

The thickness of a rolled strip, which must remain within very close limits, is one of the critical parameters in the characterization of its quality. The process of controlling this thickness frequently requires actions which may affect other important characteristics of the strip, such as profile and shape. Two control procedures are commonly used for this purpose, one on the screw-down mechanism and the other on the strip front or back tensions. One or the other may be more adequate, depending on the operational conditions. These control actions have been normally determined and executed in correspondence with the variation of only one of the parameters of the process. In the present work, a method is developed based on the application of fuzzy logic, which allows for the calculation of suitable control actions to adjust the final thickness of the strip, considering the simultaneous variation of any two operational parameters of the process.

Keywords: Strip Rolling, Gage Control, Fuzzy Logic.

Kurka, P. R. G., and Araújo, C. A., 1998, "Automatic Process for the Determination of Modal Supersets of Residual Flexibilities Used in The Modal Synthesis Method", J. of the Braz. Soc. Mechanical Sciences, Vol. 20, No. 4, pp. 656-665.

The work presents an automatic process for the selection of modes of substructures with the purpose of building the superset of a residual flexibility model. This superset is used in the modal synthesis method for the experimental analysis of large structures. The qualitative indication of modes to be eliminated in a substructure plays an important role in the precision of the synthesis process. Actual mode elimination techniques are based on arbitrary user decisions which could lead to the extinction of modes which would have an important contribution to the synthesis of the complete structure. The technique is applied here for systems without damping. Such a technique relies on a relative weighting of the modes of the substructures, based on Euclidian norm calculations.

Keywords : Modal Synthesis, Modal Supersets, Residual Flexibility, Identification, Experimental Analysis.

Meggiolaro, M. A. and Castro, J. T. P., 1998, "ViDa 98 - Visual Damagemeter To Automate the Fatigue Design Under Complex Loading", J. of the Braz. Soc. Mechanical Sciences, Vol. 20, No. 4, pp. 666-685 (in Portuguese).

*A powerful language named **ViDa 98** was developed to automate all the methods traditionally used in mechanical design to calculate the fatigue damage caused by complex loading: SN, HW (for welded structures) and ϵN to predict crack initiation, and da/dN for studying plane and 2D crack propagation based on Fracture Mechanics concepts, considering load sequence effects. It has a friendly graphical interface and runs in a Windows environment. Among a number of similar features, can be highlighted: several intelligent data banks, two rain-flow counters and a race-track filter, generators of corrected hysteresis loops and 2D crack fronts, importation and adjustment of experimental data, an equation interpreter and a complete help file, which includes an online advanced course on fatigue. Moreover, its damage models introduce various non-trivial innovations, and the interface language can be English or Portuguese.*

Keywords: Fatigue, Life Prediction, Complex Loading.

The moving wave front is used for a broad time dependent mesh refinement, based on intensity vectors and the speed of wave propagation (intensity indicator), several time steps in advance. The a-posteriori Zienkiewicz-Zhu error indicator controls the adaptive mesh refinement. An implicit-explicit algorithm for direct time integration is based upon operator splitting and mesh partitions. The algorithm avoids subcycling and uses the same time step for a coarse mesh and the local refined mesh.

Keywords: Adaptive FEM, Transient Dynamics

Mello, O. A. F., 1998, "On the Application of Flight Simulation to the Investigation of Helicopter Accidents", J. of the Braz. Soc. Mechanical Sciences, Vol. 20, No. 4, pp. 596-610.

Two applications of flight simulation to the investigation of helicopter accidents are presented. In the first, an accident with typical tail rotor loss characteristics is considered. The investigation board worked on two hypotheses, namely tail rotor shaft failure and pilot's loss of pedal control after he suddenly increased the collective pitch near the ground and delayed applying pedals as needed. A simulation was conducted using simple models of yaw dynamics and tail rotor aerodynamics, and results indicated that pedal control would still be available even with a three second pilot delay in applying the pedals, therefore the hypothesis of loss of pedal control was discarded. In the second application, a helicopter accident at sea in which the aircraft wreck had not been recovered is considered. In that case, the investigation board had to rely on information from the Cockpit Voice/Flight Data Recorder (CVFDR) and a video recorded by an undersea robot. The most significant information obtained from the FDR were extremely high vibrations in all three axes, at a frequency associated with the first harmonic of main rotor rotational speed. The investigation was directed towards several hypotheses associated with main rotor blade and assemblies that might explain the vibrations. A simulation program based on an existing general helicopter flight simulation code was developed and simulations were conducted for the assumed blade failure hypotheses. Results indicated that the excessive accelerations were consistent with the loss of a large rotating mass, due to blade fracture near the root. In both applications, simulation provided substantial grounds for the investigation boards to establish the most probable causes for the accidents.

Keywords: Helicopter, Aeronautical Accident, Flight Simulation, Flight Dynamics.

Maruyama N., 1998, "Detecting Faults in Cooling Coils of Air-Handling Units - Part I : The Method and Some Simulation Results", J. of the Braz. Soc. Mechanical Sciences, Vol. 20, No. 4, pp. 611-627.

Building Energy Management and Control systems have contributed to the reduction of energy use without affecting the occupant's comfort, however, the inability to provide early detection and compensation of faults in air-handling units has not provided extra energy saving. For further improvement of reliability, safety and performance, an early detection and diagnosis of faults is of great interest. A fault detection method which uses static neuro-fuzzy models to describe the correct operation of the plant is proposed to detect faults in cooling coils of air-handling units. Abnormal operation of the plant is detected when residuals exceed a variable threshold value which accounts for modelling errors, noisy measurements and unmodelled disturbances. Simulation results are presented for both whole operating space and typical operation data of air-handling units to demonstrate the capabilities of the proposed scheme.

Keywords: Fault Detection, Neuro-Fuzzy Modelling, Air-Handling Units.

Maruyama, N., 1998, "Detecting Faults in Cooling Coils of Air-Handling Units - Part II : The Issues of Practical Implementation", J. of the Braz. Soc. Mechanical Sciences, Vol. 20, No. 4, pp. 628-644.

Building Energy Management and Control systems have contributed to the reduction of energy use without affecting the occupant's comfort, however, the inability to provide early detection and compensation of faults in air-handling units has not provided extra energy saving. For further improvement of reliability, safety and performance, an early detection and diagnosis of faults is of great interest. A fault detection method which uses static neuro-fuzzy models to describe the correct operation of the plant is proposed to detect faults in cooling coils of air-handling units. Abnormal operation of the plant is detected when residuals exceed a variable threshold value which accounts for modelling errors, noisy measurements and unmodelled disturbances. This work points out, the major issues when designing fault detectors in cooling coils of air-handling units based on neuro-fuzzy models. A methodology is proposed which tries to overcome the drawbacks of neuro-fuzzy models and the intrinsic difficulties of modelling cooling coils. An example is presented using an actual plant. Comments on the method and its performance are given.

Keywords: Fault Detection, Neuro-Fuzzy Modelling, Air-Handling Units.

Book Review

"Dinâmica;" by Roberto A. Tenenbaum¹

1997, ISBN 85-7108-201-4 756, p., In Portuguese

Editora UFRJ², Rio de Janeiro, RJ Brazil

Classical mechanics plays an important and fundamental role in practically all the engineering curricula. Since classical mechanics is the oldest field of physics and the first one to be completely amenable to a mathematical treatment, it is an ideal topic to exercise the student's mind in formulating and exploring mathematical models of the physical reality, using physical concepts familiar -to a large extent- from everyday experience. Traditionally, the first and basic mechanics courses in the engineering curricula are simultaneous to the calculus courses. This is an excellent chance -but also a challenge- to the mechanics and in particular to the dynamics instructor to exercise new mathematical concepts, at the same time when they are first introduced to the student.

Often students may though feel overwhelmed by calculus and dynamics. Hence for many students there is a need for an intermediate dynamics course, particularly for those in mechanical and civil engineering, who will have to practice dynamics in the context of engineering problems in their professional career.

"Dinâmica" by Roberto A. Tenenbaum is an intermediate level text on the Newtonian dynamics of particles and rigid bodies, devoted mainly to engineering students, but also to students of mathematics or physics. It assumes as prerequisites a first course of applied or 'rational' mechanics, and also -to a limited extent- some familiarity with analysis and vector algebra. The book contains seven chapters and three appendices. Chapter 1 is formed by an introduction to Newtonian mechanics with historical notes, formulating the basic principles and explaining the notation used throughout the book. The second chapter is devoted to systems of free and axial vectors, introducing the concept of *central axis* and defining the equivalence of vector systems. Chapter 3 deals with the kinematics of points and of rigid bodies. First, the author defines the differentiation of a vector with respect to time in a given referential. The existence of the *angular velocity vector* of a rigid body is the content of Theorem 0, which is proved in an elegant manner. Great care is taken here and in the other parts of the book in always clearly defining the reference systems; the notation is such that the reference systems are always put in evidence, whenever they are not absolutely clear. The theorems on kinematics, needed in the sequel are all given in this chapter.

Chapter 4 is devoted to the dynamics of a single particle. Momentum, angular momentum, work and potential energy are defined here. In this chapter the author also proves the energy theorem and discusses conservation principles. Next, chapter 5 treats systems of particles and discusses continuous systems as a limit case. Some remarks on the dynamics of fluids are also contained at the end of this chapter.

The rigid body is treated in chapters 6 and 7. First, in chapter 6, the inertial properties of rigid bodies are examined in detail and the eigenvalue problem leading to principal axes of inertia is solved. Next, in chapter 7 the theorem of momentum is given and Euler's equations for the rigid body are derived. Again, the theorem of energy is derived for the rigid body, and conservation principles as well as impacts are discussed. Some particular cases of motion of the rigid body with a fixed point are also studied.

A short review of vector and matrix algebra, a discussion of the most important types of constraints and tables with the centroids and inertia properties of the most frequently encountered bodies and figures are given in the three appendices. In addition, "Dinâmica" also contains a large number of examples treated in great detail in the text, as well as a huge number of excellent problems left to solve for the student. The final results for most of these problems are also given at the end of the book.

The book deals strictly with Newtonian dynamics, more abstract formulations such as D'Alembert's principle, the principle of virtual velocities, Lagrange's equations, etc. are not touched. With view to this fact, the size of the book (more than 750 pages) seems astonishing at first. It becomes understandable if one takes into account the comprehensive way in which the material is presented. The author takes great pains to carefully examine all the points touched upon, not leaving any chance to

¹ UFRJ-COPPE-PEM-LAVI 21945-970 Rio de Janeiro, RJ roberto@serv.com.ufrj.br

² Editora UFRJ Av. Pasteur, 250 Sala 7 22295-900 Rio de Janeiro, RJ Brazil editora@forum.ufrj.br

possible misunderstandings. No references are given on more advanced topics or on other dynamics books, which one might expect from a graduate text.

The material is presented in a very systematic way, almost always going from the general to the more particular. The text is extremely clear and consistent, and all the figures are of excellent quality. This makes the book easy to use both for the instructor as well as for the student. The careful, authoritative and comprehensive way in which the material is presented, reflects the long experience of the author in teaching dynamics to generations of students. The reviewer feels that the book is particularly well suited for teaching groups of engineering students coming from a great variety of different undergraduate backgrounds

"Dinâmica" by Roberto A. Tenenbaum will fill an important gap in the landscape of engineering mechanics textbooks in Brazil and in Latin America. The reviewer does also not know of a comparable dynamics book of the same intermediate level and with similar goals on the American or European textbook market.

Peter Hagedorn

Institut f. Mechanik, TU Darmstadt
64328 Darmstadt, Germany
hagedorn@mechanik.tu-darmstadt.de

Journal of the Brazilian Society of Mechanical Sciences
Revista Brasileira de Ciências Mecânicas

Volume XX - 1998

Author Index

A

- Aguiar, Paulo Roberto;** Analysis of the Behaviour of Conventional Grinding Wheel as a Function of the Machining Parameters and the Bond Kind (in Portuguese); No. 3, pp. 390-399.
- Ahaus, Guido;** Active Control of Partially Filled, Elastically Mounted Centrifuges; No. 3, pp. 454-464.
- Alonso, Guilherme Vilalta;** Study of the Polyacrylamide Iqapol PA Influence on Drag Reduction in Turbulent Flow (In Portuguese); No. 2, pp. 219-232
- Araújo, Cleudmar Amaral;** Automatic Process for the Determination of Modal Supersets of Residual Flexibilities Used in The Modal Synthesis Method; No. 4, pp. 652-661.
- Avelino, Mila R.;** The State of the Art in Turbulence Modelling in Brazil. No. 1, pp. 1-38.
- Awruch, Armando Miguel;** Numerical Simulation of Three Dimensional Compressible Flows Using Finite Elements with Mixed Structured-Unstructured Meshes; No. 1, pp. 62-78.
- Azevedo, Luiz Filgueiras;** Comparison of Implicit Approximate Factorization Algorithms in the Solution of the Navier-Stokes Equations (in Portuguese); No. 3, pp. 353-380.

B

- Bezerra, Carlos André Dias;** Formulation of the Direct and Inverse Geometric Model of the Fully Parallel Cartesian Structure; No. 3, pp. 445-453.
- Biage, Milton;** Analysis of Impedance Probes Behavior Applied to Liquid Film Thickness Measurements; No. 4, pp. 482-501.
- Biage, Milton;** Study on the Transition of a Gas-Liquid Counter-Current Flow to a Concurrent Flow on a Vertical Flat Plate; No. 3, pp. 301-324.
- Bianchi, Eduardo Carlos;** Analysis of the Behaviour of Conventional Grinding Wheel as a Function of the Machining Parameters and the Bond Kind (in Portuguese); No. 3, pp. 390-399.
- Bishop, Steven R.;** Boundaries of Safe Motion Through a Coarse Grid-of-Starts; No. 4, pp. 560-571.
- Bismarck-Nasr, Maher N.;** On Comparing Theory and Experiment of Aerodynamic Forces and Moments on T-Tail Configurations; No. 2, pp. 233-243.
- Bortoloto, Rodrigo Gurian;** Analysis of the Behaviour of Conventional Grinding Wheel as a Function of the Machining Parameters and the Bond Kind (in Portuguese); No. 3, pp. 390-399.
- Braile, Domingo M.;** Shear Stresses and Turbulent Eddies: The Causes of Mechanical Hemolysis in a Centrifugal Blood Pump (in Portuguese); No. 4, pp. 538-548.

C

- Caldeira Pires, A.;** On the Turbulent Transport Characteristics of Non Premixed Diffusion Flames in Mutual Interaction; No. 2, pp. 164-178.
- Carajilescov, Pedro;** Analysis of Critical Heat Flux in Rod Bundles by Neural Nets (in Portuguese); No. 1, pp. 91-102.
- Carrara, Alcy Rodolfo Santos;** Flexible Robot Dynamics. No. 3, pp. 416-429.
- Carvalho, João Carlos Mendes;** Formulation of the Direct and Inverse Geometric Model of the Fully Parallel Cartesian Structure; No. 3, pp. 445-453.
- Castro, Jaime Tupiassú Pinho de;** Fatigue Propagation of Superficial Semi and Quart-Elliptical Cracks in Wet Welds (in Portuguese); No. 2, pp. 263-277.

Cavalca, Katia Lucchesi; Non-Linear Analysis of Hidrodynamical Bearings in a Vertical Shaft (in Portuguese); No. 2, pp. 244-262.

Conci, Aura; A Model for Analysis of Wire Rope with Complex Cross Section (in Portuguese); No. 2, pp. 278-297.

Costa, Carlos Eduardo S. M.; Second Law Analysis For Balanced Heat Exchangers With Negligible Pressure Drop Irreversibility; No. 2, pp. 156-163.

Cotta, Renato M.; The Generalized Integral Transform Technique in Transient Convection-Diffusion: Theory, Applications and Research Needs; No. 2, pp. 179-200.

Cuschieri, A.; Design and Control Criteria for a New Type of Surgical Robot; No. 3, pp. 430-436.

D

Dias, Antonio Carlos Pires; Analysis of the Behaviour of Conventional Grinding Wheel as a Function of the Machining Parameters and the Bond Kind (in Portuguese); No. 3, pp. 390-399.

E

Elmer, Kael-Heinz; A Time Dependent Adaptive Finite Element Method; No. 4, pp. 583-591.

F

Fernandes, Odilson Coimbra; Analysis of the Behaviour of Conventional Grinding Wheel as a Function of the Machining Parameters and the Bond Kind (in Portuguese); No. 3, pp. 390-399.

Fordham, M. J.; Rapid Thermal Processing Furnace With Three Heating Zones; No. 4, pp. 528-537.

Frank, T.; Design and Control Criteria for a New Type of Surgical Robot; No. 3, pp. 430-436.

Freire, Atila Pantaleão Silva; The State of the Art in Turbulence Modelling in Brazil; No. 1, pp. 1-38.

Freitas, Daniel S.; Modeling and Simulation of Double-Spherical Aerostatic Bearings (in Portuguese); No. 1, pp. 126-142.

G

Giassone, Adrian; Fatigue Propagation of Superficial Semi and Quart-Elliptical Cracks in Wet Welds (in Portuguese); No. 2, pp. 263-277.

Gonçalves, Regina Fátima Gibson; Control of Rolled Strips Thickness Using Fuzzy Logic (in Portuguese); No. 4, pp. 641-651.

Garcia, Luiz Fernando Taborda; Discussion About Geometrically Nonlinear Formulations for Combined Flexure and Torsion of Thin-Walled Open Bars (in Portuguese); No. 1, pp. 103-115.

H

Heitor, M. V.; On the Turbulent Transport Characteristics of Non Premixed Diffusion Flames in Mutual Interaction; No. 2, pp. 164-178.

Helman, Horacio; Control of Rolled Strips Thickness Using Fuzzy Logic (in Portuguese); No. 4, pp. 641-651.

Hervieu, Eric; Time Frequency Characterisation of Two-Phase Horizontal Air-Water Flow Regimes; No. 1, pp. 39-50.

Hewit, J. R.; Design and Control Criteria for a New Type of Surgical Robot; No. 3, pp. 430-436.

I

Ierardi, Maria Clara F.; Optical and Thermal Parameters Characterization in CO₂ Laser Application in Thermosensitive Resins Using Stereolithography; No. 2, pp. 146-155.

K

Kenedi, Paulo Pedro; Fatigue Propagation of Superficial Semi and Quart-Elliptical Cracks in Wet Welds (in Portuguese); No. 2, pp. 263-277.

Kiel, Alvin E.; Optical and Thermal Parameters Characterization in CO₂ Laser Application in Thermosensitive Resins Using Stereolithography; No. 2, pp. 146-155.

Kiether, W. J.; Rapid Thermal Processing Furnace With Three Heating Zones; No. 4, pp. 528-537.

Kurka, Paulo Roberto Gardel; Automatic Process for the Determination of Modal Supersets of Residual Flexibilities Used in The Modal Synthesis Method; No. 4, pp. 652-661.

L

Leal, Marco A.; The Generalized Integral Transform Technique in Transient Convection-Diffusion: Theory, Applications and Research Needs; No. 2, pp. 179-200.

Leite, Antonio Pralon Ferreira; Thermodynamic Analysis and Modeling of an Adsorption-Cycle System for Refrigeration from Low-Grade Energy Sources; No. 4, pp. 514-527.

Lima, Everton Nogueira; Non-Linear Analysis of Hidrodynamical Bearings in a Vertical Shaft (in Portuguese); No. 2, pp. 244-262.

Lima, Fernando Roberto de Andrade; Sensitivity Studies in a Simplified PWR-Hot-Channel Model Using Perturbation Theory by Matricial Formalism (In Portuguese); No. 2, pp. 201-218

Lira, Carlos Alberto Brayner de Oliveira; Sensitivity Studies in a Simplified PWR-Hot-Channel Model Using Perturbation Theory by Matricial Formalism (In Portuguese); No. 2, pp. 201-218

M

Machado, H. A.; Inverse Problem for Estimating the Heat Flux to a Non-Newtonian Fluid in a Parallel Plate Channel; No. 1, pp. 51-61.

Machado, José António Tenreiro; On the Statistical/Harmonic Modelling of Mechanical Manipulators; No. 3, pp. 437-444.

Maciel, Edisson Sávio de Goés; Sensitivity Studies in a Simplified PWR-Hot-Channel Model Using Perturbation Theory by Matricial Formalism (In Portuguese); No. 2, pp. 201-218

Maciel, Edisson Sávio de Goés; Comparison of Implicit Approximate Factorization Algorithms in the Solution of the Navier-Stokes Equations (in Portuguese); No. 3, pp. 353-380.

Maliska, Clovis Raimundo; Evaluation of Some Interpolation Schemes for Fluid Flow Calculations Using Finite Volumes (in Portuguese); No. 3, pp. 340-352.

Mansur, Sérgio Said; Numerical Simulation of Multitubular Heat Exchangers Equipped with Twisted Tapes Outside the Tubes (in portuguese); No. 1, pp. 79-90.

Marchi, Carlos Henrique; Evaluation of Some Interpolation Schemes for Fluid Flow Calculations Using Finite Volumes (in Portuguese); No. 3, pp. 340-352.

Maruyama Newton; Detecting Faults in Cooling Coils of Air-Handling Units - Part I : The Method and Some Simulation Results; No. 4, pp. 607-623.

Maruyama, Newton; Detecting Faults in Cooling Coils of Air-Handling Units - Part II : The Issues of Practical Implementation; No. 4, pp. 524-640.

Mazza, Ricardo Augusto; Non-Linear Analysis of a Pulse - Duplicator Flow Device (in Portuguese). No. 3, pp. 325-339.

Mello, Olympio A. F.; On the Application of Flight Simulation to the Investigation of Helicopter Accidents; No. 4, pp. 592-606.

Mercier, Pierre; Numerical Simulation of Multitubular Heat Exchangers Equipped with Twisted Tapes Outside the Tubes (in Portuguese); No. 1, pp. 79-90.

Moreira, A. L. N.; On the Turbulent Transport Characteristics of Non Premixed Diffusion Flames in Mutual Interaction; No. 2, pp. 164-178.

Munhoz, Andre; Optical and Thermal Parameters Characterization in CO₂ Laser Application in Thermosensitive Resins Using Stereolithography; No. 2, pp. 146-155.

N

Natke, Hans Güntler; A Time Dependent Adaptive Finite Element Method; No. 4, pp. 583-591.

Nohara, Ben T.; An Absorption Algorithm and Its Implementation for Irregular Ocean Waves in a Test Tank; No. 4, pp. 549-559.

O

Orlande, Helcio R. B.; Inverse Problem for Estimating the Heat Flux to a Non-Newtonian Fluid in a Parallel Plate Chanel; No 1, pp. 51-61.

Ortiz, Jayme Pinto; Study of the Polyacrylamide Iqapol PA Influence on Drag Reduction in Turbulent Flow (In Portuguese); No. 2, pp. 219-232

P

Pacheco, Pedro Manuel Calas Lopes; On the Effect of Temperature in Non-Linear Dynamics of an Elasto-Plastic Oscillator With Isotropic Hardening; No. 4, pp. 572-582.

Pinotti, Marcos; Shear Stresses and Turbulent Eddies: The Causes of Mechanical Hemolysis in a Centrifugal Blood Pump (in Portuguese); No. 4, pp. 538-548.

Poilillo, Vera Regina; Discussion About Geometrically Nonlinear Formulations for Combined Flexure and Torsion of Thin-Walled Open Bars (in Portuguese); No. 1, pp. 103-115.

Prata, Alvaro Toubes; Modeling and Simulation of Double-Spherical Aerostatic Bearings (in Portuguese). No. 1, pp. 126-142.

R

Remacre, Armando Zaupa; Reduction of Uncertainties in Characterization of Reservoirs Using Stochastic Simulation and Production History Adjustment (in Portuguese); No. 3, pp. 381-389.

Rodrigues, Luis Glauber; Reduction of Uncertainties in Characterization of Reservoirs Using Stochastic Simulation and Production History Adjustment (in Portuguese); No. 3, pp. 381-389.

Rosa, Eugênio Spanó; Non-Linear Analysis of a Pulse - Duplicator Flow Device (in Portuguese); No. 3, pp. 325-339.

S

- Saboya, Francisco Eduardo Mourão;** Second Law Analysis For Balanced Heat Exchangers With Negligible Pressure Drop Irreversibility; No. 2, pp. 156-163.
- Sampaio, Rubens;** Multibody Systems Collisions (in Portuguese); No. 1, pp. 116-125.
- Santos, Antônio Moreira;** Time Frequency Characterisation of Two-Phase Horizontal Air-Water Flow Regimes; No. 1, pp. 39-50.
- Santos, Luiz Claudio C.;** The State of the Art in Turbulence Modelling in Brazil; No. 1, pp. 1-38.
- Santos, Maria Angela Vaz;** Numerical Simulation of Three Dimensional Compressible Flows Using Finite Elements with Mixed Structured-Unstructured Meshes; No. 1, pp. 62-78.
- Savi, Marcelo Amorim;** On the Effect of Temperature in Non-Linear Dynamics of an Elasto-Plastic Oscillator With Isotropic Hardening; No. 4, pp. 572-582.
- Scarpato, Marco A. F.;** Optical and Thermal Parameters Characterization in CO₂ Laser Application in Thermosensitive Resins Using Stereolithography; No. 2, pp. 146-155.
- Schiozer, Denis José;** Reduction of Uncertainties in Characterization of Reservoirs Using Stochastic Simulation and Production History Adjustment (in Portuguese); No. 3, pp. 381-389.
- Scotti, Américo;** A Review on Special Metal Transfer Modes in Gas Metal Arc Welding; No. 3, pp. 465-478.
- Selegim Junior, Paulo;** Time Frequency Characterisation of Two-Phase Horizontal Air-Water Flow Regimes; No. 1, pp. 39-50.
- Silva Jr, Carlos Elias;** Analysis of the Behaviour of Conventional Grinding Wheel as a Function of the Machining Parameters and the Bond Kind (in Portuguese); No. 3, pp. 390-399.
- Silva, Felipe M.;** On the Statistical/Harmonic Modelling of Mechanical Manipulators; No. 3, pp. 437-444.
- Silva Neto, A. J. Silva;** Rapid Thermal Processing Furnace With Three Heating Zones; No. 4, pp. 528-537.
- Silva, Wilson Ferreira da;** A Model for Analysis of Wire Rope with Complex Cross Section (in Portuguese); No. 2, pp. 278-297
- Slade, A. P.** Design and Control Criteria for a New Type of Surgical Robot; No. 3, pp. 430-436.
- Sodré, J.R.;** A Parametric Study on the Influence of the Spark Plug Position on Combustion, Emissions and Performance of an Engine; No. 4, pp. 502-513.
- Sorrel, F. Y.;** Rapid Thermal Processing Furnace With Three Heating Zones; No. 4, pp. 528-537.
- Souza Jr., Jessé Rebello;** Boundaries of Safe Motion Through a Coarse Grid-of-Starts; No. 4, pp. 560-571.
- Souza, Selene Maria de Arruda Guelli Ulson;** Evaluation of Some Interpolation Schemes for Fluid Flow Calculations Using Finite Volumes (in Portuguese); No. 3, pp. 340-352.

T

- Tavares Junior Hugo M.;** Multibody Systems Collisions (in Portuguese); No. 1, pp. 116-125.
- Takase, Kawaoka Fábio;** Manipulating Information of Dependencies to Support CAD 3D Systems – Solids Modeling – by Application of ATMS (in Portuguese); No. 3, pp. 400-415.
- Teixeira, Paulo Roberto de Freitas;** Numerical Simulation of Three Dimensional Compressible Flows Using Finite Elements with Mixed Structured-Unstructured Meshes; No. 1, pp. 62-78.
- Tsuzuki, Marcos Sales Guerra;** Manipulating Information of Dependencies to Support CAD 3D Systems – Solids Modeling – by Application of ATMS (in Portuguese); No. 3, pp. 400-415.

U

- Ulbrich, Heinz;** Active Control of Partially Filled, Elastically Mounted Centrifuges; No. 3, pp. 454-464.

V

Vieira Jr, Milton; Analysis of the Behaviour of Conventional Grinding Wheel as a Function of the Machining Parameters and the Bond Kind (in Portuguese); No. 3, pp. 390-399.

Villaça, Sergio Fernandes; Discussion About Geometrically Nonlinear Formulations for Combined Flexure and Torsion of Thin-Walled Open Bars (in Portuguese); No. 1, pp. 103-115.

W

Wagner, Paulo R. S.; Optical and Thermal Parameters Characterization in CO₂ Laser Application in Thermosensitive Resins Using Stereolithography; No. 2, pp. 146-155.

Y

Yates, David A., A Parametric Study on the Influence of the Spark Plug Position on Combustion, Emissions and Performance of an Engine; No. 4, pp. 502-513.

Information for Authors

- SCOPE AND POLICY**
- The purpose of the Journal of the Brazilian Society of Mechanical Sciences is to publish papers of permanent interest dealing with research, development and design related to science and technology in Mechanical Engineering, encompassing interfaces with Civil, Electrical, Chemical, Naval, Nuclear, Materials, Aerospace, Petroleum, System Engineering, Food, Agriculture, etc., as well as with Physics and Applied Mathematics.
 - The Journal publishes Full Length Papers, Review Papers, Book Reviews and Letters to the Editor. Authors must agree not to publish elsewhere a paper submitted and accepted by the Journal. Papers previously published in proceedings of conferences can also be considered for publication; this event should be cited as a footnote on the title page. Copies of the conference referees' reviews should be included. Review articles should constitute a critical appraisal of the published information.
 - The decision of acceptance for publication lies with the Editors and is based on the recommendations of at least two ad hoc reviewers, and of the Editorial Board, if necessary.
- SUBMISSION**
- Manuscripts and correspondence should be sent to the Editor or, alternatively, to the nearest Associate Editor.
 - Five (5) copies of the paper are required. The Author should retain the manuscript disk until the end of the review process.
 - Manuscripts should be submitted only in **English**.
 - A manuscript submitted for publication should be accompanied by a cover page containing the full name of the Author(s), the Author for contact, institution address, phone number, e-mail address and, if the Authors so wish, the names of up to five (5) possible referees, with respective addresses.
- FORMAT**
- Manuscripts should begin with the title, followed by an Abstract and from three to five Keywords. The manuscript should not contain the Authors' names. The Abstract should state the objectives, methodology used and main conclusions, in no more than 200 words.
 - In research papers sufficient information should be provided in the text, or by referring to papers in generally available Journals, to permit the work to be repeated.
 - The paper must begin with an Introduction that is written for the general reader of the Journal, not for the specialist. This section should describe the problem statement, its relevance, significant results and conclusions from prior work, and objectives of the present work.
 - Uncertainties should be specified for experimental and numerical results.
 - Manuscripts should be typed double-spaced, on one side of the page, using A4 sized paper, with 2 cm margins. The pages should be numbered and not to exceed 24, including tables and figures. Avoid footnotes.
 - All symbols should be defined in the text. A separate nomenclature section should list, in alphabetical order, the symbols used and their definitions. The Greek symbols follow the English symbols, and are followed by the subscripts and superscripts. Each dimensional symbol must have SI (metric) units mentioned; in addition, English units may be included parenthetically. Dimensionless groups and coefficients must be so defined and indicated.
- MATHEMATICAL EQUATIONS**
- All mathematical expressions should be typewritten using only letters and symbols available on the keyboard.
 - Equations that extend beyond the text width should be restated to go in two or more lines, as necessary to fit within the page width.
 - Fractional powers should be used instead of root signs.
 - A solidus (/) should be used instead of an horizontal line for fractions, whenever possible; for example, use $2/3$ for two-thirds.

- Mathematical expressions should not be introduced along the text itself, as part of a sentence line, but typed on individual lines.
- Numbers that identify mathematical expressions should be enclosed in parenthesis. Refer to equations in the text as "Eq.(1)" or, if at the beginning of a sentence, as "Equation (1)".
- Vectors should be typed **boldface**. Do not use arrows, wavy-line underscoring, etc.

FIGURES AND TABLES

- Figures and Tables should be referred in consecutive Arabic numerals. They should have a caption and be placed as close as possible to their first reference in the text. Refer to figures in the text with the abbreviation "Fig. 1", except at the beginning of a sentence, where "Figure 1" should be used.
- The figures presenting technical data/results should have a boundary on all four sides, with scale indicators (tick marks) on all sides.
- The legend for the data symbols should be put inside the figure, as well as the labels for each curve. Lettering should be large enough to be clearly legible (1.5-2.0 mm).
- Laser print output line drawings are preferred. Drawings prepared on tracing paper or vellum, using black india ink, are acceptable.
- Photographs must be glossy prints.

REFERENCES

- References should be cited in the text by giving the last name of the author(s) and the year of publication. Either use "Recent work (Smith and Farias, 1997)" or "Recently Smith and Farias (1997)". With four (4) or more names, use the form "Smith et al. (1997)". If two or more references would have the same identification, distinguish them by appending "a", "b", etc., to the year of publication.
- Acceptable references include journal articles, numbered papers, dissertations, thesis, published conference proceedings, preprints from conferences, books, submitted articles, if the journal is identified, and private communications.
- References should be listed in alphabetical order, according to the last name of the first author, at the end of the paper. Some sample references follow:
- Soviero, P.A.O. and Lavagna, L.G.M., 1997, "A Numerical Model for Thin Airfoils in Unsteady Motion", RBCM- J. of the Brazilian Soc. Mechanical Sciences, Vol.19, No. 3, pp. 332-340.
- Bordalo, S.N., Ferziger, J.H. and Kline, S.J., 1989, "The Development of Zonal Models for Turbulence", Proceedings of the 10th Brazilian Congress of Mechanical Engineering, Vol.1, Rio de Janeiro, Brazil, pp. 41-44.
- Sparrow, E.M., 1980a, "Forced Convection Heat Transfer in a Duct Having Spanwise-Periodic Rectangular Protuberances", Numerical Heat Transfer, Vol.3, pp. 149-167.
- Sparrow, E.M., 1980b, "Fluid-to-Fluid Conjugate Heat Transfer for a Vertical Pipe-Internal and External Natural Convection", ASME Journal of Heat Transfer, Vol.102, pp. 402-407.
- Silva, L.H.M., 1988, "New Integral Formulation for Problems in Mechanics" (In Portuguese), Ph.D. Thesis, Federal University of Santa Catarina, Florianópolis, S.C., Brazil, 223 p.
- Coimbra, A.L., 1978, "Lessons of Continuum Mechanics", Ed. Edgard Blücher, S.Paulo, Brazil, 428 p.
- Clark, J.A., 1986, Private Communication, University of Michigan, Ann Harbor.
- Upon notification of acceptance, Authors should submit two copies of the final version and the manuscript disk, in Windows or Macintosh, Word or WordPerfect, thus avoiding retyping, with subsequent reduction of errors.

FINAL VERSION OF THE
MANUSCRIPT

(Contents Continued)

- Detecting Faults in Cooling Coils of Air-Handling Units - Part II: The Issues of Practical Implementation
Newton Maruyama 628

- Control of Rolled Strips Thickness Using Fuzzy Logic (In Portuguese)
Regina Fátima Gibson Gonçalves and Horacio Helman 645

- Modal Analysis**
- Automatic Process for the Determination of Modal Supersets of Residual Flexibilities Used in the Modal Synthesis Method
Paulo Roberto Gardel Kurka and Cleudmar Amaral de Araújo 656

- Fatigue**
- ViDa 98 - Visual Damagemeter to Automatize the Fatigue Design Under Complex Loading (In Portuguese)
Marco Antonio Meggiolaro and Jaime Tupiassú Pinho de Castro 666

- Abstracts - Vol. 20 - No. 4 - December 1998** 686

- Errata** on a Paper by Edisson Sávio de Góes Maciel and João Luiz Filgueiras de Azevedo 665

- Book Review**
- *Dinâmica*, by Roberto A. Tenenbaum
Peter Hagedorn 690

- Authors Index - Vol. 20 - 1998** 692

- Information for Authors** 698

<i>In Memoriam Prof. Cirus M. Hackenberg</i>		484
<i>Two-Phase Flow</i>		
• Analysis of Impedance Probes Behavior Applied to Liquid Film Thickness Measurements	Milton Biage	486
<i>Internal Combustion Engines</i>		
• A Parametric Study on the Influence of the Spark Plug Position on Combustion, Emissions and Performance of an Engine	J.R. Sodré and David A. Yates	506
<i>Adsorption Cooling</i>		
• Thermodynamic Analysis and Modeling of an Adsorption-Cycle System for Refrigeration from Low-Grade Energy Sources	Antonio Pralon Ferreira Leite	518
<i>Furnace Modeling</i>		
• Rapid Thermal Processing Furnace with Three Heating Zones	A. J. Silva Neto, M. J. Fordham, W. J. Kiether and F. Y. Sorrel	532
<i>Bioengineering</i>		
• Shear Stresses and Turbulent Eddies - The Causes of Mechanical Hemolysis in a Centrifugal Blood Pump (In Portuguese)	Marcos Pinotti and Domingo M. Braile	542
<i>Ocean Waves</i>		
• An Absorption Algorithm and its Implementation for Irregular Ocean Waves in a Test Tank	Ben T. Nohara	553
<i>Dynamics</i>		
• Boundaries of Safe Motion Through a Coarse Grid-of-Starts	Jessé Rebello de Souza Jr. and Steven R. Bishop	564
• On the Effect of Temperature in Non-Linear Dynamics of an Elasto-Plastic Oscillator with Isotropic Hardening	Marcelo Amorim Savi and Pedro Manuel Galas Lopes Pacheco	576
• A Time Dependent Adaptive Finite Element Method	Karl-Heinz Elmer and Hans Günther Natke	587
<i>Flight Simulation</i>		
• On the Application of Flight Simulation to the Investigation of Helicopter Accidents	Olympio A. F. Mello	596
<i>Fuzzy Logic</i>		
• Detecting Faults in Cooling Coils of Air-Handling Units - Part 1: The Method and Some Simulation Results	Newton Maruyama	611